University College London

Computational Study of Acid-Catalyzed Reactions in Zeolites

Thesis submitted for the degree of Doctor of Philosophy (PhD) by

Rushita Mehta

Supervisors

Prof. Furio Cora & Dr. Robert Bell

University College London
Department of Chemistry
November, 2020

Declaration

I, Rushita Mehta, hereby declare that this these titled "Computational study of acid-catalyzed reactions in zeolites" is my own work and that all materials from other sources have been properly and fully acknowledged.

Sign: .....

Date: .....

Abstract

Aldol condensation is a very important reaction in organic synthesis because it leads to the formation of C-C bonds. Because of that, the use of different catalysts and in particular the use of zeolites for the catalysis of this reaction has been previously studied. The first step of aldol condensation is the the acid-catalyzed keto-enol tautomerization of the aldehyde or ketone. In this thesis, we study all the possible locations of BA sites in the vicinity of each of the defined inequivalent T site positions in FER and MOR zeolites and establish the most stable location of proton siting at force field and periodic DFT level. The reactions involving the small carbonyl compounds, acetaldehyde and acetone, are studied at the specific acid site locations in both zeolites in order to discover which are the active sites that can stabilize the reactants and therefore how the existing catalyst can be improved. Besides the H-bonding and other interactions, the confinement effect are of equal importance in the determination of factors that influence the reactivity of these complexes.

In order to understand the keto-enol tautomeric mechanism in zeolites and identify the transition states, constrained geometry optimizations were performed of acetaldehyde in FER and MOR using periodic DFT. From this we determined the formation of enol product via and an one and two-step concerted mechanism. The calculations reveal that C-β deprotonation is the kinetic bottleneck for enol formation. The concerted mechanism was performed at each of the inequivalent T position in both zeolites. We found that proton transfer is a consequence of a cooperation between the acid site and its total environment acting on the molecular adsorbate. The adsorption and stability of the intermediates is dependent upon the

heterogeneity of acid sites and their local geometry, the pore channels and cavities and interactions such as dispersive and H-bonding that do not reflect, and are often independent of, acid strength.

Thirdly, we studied the keto-enol tautomerization of acetaldehyde in FER and MOR in the presence of a single water or methanol molecular and found the activation barriers to reduce further with an increase in stability of the adsorbed enol form with larger reverse barriers in the larger pores of FER. We establish the importance of the specific role of the H-bonding using these solvent molecules. In the smaller pores of MOR, the presence of a solvent supresses the catalytic interconversion due to steric repulsion.

Lastly, we explored the location of monovalent alkali ions in FER and found that the most stable location of the cations is in the FER cavity and dependent upon the Al position. We studied the effect of hydration on the mobility of the cesium ion in the cavities of FER using static DFT calculations supplemented with ab initio molecular dynamics. We estabished the cesium ion prefers to coordinate with the framework oxygens of the zeolite rather than oxygen atoms of the water molecules as well as the position of the cesium ion is affected by the Al siting. The coordination number of cesium is ~ 10 with the ion interacting with only 1-3 water molecules. In addition, we identified a self-organization of water molecules across the channels forming a H-bonding network.

Table of contents

Acknowledgements

First of all, I would like to thank my supervisors, Prof. Furio Cora and Dr. Robert Bell, for providing me with the opportunity to carry out this research, as well as the generous support and guidance throughout the years. I am very grateful for all the help and the friendly atmosphere during our meetings. Also, I would like to thank all the members of Rooms 105, for all their help, lively discussions and laughter when most needed. I would like to thank EPSRC and the BP chemicals (Dave Law and Russell Taylor) for the funding and also the latter for their guidance. Finally, I want to especially thank my family, my husband, and friends for all the constant love, support, encouragement and motivation throughout this PhD. This thesis would not have been possible without them.

List of Tables

List of Figures

Chapter 1

Introduction

1.1 General Overview of Zeolites

A zeolite is defined as a crystalline aluminosilicate with a three-dimensional framework structure consisting of TO_4 tetrahedra connected to form a network containing uniformly sized pores of molecular dimensions. (Catlow. *et al*., 1995) The constituent T atoms of the framework may be silicon and aluminum linked by single oxygen atoms, the ordering of which is defined by Lowenstein's rule (Lowenstein, 1954) - a disinclination for tetrahedral units of Al to exist adjacent to one another. These tetrahedra join to create rings, cages, and supercages and then join to subsequently form pores and channels. These are usually occupied by H_2O molecules and extra-framework cations that are commonly exchanged. In the hydrated phases, dehydration occurs at modest temperatures (500 - 600 K) and are largely reversible.

Zeolites are also classified as microporous materials and, as their pores are of molecular size, can be used as molecular sieves (Barthomeuf, 1991, Flanigen, 2001, Smith, 1988). Their exceptional applicability stems from their high hydrothermal stability, their ability to act as molecular sieves for selective adsorbents, their relatively high acid strength, the associated high internal surface area, and the reproducibility with which they can be synthesized and modified. Each of these notable properties derives directly from their crystalline structure. Their well-determined topology and microporous structure with these associated properties render them as attractive materials in a wide range of applications such as ion-exhangers, in adsorption processes, and in heterogeneous catalysis.

Zeolites occur naturally as minerals, although most of the materials used in industrial applications are synthesized using hydrothermal procedures, in which an aqueous synthesis gel containing Si and Al, inorganic and/or organic cation sources, usually in a basic (high pH) medium is treated under moderate temperatures and pressures in which the material crystallizes. The structural formula of a zeolite for a crystallographic unit cell is:

$$M_{x/n}[(AlO_2)_x(SiO_2)_y].wH_2O$$

where M represents the exchangeable cation of valence n, x is the number of AlO4 tetrahedra, y is the number of SiO4 tetrahedra and w is the number of water molecules per unit cell. The ratio between y and x is called the Si/Al ratio (Catlow. *et al*., 1995). The exact Si/Al ratio depends on the crystalline size and the porosity.

1.1.2 Framework Structure

The primary building unit (PBU) of the zeolite structure has a central atom, Si or Al, surrounded by four oxygen atoms at the apexes in a form of a tetrahedron - TO_4. Each oxygen is shared between two tetrahedra. **Figure 1-1** shows a schematic representation of the tetrahedral PBUs, which are the building blocks of the framework structure. In accordance to the Lowenstein's rule where two AlO_4 members cannot be located in direct vicinity in a zeolite structure implies that the zeolites must have a minimum Si/Al ratio of unity. Zeolites constructed from SiO_4 and AlO_4 tetrahedra results in a negatively charged structure of which is compensated by extraframework cations, namely alkali and alkaline-earth, transition metals and organic cations. These cations in the channels are commonly exchanged and are usually allowed to move freely inside the zeolite.

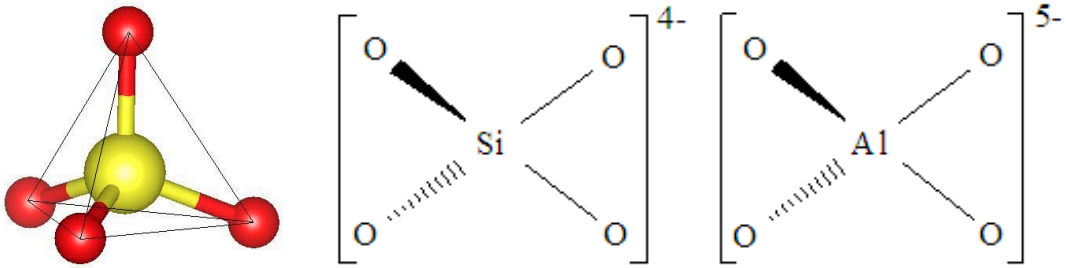

Figure 1-1. Tetrahedral arrangement of SiO_4 or AlO_4 primary building unit of the zeolite structure (Si or Al atom shown in yellow surrounded by 4 oxygen atoms in red spheres)

Meier (Meier, 1968) introduced a concept based on Secondary Building Unit (SBU) in order to simplify and systematically classify the zeolite structure description. The tetrahedral units are connected to form larger units, known as SBU. SBU's which may contain up to 16 T-atoms, are derived assuming that the entire framework is made up of one type of SBU only. It is noted that they are invariably non-chiral. A zeolite's unit cell always contains an integral number of them. At present, 23 different types of SBUs are known to exist (Baerlocher *et al*., 2007). Breck (Breck, 1974) proposed a structural classificiation system detailing seven major groups based on the geometry of SBUs and a schematic representation is shown in **Figure 1-2**. The corners of the units represent Si or Al atoms and the connecting lines represent the shared oxygen atoms.

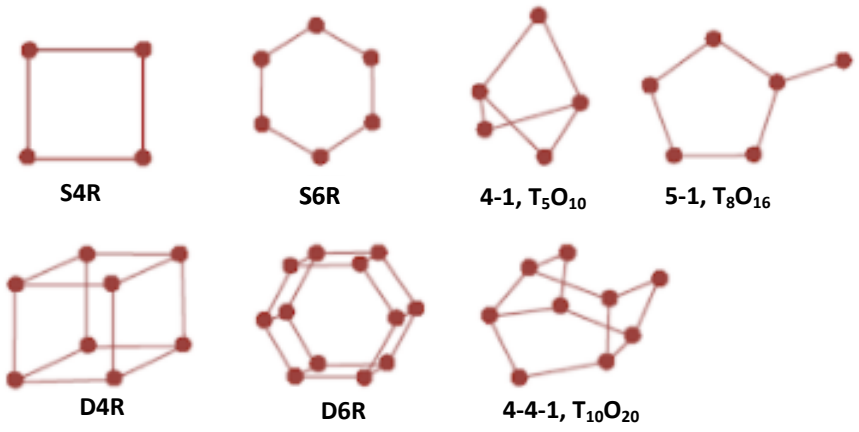

Figure 1-2. Seven Secondary Building Units (SBU) groups proposed by Breck.

These SBU's connect to form a wide range of polyhedra such as rings, prisms, cages, pores and channels, which in turn connect to form the infinitely extended frameworks of the various specific zeolite crystal structures. Thus, the way that the SBU's are assembled determines the morphology of the zeolite. Each structure is described by its own system of channels, their cavities and connectivity, wherein the recurring polyhedra features are also commonly shared with other zeolites.

The size of the ring in a zeolite depends on the number of tetrahedrons that constitute it, known as "members" of the rings. A ring therefore consisting of n tetrahedrons is called n-Membered Ring (n-MR). The size of the rings in the framework determines the pore size in different zeolites. The entrance to the pore is known as a window. In general, zeolites can also be classified by their topologies defining the type and size of small (< 4.5 Å, 8-MR), medium (< 6 Å, 10-MR), large (< 8 Å, 12-MR) and ultralarge micropores (> 8 Å, > 14-MR). The variability of these pore dimensions permits a selective accommodation of molecules inside this network and can promote or inhibit different reaction intermediate in catalytic reactions. The connectivity between the pores, forming the latter network determines the diffusion of guest molecules in one, two or three dimension channel systems. The International Zeolite Association (IZA) has a structure commission whose purpose is to clarify and collate the new topologies and assign new structure type codes. This commission assigns three letter codes to each framework topology and are based on the name of the naturally occurring or synthetic zeolites. The International Zeolite Association (IZA) has a structure commission whose purpose is to clarify and collate the new topologies and assign new structure type codes. This commission assigns three letter codes to

each framework topology and are based on the name of the naturally occurring or synthetic zeolites.

1.2 Brønsted Acidity in Zeolites

In this thesis, we focus on the use of zeolites as catalysts in chemical reactions. Despite the important properties of zeolites mentioned earlier having a successful application in heterogeneous catalysis, the essential factor for most catalytic purposes is the presence of isolated and well-defined active sites in the zeolite framework. As mentioned, the substitution of tetrahedrally coordinated framework Si atom with a trivalent Al atom results in a negatively charged structure of which can be compensated by cations (alkali and alkaline, transition metal and organic cation), occupying extra-framework sites in the channels and cages. These cations are commonly exchanged and are usually allowed to move freely inside the zeolite. The most important compensation is by protons which bond to the bridging oxygen atoms, thereby creating Brønsted Acid (BA) sites (**Figure 1-3**) (Corma, 1995, Sauer, 1989, Vansanten and Kramer, 1995). Protons leading to BA sites are usually introduced in zeolites after crystallization by either direct ion-exchange or by thermolyzing ammonium or other proton precursor cations. (Pellet, *et al*., 1988) In contrast to metal cations, the bridging hydroxyl group occupies a tetrahedon apex and is not shared between adjacent tetrahedra leading to an interruption in the framework. Protons cause substantial changes in the bonds surrounding the newly formed hydroxyl groups. The three O-Al, O-Si, and O-H bonds are covalent bonds superimposed by small electrostatic interactions and the O atom in this non classical simulation has therefore a formal three-fold coordination similar to that present in the hydronium cation, H_3O^+. The geometric

restrictions imposed by the crystalline structure of the zeolite limits the flexibility around this O atom, thus weakening the OH bond and generating acidity.

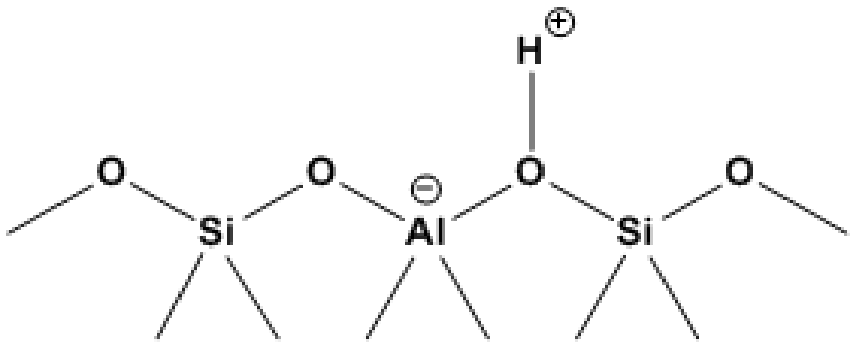

Figure 1-3. Representation of Brønsted acidity in zeolites

1.2.1 Factors controlling the intrinsic acidity

The location, strength and accessibility of BA sites is dependent upon zeolite synthesis including the structural directing agent (SDA), time, temperature, concentration and Al content. Clearly, the number of BA sites is dependent upon the framework Si/Al ratio and hence the Al distribution in a zeolite is considered to be the primary determinant for the acid strength. An increase in the acid strength with rising Si/Al ratio essentially means that the O-H bond becomes more ionic in Si-rich zeolites based on Si having a higher electronegativity than Al, thus shifting the electrons from the proton to the O atom. There is a balance between total acidity (i.e. number of acid sites) and strength of acidity. As Si/Al ratio rises, the number of acid sites will decrease, but their strength will increase. Conversely, a high Al content structure will have a large number of relatively weak acid sites. This is due to proton crowding in zeolite pores. From previous theoretical calculations, the arrangement of Al atoms have a dominant influence on the acidity. To quantify the effect of the Si/Al ratio on the acid strength, the influence

of which depends on the zeolite structure type, Barthomeuf *et al.* (Barthomeuf, 1987) used the concept of topological densities to evaluate the number of next nearestneighbour (NNN) Al sites (in up to 5 layers surrounding a given Al site) for various zeolites. This essentially means that at high Si/Al ratio, and consequently a low Al content, in the unit cell all Al atoms are isolated possessing a high acid strength. With increasing the number of Al in the lattice, the number of strong acid site rises. If there are Al atoms instead of Si atoms in the second coordination sphere, the number of strong acid site diminishes, although the total number of acid site increases further. The closeness of the Al atoms causes the Si-O-Al angle to change leading to a decrease in the acidity (Dwyer and OMalley, 1988). This explanation suggests that the strong acidity is connected with isolated Al atoms and that the strong acidity reaches a maximum value at that Si/Al ratio of the lattice at which no next Al neighbor exists in the second coordination sphere.

The presence of these bridging hydroxyl groups, with their BA characteristics, have opened zeolites to a large number of industrial applications making them the most widely used solid acid catalysts in the industry. They are employed in large-scale commercial processes such as oil refining, petrochemistry, and the fine chemical production industries for BA catalyzed reactions such as cracking, hydrocracking, isomerization and alkylation of hydrocarbons, as well as the conversion of methanol to olefins (MTO) and methanol to gasoline (MTG) processes (Bhan and Iglesia, 2008, Haw, *et al*., 2003, Yilmaz and Muller, 2009).

The ease and speed at which proton transfer process occurs in zeolites depends on several factors making it difficult to quantify the intrinsic acid strength and correlate

acidity with catalytic activity in the hopes of optimizing zeolite design. The microporous structure in zeolites on the basis of the geometrical curvature of their internal surface is essentially complex. This includes the shape selectivity effects, which modify the adsorption and diffusion of reactants and products, or prevents the formation of certain transition states and intermediates with the zeolite framework. Additionally, the heterogeneity of Brönsted acidity contains a distribution of the sites with various intrinsic acid strengths associated to differences in location within pores, channels and cavities, local geometry and the proton pointing in different chemical environments. All these attributes influence the overall catalytic performance of acidic zeolites and make it difficult to ascertain an acidity scale as well as a clear correlation between acidity and reactivity (Boronat and Corma, 2015, Derouane, *et al*., 2013).

All these above mentioned aspects of zeolite acidity have been studied extensively by various authors. The characterization of the nature, strength, distribution and density of acid sites in zeolites has been established by several techniques, which in turn provide information to predict the catalytic activity in acidic zeolites (Boronat and Corma, 2015, Derouane, *et al*., 2013, Farneth and Gorte, 1995, Sandoval-Diaz, *et al.*, 2015). Conventionally, the acidic properties in zeolites are assessed experimentally by the adsorption of basic molecules such as amines, carbon monoxides and pyridine. Upon adsorption these bases react with the BA sites and the acid strength is correlated either directly to the heats of adsorption measured by calorimetry or temperature-programmed desorption (TPD) or indirectly to the degree of perturbation of the adsorbed molecules which can be monitored by spectroscopy *i.e.* Fourier transform infrared (FTIR) solid-state nuclear magnetic resonance (NMR)

(Bordiga, *et al*., 2015, Gorte and White, 1997, Lercher, *et al*., 1996, Sato, 1997, Zheng, *et al*., 2016).

The relationship between acidity and activity has also gained increased support from theoretical hetergeneous catalysis (Gounder and Iglesia, 2012, Sauer, *et al.*, 1994, van Santen and Kramer, 1995, van Speybroeck, *et al.*, 2015). The increase of computational capabilities has allowed for more detailed quantum chemical calculations both on the nature of the acid sites on zeolites and on its action in acid-catalyzed processes. One of the methods defining the strength of a BA site is by determining the deprotonation energy (DPE), the energy required to dissociate the Brønsted proton to an infinite distance from its conjugate anion (zeolite anion). DPE values do not depend on the proton acceptor, thus providing an acid strength scale that is independent of the reacting or adsorbing molecules involved (Brand, *et al*., 1992, Brand, *et al*., 1993, Brandle and Sauer, 1998, Grajciar, *et al*., 2010). Although this magnitude cannot be measured experimentally making comparisons unlikely and unable to give an idea of the degree of accuracy of the models used in theory. It is now widely accepted that the intrinsic acidity of BA sites in high Si/Al ratio zeolites determined by the deprotonation energy is independent of zeolite structure and site location within the framework. (Brandle and Sauer, 1998, Sauer and Sierka, 2000) Jones and Iglesia (Jones and Iglesia, 2015) performed a detailed study of deprotonation energies of isolated BA sites in several zeolites with different crystalline structure including chabazite, ferrierite (FER), mordenite (MOR), faujasite and MFI. In their study they found that the statisical ensemble average of the DPE values at each crystallographic unique Al position were similar among the zeolites indicating that the stability of the conjugate anions and the acid strength of these materials only reflect on the presence of the heteroatom (e.g. Al)

and not their specific siting or local confining environment. An alternative acidity descriptor for zeolites is the adsorption heat of bases which can be compared with experimental data. A few theoretical studies have demonstrated that the adsorption of probe molecules can be used as a good descriptor for the energy of transition states and intermediates of important catalytic reactions although other studies claim that the adsorption is dependent upon interactions such as the dispersive and H-bonding as well as the pore topology that do not reflect, and are often independent of, acid strength. (Borges, *et al*., 2005, Boronat and Corma, 2019, Brogaard, *et al*., 2014, , Liu, *et al*., 2017, Trombetta, *et al*., 1998 Wang, *et al*., 2014). In the next section, we focus on the zeolites, ferrierite (FER) and mordenite (MOR) in this thesis, and assess the acidity and catalytic activity examined previously using these techniques.

1.3 Ferrierite

1.3.1 Structure and Synthesis

FER zeolite has a two-dimensional pore structure as portrayed in **Figure 1-4 (a)**, with a main 10 MR channels [4.2 × 5.4 Å] running parallel to the *c* direction intersecting with perpendicular 8MR channels [3.5 × 4.8 Å] parallel to the *b* direction. (Arean, *et al*., 2007, Morris, *et al*., 1994, Pinar, *et al*., 2013, Vaughan, 1966) Between these intersections along the 8-MR channel, a cavity that is only accessible through the 8MR openings is formed. These FER cavities extend for 6.0 × 7.0 Å] in the *a* direction and are separated by 6-MR (Bordiga, *et al*., 2000). As reported by Pickering *et al*. (Pickering, *et al*., 1989) the conventional unit cell of zeolite FER is orthorhombic with *Immm* space and lattice vectors a = 18.651 Å, b = 14.173 Å, and c = 7.404 Å. The conventional unit cell of FER framework consists

of 108 atoms (36 framework atoms and 72 oxygen atoms). Dědeček *et al.* (Dědeček, *et al.*, 2011) determined the complete Al distribution in FER zeolite through a complex study combining Atomic Absorption, X-ray fluorescence, X-ray photoelectron, NMR and UV-visible spectroscopies, Co^{2+} exchange and DFT calculations. In their study, employing one isolated Al atom per unit cell identified five distinguishable structures corresponding to Al substitutions within the four T sites of the FER framework (Pickering*, et al.*, 1989), shown in **Figure 1-4 (b)**. The 16-fold T1 site splits into two 8-fold subsets (T1a and T1b) that of the T1 site. T1a and T1b differ in both the local $AlO4^{-}$ geometry as well as the ^{27}Al isotropic chemical shift. The 10-MRs are composed of T atoms in sites T1, T2, and T3, whereas 8MRs are composed of atoms in T1 and T2 sites. T4 site is exclusively located in the 6MR. With the four T sites, there are eight symmetry independent oxygen sites (O1 – O8). (Vaughan, 1966) Three of the oxygen sites (O4, O5 and O8) lie between equivalent T atoms, while the remaining five oxygen sites (O1, O2, O3, O6 and O7) lie between non-equivalent T atoms. (O3 does not lie between equivalent T atoms as T1 site is split into T1a and T1b).

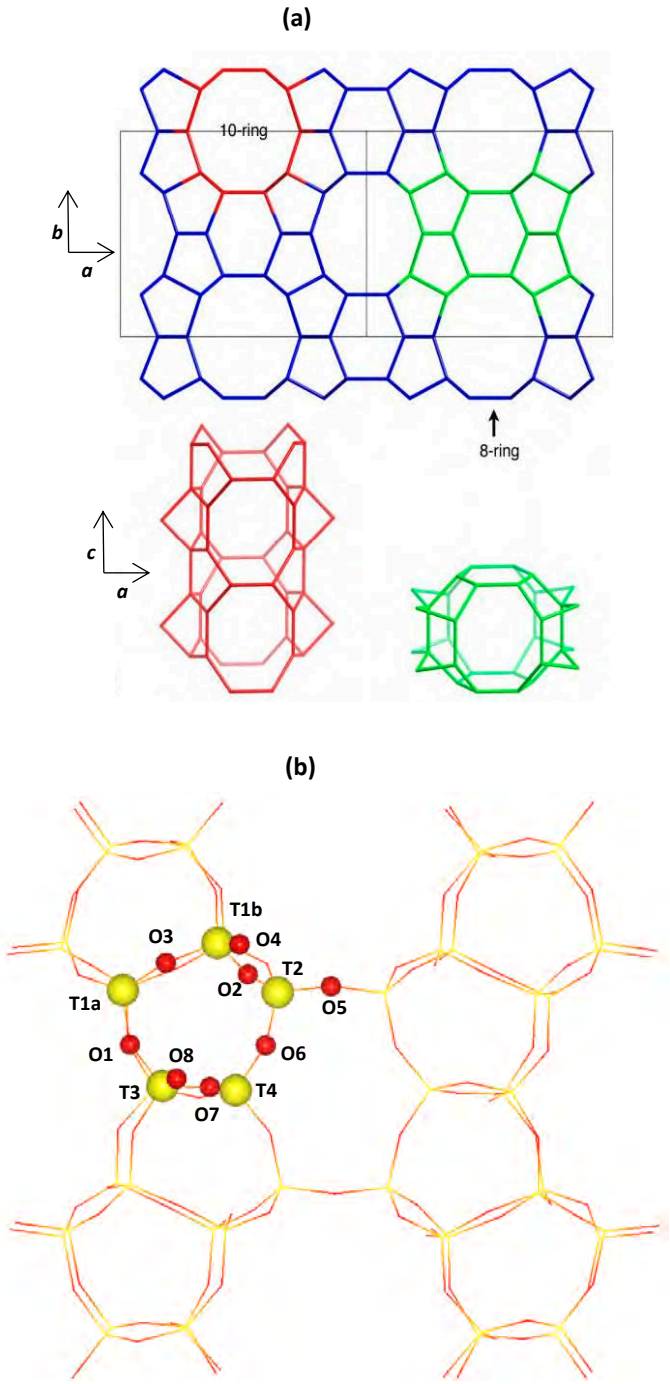

Figure 1-4. (a) Framework structure of FER viewed in c direction (top) with top views (bottom) of the 10 MR channels (red) and the FER cavity (green). Bridging oxygens have been omitted for clarity. **(b)** Location of non-equivalent T site positions – T1a, T1b, T2, T3 and T4 for Al substitution and oxygen sites (O1 – O8).

1.3.2 Acid Site Probing

FER in its proton exchanged form is of commercial interest as a catalyst for the skeketal isomerisation of alkenes. (Houzvicka and Ponec, 1997, Mooiweer, *et*

al., 1994) The concentration, strength, accessibility of acid sites in FER has been studied previously. (Domokos, *et al*., 2000, Pinar, *et al*., 2009, Roman-Leshkov, *et al*., 2011) The adsorption of small basic molecules such as pyridine and ammonia have been used extensively in order to probe the accessibility of the acid sites. The experimental conditions used for adsorption are also vital as greater accessibility is achieved when the temperature is increased and the longer the time is allowed to lapse before the measurement is taken. Trombetta *et al.* (Trombetta, *et al*., 1998) and Wichterlová *et al*. (Wichterlová, *et al*., 1999) reported that at relatively low temperatures of 300 - 400 K and short time scales pyridine could be used to probe the external acid sites and not able to enter the FER cavity. Although Pieterse *et al*. (Pieterse, *et al*., 1999) reported that at higher temperatures of 573 K and a pyridine partial pressure of 10^{-2} mbar, found that 46% of the acid sites were accessed by pyridine in the first 60 min and that 78% could be accessed in 1550 min. For the remaining 22% of acid sites, 2300 min were required with an increase of the partial pressure to 10-1 mbar. The remaining fraction of acid sites is primarily accessible via the 8-MR window indicating a high barrier exists for pyridine to pass this window and thus sterically demanding reactions are less likely to take place within it. However, experiments presented for 10^{-1} mbar pyridine at 573 K show clearly that pyridine is able to reach all of the BA sites in line with molecular modelling, suggesting that a combination of high pressure and pyridine partial pressure allows to quantitatively probe Brønsted acidity of FER. With the use of ammonia probe, it has been found to adsorb at all acid sites readily and TPD of ammonia obtained by IR data indicated that all acid sites have similar acidity. (Zholobenko, *et al*., 1998) Additionally, the IR bands associated to the BA sites vibrating in 8-MR and 10-MR channels have very similar peak positions.

Altering the SDA in the synthesis may be used to control the location of Al atoms and hence acid site distribution in the structure. Raman-Leshkov *et al*. (Roman-Leshkov, *et al*., 2011) used a combination of tetramethylammonium (TMA) cations with differently sized cyclic amines, pyrrololidine (Pyr) and hexamethyleneimine (HMI), to synthesize the FER zeolite and found that the use of Pyr produced a zeolite with acid sites mostly located in the 8-MR channels, while the use of HMI generated acid sites located mostly in the 10-MR channels. These FER samples were used to study the effect on the catalytic behaviour of dimethyl ether (DME) carbonylation and found that there was a better rate of conversion with a zeolite with more acidic sites located within 8-MR channels. Conversely Domokos *et al*. (Domokos, *et al.*, 2000) found that for the isomerization of n-butene to isobutene it was essential to have fewer acid sites in the smaller channels as they contributed to sitde reactions resulting in the formation of by-products such as propene and pentene. Additionally, it was concluded that alkali cations may also be used to direct acid sites as they adsorb preferentially in FER cavity, and therefore, more acid sites are accessible in the larger channels (Sarv, *et al*., 1998). Furthermore, it was shown before that alkali ions located in the FER cavity may block the transport of molecules. (Pickering, *et al*., 1989)

1.4 Mordenite

1.4.1 Structure and Synthesis

The silicon framework of MOR zeolite is composed of 4 and 5-MRs that link to form two types of cavities in the structure: a main channel circumscribed by 12-MRs running along the c direction, measuring 6.5 × 7.0 Å and a smaller 8-MR channels running parallel to the main channels, measuring 2.6 × 5.7 Å (Alberti,

1997, Dominguez-Soria, *et al*., 2007, Meier, 1986). These two channels are connected by 8-MR openings, 3.4 × 4.8 Å, running along in the *b* direction, and are referred to as 'side pockets'. As shown in **Figure 1-5 (a)**, the linking 8-MR b tubes are staggered at the join with the strongly compressed 8MR *c* channels. Therefore for diffusion of large ions or molecules the structure of MOR offers one-dimensional passageways. The topological symmetry of MOR zeolite is orthorhombic and for a purely siliceous framework, the space group is *Cmcm* (Demuth, *et al*., 2000). The orthorhombic unit cell contains 144 (48 framework 23 atoms and 96 oxygen atoms) with lattice parameters given by Alberti *et al*. (Alberti, *et al*., 1986) a = 18.094 Å, b = 20.516 Å, and c = 7.524 Å. There are four symmetrically independent tetrahedral sites: T1-T4 with 10 different crystallographic oxygen sites, O1-O10 sites. (Alberti, *et al*., 1986, Oumi, *et al*., 2007), shown in **Figure 1-5 (b)**. Specifically, six of the 10 oxygen sites (O5 – O10) lie between equivalent T atoms while the other four oxygen sites (O1 – O4) lie between non-equivalent T atoms. O2, O3, O7 and O10 sites are located in the main channel, O1 and O9 are located in the smaller 8MR channel, O5 and O6 are located at the side pockets (intersection between the main and small channel), O4 and O8 are located in the chains of 5-MRs.

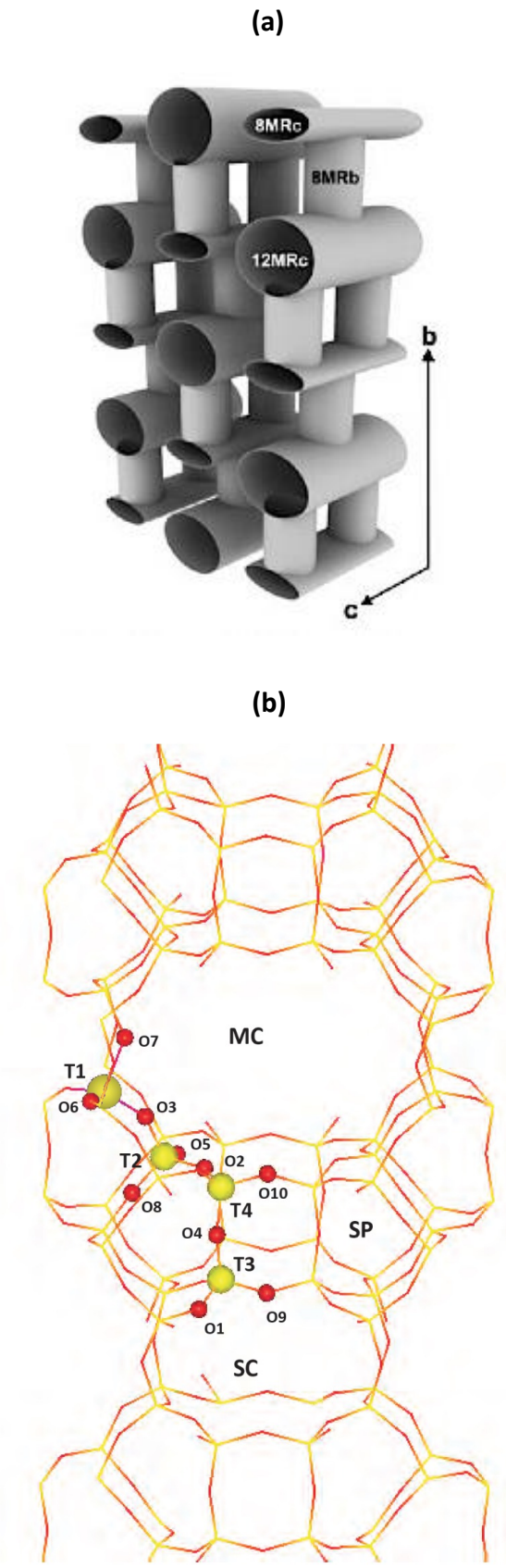

Figure 1-5. MOR zeolite framework. (a) de facto unidirectional MOR structure. (Note: 8MRb is referred to side pockets (SP). (b) Location of Al atom in four non-equivalent T sites (T1 – T4) and oxygen sites (O1-O10).

1.4.2 Acid site probing

The accessibility, nature and distribution of the acid sites in MOR are also dependent upon several factors in the same way as FER. The accessibility of the acid sites has also been probed using basic molecules and at a given temperature and adsorption time it has been found that more pyridine is adsorbed in MOR than FER. (Agullo, *et al*., 2007) presumably due to the larger channels of the MOR. Auroux and Datka (Auroux and Datka, 1997) reported the adsorption of pyridine in MOR at various Na/H exchange degrees followed by microcalorimetric and IR spectroscopic studies. At low exchange degree, all protons formed hydroxyls in the large channels and the acid strength increased at higher exchange degrees. At 47% of exchange, the acid strength of hydroxyls in the large channels was constant, indicating that the replacement of Na^+ ions by protons in side pockets did not influence the properties of the BA sites in large channels. The hydroxyls in the side pockets did not react and were inaccessible to pyridine being a bulky reactant. Chen *et al*. (Chen, *et al.*, 1992) and Parillo *et al*. (Parrillo and Gorte, 1993) reported the heats of adsorption of pyridine was independent upon pyridine loading. The constant value of adsorption heat suggested that pyridine reacts with all the accessible hydroxyls in larger channels without selecting the most acidic ones. Auroux and Datka (Auroux and Datka, 1997) confirmed this by IR studies of pyridine adsorption, the stretching frequency of hydroxyls consume by pyridine was independent on the amount of pyridine adsorbed. Pyridine being a strong base cannot discriminate between hydroxyls of differing acid strength. On the other hand, IR and TPD studies of ammonia desorption suggested heterogeneity of OH groups in the large channels of MOR.

Ammonia, penetrating both both large and small channel, was also used as a probe

molecule. It was found that the acid strength increased with the degree of Na/ H exchange and with the degree of dealumination (increasing Si/Al ratio) through microcalometric, NMR, TPD and IR studies (Bankos, *et al*., 1988, Guisnet, *et al*., 1997, Mishin, *et al*., 1993). The stepwise dependence of adsorption heat of ammonia suggested heterogeneity of acid sites both in large channels and in the side pockets of MOR with various Si/Al ratio and with various exchange level (Bankos *et al*., 1988, Mishin, *et al*., 1993, Tsutsumi and Nishimiya, 1989). Niwa *et al*. (Niwa, *et al*., 2005) reported that increasing the ion-exchange degree (NH_4^+/ Na^+ ratio) led to a high preference of hydroxyls forming in the side pockets. Niwa *et al*. (Niwa, *et al*., 2005) reported using IRMS-TPD of ammonia that the acidity of Bronsted OH situated on 8-MR was stronger. With this method, the bands corresponded to bridged hydroxyl groups in the region between 3550 - 3650 cm^{-1} followed at increasing temperatures, and simultaneously the concentration of desorbed ammonia was measured by MS. With this method it was possible to calculate calculate the desorption enthalpies of ammonia, 147 kJ mol^{-1} in 12-MR and 158 kJ mol^{-1} in 8-MR channels, confirming the higher acid strength of the BA sites in the side pockets. Parrillo *et al.* (Parrillo and Gorte, 1993) reported higher heats of adsorption for pyridine, -200 kJ mol^{-1}, probably due to the higher basicity of pyridine when compared to ammonia. The amount of acid sites determined by ammonia was higher than determined by pyridine, possibly due to the fact that ammonia is a relatively small molecule and can enter the side pockets with relatively less steric hindrance. Zholonko *et al*. (Zholobenko, *et al*., 1993) found two types of BA sites in the MOR based on FTIR spectroscopy, one in the larger channels at a higher frequency of 3612 cm^{-1}, with a lower effective acidity, and one in the smaller channels at a lower frequency

of 3585 cm^{-1}, with a higher effective acidity. Niwa *et al*. (Niwa, *et al*., 2005) performed theoretical calculations at low computational costs as well which confirmed the stronger acidity of the hydroxyls located in the 8-MR channels. On the other hand, Dafkta *et al*. (Datka, *et al.*, 1996) measured the extinction coefficient of OH bands and identified a stronger acidity in the 12-MR.The distribution of the acidity is a matter of controversy. On the contrary,, in several microcalometric studies the heat of adsorption of ammonia displayed a plateau of nearly constant heats instead of a stepwise curve indicating that the OH groups in MOR were homoegeous (Chen, *et al*., 1994, Parrillo and Gorte, 1993, Spiewak, *et al*., 1994).

The selective carbonylation of methanol or DME with CO is most active at FER and MOR zeolites, probably due to the common feature of the presence of 8-MR channels in both zeolites. Similar to FER, there is a better conversion of the carbonylation of DME in the smaller channels of MOR (Bhan, *et al*., 2007). Lukyanov *et al.* (Lukyanov, *et al*., 2004) and Niva *et al*. (Niwa, *et al*., 2005) reported a higher catalytic activity for hexane and octane cracking on acid sites located on the 8-MR channels. The catalytic activity of octane cracking declined rapidly on MOR with a high concentration of stronger acid sites located in the side pockets, whereas MOR with weaker acid sites located in the larger channels displayed a slow deactivation behaviour. This is due to coking occurring easily on the strong acid sites and the small steric capacity of the 8-MR leading rapid deactivation.

1.5 Aldol Condensation Reaction

1.5.1 General Overview: Acid catalyzed mechanism

The condensation reaction between two molecules of a carbonyl compound (self-condensation), involving the transfer of the α-hydrogen atom from one molecule to the oxygen of the other molecule with simultaneous linkage of the molecules through the carbon valences, is known as aldol condensation. The reaction can also take place between two different carbonyl compounds, which is known as cross-aldol condensation. For the self-condensation reaction, the reactant is either an aldehyde or a ketone whereas for the cross-aldol condensation the reactants may be two different aldehydes, two different ketones, or an aldehyde and a ketone. The product of the condensation reaction is in any case a β-hydroxyaldehyde or a β-hydroxyketone, containing a new C-C bond formed between the α-carbon of one molecule and the carbonyl carbon of the other. The general reaction of the aldol condensation is displayed in **Figure 1-6**.

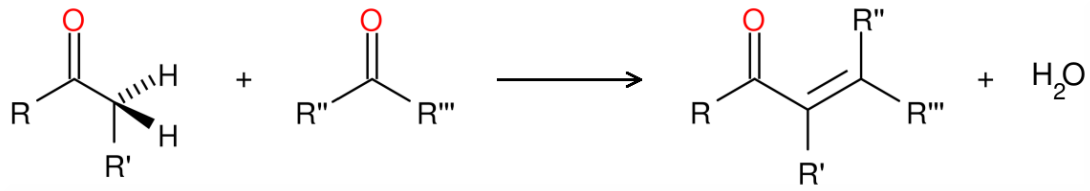

Figure 1-6. General reaction for the aldol condensation catalyzed by acids or bases.

The aldol condensation consists of reaction between an enol or enolates and carbonyl compounds. It is an important reaction in organic synthesis because it leads to the formation of a carbon-carbon bond. It is a reaction that involves heating aldehyde or ketone under acid or base catalysis to form α,β-unsaturated ketone or or aldehyde. In this thesis, we focus on aldol condensations catalyzed by acids. The homogeneous acid-catalyzed aldol condensation mechansim consists of three steps: keto-enol

acid-catalyzed aldol condensation mechansim consists of three steps: keto-enol tautomerization, condensation between the enol and aldehyde or ketone, and elimination of water to form conjugated enone. The complete mechanism is displayed in **Figure 1-7**:

1) The acid (H^+) acts as a proton donor and activates the carbonyl oxygen into a protonated form

2) Intermediate 1 reacts with the conjugate base (*i.e.* OH^-) of the acid to produce the enol (intermediate 2)

3) The nucleophillic enol (intermediate 2) reacts with another carbonyl compound in its protonated form - (intermediate 1) to yield the aldol product (β-hydroxyaldehyde or β-hydroxyketone)

4) The aldol undergoes spontaneous dehydration due to base catalyzed dehydration to form the α,β-unsaturated ketone or aldehyde

In this thesis, we primarily focus on the keto-enol tautomerization step, the rate-determining step in the aldol condensation mechanism. Aldehydes and ketones both exist in two isomeric forms known as keto and enol tautomers. They differ in the location of a hydrogen atom and the type of double bond. As shown in **Figure 1-7**, the keto form contains a carbonyl group (C=O) which is normally in rapid equilibrium with the enol tautomer, containing a pair of double bonded carbon atoms adjacent to a hydroxyl (-OH) group, C=C-OH. The keto form is more stable predominating the equilibrium for most aldehydes and ketones, though the enol form is the important initial step to aldol condensation and other reactions. (Boekfa, *et al*., 2010, Solans-Monfort, *et al*., 2002) As shown in **Figure 1-7**, tautomerization is a process by which protons are transferred from one site to another by a series of steps in which the acid is an intermediary. In this

thesis, we focus on the molecules, acetaldehyde and acetone, as these basic reactants were selected because of the primacy of the carbonyl group in many simple transformations.

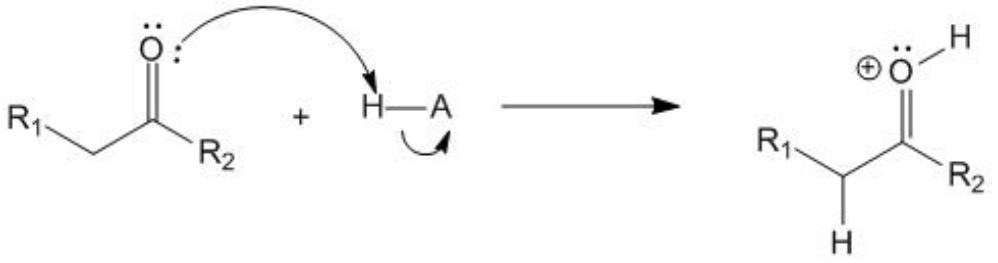

Intermediate 1

Step 1 - *Acid activates carbonyl carbon by donating a proton.*

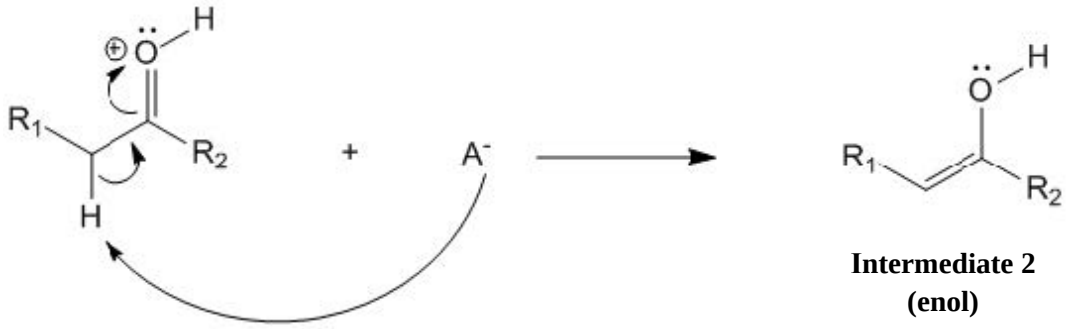

Intermediate 2 (enol)

Step 2 - *Reaction with conjugate base of acid to produce enol*

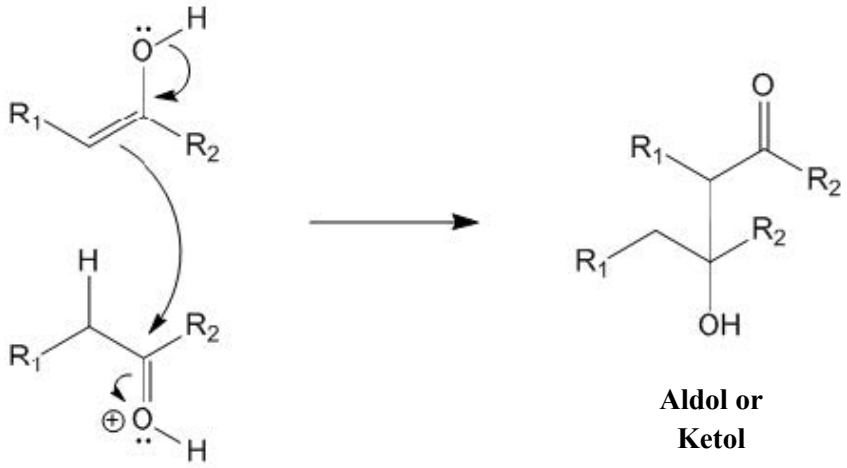

Aldol or Ketol

Step 3 - *Reaction of two intermediates to produce the aldol or ketol*

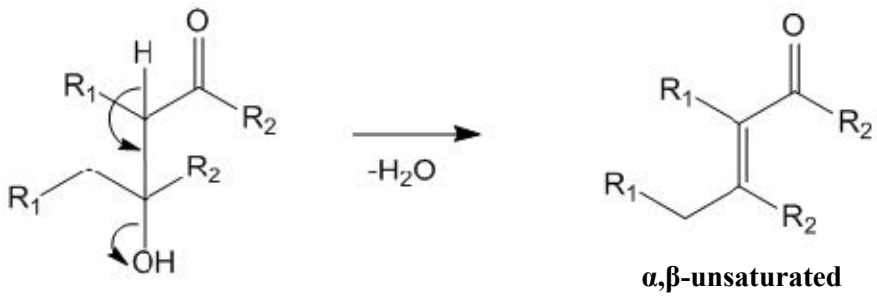

α,β-unsaturated ketone or aldehyde

Step 4 - *The aldol or ketol undergoes spontaneous dehydration to produce the alpha,beta-unsaturated carbonyl compound*

Figure 1-7. Acid catalyzed mechanism of the aldol condensation reaction in liquid phase.

The product of aldol reaction contains a functional group capable of further transformations, thus providing access to a host of useful materials. Aldol condensations are especially useful in biomass upgrading because the facile dehydration removes oxygen, increases the carbon to oxygen ratio, and assists in the conversion of biomass-derived oxygenates to liquid hydrocarbons. Therefore, this coupling reaction is widely used to convert smaller oxygenates to larger feedstocks suitable for producing into fuels and chemicals. (Anbarasan, *et al*., 2012, Resasco, *et al*., 2016, Subrahmanyam, *et al*., 2010) Essentially, the aldol condensation consists of the production of higher aldehydes and ketones from lower, readily available aldehydes and ketone. Although selective condensation to the aldol products has proved to be a difficult task as it involves very reactive substrates, which are able to develop a network of reactions. When the desired product results from the condensation of the aldehyde or ketone, self or cross-condensation is the main reaction, followed by secondary reactions such as oligerization and polymerization (Biaglow, *et al*., 1995, Boekfa, *et al*., 2010, Diaz, *et al*., 1992, Ehresmann, *et al*., 2002).

Aldol condensations are generally carried out at mild temperatures (273 - 473 K) in the presence of a homogeneous or heterogeneous acid, base or amphoteric catalyst (alkali metals (DiCosimo, *et al*., 1996, Ji, *et al*., 1997, Salvapati, *et al*., 1989), metal oxides (Rekoske and Barteau, 2011), mixed metal oxides (Faba, *et al*., 2013, Kunkes, *et al*., 2009), hydroxyapatite (Tsuchida, *et al*., 2008), amines grafted onto supports (Sankaranarayanapillai, *et al*., 2015), and metal-substituted zeolites (Gabriels, *et al*., 2015, Kozlowski and Davis, 2013)). Aldol condensations in the presence of homogeneous acid catalysts produces

environmentally hazard waste due to their non-recyclability and lacks product selectivity by forming side reactions. Growing concerns about the environmental impacts of such corrosive materials has prompt a movement toward more green heterogeneous catalysts. In recent years, improvements in heterogeneous catalyst systems possessing acid-base bifunctionality showed greater reaction rates by stabilizing the transition states on the acid-pair sites. In particular, zeolites have emerged as promising solid catalysts for aldol condensations due to their shape selective properties of their microcrystalline pore structures and their tuneable acid sites. Additionally, tautomerization is dependent upon the nature of the acidity of zeolite, as the initial step is the protonation of the carbonyl oxygen of aldehyde or ketone by the hydroxyl group of the BA site of the zeolite (Boekfa, *et al*., 2010, Solans-Monfort, *et al*., 2002). In the next section, we review aldol condensations of acetaldehyde and acetone in zeolites and how factors such as reaction temperature, reactant molar ratio, structure of reactant molecules and nature of the catalyst determine the selectivity of the process toward heavier desired products.

1.5.2 Aldol condensations of acetone in zeolites

The catalytic self-aldol condensation of acetone in solution and gas phase (on oxides and acid catalysts) has been studied extensively (Zakharov, *et al.*, 2008, Chiang, *et al*., 1989, Lee, *et al*., 1997, Salvapati, *et al*., 1989, Holmes and Lossing, 1982). It is a complex reaction and numerous products are possible via competitive self- and cross- condensation between reactants and primary product, displayed in **Figure 1-8**. To reduce the amount of condensation that occurs in these cases it is best to lower the temperature and remove the acid catalyst. Self-condensation of acetone initially

produces diacetone alcohol, as an aldol product, although in order to obtain high yields of diacetone alcohol, the condensation reaction must be halted before diacetone alcohol reacts further. Thus, catalytic conversion of acetone to diacetone alcohol can be controlled at low temperatures (273 - 293 K). Subsequent dehydration of diacetone alcohol forms mesityl oxide, which is obtained at good yield at mild reaction temperatures, 293 - 473 K. At higher temperatures, > 473 K, aldol condensation of acetone shows more complex reaction pathways and yields acyclic, cyclic and aromatic trimers (phorones, isophorone, and mesitylene) Generally, phorone yields are low because the acidic catalysts also promote coupled cyclization and dehydration reactions that produce mesitylene, the thermodynamically favoured product at higher temperatures. (DiCosimo, *et al*., 1996) Trimerization of acetone under basic conditions produces isophorone, a potential intermediate to form 3,5-xylenol. Along with isophorone, acetone condensation also tends to give significant amounts of C_{12} and C_{15+} compounds because of the high reactivity of the intermediates.

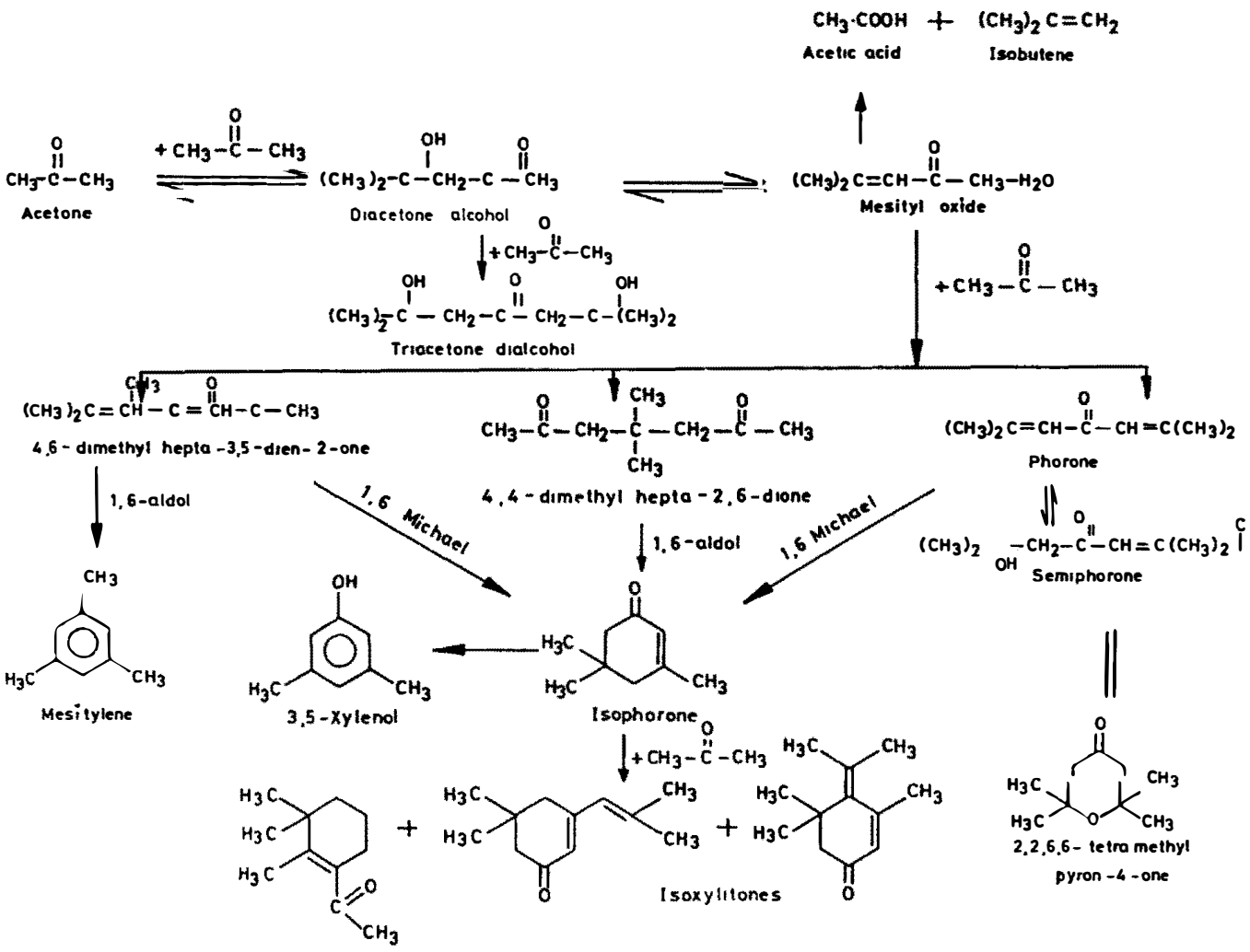

Figure 1-8. Catalytic self-condensation reactions of acetone in gas and solution phase. (Salvapati, *et al*., 1989)

The adsorption of acetone on acid catalysts provides an insight on the nature of the stoichiometric complex at the Bronsted sites as well as the reactivity of the species to nucleophillic attack (Biaglow, *et al*., 1995, Gorte and White, 1997, Panov and Fripiat, 1998, Sepa, *et al*., 1996). The adsorption complex formed by acetone is rigid and involves H-bonding between the BA sites of the zeolite framework and and lone pair on the oxygen of acetone. Previous FTIR studies have suggested acetone to form medium-strong H bonds with zeolites, as the intensity of the stretching band of free bridging hydroxyls at 3640 - 3550 cm^{-1} decreases, and two broad bands at 2820 - 2800 cm^{-1} and 2400 - 2370 cm^{-1} increases. (Florian and Kubelkova 1994, Kubelkova and Novakova, 1991) This is attributed to the OH stretching vibrations in the interaction complex. Measurements of the ^{13}C NMR chemical shift anisotropy of acetone in H-ZSM-5 zeolite as a function of coverage demonstrate a stability of 1:1 stoichiometric complex. (Xu, *et al*., 1994, Sepa, *et al*., 1996) The localized adsorption complex is stable and does not undergo reactions at room temperature and surface coverages below one acetone per BA site. At higher coverages, acetone becomes more mobile which is proven by the disappearance of spinning sidebands, present at lower coverages, in the ^{13}C NMR spectrum. (Biaglow, *et al*., 1995) The mobility of adsorbed acetone seems to play a primary role in the bimolecular condensation. Biaglow *et al.* (Biaglow, *et al*., 1995) studied the transformation of acetone over H-ZSM-5 zeolites with a different coverages and temperatures. It was observed that the rate of reaction is critically dependent upon the surface coverage and temperature. When a localized complex between acetone and BA sites is formed, the transformation in mesityl oxide does not occur. By increasing the coverage or temperature, acetone dehydrates to form mesityl oxide. ^{13}C NMR

spectroscopy has been used to study the reactivity of adsorption complexes of acetone with zeolite acid sites toward aldol condensation. The formation of reactive complex between the ketones and the BA sites of the zeolites is involved as a precursor to condensations at low temperatures. The strength of complex formation was reflected in the degree of proton transfer from zeolite framework to the ketone, and this recorded into significant ^{13}C-acetone isotropic chemical shift changes. From these studies, a dominant characteristic of the ^{13}C NMR experiments was the observation of large downfield shifts for selected carbons probably due to complex formation with partial proton transfer from BA sites to the basic oxygen of the ketones. The adsorption complexes of the condensation products also resulted in H-bonded complexes at low coverages whereby a complete proton transfer to form stable long-term cations was not identified. Further support that the interactions which lead to the downfield shifts are due to H-bonds comes from ab initio calculations based on cluster models simulating zeolites. Although Sepa *et al*. (Sepa, *et al*., 1996) and Kassab *et al*. (Kassab, *et al*., 1999) noted that there is no simple relationship between the strength of the H-bond and isotropic chemical shift. Significant changes in the chemical shifts occur with phase change and adsorption in non-acidic silicalite.

Both IR and NMR technique were also used to study the reactivity of acetone complexes with zeolite acid sites toward aldol condensation. (Xu, *et al*., 1994, Bell and Gold, 1983, Kubelkova, *et al*., 1991, Biaglow, *et al*., 1995) Xu *et al.* (Xu, *et al.*, 1994) studied the chemistry of the aldol condensation of acetone as well as the formation of secondary products on a variety of zeolites such as HY, H-ZSM-5, CsY

and Cs-ZSM-5. The secondary products include double bond migration, hydride transfer and cracking. It was found that higher reaction times, more acidic zeolites and elevated temperatures favour the formation of secondary reaction products. In their study, the method of formation of the zeolite especially the presence of metals in the framework or in the pores affects the rate of the condensation reaction. It has been found that alkali metal exchanged zeolites are less active for condensation reactions. A small amount of diacetone alcohol and mesityl oxide was observed in these zeolites. On the other hand, higher acidity zeolites increase the rate of condensation reactions. The significantly stronger acidity of HY was reflected in its activity to aldol chemistry as well as secondary reactions (**Figure 1-9**). Aldol condensations were dominant through 393 K and the formation of aromatics progressed at this relatively low temperature. Diacetone alcohol was not observed as it dehydrates rapidly to form mesityl oxide. The secondary reactions became obvious when the temperature was increased to 433 K. Mesityl oxide cracked in the presence of water to form acetic acid (183 ppm) and isobutylene, which has been reported by Lazo *et al*. (Lazo, *et al*., 1991) as well, immediately oligermized and cracked to form a mixture of products including isobutene. CO_2 (126 ppm) was formed at this temperature as well, possibly due to the cracking of phorone followed by decarboxylation of the resulting α, β unsaturated acid. Increasing the temperature to 523 K resulted in a mixture of aromatics, C_3 to C_6 branched alkanes, CO_2 and acetic acid. Similar findings of secondary reactions observed in HY were found in HZSM-5 zeolite. The essential disparity was that the yield of acetic acid was higher on the latter catalyst and that of CO_2 was lower. This could potentially mean that cracking becomes a competitive reaction to aldol condensation at an earlier stage in the chemistry on H-ZSM-5 relative to HY. In addition, the influence of co-adsorbates such as water has has a minimal effect on the aldol condensations of

acetone, which in comparison to acetaldehyde plays a minimal effect on the aldol condensations of acetone, which in comparison to acetaldehyde plays a major role in the reactive complexes. (Munson and Haw, 1993) This could suggest the presence greater affinity of HSZM-5 for less polar adsorbates or the reduced magnitude of hydrate formation for acetone compared to acetaldehyde.

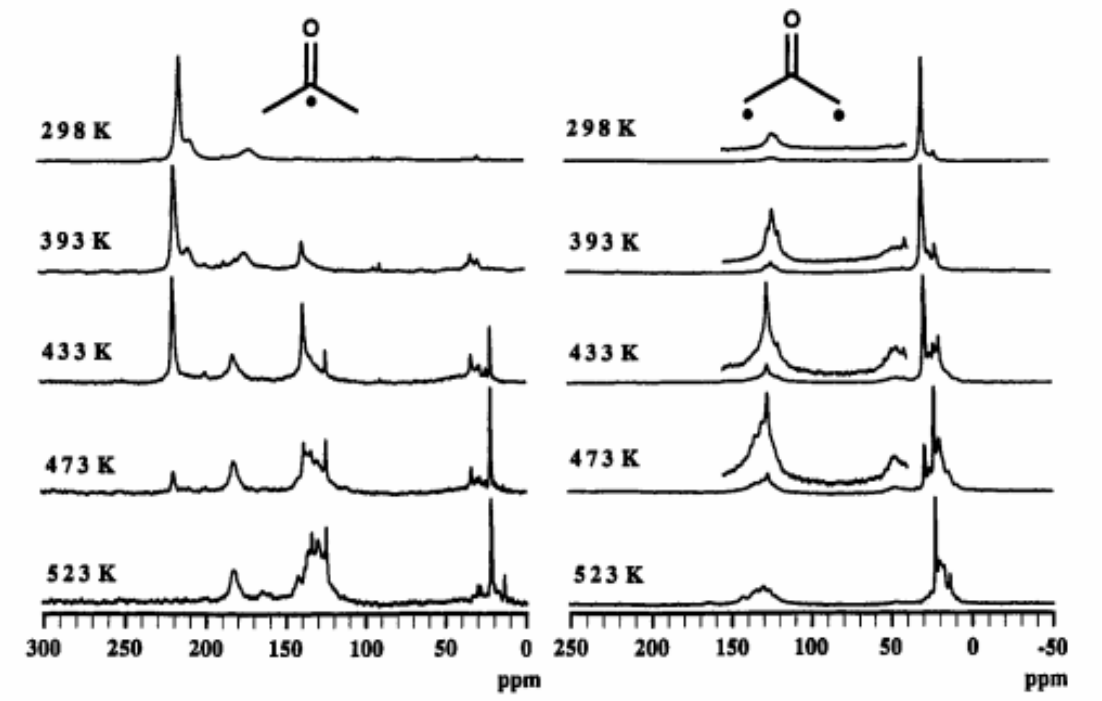

Figure 1-9. ^{13}C MAS NMR studies of the reactions of acetone-2-^{13}C and acetone-1,3-$^{13}C_2$ on zeolite HY. Mesityl oxide (210 and 175 ppm in the 2-^{13}C spectra, and 123 ppm in the 1,3-$^{13}C_2$ spectra) formed at 298 K. Secondary reactions at 433 K and above included the formation of acetic acid (183 ppm) isobutane (24 ppm) and CO_2 (126 ppm) in the 2-^{13}C spectra.

1.5.3 Aldol condensations of acetaldehyde in zeolites

Acid-catalyzed condensation reactions of acetaldehyde has been previously studied on H-ZSM-5 zeolite at different surface coverages, temperatures and pressures. Using ^{13}C NMR measurements the adsorption of acetaldehyde on H-ZSM-5 suggests a H-bonded complex at room temperature and at low surface coverage, less than one molecule per acid site; similarly observed in acetone. (Biaglow, *et al*., 1995) In

addition, the self-condensation of acetaldehyde to form crotonaldehyde was also observed (**Figure 1-10**). Increasing the temperature and surface coverages, both of which increases the mobility of the adsorption complex, promoted the concentration of the crotonaldehyde. Munson *et al*. also observed the adsorption of acetaldehyde on H-ZSM-5 using ^{13}C NMR spectroscopy at various temperatures. Following the adsorption at 298 K resulted in a complex mixture of products as almost all of the acetaldehyde was condensed. Increasing the temperature to 433 K resulted a cracking process of these products, and CO and CO_2 were formed at 523 K.

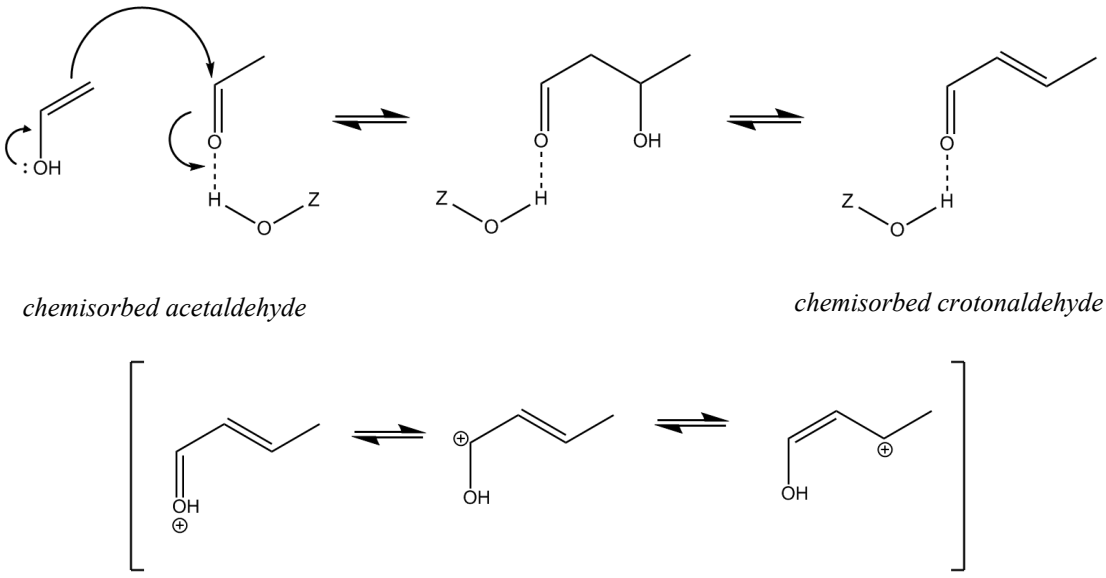

chemisorbed acetaldehyde *chemisorbed crotonaldehyde*

Figure 1-10. Self-condensation of acetaldehyde to form crotonaldehyde at BA site of zeolite (Biaglow, *et al*., 1995)

Diaz *et al*. (Diaz, *et al*., 1992) reported the condensation reactions of acetaldehyde on H-ZSM-5 using IR spectroscopy. Several adsorptions were carried on activated H-ZSM-5 using various pressures of acetaldehyde vapour at 313 K. At pressures lower than 3 Torr indicated that the primary interaction between the acetaldehyde and bridging hydroxyl of the zeolite corresponds to a proton-transferred structure, that is, to an ion-pair. This is concluded as the stretching vibration of the hydroxyl

band at 3600 cm^{-1} disappears and the carbonyl vibration shifts to lower frequencies. At these low pressures, the adsorbed acetaldehyde indicated the possible formation of crotonaldehyde as a product of the aldol condensation or as an intermediate of additional condensation reactions.

As mentioned above, where the aldol product of the self-condensation of acetone, diacetone alcohol was not observed, likewise acetaldol, the aldol product in the self-condensation reaction of acetaldehyde, was difficult to detect also. The vibrational bands for this intermediate were not present as dehydration is a fast process in acid catalysis. Two intense vibrational bands were observed, 1630 cm^{-1} assigned to the C=O stretching vibration interacting with the bridging hydroxyls of the zeolite surface, and 1597 cm^{-1} corresponding to a C=C stretching vibration conjugated to the carbonyl group. At pressures higher than 3 Torr, the vibrational bands became broader in the bending region, indicating the possible formation of conjugated double bonds due to multiple condensation reactions. In other words, the adsorption of acetaldehyde at relatively high pressures induces the presence of oligomers by polymerization reactions.

Munson *et al*. (Munson and Haw, 1993) studied the influence of co-adsorbates such as water or oxygen present in the H-ZSM-5 catalyst on the condensation reactions of acetaldehyde. The adsorption of water toned down the activity of the zeolite allowing the selective conversion of acetaldehyde (which was stable at 298 K) to crotonaldehyde at 353 - 393 K. Crotonaldehyde was stable up to 433 K. This possibly suggested that co-adsorbed water influences the acidity of the strong BA sites of H-ZSM-5 to scale down to that of the less acidic hydronium-ZSM-5 and

subsequently affecting the acid catalyzed aldol condensation reactions. Moderating the acidity of H-ZSM-5 by co-adsorption of water also allowed the selectivity of other selective reactions. The presence of water and oxygen as co-adsorbates in the zeolite resulted in acetaldehyde to be converted to acetic acid in high yields at increasing temperatures, as demonstrated in the ^{13}C NMR chemical shifts. A separate control experiment verified that acetic acid is unreactive on the zeolite under these conditions. A previous study by Maslov *et al.* (Maslov and Blyumberg, 1976) presented that the oxidation process of aldehydes to carboxylic acids is a well-established reaction in solution, and provided that the acidity is moderated by co-adsorption of water, it is the prevailing reaction in H-ZSM-5 under these conditions.

1.6 Computational studies of keto-enol tautomerism in zeolites and the effect of confinement

Relatively few computational studies have investigated aldol chemistry, and these have primarily focused on the keto-enol tautomerization step. In the gas phase it is believed that the initial enolisation of the acetone or acetaldehyde proceeds via a transition state where the hydrogen ion moves directly from the carbon closest to the carbonyl to the carbonyl oxygen (Holmes and Lossing, 1982, Boekfa, *et al*., 2010) whilst in solution it is though that the hydrogen ion is passed via the interacting water molecules (Salvapati, *et al*., 1989, Boekfa, *et al*., 2010). In zeolites it is thought that the hydrogen ion is passed via the zeolite and there is experimental evidence supporting this showing H/D exchange between the zeolite and acetone. (Xu, *et al*., 2003)

Boekfa *et al*. (Boekfa, e*t al*., 2010) performed theoretical studies on the tautomerization of acetone in zeolites with differing pore sizes, H-FER, H-ZSM-5 and H-MCM-22. In their study, the relative strengths of host-guest H-bonding interactions with BA sites at reactant (adsorbed acetone) and transition state were found to be crucial in determining activation energies. The keto-enol tautomerization activation energies and the reaction energies were found to decrease with increasing zeolite pore sizes, as smaller pores perturb host-guest H-bonding. The larger cavity of MCM-22 could better accommodate the adsorbed acetone and enol by allowing these intermediates to be closer to the acid site for stronger interactions. In addition, the adsorbed enol was found to be highly unstable as the the structures of the transition state the enol product were found to be very similar and therefore the reverse transform to adsorbed acetone is facile with a small activation barrier.

The keto-enol tautomerization of acetaldehyde on H-ZSM-5 zeolite was studied theoretically by Solans-Monfort *et al*. (Solans-Monfort, *et al*., 2002). Here, the adsorption of acetaldehyde on the zeolite corresponds to a H-bonded complex and not an ion pair, and produces a red shift of the C=O stretching mode wherein the computed value of the IR band is in good agreement with the experimental one. From these theoretical studies it can be concluded that while complete proton transfer did occur in the stable complex, the affinity of the base for the proton at the acid site leads to a spatially localized, stoichiometric, H-bonded adsorption complex. The bonding and stabilization of the adsorption complex is probably a result of these important interactions: the highly localized H-bonding, the short-range repulsive and the attractive long range interactions with the channel walls. All these interactions are crucial in reaction, the protonic site and its environment localize and polarize the

molecule, thereby activating it for nucleophillic attack. The long range interactions include the electrostatic (Coulombic) and disperive van der Waals interactions, and the extent of stabilization by these interactions is dependent upon the number and strength of contacts between the confined species and the surrounding framework oxygen atoms, that is, the size and shape of the guest species with those of the zeolite host channels and cavities.

The confinement concept introduced by Derouane *et al*. (Derouane, *et al*., 1988) stems from remarkable features that zeolites possess resulting from their surface curvature of their internal surface. The confinement effect derives from the dispersive van der Waals interactions. When the size of the host structure and the guest molecule becomes comparable, it optimizes their van der Waals interaction leading to selective adsorption and enhanced diffusion. Many efforts have been done to quantitatively evaluate the confinement effects in zeolites. Methods based on classical force fields have been widely used to simulate molecular adsorption and diffusion in zeolites, because of their computational efficiency and accuracy (Smit and Maesen, 2008). However, they are not suited to describe chemical reactions involving bond breaking and formation, and therefore quantum mechanical (QM) methods, despite being computationally more expensive, have been applied to the study of reactivity in zeolites (Sauer, *et al*., 1994, van Santen and Kramer, 1995, van Speybroeck, *et al*., 2015). Density functional theory (DFT) is currently the preferred method for carrying out electronic calculations for large systems, because it provides a good balance between computational simplicity and accuracy. One of the main challenges in DFT is the description of dispersion interactions, which cannot be described by local density functionals. Over the

last years, there has been significant interest in the development of density functionals to capture dispersion interactions. (Goltl, *et al*., 2012, Gomes, *et al*., 2012, Klimes and Michaelides, 2012) Among them is the DFT-D methodology proposed by Grimme, which combines excellent computational efficiency with reasonable accuracy, with an average deviation from experimental values of 5 kJ mol^{-1}. (Grimme, 2004, Grimme, 2006) Despite DFT methodology used in the studies by Boekfa *et al*. and Solans Monfort *et al*., dispersion effects were not accounted for or not described adequately.

QM methods are applied to a cluster models in which a portion of the zeolite is taken into account, a hybrid scheme combining clusters treated at QM level incorporated in an extended zeolite framework treated with force fields, or to a fully extended zeolite environment described by periodic boundary conditions (PBC). In the studies by Boekfa *et al*. and Solans Monfort *et al*. quantum clusters and hybrid schemes were used, calculations were performed on relatively large (34T and 63T) zeolite clusters, although there was no study of convergence with respect to the system size, leaving open the question of an optimal cluster size for future calculations. Migues *et al*. (Migues, *et al*., 2014) performed acetone tautomerization on H-ZSM-5 and HY zeolites and found that the use of various cluster sizes was an insufficient criterion for converging barriers with respect to the system size.

The use of model and method is important to simulate zeolites. The use of the cluster approach where a few atoms are relaxed, makes us question how big is big enough? In this thesis, we use a fully periodic system which would eliminate the cluster size convergence criteria as all atoms would be relaxed and treated on the same level. We use DFT-D to accurately account for the dispersion interactions. In

the studies by Boekfa *et al*. and Solans Monfort e*t al*. the condensation step wasnot investigated. Migues *et al*., studided the mixed aldol condensation of acetone and formaldehyde on H-ZSM-5 and HY zeolites and determined that the acetone tautomerization step remains to be the rate-determining step, consistent with the accepted mechanism in homogeneous acid-catalysis. Thereby in this thesis, we focus on the keto-enol tautomerization step of acetaldehyde and acetone taking place in acidic zeolites.

1.7 Objectives of the thesis

In Chapter 1, we have seen that aldol condensation reactions of acetaldehyde and acetone can be catalyzed by zeolites and how factors such as nature of the catalyst, reactant molar ratio, reaction temperature and pressure determine the selectivity of the process toward heavier desired products. As evident from the literature review, the keto-enol tautomerization of molecules in zeolites is gaining momentum, with computational modelling being key in providing insights at an atomistic scale of the physio-chemical phenomena and an understanding of the reaction mechanism. To this end, the next chapter will provide details into the methods used for this body of work, mainly describing the DFT theory implemented in the running and analysis of simulations and the choice of model i.e. periodic boundary conditions (PBC), along with the equations of these techniques. The first research chapter, Chapter 3, of this thesis will look at the energetics of single Al/Si substitution compensated by protons at each T site for zeolites, MOR and FER. We use interatomic potentials (described in Chapter 2 along with the equation of these techniques) as a starting point (and then further optimize these calculations using quantum mechanics. This first step provides insight into the preference of proton position which somewhat influence

the adsorptions of reactants. Following on from this, we evaluate the adsorption of acetaldehyde and acetone at each of the thermodynamically favoured acid sites. From this, we evaluate the intrinsic acid strength by reflecting the importance of H-bonding as well as the shape selectivity effects of zeolites on the stabilization of these reactants. In Chapter 4, we study the keto-enol tautomeric mechanism of acetaldehyde at each of these proton positions in both zeolites. Our aim here is to observe whether proton transfer from the hydroxyl group of the acid site to the carbonyl oxygen of acetaldehyde induces the formation of enol product. We investigated a detailed one and two-step concerted mechanism of keto-enol tautomerization. We study the geometric structures of the reactants, transition states and products and determine how zeolite acidity, steric constraints, confinement effect and local geometry of the pore structures of zeolites have an effect on the intermediates and more importantly the catalytic activity. In Chapter 5, we observe the influence of co-adsorbates such as water and methanol on the one and two-step concerted mechanism of keto-enol tautomerization of acetaldehyde. Lastly in Chapter 6, we take our research in a different direction by studying the location of monovalent alkali ions at each of the single Al/Si substitution in FER zeolite. We research this using interatomic potentials and DFT approach. Following this, we observe how hydration affects the mobility of the largest monovalent cation, cesium, in the channels of FER zeolite. We simulate this using *ab initio* molecular dynamics (AIMD) method, explained in Chapter 2.

Chapter 2

Computational Methodology

In this chapter, we discuss the methods and theory behind the simulations that have been employed through the research presented in this thesis. The aim of computational chemistry is to calculate the energy of a system as a function of its coordinates. From this a number of properties can be derived. Broadly speaking, the energy of the system can be calculated by two different methods. Molecular mechanics which ignores all electronic structure of the atoms and uses a potential function which is fitted to a particular molecular interaction and electronic structure methods which are based on quantum mechanical principles. Each method has a subset of methods some of which combine these two fundamental methods.

2.1 Molecular Mechanics

As already mentioned force field or Molecular Mechanics (MM) methods ignore the motion of the electrons around an atom and instead treat the atom as a classical particle. This application of the Born-Oppenheimer apprximation where the motion of the nuclei can be considered slow compared to the motion of the electrons and as such only the positions of the nucleus need be considered as the motion of the electrons adapt instantly to nuclear movement. In MM a force field is used to model the interactions of the atoms in the system. The force field is broken down into intramolecular components such as bond stretches and bending and intermolecular interactions such as van der Waals

(vdW) forces. Equation 2.1 expresses the total force field energy and its components required to manipulate a molecule.

$$E_{sys} = E_{bond} + E_{angle} + E_{torsion} + E_{elec} + E_{vdW} \quad (2.1)$$

Where E_{sys} is the total system energy, E_{bond}, E_{angle} and $E_{torison}$ describe the bond stretch, angle deformation and bond torsion (intramolecular-terms) and E_{elec} and E_{vdW} describe the energy contributions from electrostatic and van der Waals interactions (non-bonded intramolecular terms)

2.1.1 Intramolecular interactions

A simple harmonic oscillator approximation is applied when considering the bond between two particles where the energy varies with the square of the displacement from the reference bond length.

$$E_{bond} = \frac{k}{2}\left(l_{ij} - l_0\right)^2 \quad (2.2)$$

where l_0 is the equilibrium bond length and k is the harmonic spring constant for the particular bond. Another potiential which can be used when considering the bond between two particles is the Morse potential, names after physicist Philip M. Morse (Morse, 1929). It is a better representation of the vibrational structure of the molecule than the harmonic potential mentioned above and accounts for the anharmonicity of real bonds. The potential energy of bond stretching is described by:

$$E_{bond} = D_e\left(1 - e^{-a(l_{ij}-l_0)}\right)^2 \quad (2.3)$$

D_e is the depth of the potential energy minimum and a is the potential well depth. The three-body angular bond potential describes the angular vibrational motion occurring between three atoms and is traditionally treated the same way as a bond

length, described by a harmonic bending potential

$$E_{angle} = \frac{k}{2}\left(\theta_{ijk} - \theta_0\right)^2 \quad (2.4)$$

Where k is a harmonic spring constant, the θ_0 is the equilibrium bond angle. Since less energy is required to deform an angle, than is required to stretch a bond, the force constants associated with angle deformations are far smaller. The final type of deformation that will be discussed are the torsional terms. Not all force fields use torisonal terms (we have not in this thesis) as often it is possible to rely on non-bonded interactions with atoms at the end of each torsion i.e. at the 1,4 positions to describe the energy profile. A common form of torsional potential is the harmonic potential:

$$E_{torision} = \frac{k}{2}\left(\emptyset_{ijkl} - \emptyset_0\right)^2 \quad (2.5)$$

where $\emptyset_0$ is the equilibrium dihedral angle and k is harmonic spring constant for the deformation.

2.1.2 Intermolecular Interactions

For interactions that are not defined by the connectivity of bonds in the molecules, the terms are instead dependent on the distance between particles or atoms. These interactions can be considered to consist of two parts: electrostatic or coulombic and van der Waals (vdW) interactions.

Electrostatic interactions are calculated using Coulomb's law:

$$V = \sum_{i=1}^{N_A}\sum_{j=1}^{N_B}\frac{q_i q_j}{4\pi\epsilon_0 r_{ij}} \quad (2.6)$$

where N_A and N_B are the numbers of point charges in each molecule, q_i and q_j are the values of the point charges, r_{ij} is the separation between the point charges and ϵ_0 is the permittivity of free space. The electrostatic term becomes less accurate for highly polarisable ions or groups, and this is when polarisable force-fields would be required (explained in the next section).

vdW force include long range dispersive forces and short range repulsive forces. The long range forces result from instantaneous dipoles forming on particles which then induce a dipole in a neighbouring particle. This results in an attraction between the particles. Short range repulsive forces arise due to the Pauli exclusion principle where two electrons in a system are not allowed to have the same quantum number. This results in the electrons of two nearby nuclei dispersing and hence reducing the density of electrons in the internuclear region. This leads to a repulsion between the now less shielded nuclei. The most common form of potential used to represent vdW forces is the Lennard-Jones 12-6 potential (Jones, 1924) which does not require the calculating of large numbers of square roots and exponentials. It depends only on two parameters and is expressed as:

$$V(r) = 4\epsilon\left[\left(\frac{\sigma}{r}\right)^{12} - \left(\frac{\sigma}{r}\right)^{6}\right] \tag{2.7}$$

where σ is the collision diameter, the point at which the vdW energy is zero and ϵ is the well depth. Dispersion-attraction forces are mediated by the r^{-6} term and the short-range repulsions are accounted for by the r^{-12} term. Another potential, which fits the criteria to describe the attractive and repulsive forces, is the Buckingham potential. It is known from atomic theory that the electron density decreases exponentially with increasing distance from the nucleus, therefore the use of an

exponential function defining the repulsive component is justified.

$$V(r) = \epsilon \left[\frac{6}{\alpha - 6} exp \left[\frac{r}{r_m} - 1 \right] - \frac{\alpha}{\alpha - 6} \left(\frac{r_m}{r} \right)^6 \right] \quad (2.8)$$

This potential has three parameters, like the L-J 12-6 potential, ϵ and r_m describe the energy well depth and distance, while is α a single constant. This replaces the repulsive r^{-12} term with an exponential term which better represents the repulsions at short range. However, when running simulations as at very short separations the potential becomes strongly attractive which can result in fused nuclei. It is therefore common in simulations to employ a cutoff below which the Buckingham potential does not apply.

2.1.2.1 Shell Model

It was previously stated that electrons are essentially ignored in MM. However, in some systems the polarisation of atoms, oxygen being an excellent example, is very important to the structure and hence derived properties. The shell model of Dick and Overhauser (Dick and Overhauser, 1958) allows ions to have a polarisation description. The model divides the ion into a core part and a shell part. The core contains all the mass which is attached by a spring to the mass-less shell. The spring possesses a force constant which is consistent with Hooke's law. Both the shell and the core have a charge the sum of which is the total charge on the ion.

$$V_{spring} = \frac{k_{spring}}{2} (l - l_0)^2 \quad (2.9)$$

where l_0 is the equilibrium spring distance, and k_{spring} is the force constant for the spring. Modelling the polarisation of oxygen ions is extremely important in zeolites as this is necessary to give the correct T-O-T angle. (Sanders, *et al*., 1984)

2.2 Electronic Structure Methods

Electronic structure methods assume nothing about the system in question and solve the electronic state of the system in order to calculate the desired properties. This is achieved by applying the laws of quantum mechanics, the basis of which is the Schrödinger equation.

2.2.1 Schrödinger equation

The time- independent Schrödinger equation (Schrodinger, 1926) as the key equation of quantum mechanics, for a system of M nuclei and N electrons, described respectively by the coordinates $R = R_1$, $R_M$and $r = r_1, \ldots r_N$ has the general form:

$$\hat{\mathrm{H}}\psi(r, R) = E\psi(r, R) \tag{2.10}$$

Where $\hat{\mathrm{H}}$ is the Hamiltonian operator and $\psi(r,\ R)$ is the wave function and eigenstates of the Hamiltonian where each of them has an associated eigenvalue, E, a real number representing the energy and satisfies the eigenvalue equation. A more complete description of the Hamiltonian is:

$$\hat{\mathrm{H}} = \hat{T}_e + \hat{T}_N + \hat{V}_{eN} + \hat{V}_{ee} + \hat{V}_{NN} \tag{2.11}$$

Where $\hat{T}_e$ and $\hat{T}_N$ are the kinetic energy operators of electrons and nuclei respectively:

$$\widehat{T_e} = -\sum_{j>i}^{N} \frac{1}{2} \nabla_i^2 \tag{2.12}$$

$$\widehat{T_N} = -\sum_{j>i}^{N} \frac{1}{2M_I} \nabla_I^2 \tag{2.13}$$

Where M_I represents the ratio of the mass of nucleus I to the mass of an electron. The Laplace operator (∇) is the second derivative with respect to the spatial coordinates of the electron or nucleus.

$\hat{V}_{eN}$, $\hat{V}_{ee}$and $\hat{V}_{NN}$ are the potential energy operators of attractive electron-nucleus, repulsive electron-electron, and nucleus interactions:

$$\hat{V}_{eN} = \sum_{i=1}^{N} \sum_{I=1}^{M} \frac{Z_I}{r_{iI}} \tag{2.14}$$

$$\hat{V}_{ee} = \sum_{i=1}^{N} \sum_{j>i}^{N} \frac{1}{r_{ij}} \tag{2.15}$$

$$\hat{V}_{NN} = \sum_{I=1}^{M} \sum_{J>I}^{M} \frac{Z_I Z_I}{R_{IJ}} \tag{2.16}$$

The above equations are given in atomic units, where r_{ij} , r_{iI} and R_{IJ} are the i^{th} - j^{th} electrons, i^{th} electron - I^{th} - J^{th} nuclei. Distances respectively. Z_I and Z_J are the atomic numbers of nuclei I and J.

The exact solution to this Schrödinger equation for many-body problem which involves dealing with a system of Nelectrrons and M nuclei is impossible and a series of approximations are necessary to help simplify the problem. One of these is the Hartree-Fock method.

2.2.2 Hartree-Fock Method

The first approximation in HF theory is that the electronic wavefunction can be approximated as the product of single-electron functions (orbitals), each of which do not explicitly depend on the motion of the other electrons. The Hartree-Fock equation may be written:

$$\hat{F}(1)\Phi_i(1) = \varepsilon_i\Phi_i(1) \tag{2.17}$$

where $\hat{F}$ is the Fock operator, ε_i is the energy of electron i, and $\Phi_i(1)$ is the function describing electron i in orbital 1. The above equation can be rewritten as:

$$\hat{F}(1)\Phi_i(1) = \left(\frac{1}{2}\nabla_i^2\right)\Phi_i(1) - \sum\left(\frac{Z_A}{r_{1A}}\right)\Phi_i(1) + \sum_{j\neq i} J_j(1)\Phi_i(1) + \sum_{j\neq i} K_j(1)\Phi_i(1)$$

The first term is the kinetic energy term, while the second term represents the coulombic term for the interaction between the electron and nucleus A. The third term is the Coulomb operator ($\hat{J}$) because it leads to energy terms corresponding to the electrostatic repulsion between an electron in orbital Φ_i with electrons in every other orbital, and the last term is called the exchange operator ($\hat{K}$) because it takes into account the modification in the energy due to the effects of spin correlation between electrons of the same spin. However, the disadvantage of the method is electron correlation is completely ignored. That is, a particular electron is assumed to be moving in an average potential of all the other electrons, which of course is not the case as electronic motion is correlated and electrons will tend to avoid each other. Thus, the requirement of a computational method that successfully incorporates the effects of both exchange and correlation has led to the density functional theory approach.

2.2.3 Density Functional Theory

Density functional theory (DFT) solves the Schrödinger equation where the basic variable used is the ground-state electron density rather than N-electron wave functions. Fundamental to this theory, which is the most widely used method in the context of solid state simulation, are the Hohenberg-Kohn (Hohenberg and Kohn, 1964) and Kohn-Sham equations (Kohn and Sham, 1965).

2.2.3.1 Hohenberg and Kohn theorems

The first approach for solving many-body electron problem of Schrödinger equation was postulated by Hohenberg and Kohn (Hohenberg and Kohn, 1964). The two theorems can be formulated as follow:

- The first states that the external potential due to the nuclei $V_{ext}\,(r)$, felt by an arbitrary number of electrons is uniquely determined by the ground state electron density $n_0\,(r)$. It therefore follows that all the properties of a physical system can be calculated if the electrons density is known.
- Second theorem states that for any external potential $V_{ext}\,(r)$, there is a functional for the energy $E[n(r)]$ of an electronic system. The ground state energy of a system for a given external potential is the global minimum of this functional and the electron density which gives the minimum value of the functional must be the electron density in the ground state $n_0\,(r)$. Thus the total energy functional can be written as follows:

$$E[n(r)] = \int V_{ext}\,(r)n(r)dr + F[n(r)] \qquad (2.19)$$

The functional $F[n(r)]$, is the electronic part of the Hamiltonian and contains the kinetic energy of electrons as well as electron-electron repulsion, exchange and correlation energies.

The Schrödinger equation can be rewritten now as a function of the electron density, $[n(r)]$:

$$\left[\hat{T}[n(r)] + \hat{V}_{ee}[n(r)] + V_{ext}[n(r)]\right]\psi = E[n(r)]\psi \quad (2.20)$$

Despite all the above demonstrations, there is still the problem of calculating the electron-electron repulsion term of above equation and thus no practical way of determining the ground state density of the system. This issue was solved by Kohn and Sham (Kohn and Sham, 1965).

2.2.3.2 The Kohn and Sham Theory

Kohn and Sham developed the approach of the early density functional theory by assuming that the many-body electronic wave function acts in a same way as a fictitious single particle non-interacting wave functions which are called Kohn-Sham (KS) one –electron orbitals ψ_i and defined as follows:

$$n(r) = \sum_{i=1}^{N} |\psi_i| \quad (2.21)$$

The Kohn-Sham equation is therefore used to find the one-electron orbital that minimize the equation of energy:

$$\hat{H}^{KS}\psi_i = \varepsilon_i^{KS}\psi_i \quad (2.22)$$

Thus the Kohn-Sham Hamiltonian, $\hat{H}^{KS}$, acting on each electron is:

$$\hat{H}^{KS} = -\frac{1}{2}\nabla_i^2 \sum_{A=1}^{M} \frac{Z_A}{|r-R_A|} + \frac{1}{2}\int \frac{n(r')}{|r-r'|}dr' + V_{xc}(r) \quad (2.23)$$

where the first term represents the kinetic energy of the non-interacting system, the second term represents the external potential from nuclei (A) felt by the electron, where there is a distance $r - R_A$ betweem the electron and nuclei, the third term represents the coulombic repulsion between the particular electronic density with the

other electrons in the system and the last term represents the exchange-correlation potential which is equal $\frac{\delta E_{xc}[n(r)]}{\delta n(r)}$. $E_{xc}[n(r)]$ is the exchange-correlation energy which accounts for the differences between interacting and non-interacting systems and, as it is unknown, approximations must be made to describe this term.

2.2.3.3 Exchange correlation functional

The exchange-correlation term $E_{xc}[n(r)]$ consists of a correction to the one - particle kinetic energy and coulombic repulsion. It is the difference between the energy obtained from the non-interacting system and the exact energy from the real system. The exchange-correlation term also includes a correction for electron self-interaction where an electron has coulombic interaction with itself. The exact functional form is known only for a homogeneous electron gas so approximations must be made in order to solve more complex systems. Two of the most commonly used approximations for calculation of exchange-correlation functional are local density approximation (LDA) and generalised gradient approximation (GGA).

In the LDA, the exchange-correlation energy at point r is determined using only the electron density, $n(r)$, at that point, and not dependent, on the density at other points. In this approximation, the exchange-correlation of a real system behaves locally as a uniform, homogeneous electron gas of the same system. The LDA exchange-correlation energy has the form:

$$E_{xc}^{LDA}[n(r)] = \int n(r)\, \varepsilon_{xc}^{hom}[n(r)]dr \tag{2.24}$$

where ε_{xc}^{hom} is the exchange-correlation energy per particle of a uniform electron gas. Generally LDA is good for systems such as metals where the electron density

is relatively uniform. It has been shown to result in overbinding, shortening of bonds, and to poorly represent hydrogen bonds. (Filippi, *et al*., 1994, Hohenberg and Kohn, 1964)

An improvement to the local density approximation is the generalised gradient approximation (GGA), as an independent variable leading to GGA exchange-correlation approximation which introduces non-local effects on the functional:

$$E_{\boldsymbol{x}}^{GGA}[n(r)] = \int n(r)\, \varepsilon_{xc}^{LDA}[n(r), \nabla\, n(r)]dr \qquad (2.25)$$

This functional considers fast varying changes in the elextron density, which are not accounted for by LDA, resulting in better geometries, vibrational frequencies, charge densities and binding energies than LDA. The most common GGA functionals are Perdew, Burke and Enzerhof (PBE) (Perdew, et al., 1996) and Perdew and Wang (PW91)(Perdew and Wang, 1992). The PBE functional was chosen for our study concerning the location of extraframework cations in FER zeolite (Chapter 6). Hybrid functionals incorporate a portion of the exact exchange from Hartree-Fock theory with exchange and correlation from other sources (*ab initio* or empirical) have been introduced (Becke, 1993) and they are generally preferred over purely LDA and GGA functionals. One of the most commonly used versions of hybrid functional is B3LYP, which stands for Becke, 3-parameter, Lee-Yang-Parr (Becke, 1993). It takes the form:

$$E_{xc}^{B3LYP} = E_{xc}^{LDA} + a_0(E_x^{HF} - E_x^{LDA}) + a_x\,(E_x^{B88} - E_x^{LDA}) + a_c(E_c^{LYP} - E_c^{LDA}) \qquad (2.26)$$

where the x and$c$ subscripts designate exchange and correlation, respectively, and E_x^{B88} and E_c^{LYP} refer to Becke's formulation of the GGA exchange and the correlation as derived from Lee, Yang and Parr, respectively. In the standard formulations, the parameters have the values of a_0 = 0.20, a_x = 0.72 and a_c= 0.81. We have used this functional throughout our thesis.

2.2.3.4 Grimme

Standard DFT failed to describe properly the weak, non-local, long range dispersion forces, which may be occuring within the system. The most common form of dispersion correction for DFT is the Grimme method known as DFT-D3 (Grimme, 2004, Grimme, 2006). In the D3 correction method of Grimme *et al.* (Grimme, 2004) the following vdW-energy is used:

$$E_{disp} = -\frac{1}{2}\sum_{i=1}^{N_{at}}\sum_{j=1}^{N_{at}}\sum_{L}{}' \left(f_{d,6}(r_{ij,L})\frac{C_{6ij}}{r_{ij,L}^{6}} + f_{d,8}(r_{ij,L})\frac{C_{8ij}}{r_{ij,L}^{8}}\right), \quad (2.27)$$

Unlike in the method D2, the dispersion coefficients C_{6ij} are geometry-dependent as they are adjusted on the basis of local geometry (coordination number) around atoms i and j.

2.2.4 Basis sets

Basis sets are used in quantum mechanical calculations to define molecular orbitals in the form of atomic functions. There are two main types of basis sets, atom centred and plane wave. An atom centred basis set consists of a number of atomic functions which define the electron population at a given distance from the nucleus. There are a number of different functions available anf the most common ones will be discussed now. The first is a Slater type orbital (STO) whch has the functional form:

$$R(r) = Nr^{n-1}e^{-\varsigma r^2} \quad (2.28)$$

where r is the distance from the nucleus n is the principle quantum number, N is a normslisation constant and ς is the effective charge of the nucleus as there is a partial shielding of the core due to the electrons. The drawback with using STOs in molecular

orbital calculations is that some of the integrals are extremely difficult to evaluate especifically when the orbitals are centred on different nuclei.

A more commonly used function is one based on Gaussians, Gaussian type orbitals (GTO) have the form:

$$R(r) = x^a y^b z^c e^{-\alpha r^2} \tag{2.29}$$

where α determines the radial extent of the orbital, a, b and c determine the order and x, y and z are Cartesian variables, of the Gaussian function. A function with $a + b + c = 0$ is a zeroth order function and can be compared to a s orbtal. A first order function has $a + b + c = 1$ and can be related to the p_x, p_y and p_z orbitals, and so forth up the orders. It is unlikely that simply representing the occupied atomic orbitals in a quantum calculation will be sufficient, and it is common to include higher unoccupied orbitals in order to improve the accuracy of the calculation. The basis set can be split into two basis functions (double zeta) that correspond to the valence orbitals. Further splitting gives triple zeta, quadruple zeta etc. functions, although it is uncommon to go further than quadruple zeta. An alternative method is to double the number of functions used for the valence electrons but keep single functions for the inner shells. The logic behind this is that the properties of interest will be defined by the valence electrons as these are the ones that will interact. This method is so popular that it has been given its own notation. For example the 3-21G basis set has three Gaussian functions to describe the core electrons and the valence electrons are described by two contracted and one diffuse Gaussian. Further improvements can be made by including a polarisation function. For example a hydrogen atom will have a spherical electron cloud when in isolation. When however it is in a molecule, there will be a perturbation of the electron cloud towards

the other nuclei and give a sp hybrid. The solution to this problem is to introduce polarisation functions to the basis set. A polarisation function has a higher angular quantum number and so will correspond to p orbitals in our hydrogen atom example. The polarisation function is denoted by an asterick *. A 6-31G* basis set has polarisation functions on the heavy atoms and a 6-31G** basis set also includes polarisation functions on the light (hydrogen and helium) atoms. The final addition that can be made to a basis set is to deal with atoms which have a significant amount of electron density far away from the nucleus. This occurs for example when an atom has a lone pair. In this case a highly diffuse function is added to the basis set and a basis set with this included is given the '+' notation. A 6-31+G basis set has a single set of diffuse functions s- and p- type Gaussian functions. In a manner analogous to the polarisation functions, a double plus (6-31++G) means that the diffuse functions are included on the light atoms as well. With regards to plane waves basis sets, the orbital wavefunction is described by a finite number of plane waves. Since the deeply bound core electrons within plane wave basis sets require a huge amount of basis functions for their description, the computational cost is high. To solve this problem, plane wave basis sets are often used in combination with an effective core potential or pseudo-potential (nonlocal operators i.e. they are not simple functions) and the plane waves are only used to describe the valence charge density. This is because core electrons tend to be concentrated very close to the atomic nuclei. Gaussian plane waves (GPWs) require pseudo-potentials to describe the high variance of wavefunctions close to the nucleus.

2.3 Transition States

One of the most important problems in theoretical chemistry and condensed matter

is the identification of a lowest energy path for the rearrangement of a group of atoms from one stable configuration to another. Such a path is often referred to as the 'minimum energy path' (MEP). An optimized structure corresponds to a minimum point on the potential energy surface (PES) and is located by means of a 'minimization' algorithm and it may refer to either minima or transition state. It is frequently used to define a 'reaction coordinate' (Marcus, 1966) for transitions, such as chemical reactions, changes in conformation of molecules, or diffusion processes in solids. Note that the PES can have several local minima and those minima are linked by transition states along the reaction coordinates **(Figure 2-1)**.

A transition state is a saddle point that represents the high energy state for atomic rearrangement between two minima along the reaction coordinate. The activation energy, the most important parameter characterizing a transition state, corresponds to the difference between the initial minima state and the saddle point **(Figure 2-1)**.

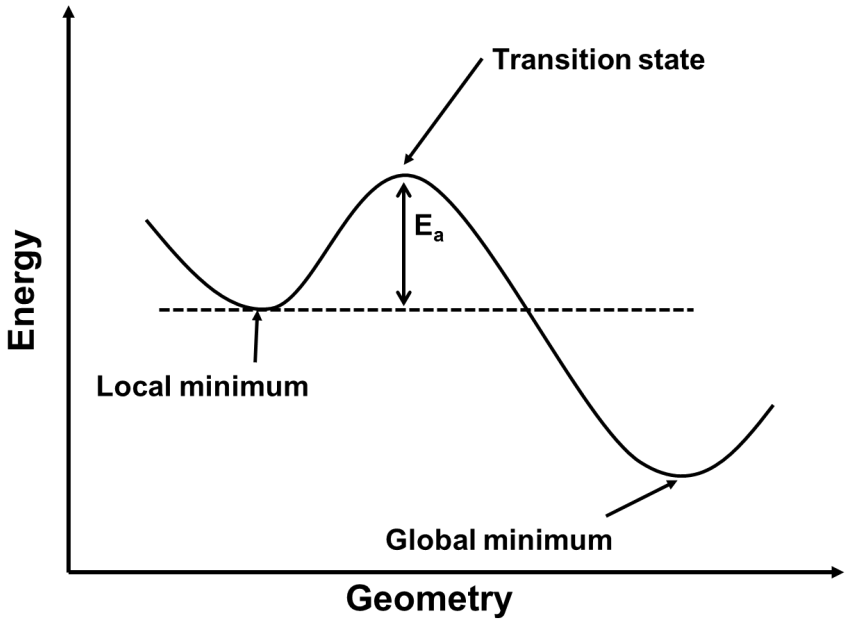

Figure 2-1. Schematic representation of two minima linked by a transition state. E_a represents the activation energy.

Many methods have been developed for finding the reaction path and saddle points. Usually periodic codes based on plane waves pseudo-potential approach adopt the nudged elastic band (NEB) approach (Mills and Jonsson, 1994). The NEB has the advantage of requiring energy and gradient only to discover the minimum energy path, at the expense of a relatively high number of images needed to improve the accuracy of the search. In this thesis, the method we adopt to locate the transition state is different from NEB and it is called distinguished reaction coordinate (DRC). DRC can be successfully used for systems of any dimensionality (molecules, polymers, slabs and crystals).

DRC method involves a scan calculation along the internal coordinate that governs the reaction. This scan calculation consists in evolving, step by step and in a controlled way, the selected internal coordinate so to move from reactants to products by crossing a point of maximum energy. At each step, constrained geometry optimizations will be performed, keeping the value of the reaction coordinate frozen while all other internal coordinates are relaxed, so a 'pseudo-optimized' structure is computed. At the end of the scan calculation, a complete energy profile can be obtained for each elementary step along the chosen reaction coordinate.

2.4 Vibrational frequencies

Evaluating the vibrational modes of a system is useful for several reasons including i) to ensure whether the optimized geometry is a minimum or a transition state on the PES and ii) to simulate the IR or Raman spectra, which can be compared with experimental data.

The vibrational frequencies are obtained from the second derivative of the potential energy. The second derivative of the energy are computed numerically by using the analytical first derivatives (gradients). Frequencies are obtained by diagonalizing the mass-weighted Hessian matrix (Equation 2.30) in Cartesian coordinates. The eigenvalues and eigenvectors of the Hessian matrix correspond to the vibrational frequencies and vibrational modes, respectively, of the system.

$$H = \begin{matrix} \frac{\partial^2 f}{\partial x_1^2} & \cdots & \frac{\partial^2 f}{\partial x_1 \partial x_n} \\ \vdots & \ddots & \vdots \\ \frac{\partial^2 f}{\partial x_n \partial x_1} & \cdots & \frac{\partial^2 f}{\partial x_n^2} \end{matrix} \tag{2.30}$$

A stationary point is confirmed as a local minimum if all second derivatives are negative *i.e.*, the vibrational frequencies are all real, whereas if one imaginary frequency is found then, the stationary point can be assigned to be saddle point.

2.5 Periodic Boundary Conditions

All of the calculations undertaken in this thesis involve the use of a model model with periodic boundary conditions. The solutions to the Schrödinger equation in a periodic potential are Bloch functions, which have the form:

$$\varphi_k(r) = u_k(r) e^{ik.r} \tag{2.31}$$

where $u_k(r)$ has the period of the lattice, i.e. $u_k(r) = u_k(r + a)$ has a lattice vector a, and k is one of the set of allowed wavevectors determined by the symmetry of the system. Bloch's theoerem states that the one-electron eigenfunctions can be expressed as the product of a plane wave and a function with the periodicity of the

lattice. These form a complete set of eigenfunctions. Due to the translation symmetry, it is sufficient to calculate the eigenfunction for value of k that lie in the first Brillouin zone, which is the reciprocal lattice equivalent of the primitive unit cell, in order to describe any eigenstate of the electronic wavefunction.

Although *k* essentially forms a continuum in the first Brillouin zone due to the high density of points, it is smoothly-varying, and as such a particular point in *k*-space has a similar value to the other points close to it. The eigenfunction can be then estimated by summing over a finite number of *k*-points sampled with a regular mesh in reciprocal space, the so-called Monkhorst-Pack (Monkhorst and Pack, 1976) scheme. As the mesh becomes finer, the approximation of the sum to the integral over all space becomes more accurate.

PBC allows simulations of bulk solids to be performed where they would otherwise require a large number of atoms. The simulation cell is surrounded by an infinite number of images of itself by rigid translation in all the three Cartesian directions (x, y and z). If a particle leaves the simulation cell an image of this particle appears on the opposite side (**Figure 2-2**) keeping the number of particles constant. Since this means we have an infinite number of non-bonded interactions a cut-off is applied: generally we apply the minimum image convention where each particle only interacts with each other particle once, whether it be in the actual simulation cell or one of the images.

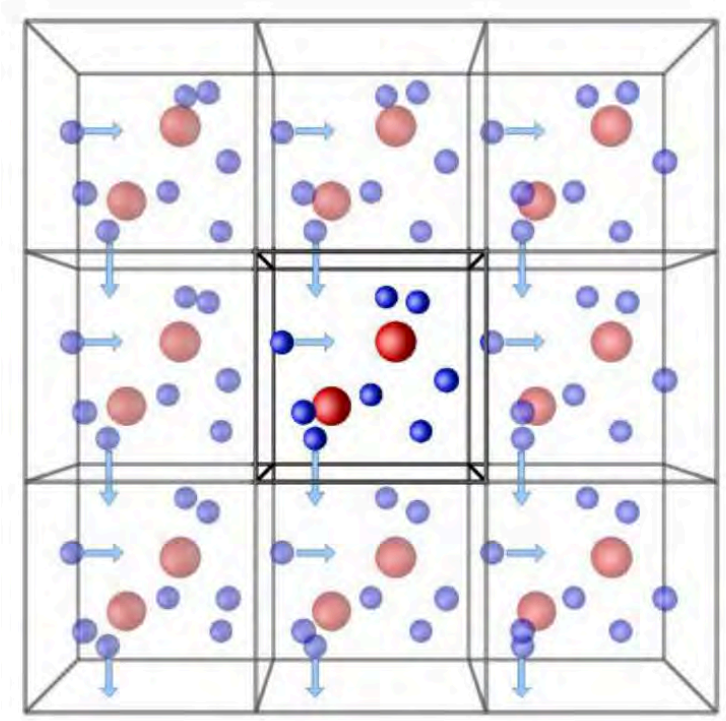

Figure 2-2. A graphical representation of PBC - as one blue atom leaves the centre of the box, another simultaneously enters the central box from the opposite side.

An alternative method for modelling zeolites is a embedded cluster approach by making quantum mechanical calculations on solids practicable. These methods include combined quantum mechanics/ molecular mechanics (QM/MM) methods, as well as the more general two-layered Our own N-layered Integrated molecular Orbital and molecular Mechanics (ONIOM) method (Svensson, *et al*., 1996).

Here, only a finite number of atoms is considered of the zeolite and the partitioning the system into two layers treated at different methods of accuracy. Typically, this includes a representative model of a zeolite active site itself and a part of the structure near it to mimic the local properties of the zeolite lattice. According to the ONIOM approach, the calculation of energies can be simplified by treating the active region (i.e. the active acidic site of a zeolite catalyst) with a high-level quantum mechanical (*ab initio* or density

functional) approach, and the extended framework environment with a less MM force fields methods. An important feature for combination method is the treatment at the boundary region between the different levels of calculation. With ONIOM the covalent bond at the boundary region have to cut to generate the inner cluster and have to be saturated, usually with hydrogen atoms to avoid dangling bond.

2.6 Molecular Dynamics

In molecular dynamics (MD) the system configurations are generated by integrating Newton's laws of motion. These can be summarised as follows:

1. A body continues to move in a straight line at a constant velocity unless a force acts upon it.
2. Force equals the rate of change of momentum.
3. To every action there is an equal and opposite reaction.

The result is a trajectory of how the position and velocity of the atoms vary with time and is obtained by solving the differential equations derived from Newton's second law, $F = ma$.

$$\frac{d^2x_i}{dt^2} = \frac{F_{x_i}}{m_i} \tag{2.32}$$

where F is the force, m is the mass and a is acceleration. Equation 2.32 describes the motion of a particle of mass m_i along one coordinate, x_i, and has a force, F_{x_i} on the particle in that direction.

We can solve Newton's laws of motion for a system of interacting bodies, *i.e.* our chemical system of interest, and generate a trajectory which can then be analysed and the relevant chemical properties extracted. The difficulty arises because we have many bodies interacting under a continuous potential with their motion coupled together. Several methods have been derived to solve these problems, the most relevant of which will now be discussed.

2.6.1 Finite Difference Methods

Finite difference methods are used to generate trajectories with continuous potentials. The integration is broken down into many small steps, separated by a fixed time step δt. The force on each particle is calculated at time $t$as a vector sum of its interactions with other particles. From the forces the accelerations can be calculated and these used with the positions and velocities at time t to calculate the positions and velocities at time δt. All of the algorithms for integrating the equations of motion using finite difference methods assume that the dynamic properties can be approximated to Taylor series expansions:

$$r(t+\delta t) = r(t) + \delta t v(t) + \frac{1}{2}\delta t^2 a(t) + \frac{1}{6}\delta t^2 b(t) + \frac{1}{24}\delta t^2 c(t) + \cdots \quad (2.33)$$

$$v(t+\delta t) = v(t) + \delta t a(t) + \frac{1}{2}\delta t^2 b(t) + \frac{1}{6}\delta t^2 c(t) + \ldots \quad (2.34)$$

$$a(t+\delta t) = a(t) + \delta t b(t) + \frac{1}{2}\delta t^2 c(t) + \ldots \quad (2.35)$$

where v is the velocity (1st derivative of the positions with respect to time, a is the acceleration (2nd derivative) and b is the third derivative etc. The Verlet algorithm (Rowlinson, 1986) is one of the most popular for integrating the equations of motion. The Verlet algorithm uses the positions and accelerations at time t and

the positions from the previous step $r(t-\delta t)$to calculate the positions at $r(t+\delta t)$. This leads to the following equations:

$$r(t+\delta t) = r(t) + \delta v(t) + \frac{1}{2}\delta t^2 a(t) + \cdots \quad (2.36)$$

$$r(t-\delta t) = r(t) + \delta t v(t) + \frac{1}{2}\delta t^2 a(t) + \cdots \quad (2.37)$$

These two equations can then be added to give:

$$r(t+\delta t) = 2r(t) - r(t) + \delta t^2 a(t) \quad (2.38)$$

Clearly, the velocities do not appear in the above equations, and so when using the Verlet algorithm, velocities must be calculated retrospectively:

$$v(t) = [r(t+\delta t) - r(t-\delta t)]\ /2\delta t \quad (2.39)$$

The advantage of the Verlet algorithm is that it is straightforward and the memory requirements are modest. However, there are a few drawbacks to the method, particularly that position $r(t+\delta t)$is obtained by adding $\delta t^2 a(t)$, which is small, to the difference of two large terms, $r(t+\delta t) - r(t-\delta t)$, which can lead to a loss of precision.

A variation of the Verlet algorithm is the velocity Verlet method (Verlet, 1967) The velocity Verlet method is a three step process and is implemented as follows:

$$r(t+\delta t) = r(t) + \delta t v(r) + \frac{1}{2}\, t^2 a(t) \quad (2.40)$$

$$v(t+\delta t) = v(t) + \frac{1}{2}\delta t[a(t) + a(t+\delta t)] \quad (2.41)$$

To calculate the new velocities, the accelerations at $t$and $t+\delta t$ are required, and so the first step in the velocity Verlet method is to calculate the positions at $t+\delta t$ using the velocities and accelerations at time t. Velocities at time $t+\frac{1}{2}\delta t$ are found using:

$$v\left(t + \frac{1}{2}\delta t\right) = v(t) + \frac{1}{2}\delta t a(t) \quad (2.42)$$

Forces from the current positions are calculated which in turn give the accelerations at $t + \delta t$ and finally the velocities at $t + \delta t$ can be calculated:

$$v(t + \delta t) = v\left(t + \frac{1}{2}\delta t\right) + \frac{1}{2}\delta t a(t + \delta t) \quad (2.43)$$

The velocity Verlet method has the advantage over the standard Verlet algorithm in that it gives positions, velocities, and accelerations at the same time without compromising precision.

2.6.2 Statistical Ensemble

A statistical ensemble is a finite collection of all possible systems that have different microscopic states but the same thermodynamic state. The simplest ensemble is the microcanonical one, i.e. NVE ensemble, in which the number of particles (N), the cell volume (V), and the total energy (E) are conserved. However, this ensemble does not represent the majority of real systems; temperature and pressure are required for more realistic simulations. A key ensemble method used is the canonical or constant NVT method with a thermostat. In this NVT ensemble, along with N and V, temperature T is kept constant. The temperature of a system is related to the time average of the kinetic energy for an unconstrained system:

$$K.E_{NVT} = \frac{3}{2}Nk_BT \quad (2.44)$$

where $K.E_{NVT}$ is the average kinetic energy and K_B is the Boltzmann constant. The approach initially used to maintain a constant temperature of the system is to scale

the kinetic energy i.e. scale the velocities. The velocity of the system is multiplied by a factor λ at time t, the associated temperature is calculated as follows:

$$\Delta T = \frac{1}{2}\sum_{i=1}^{N}\frac{2}{3}\frac{m_i(\lambda v_i)}{Nk_B} - \frac{1}{2}\sum_{i=1}^{N}\frac{2}{3}\frac{m_i v_i^2}{Nk_B} \tag{2.45}$$

$$\Delta T = (\lambda^2 - 1)T_{(t)} \tag{2.46}$$

$$\lambda = \sqrt{T_{new}/T_{(t)}} \tag{2.47}$$

where T (t) is the temperature at time t, m is the particle mass and *v* is the particle velocity. The velocities are multiplied at each time step by the factor λ, the current temperature is calculated from the kinetic energy and the required temperature. One problem with this approach is, that it does not allow fluctuations in temperature which are present in the canonical ensemble. An improvement on this method was made by Berendsen *et al.* (Berendsen *et al*., 1984) where the system is coupled to an external heat bath that is fixed at the desired temperature. Heat is then supplied or removed from the system to stabilise to the required temperature. The velocities are scaled at each time step, so that the rate of change of temperature is proportional to the difference in temperature between the bath and the system,

$$\frac{dT_{(t)}}{dt} = \frac{1}{\tau}\left(T_{bath} - T_{(t)}\right) \tag{2.48}$$

This leads to the scaling factor for velocities:

$$\lambda^2 = 1 + \frac{\delta t}{\tau}\left(\frac{T_{bath}}{T_{(t)}} - 1\right)$$

where τ is a coupling constant which determines how strongly the bath and system are coupled together and δt is the time step. When $\tau = \delta t$ the method is equal to the velocity scaling method discussed previously.

2.7 Computer Codes and High-Performance Computers

The starting point for the majority simulation techniques is the calculation of the energy. The initial calculations were performed using The General Utility Lattice Program (GULP) based on force field methods. With subsequent treatment of the nuclear degrees of freedom, the DFT calculations were performed, as implemented in the program CRYSTAL (Dovesi, *et al*., 2005). The CRYSTAL package performs ab initio calculations of the ground state energy, electronic wave function and properties of periodic systems within Hartree Fock, density functional or various hybrid approximations. We have also performed a series of AIMD simulations using the CP2K/QUICKSTEP package (VandeVondele, *et al*., 2005), which is the implementation of the Gaussian plane wave method for ab initio Born-Oppenheimer molecular dynamics within the Kohn-Sham framework of density functional theory. High Performance Computing clusters were used for running these simulations, namely the UK National Supercomputing Service, Archer, and UCL's Research Computing Services, Legion and Grace.

Chapter 3

Location of acid sites and their interaction with carbonyl species in MOR and FER zeolites

3.1 Introduction

As was stated in the introduction of this thesis, silicon-rich zeolites, FER and MOR, containing Brønsted acidic protons, have major importance as catalysts in commercially key processes. In particular the reactions of acetaldehyde and acetone are of interest here, as these small carbonyl compounds are initiated with H-bonding or proton transfer (Biaglow, *et al*., 1995, Boekfa, *et al*., 2010, Sepa, *et al*., 1996, Solans-Monfort, *et al*., 2002, Xu, *et al*., 1994).

Positioning of BA sites is found to be dependent upon the Al distribution derived from the zeolite synthesis (Gabova, *et al*., 2003). The location of Al and H atoms in MOR zeolite have been extensively studied both experimentally and theoretically. Alberti (Alberti, 1997) determined from a cross check of crystallochemical and spectroscopic data that T3 is the most preferential position for a single Si/Al substitution followed by T4. For deprotonated structures, Brändle and Sauer (Brändle and Sauer, 1998) used a QM-MM scheme and established the most stable position of Al atom is T4 followed by the T2, T1 and T3 positions. In contrast, Benco *et al.* (Benco, *et al*., 2005) found by periodic DFT calculations that the stability of the Si/Al substitution decreases in the order T2 > T3 > T1 > T4. Both studies reported only a modest difference in energies between the

most and least stable positions (4.4 or 7.4 kJ mol^{-1}). In terms of the distribution of BA sites, early diffraction studies non dehydrated MOR zeolite (Mortier, *et al*., 1975) and previous theoretical studies (Boronat, *et al*., 2004, Demuth, *et al*., 2000) concluded that there is no preferential attachment of protons to the different oxygen sites, indicating the possibility of a variety of distinct BA sites. On the basis basis of FTIR spectroscopy studies loaded with probe molecules, Makarova *et al*. (Makarova, *et al*., 1997) and Lukyanov *et al.* (Lukyanov, *et al*., 2014) suggested that around 67% of the protons are accessible from the main channel (MC) and 33% from the side pockets (SP) and smaller channels (SC). The experimental estimates of the BA site distributions are made on the basis of the assignment of low and high frequency IR bands to hydroxyls in the small 8-MR channel or SP and main 12-MR channel respectively. However this assumption is in contrast to theoretical as well as some recent experimental results suggesting no significant difference between the OH stretching frequencies of BA sites located in the MC or SC/SP and the observed low frequency was possibly due to the migration of the proton to another oxygen or the presence of two nearby Al sites which can induce different energy surfaces (Dominguez-Soria, *et al*., 2007). Further differentiation between the BA sites has been proposed suggesting that the number of distinct BA sites varied between 3 ~ 5 although the assignments of these BA sites to the particular oxygens were contradictory. For instance the preferred location in the SC are O1 (Huo, *et al*., 2012, Simperler, *et al*., 2004), O6 (Bevilacqua and Busca, 2002, Brandle and Sauer, 1998, Martucci, *et al*., 2000) and O9 (Alberti, *et al*., 1986, Marie, *et al*., 2004), although all authors considered the existence of only one distinct type of BA site in the SC. The agreement on the exact locations of BA sites in the large channels were also quite poor; where all the possible oxygen sites were suggested by these authors.

Concerning the Al location in FER zeolite, IR studies (Bordiga, *et al*., 2000) and periodic DFT calculations (Benco, *et al*., 2007) have identified T2 as the site with the highest Al population. Benco *et al*. (Benco, *et al*., 2007) stated that the relative energies with a single Al/Si substitution computed by the absence of any charge-balancing cation in the four different T sites are 0, 13, 15, and 22 kJ mol^{-1} for T2, T3, T4, and T1; proving the energy difference to be marginal. On the other hand, neutron diffraction studies (Martucci, *et al*., 2000) have determined that the preferential occupation of Al is in T1 and T3 sites. On the other hand, neutron diffraction studies (Martucci, *et al.*, 2000) have determined that the preferential occupation of Al is in T1 and T3 sites. Previous theoretical calculations, at the periodic DFT level (Feng, *et al*., 2017, Grajciar, *et al*., 2010, Nachtigall, *et al*., 2009) and ONIOM cluster scheme (He, *et al*., 2017, Liu, *et al.*, 2014) were used to determine the location and stability of BA sites, with a Si/Al ratio of 35, but exhibited inconsistencies. A common feature of all these studies quoted is the small difference in relative stability of the proton at different framework oxygens. In this situation, the intrinsic approximations of each computational study related for instance to the choice of PBC or embedded cluster, the DFT functional & basis set type, may alter the relative stability of different sites.

Here we attempt to study all the possible locations of BA sites in the vicinity of each of the defined inequivalent T site positions in FER and MOR zeolites and establish the most stable location of proton siting. With the complex study by Dedecek *et al.* (Dedecek, *et al*., 2011) 'claiming' to have identified the existence of T1a and T1b sites, we studied the proton location at these two sites in order

to validate the theory. The reactions involving the small carbonyl compounds are studied at the specific acid site locations in both zeolites in order to discover which are the active sites that can stabilize the reactants and therefore how the existing catalyst can be improved. Besides the H-bonding and other interactions, the confinement effect are of equal importance in the determination of factors that influence the reactivity of these complexes (Namuangruk, *et al*., 2006). In this chapter, using periodic DFT calculations we aim for a comprehensive understanding of the effects of acid site and zeolite framework confinement on the adsorption of these basic molecules.

3.2 Computational Details

For each structure type, the first aim was to identify a representative Brønsted site, based on a common energy minimization protocol. The main criteria were the thermodynamic stability of the structure and more importantly, the accessibility of the acid proton. The initial coordinates of FER and MOR zeolites were taken from the International Zeolite Database (IZA) (McCusker, 2007). For the all-silica form, the unit cell parameters of FER were previously optimized (Pickering, *et al*., 1989), a = 19.147, b = 14.304 and c = 7.575 Å and for MOR the lattice parameters were previously optimised a = 18.256 Å and b = 20.534 Å and c = 7.542 Å in order to sufficiently enclose the small 8-MR channels. Starting from a pure silica form, each of the symmetrically distinct T atoms was substituted with an Al atom and to compensate the charge difference, a proton (H^+) was placed on each of the four adjacent bridging oxygen atoms. The hydrogen is placed initially at 1.0 Å distance from the oxygen and in the plane of the Al-O-Si bond, which is a

suitably accurate starting point for minimization when optimizing the structure (Demuth, *et al.*, 2000, Simperler, *et al*., 2004). The molecular graphic program Moldraw (Ugliengo, *et al*., 1993) was used for he visualization and geometrical manipulation of all the structures. For a structure with n different T atoms, 4n starting configurations were produced for lattice energy minimization. Minimizations were carried out using PBC with 1 Al atom in the conventional unit cell of each zeolite, thus the Si/Al ratios were 35 for FER and 47 for MOR. The minimizations were initially carried out using the GULP program (Gale and Rohl, 2003). The potentials used were those derived by Catlow *et al.* (Gale and Henson, 1994, Jackson and Catlow, 1988, Sanders, *et al*., 1984, Schroder, *et al*., 1992), shown in **Appendix: Table 8-1 and 8-2**. The O-H bond was represented by the Morse potential terms originally derived by Saul *et al.* (Saul, *et al.*, 1985) from ab initio calculations. The shell model is included to allow for the polarization of framework oxygen. Minimizations were carried under constant pressure; that is, unit cell parameters were allowed to vary as well as atomic positions. The GULP minimized structures were then further optimized to more accurate structures using periodic DFT in the CRYSTAL code (Dovesi, *et al*., 2005) which implements Kohn-Sham for the study of periodic systems and allows performing full optimization (both internal coordinates and cell size (Civalleri, *et al*., 2001) of molecules and crystals. Those structures resulting in the lowest protonation energies were taken as the most thermodynamically favoured and were used to study the adsorption of an acetaldehyde or acetone molecule with the CRYSTAL code. The B3LYP hybrid exchange-correlation functional (Becke, 1993, Lee, *et al*., 1988, Stephens, *et al*., 1994, Vosko, *et al*., 1980) was adopted for all the calculations. The FER and

MOR framework was calculated using PBC in P1 space group to allow full optimization without symmetry constraints. The electronic distribution was described as a linear combination of atomic orbitals and the basis functions are expressed analytically as a contraction of Gaussian-type orbitals (GTO). The GTO basis sets used for the geometry optimization of all the structures, are of triple valence plus polarisation quality (6-311G **) for all atoms. All basis sets were provided from the online library of the CRSYTAL code. (Dovesi, *et al.*, 2005) The tolerances that control the Coloumb and exchange series have been chosen so that when the overlap between two atomic orbitals is smaller than 10^{-6} (for the Coloumb) or 10^{-12} (for the exchange) the corresponding integral is disregarded included in long range electrostatic sums. The SCF process is stopped when the energy difference between two cycles is smaller than 10^{-9} Hartree. The empirical DFT-D3 dispersion correction proposed by Grimme (Grimme, 2006) has been used throughout. In this scheme, the total energy is given as

$$E_{total} = E_{elec} + E_{disp}$$

Here, E_{elec} is the calculated DFT electronic energy obtained using the given exchange-correlation functional and E_{disp} is the empirical dispersion energy obtained using the Grimme method. The adsorption energies, E_{ads}, were calculated as:

$$E_{ads} = E(complex) - E(zeolite) - E(molecule)$$

Where E(complex) represents to the total energy of the adsorbate-zeolite system, $E(zeolite)$ represents the energy of the free zeolite and $E(molecule)$ represents the energy of the molecule (acetaldehyde or acetone) in gas phase. A negative adsorption energy indicates a favourable adsorption.

3.3 Results and Discussion

3.3.1 Proton location and stability of acid sites in MOR zeolite

Considering the four inequivalent T sites, we established 12 distinct possibilities to protonate an oxygen nearest neighbour to Al atom. The relative energies (ΔE_{rel}) were calculated with respect to the most stable BA site, this is Al1 – O7 – Si1 (i.e. the Al atom is located in T1 position and on the proton is attached to the O7 oxygen site which is bound to a Si atom located in T1 position) for FF method, and Al3 – O1 – Si1 for the periodic DFT method, shown in **Table 3-1**, along with the proton locations in the zeolite structure which is depicted in **Figure 3-1.**

BA sites	H location		ΔE_{rel} kJ mol^{-1}	
	FF	*Periodic DFT*	*FF*	*Periodic DFT*
Al1 – O7 – Si1	MC	M7*	0.00	24.84
Al1 – O3 – Si2	MC	MC	1.98	32.35
Al1 – O1 – Si3	SC	SC	6.59	28.32
Al1 – O6 – Si1	I_{SC-SP}	I_{SC-SP}	10.71	25.39
Al2 – O3 – Si1	MC	M7*	14.25	12.35
Al2 – O2 – Si4	I_{MC-SP}	I_{MC-SP}	8.01	24.81
Al2 – O8 – Si2	5-MR	5-MR*	18.04	24.99
Al2 – O5 – Si2	I_{MC-SP}	I_{MC-SP}	9.30	26.75
Al3 – O4 – Si4	5-MR *	5-MR*	20.86	35.27
Al3 – O1 – Si1	SC	SC	1.14	0.00
Al3 – O9 – Si3	SC	I_{SC-SP}	16.81	34.29
Al4 – O2 – Si2	I_{MC-SP}	I_{MC-SP}	5.70	32.52
Al4 – O4 – Si3	5-MR	5-MR*	20.64	26.52
Al4 – O10 – Si4	MC	MC	16.14	38.57

Table 3-1 Relative energies of isolated BA sites in MOR zeolite computed with respect to the energetically most favourable BA site, [Al1 – O7 – Si1] for FF and [Al3 – O1 – Si1] for periodic DFT. Most stable BA sites for each unique T site position of Al using periodic DFT via CRYSTAL code is depicted in bold. The stars (*) denotes the BA sites involved in a strong intra-zeolite H bond. The location of the proton is noted for each site and is depicted in Figure 3-1.

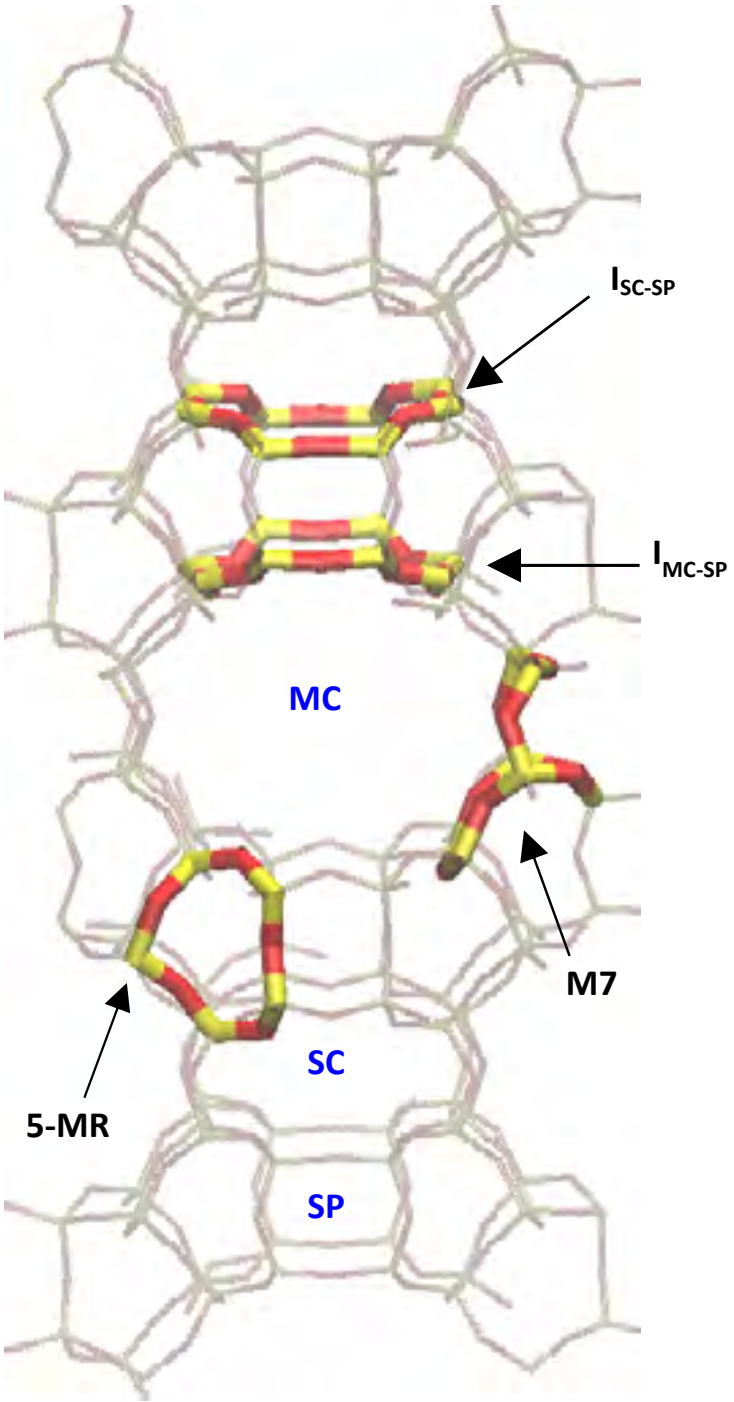

Figure 3-1 Location of proton of the isolated BA sites in MOR zeolite: M7 ring located in the MC, I_{MC-SP} is the 8-MR window intersection between the MC and SP and I_{SC-SP} is the 8-MR window intersection between the SC and SP, chains of 5-MR which are inaccessible for interaction with molecules.

The BA sites, Al2 – O8 – Si2, Al3 – O4 – Si4 and Al4 – O4 – Si3, are located in the chains of the 5-MR where the hydrogen of the bridged hydroxyl group interacts strongly with an oxygen atom on the opposite side of the ring. These sites however are inaccessible for adsorption of the carbonyl compounds. Alberti *et al.* (Alberti, 1997) deduced that among the ten inequivalent O sites, O4 and O8 cannot be active BA sites because they are inaccessible to molecules as small as ammonia. In addition, in both FF and DFT calculations of our study population at sites O4 and O8 results among the least stable sites, possibly because of the limited space available within the 5-MR. Hence, in the following discussion, we have only considered the other eight framework oxygen sites as possible BA sites and will not consider O4 and O8 further.

The energy difference calculated between the most and least stable BA site is ~ 17 kJ mol^{-1} using FF and ~ 39 kJ mol^{-1} using periodic DFT. The different proton locations are therefore close in energy to each other and so it likely that in real conditions all of them would be populated to some extent. Thereby proving to be a challenge in identifying distinct sites. As mentioned, the most stable BA site obtained using GULP is Al1 – O7 – Si1 where the proton is located in the MC. The order of stability of the BA sites obtained with the FF method is similar to an earlier study by Simplerer *et al.* (Simperler, *et al*., 2004) using an Al/Si ratio of 94. The BA site, Al1 – O3 – Si2, also located in the MC with an energy value of 1.98 kJ mol^{-1} was found to be the most stable site in their study and in good agreement with previous LDA and GGA calculations with an Al/Si ratio of 47 (Demuth, *et al*., 2000). In our quantum chemical results, however, this particular BA site is established to be one of the least stable protonated site with an energy value of 32.35

kJ mol^{-1}. In general the force field calculations yield results only in relative stability of protonation sites in QM and FF qualitative agreement with the QM, in that energy differences are small but the calculations differ substantially. The FF geometry optimizations however did provide a good starting geometry for periodic DFT, improving the optimization time compared to that of crystallographic geometry. The only major difference we observe are at BA sites Al1 – O7 – Si1 and Al2 – O2 – Si4 (**Figure 3-2**). With periodic DFT method, the proton is located at the surface of the MC in the M7 ring forming an intra-zeolite H-bond with an oxygen atom on the opposite side of the ring at an intermolecular distance of 1.90 and 1.73 Å.

The main geometrical parameters of the optimised structures are listed in **Table 3-2**. The substitution of Al and protonation induces an increase of the Al – O and Si – O bond lengths, with a correlated decrease in the intertetrahedral angles from a pure siliceous model. Compared to the GULP results, the O-H bond lengths are shorter by ~ 0.03 Å resulting in a stronger bond of the hydroxyl group, the Al-O bond is reduced by ~0.04 Å while the Si-O bond is increased by ~ 0.03 Å and in addition there is a more pronounced decrease of the Al – O – Si angles by ~ 18°, when using periodic DFT method.

In the quantum chemical calculations, the most energetically favourable BA site is Al3 – O1 – Si1 with proton pointing towards a void space in the SC (**Figure 3-2**), which is in good agreement with earlier solid-state NMR studies (Huo, *et al*., 2012). At this site, the Si – O –Si angle in a purely

siliceous structure is 174.3 ° in comparison to the other sites with more acute angles (~132 – 147 °). This larger intertetrahedral angle allows for a higher capacity to accommodate distortions (in particular elongation of T-O bonds) arising from Si/Al substitution and protonation. Except for the Al3–O1–Si1 angle, which is reduced by about 55° compared to that of purely siliceous zeolite, all the other Al – O – Si angles undergo more modest changes of ~ 25°.

FTIR spectroscopy studies suggest that the most likely sites for BA protons are O2, O7 and O9 which is further supported by ab initio DFT calculations and a cross check of crystallochemical and spectroscopic data. (Alberti, *et al*., 1986, Bucko, *et al*., 2002, Marie, *et al*., 2004). The acidic hydroxyl O9 – H at T3 site is one of the least stable sites with an energy value of 34.29 kJ mol^{-1} and so this site is unlikely to be protonated with Al occupied at T3 site. We found that the probability of protonation occurring at O2 and O7 oxygen sites located in the main 12-MR channel is equivalent to protonation occurring at O5 and O6 oxygen sites located at the intersection of the MC and SP and in the small 8-MR channel since energy values are essentially the same (24.84 – 26.75 kJ mol^{-1}). This suggests that the classification of the BA sites according to their position in either the large or small cavity is not explicit. This is further supported when the Al dopant is located at T1 positions as the oxygen sites lie both in the MC (O3 and O7) and SC (O1 and O6) and have similar energy values 24.84 – 32.35 kJ mol^{-1}, which is contrast to an earlier theoretical study with isolated acid sites (Si/Al ratio = 23) that found O6 oxygen site is a better protonation site and hence T1 site is more stable in the SC. In addition, according to our results protonation at O1 site

is preferred at T3 over T1 and in agreement with previous studies suggesting that T3 site is much more likely to be occupied by Al atoms (Alberti, 1997, Bodart, *et al*., 1986, Debras, *et al*., 1983).

The acid sites are distributed evenly between the different crystallographic positions. While Al siting derives from synthesis, H can hop between the oxygens if the energy difference is small enough. For the adsorption of the small carbonyl molecules we focused on the most stable oxygen sites for each of the distinct four T site positions for Al based on the periodic DFT calculations (highlighted in bold in **Table 3-1**): Al3 – O1 – Si1 (0.00 kJ mol^{-1}) > Al2 – O3 – Si1 (12.35 kJ mol^{-1}) > Al1 – O7 –Si1 (24.84 kJ mol^{-1}) > Al4 – O2 – Si2 (32.52 kJ mol^{-1}). The structures and geometrical parameters of these most stable oxygen sites for each of the four inequivalent T site are displayed in **Figure 3-2**. In agreement with previous theoretical work, these sites represent the most favourable sites for the four different Al locations (Bucko and Hafner, 2015, Chibani, *et al*., 2016, Demuth, *et al*., 2000, Diaz, *et al*., 2013, Huo, *et al*., 2012).

BA sites	*Pure siliceous model*		*Single Al/Si substitution*							
	r(Si – O)	∠(Si – O – Si)	*r*(Al – O)		*r*(Si – O)		*r*(O – H)		∠(Al) – O – Si	
			FF	Periodic DFT	FF	Periodic DFT	FF	Periodic DFT	FF	Periodic DFT
Al1 – O7 – Si1	1.631	143.0	1.924	1.895	1.692	1.698	1.000	0.988	136.4	133.6
Al1 – O3 – Si2	1.627	146.9	1.917	1.903	1.685	1.704	1.002	0.973	138.3	129.9
Al1 – O1 – Si3	1.627	143.8	1.913	1.888	1.694	1.713	1.001	0.976	137.2	119.8
Al1 – O6 – Si1	1.628	144.7	1.919	1.904	1.692	1.709	1.002	0.972	140.3	132.1
Al2 – O3 – Si1	1.629	146.9	1.916	1.910	1.687	1.702	1.002	1.000	141.6	136.4
Al2 – O2 – Si4	1.627	141.6	1.909	1.891	1.693	1.712	1.001	0.972	137.4	132.8
Al2 – O5 – Si2	1.631	138.8	1.902	1.900	1.686	1.711	1.002	0.972	138.2	132.6
Al3 – O1 – Si1	1.617	174.3	1.916	1.887	1.689	1.716	1.001	0.972	134.9	121.9
Al3 – O9 – Si3	1.634	132.1	1.930	1.890	1.700	1.711	0.999	0.972	136.8	127.3
Al4 – O2 – Si2	1.626	141.4	1.916	1.887	1.686	1.703	1.001	0.972	136.2	132.3
Al4 – O10 – Si4	1.628	141.6	1.923	1.885	1.695	1.707	1.000	0.974	136.5	134.6

Table 3-2 Optimized structural parameters of the selected BA sites in MOR zeolite, interatomic distances (Å) and bond angles (°). BA sites highlighted in bold are the most stable sites for each distinct T position.

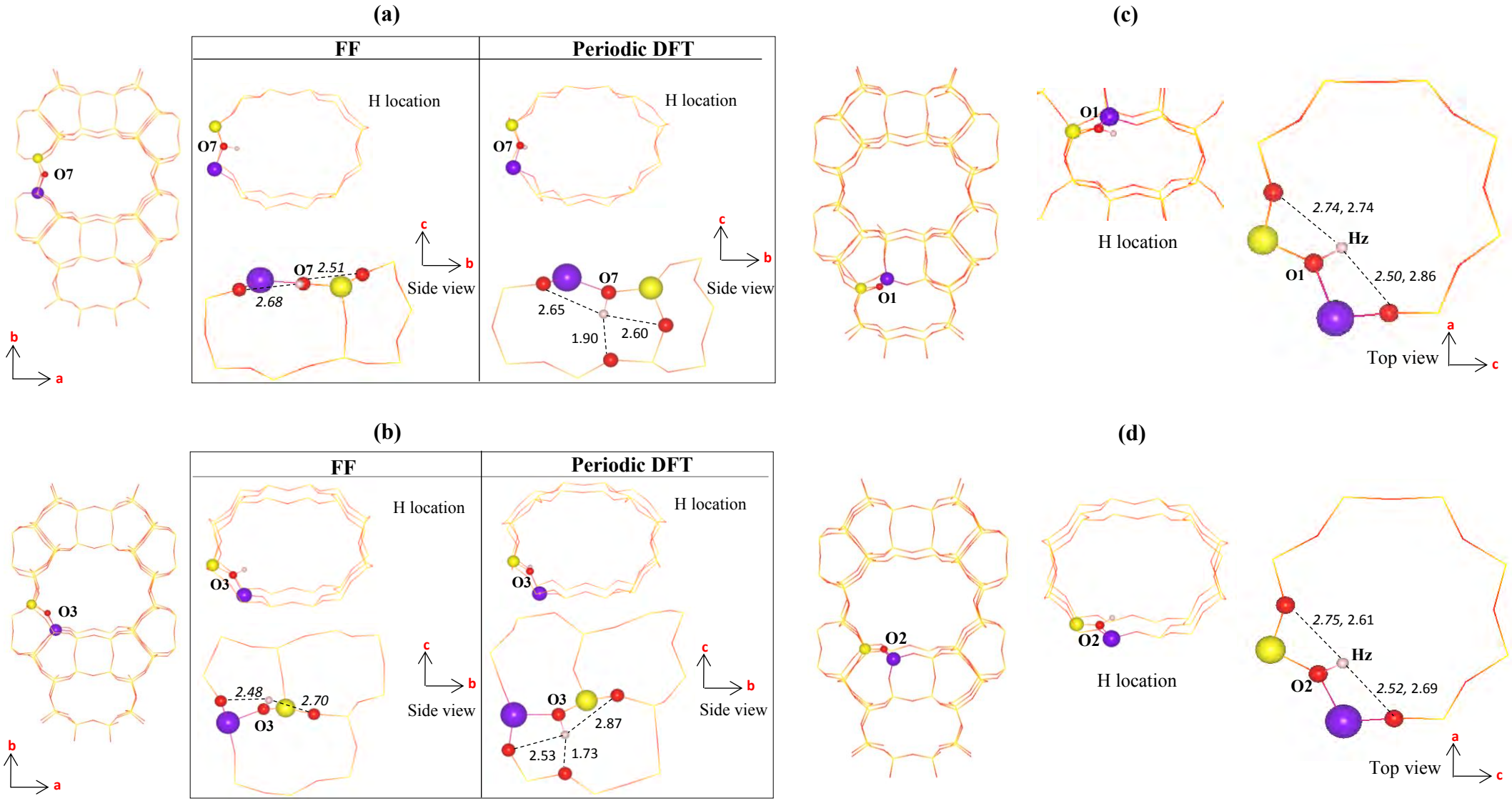

Figure 3-2 Location of proton in the most stable sites for each unique T site position in MOR zeolite using FF and periodic DFT method. **(a)** Al1 – O7 – Si1 **(b)** Al2 – O3 – Si1 **(c)** Al3 – O1 – Si1 **(d)** Al4 – O2 – Si2. The bond parameters in italics correspond to FF and in plain to periodic DFT method.

3.3.2 Proton location and stability of acid sites in FER zeolite

The high-silica model which we use in our calculations of FER has a Si/Al ratio of 35. The thermodynamically most stable structure is protonated on O2 oxygen site with Al substituted on T2 position. **Table 3-3** shows the relative stabilization energies calculated for all the possible BA sites that may exist in the vicinity of each of the five distinguishable Al positions in FER zeolite, with respect to the most stable BA site, Al2 – O2 – Si1b, for both FF and periodic DFT method levels of theory . The proton location in the zeolite structure which is depicted in **Figure 3-3**.

BA sites	**H location**		**ΔE_{rel} kJ mol^{-1}**	
	FF	*Periodic DFT*	*FF*	*Periodic DFT*
Al1a – O3 – Si1b	5-MR	5-MR*	33.86	29.15
Al1a – O1 – Si3	MC	M5*	26.22	30.16
Al1a – O4 – Si1a	I	I	18.55	13.81
Al1a – O2 – Si2	I	I	17.39	31.68
Al1b – O3 – Si1a	5-MR	5-MR*	26.84	11.39
Al1b – O1 – Si3	MC	M5*	23.16	26.39
Al1b – O4 – Si1b	I	I	18.55	13.74
Al1b – O2 – Si2	I	I	15.25	10.62
Al2 – O5 – Si2	I	I	41.66	33.75
Al2 – O2 – Si1b	I	I*	0.00	0.00
Al2– O6 – Si4	P6	P6	20.26	20.43
Al3 – O1 – Si1a	MC	M7*	13.20	5.14
Al3 – O7 – Si4	P8	P8	8.47	22.79
Al3 – O8 – Si3	P8	P8	17.05	18.03
Al3 – O1 – Si1b	MC	M7*	16.39	4.38
Al4– O6 – Si2	P6	P6	22.65	20.29
Al4 – O7 – Si3	P8	P8	28.52	24.76

Table 3-3 Relative energies of the isolated BA sites in FER zeolite with respect to the energetically most stable site, Al2 – O2 – Si1b, for both FF and periodic DFT method. Thermodynamically stable BA sites for each non-equivalent framework T position of Al obtained from periodic DFT is depicted in bold. The stars (*) denotes the BA sites involved in an intra-zeolite strong H-bond.

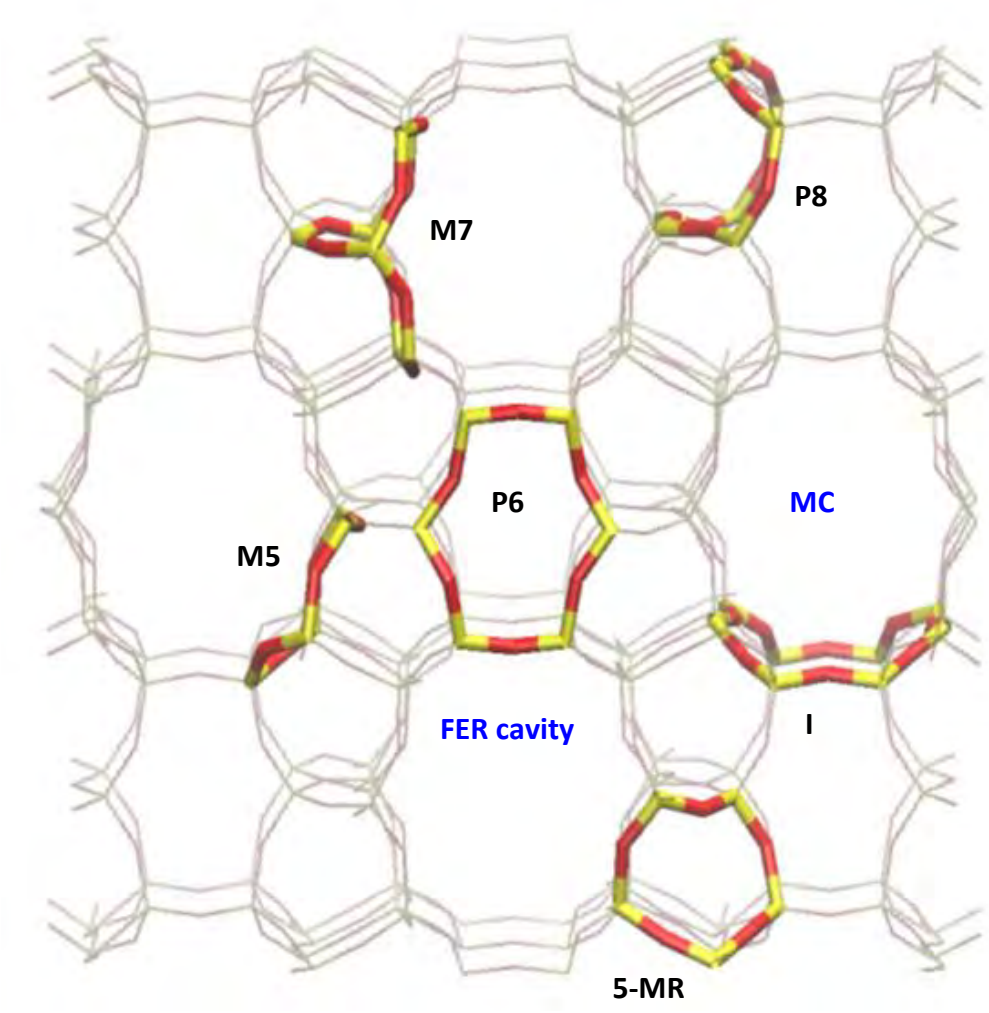

Figure 3-3 Location of proton of the isolated BA sites in FER zeolite: M7 and M5 rings in the MC, P6 and P8 rings in perpendicular channel of FER cavity, I is the 8-MR window intersection between the two channels, chains of 5-MR inaccessible for adsorbates.

The nomenclature introduced originally for Cu-MFI (Nachtigallova, *et al*., 1999), and recently adopted also for FER (Bludsky, *et al*., 2005, Garrone, *et al*., 2006), is used for the alkali ion sites in FER; the sites in the main channel, perpendicular channel, and at the channel intersection are denoted M, P, I, respectively. In contrast to MOR zeolite, the relative stabilization energies in FER calculated using FF calculations and periodic DFT method are in good agreement, with a maximum difference of ~ 15 kJ mol^{-1} at Al1a – O2 – Si2 site. The positioning of the proton at each BA site is also similar in both methods with the exception of O1-H between

T sites 1 and 3 which is located in the main channel but oriented in M5 or M7 rings due to the formation of an intra-zeolite H bond. The geometrical parameters are displayed in **Table 3-4**. On the whole, the substitution of Si by Al leads to a strong but localized deformation of the tetrahedral network. All Al-O bonds within the AlO4 tetrahedra are elongated relative to Si-O bonds, and the intertetrahedral angles are reduced. The bond lengths do not vary significantly between the different sites, with variation for each type of distance is within ~ 0.05Å in total. The spread of the angles observed is within ~ 20 °.

BA Sites	*Pure siliceous zeolite*		*Single Al/Si substitution*							
	r(Si – O)	∠(Si – O – Si)	*r*(Al – O)		*r*(Si – O)		*r*(O – H)		∠ (Al – O – Si)	
			FF	*Periodic DFT*	*FF*	*Periodic DFT*	*FF*	*Periodic DFT*	*FF*	*Periodic DFT*
Al1a – O3 – Si1b	1.592	169.8	1.918	1.895	1.700	1.713	1.003	0.983	148.3	127.4
Al1a – O1 – Si3	1.600	149.9	1.923	1.881	1.687	1.702	1.001	0.993	134.0	120.0*
Al1a – O4 – Si1a	1.604	145.4	1.880	1.885	1.691	1.711	1.003	0.976	138.7	123.6
Al1a – O2 – Si2	1.586	158.4	1.900	1.889	1.697	1.710	1.003	0.974	143.1	137.4
Al1b – O3 – Si1a	1.598	169.8	1.913	1.843	1.695	1.689	1.004	1.026	152.7	149.2
Al1b – O1 – Si3	1.604	142.1	1.917	1.890	1.691	1.705	0.999	0.994	132.6	121.2
Al1b – O4 – Si1b	1.601	144.6	1.880	1.885	1.691	1.711	1.003	0.976	138.7	123.6
Al1b – O2 – Si2	1.601	140.8	1.907	1.883	1.702	1.714	0.999	0.979	130.5	123.9
Al2 – O5 – Si2	1.590	166.6	1.919	1.898	1.667	1.694	1.006	0.978	146.8	128.4*
Al2 – O2 – Si1b	1.608	140.8	1.922	1.891	1.690	1.708	1.001	0.981	133.8	124.1
Al3 – O1 – Si1a	1.597	149.9	1.923	1.870	1.687	1.697	1.000	1.014	134.5	132.6
Al3 – O1 – Si1b	1.604	142.1	1.926	1.869	1.686	1.696	1.000	1.015	132.7	134.1
Al4 – O6 – Si2	1.608	151.3	1.917	1.893	1.691	1.701	1.004	0.979	139.4	125.9

Table 3-4 Optimized geometrical parameters of the selected BA sites in FER zeolite, interatomic distances (Å) and bond angles (°). BA sites highlighted in bold are the most stable sites for each distinct T position.

Previous quantum chemical studies with high-silica models of 35 and 71 (Grajciar, *et al.*, 2010, Nachtigall, *et al.*, 2009, Simperler, *et al.*, 2004) have reported that the lowest energy BA site calculated is indeed Al2 – O2 – Si1b, with proton pointing towards the 8-MR window channel intersection. This site forms an intra-zeolite H-bond even though the 8-MR is not as narrow in comparison to the other rings – 5 and 7 MR's. **Figure 3-4** shows the H-atom of the hydroxyl group is attracted to an oxygen atom opposite to the acid site, with a bond length of 2.04 Å. The least stable proton site is Al2 – O5 – Si2 with an energy of 33.75 kJ mol^{-1}, with proton pointing at the intersection channel, in agreement with earlier theoretical data (Feng, *et al.*, 2017, Grajciar, *et al.*, 2010, Nachtigall, *et al.*, 2009, Simperler, *et al.*, 2004). These studies suggest that if T2 site is populated by Al, the acidic proton is unlikely to be located at the O5 oxygen site. Although these studies display an ∠ (Al – O – Si) angle ranging from 149 – 159.9 °. In our study, the angle at this site is 128.4 °, reduced considerably before Al/Si substitution from 166.6 ° in a pure siliceous model. The distortions for the Al2 – O5 – Si2 angle indicate a large local strain on this bond, hence the increase in energy value obtained.

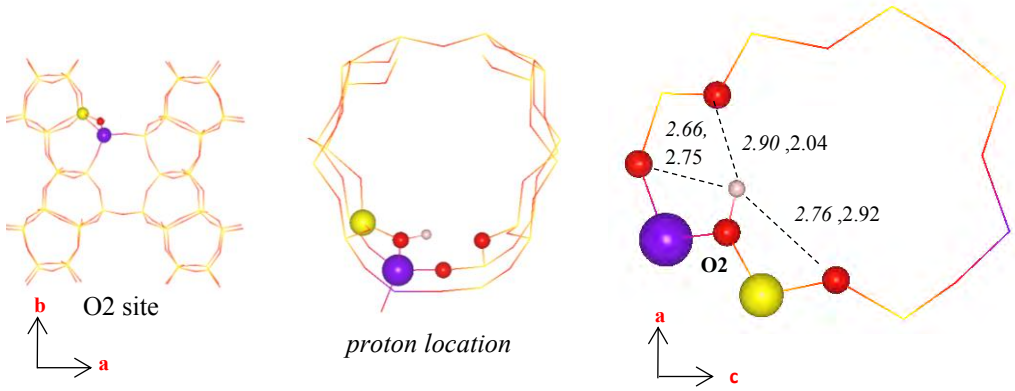

Figure 3-4 Location of proton at most stable BA site, Al2 – O2 – Si1b, using both FF (italics) and periodic DFT (plain) methods. Bond distances in Å.

The second most stable BA sites are located on O1 oxygen site with Al at T3 position, Al3 – O1 – Si1a and Al3 – O1 – Si1b with energy values of 5.14 and 4.38

kJ mol^{-1}. At this particular oxygen site the agreement between FF and periodic DFT methods becomes less satisfactory as an intra-zeolite H bond is formed only in the DFT calculations. The proton is located at the surface of the main 10-MR channel forming a very strong H-bond (1.57 Å) with non-AlO_4 oxygen atom on the opposite side in the M7 ring, shown in **Figure 3-5.** This explains energy stabilization achieved and it can be established that these two BA sites are essentially the same. Due to the formation of a very strong H-bond, the hydroxyl group is weakened with an elongated O-H bond distance of 1.014 and 1.015 Å compared to the remaining BA sites, 0.974 – 0.994 Å **(Table 3-4)**.

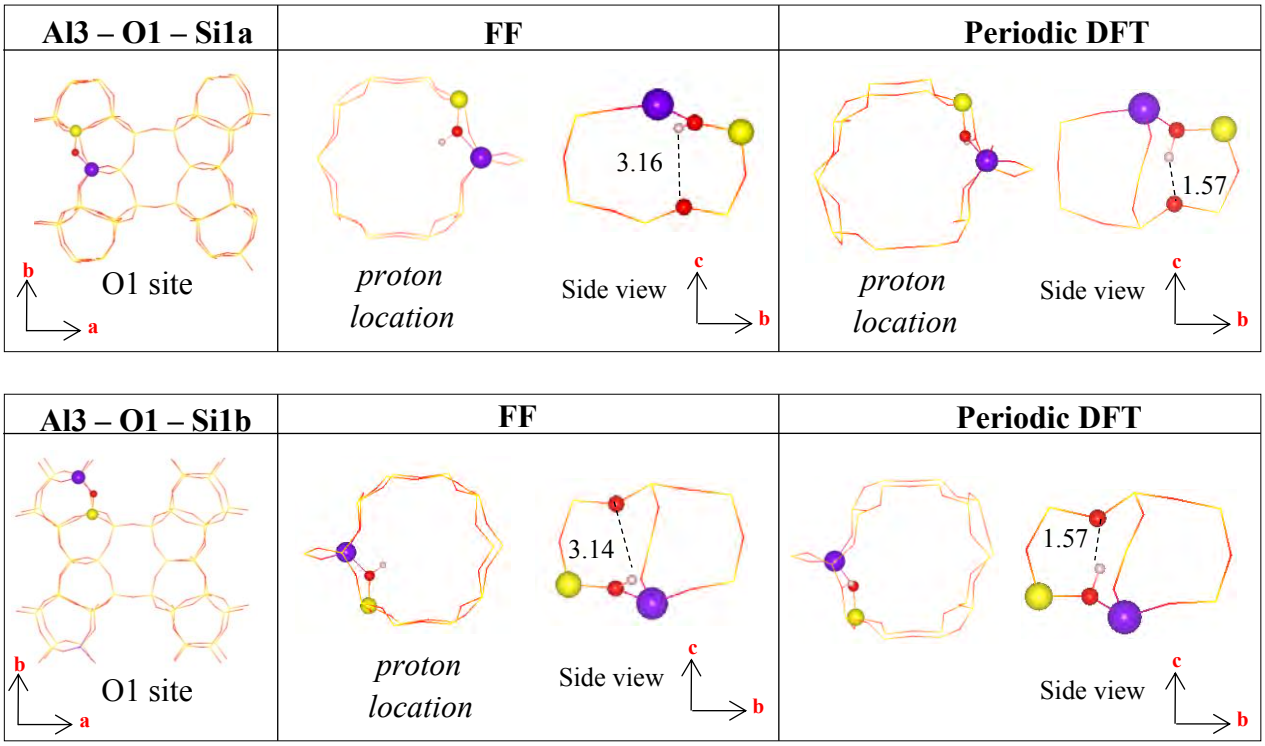

Figure 3-5 Optimized structures of BA sites Al3 – O1 – Si1a and Al3 – O1 – Si1b using FF and periodic DFT. Bond distances in Å.

We calculated all the possibilities of protonation at the oxygen sites (O1 – O4) when Al is located in T1a and T1b sites in order to deduce whether Dedecek *et al.* (Dedecek,

et al., 2011) observation of these two sites indeed differ in their local AlO_4^- geometry. The comparison between the two sites on all four oxygen sites in terms of their stabilization energies using both methods is shown in **Figure 3-6**. The energies obtained from GULP calculations are in good agreement between the two T1 sites for all four oxygen sites, with a maximum difference of ~ 7 kJ mol^{-1} at O3 site. Protonation at oxygen sites O1 and O4 have similar energies between the T1 sites when calculated with the quantum chemical method as well (Al1a – O1 – Si3: 30.16 kJ mol^{-1}, Al1b – O1 – Si3 = 26.39 kJ mol^{-1} and Al1a – O4 – Si1a = 13.81 kJ mol^{-1}, Al1b – O4 – Si1b = 13.74 kJ mol^{-1}). The optimized structures of these BA sites along with their geometrical parameters are displayed in **Figure 3-7** and **Figure 3-8.** At O1 oxygen site, the hydroxyl group forms H-bonds with oxygen atoms across the M5 ring for both T1 sites and the closest non-AlO_4 oxygen atom has the interatomic distance of 1.76 Å at T1a and 1.79 Å at T1b. At O4 oxygen site, the proton is pointing at the 8-MR window intersection, forming weaker H-bonds with the AlO_4 oxygen atoms for both T1 sites (2.39 – 2.79 Å). Additionally, the *r*(O-H) distance are calculated at 0.993 and 0.994 Å for T1a and T1b at O1 oxygen site and 0.976 Å for both T1 sites at O4 oxygen site. The <(Al – O – Si) at O1 oxygen site are 120 and 121 ° for T1a and T1b and at O4 oxygen site is 123.6 ° for both T1 sites. From this findings, we can confirm the BA sites involving O1 and O4 oxygen sites with Al atom located at T1a and T1b position are essentially the same within the numerical accuracy of the calculations. In addition to this, the protonation at O4 oxygen site when using periodic DFT causes a distortion of the 8-MR window when calculated using periodic DFT.

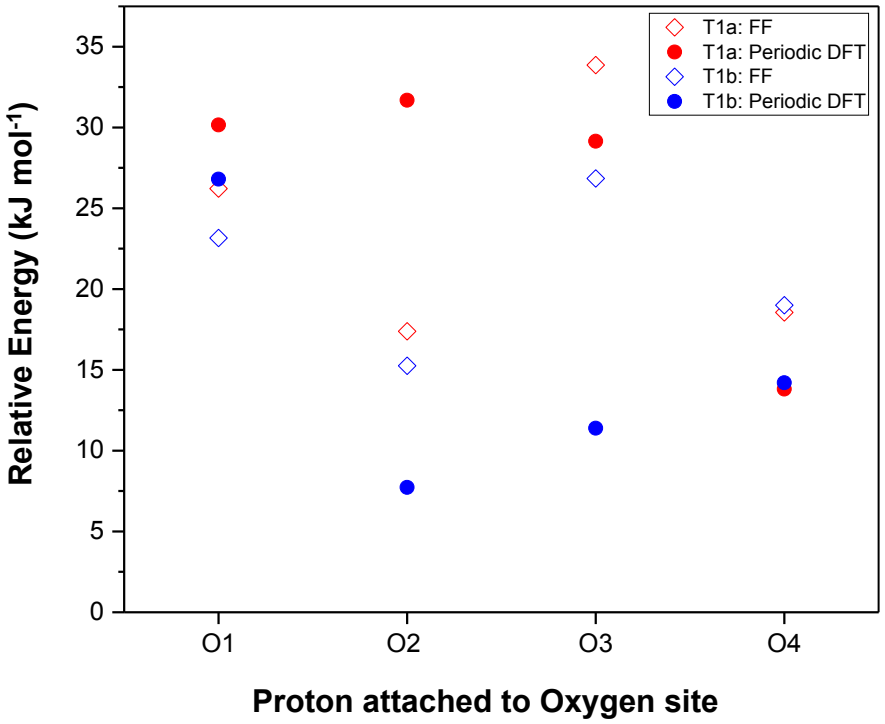

Figure 3-6 Relative stabilization energies (in correspondence to the most stable BA site: Al2 – O2-Si1b) of the protonation of the oxygen sites, O1-O4, adjacent to Al dopant at both T1a and T1b sites using both FF and periodic DFT methods.

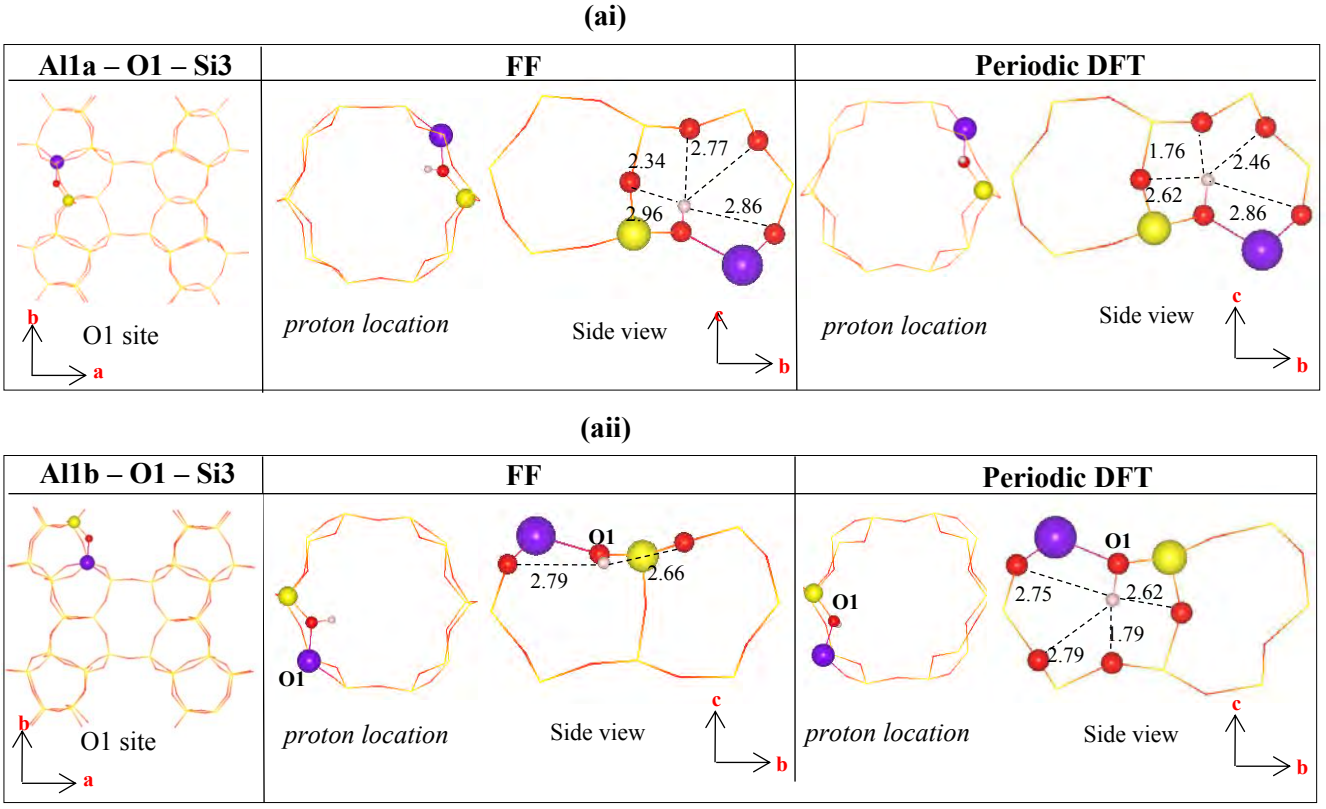

Figure 3-7 Optimized geometries of proton location at BA sites (ai) Al1a – O1 – Si3 and (aii) Al1b – O1 – Si3. Intermolecular distances in Å.

(ai)

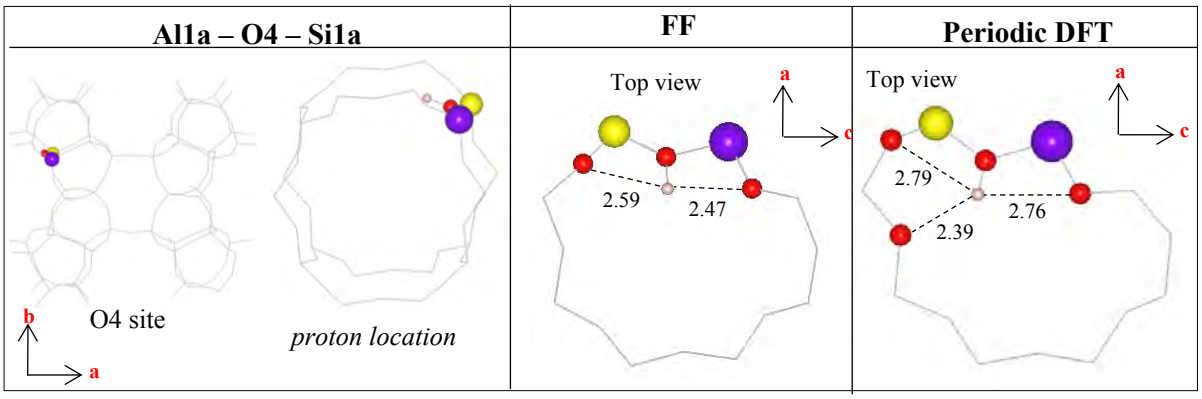

(aii)

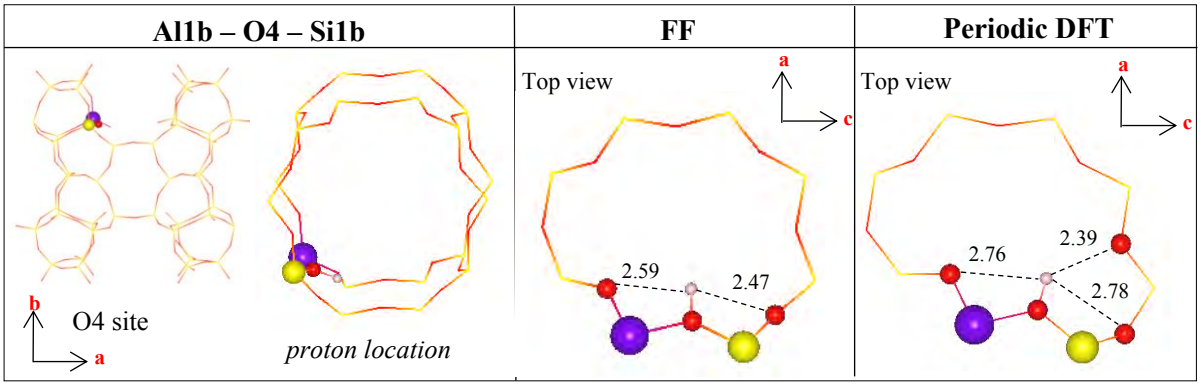

Figure 3-8 Optimized geometries of proton location at BA sites (ai) Al1a – O4 – Si1a and (aii) Al1b – – O4 – Si1a FER zeolite using using FF and periodic DFT calculations. Intermolecular distances in Å.

With regards to the protonation at O2 and O3 site in both T1 positions, the energies differ when calculated using the quantum chemical method. Protonation at O3 oxygen with Al at T1a has an energy value of 29.15 kJ mol^{-1}, while at T1b site the energy decreases to 11.39 kJ mol^{-1}. This may suggest that the T1a and T1b sites at this particular oxygen site. The proton is located in the 5-MR ring at both T1 sites and due to this narrow ring, both BA sites are involved in an intra-zeolite H bond although to different non-AlO_4^- oxygen atoms, shown in **Figure 3-9.** At T1a, the H-bond has a distance of 1.95 to the closest non-AlO_4^- oxygen atom, whereas at T1b a very strong H-bond is formed at a distance of 1.50 Å weakening the hydroxyl group, 1.026 Å. The *r*(O-H) at T1a is 0.983 Å. Since T1b is involved in a stronger intra-zeolite H-bond compared to T1a, this would suggest the energy

difference between the two. Thus further calculations need to be performed in order to verify Dedecek *et al.* (Dedecek, *et al.*, 2011) theory. Nonetheless, these two BA sites provide a steric hindrance and a narrow space for interaction with the small carbonyl compounds and therefore will not be considered for reaction purposes.

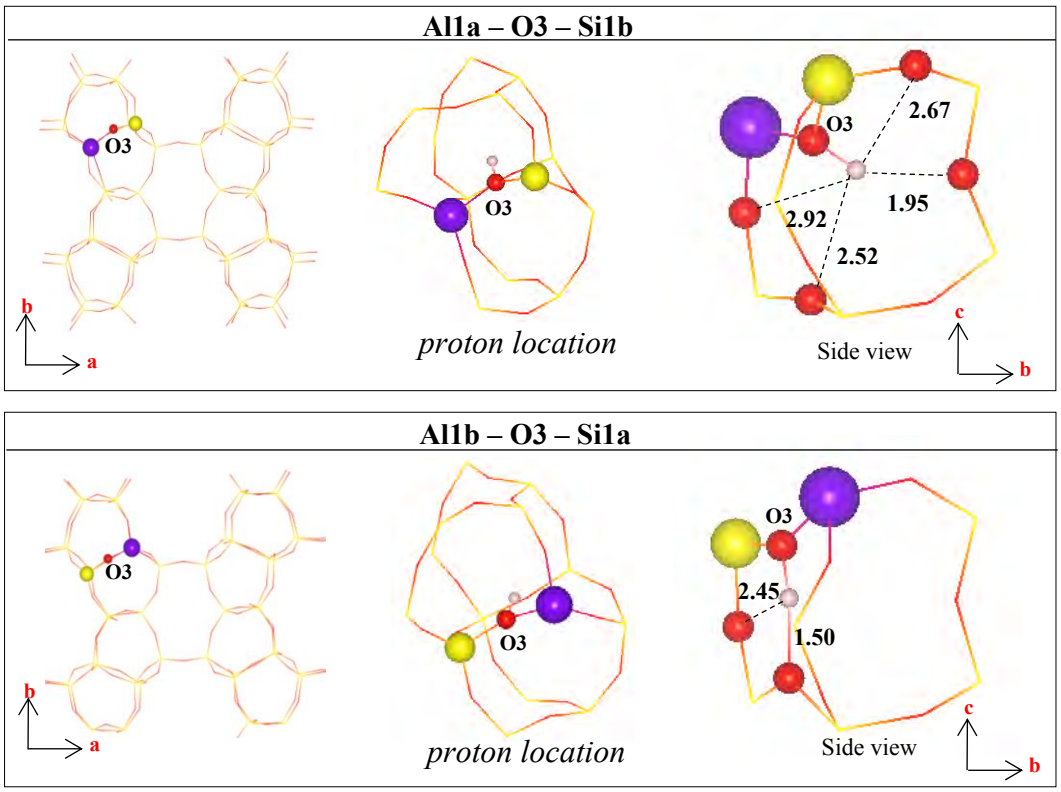

Figure 3-9 Optimized geometries of proton at O3 site with Al dopant at T1a and T1b position. Intermolecular distances in Å.

With regards to the proton located at O2 site at both T1 sites, the relative energies differ considerably when calculated by periodic DFT, 31.68 kJ mol^{-1} at T1a site and 7.73 kJ mol^{-1} at T1b site. Several calculations were performed to confirm the energy difference and obtained similar values. The proton is located at the 8-MR window intersection between the main 10-MR channel and the side channel. **Figure 3-10 (a)** shows local geometry being perturbed of the 8-MR window when proton is located at O2 oxygen site at both T positions. With Al dopant at

T1a, the calculated distance between $O2_A$ and $O2_B$ on the opposite side of the ring at 4.73 Å, and r(H – $O2_B$) distance is 4.21 Å. On the other hand, the $O2_C$ located between Si1b and Si2 (where Al atom is not located) forms a distance with $O2_D$ at 3.45 Å. With Al dopant at T1b, $O2_D$ – $O2_C$ intermolecular distance is 2.79 Å, with proton forming an intra-zeolite H-bond at 2.08 Å (H – $O2_C$). $O2_B$ located between Si1a and Si2 has a bond length of 5.12 Å with respect to $O2_A$ on the opposite side of the ring. From our results, the formation of the intra-zeolite H-bond with an oxygen atom on the opposite side the 8-MR at T1b causes a larger distortion compared to at T1a where this is does occur. Our results do however disagree with their study. in terms of the positioning of the T1a and T1b sites in the FER zeolite, shown in **Figure 3-10 (b).** By calculating the probability of the protonation at all four oxygens bound to Al at both T1a and T1b, we have established that these two sites are indeed different.

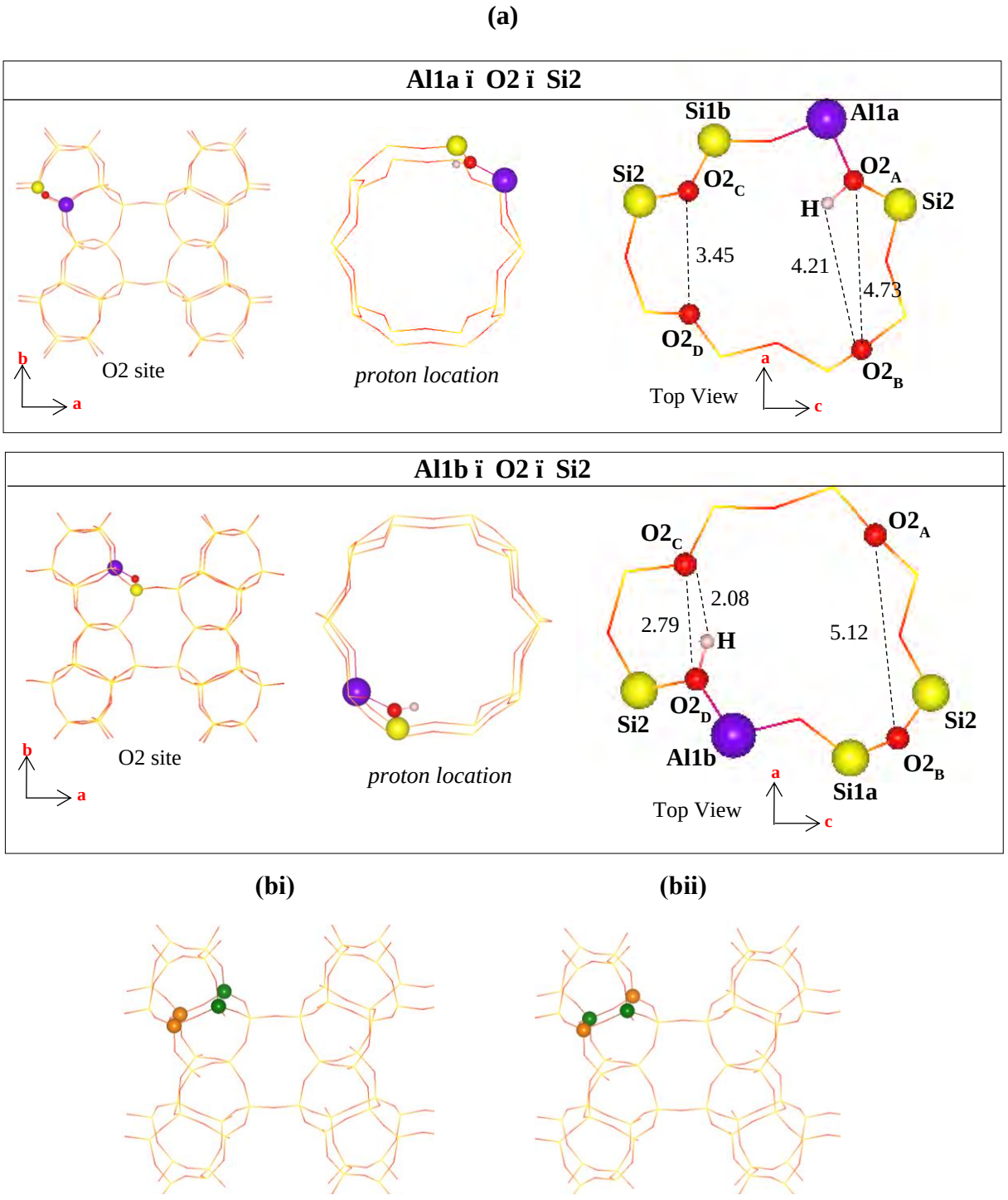

Fig ure 3-10 (a) Proton on O2 site with Al dopant at both T1a and T1b sites. $O2_{a\text{-}d}$ represents the O2 sites in the 8MR between the T(Si or Al) atoms in order to demonstrate the difference in the local geometry at T1a and T1b when occu pied by Al atom. (b) Location of T1a and T1b sites in FER zeolite established by (bi) Dedecek *et al*. and (bii) our calculated result. (T1a atoms are coloured in green and T1b atoms are coloured in orange.

With Al dopant at T4 position, the proton can only be located in the side FER cavity on either O6 or O7 oxygen site. Both these BA have similar relative energies with Al4 – O6 – Si2 being slightly more favourable at 20.29 kJ mol^{-1}. The proton is located in the plane of the P6 ring and since this ring is considered flat the proton is therefore forced to interact with the oxygens of the ring, shown in **Figure 3-11**.

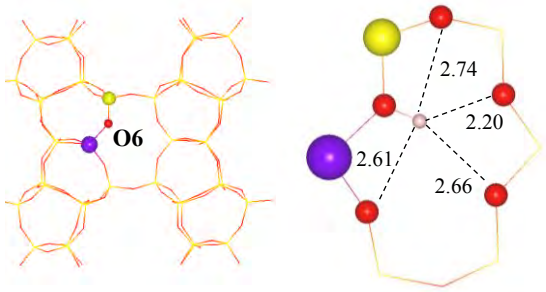

Figure 3-11 Optimized geometrical parameters of Al4 – O6 – Si2 BA site. Intermolecular distances of intra-zeolite H-bond in Å.

Based on the relative stabilization energies there is no preferential attachment of protons to the different oxygen sites. We have therefore established 13 possible distinct BA sites in FER for protonation to occur. Majority of the BA sites are located in the FER cavity ~ 40 % (O6-H, O7-H, O8-H) and at the 8MR window intersection ~ 40 % (O2-H, O4-H, O5-H), with only ~ 15 % (O1-H) situated at the surface of the 10MR main channel and ~ 5% (O3-H) positioned in the 5-MR (reactions with carbonyl compounds not possible). This correlates well with previous computational studies with similar proton location (Grajciar, *et al*., 2010, Liu, *et al*., 2014). Since there is no significant variance in terms of energy, we focused on the most stable BA sites in the vicinity of Al atom at each of the distinct T site positions for the adsorption of the carbonyl compounds (highlighted in bold in **Table 3-3**) – Al2 – O2 – Si1b (0.00 kJ mol^{-1}) > Al3 – O1 – Si1b (4.38 kJ mol^{-1}) > Al1b – O2 – Si2 (10.62 kJ mol^{-1}) > Al4 – O6 – Si2 (20.29 kJ mol^{-1}), which is similar to the ones obtained by Grajciar *et al.*

(Grajciar, *et al*., 2010). Since we have calculated all the possible BA sites for Al in T1a and T1b sites and found only a difference at the O2 oxygen site, for comparison reasons we thought it would be appropriate to focus on the least stable BA site with Al at T1a site: Al1a – O1 – Si3 (30.16 kJ mol^{-1}) as it is also located on the surface on the main channel in the M5 ring.

3.3.3 Acetaldehyde and Acetone Molecule

The adsorption of acetaldehyde and acetone molecules has been studied at the lowest energy hydrogen position for each distinct T site in both zeolites MOR and FER. Prior to the adsorption of these small carbonyl compounds in the zeolites, we have calculated their structural parameters in the gas phase and compared it with the available experimental data to ensure our calculations are accurate and reliable. The calculated bond distances and angles are summarized in **Table 3-5** showing excellent agreement with earlier experimental and theoretical studies.

	Acetaldehyde				**Acetone**		
	Our work	Exp A.	Exp B.	B3LYP	Our work	Exp C.	M06-2X[a]
O – C	1.211	1.22 ± 0.02	1.216	1.20	1.216	1.22 ± 0.03	1.21
C – C	1.515	1.50 ± 0.02	1.501	1.51	1.526	1.50 ± 0.02	1.52
< CCO	124.5	121 ± 2	123.9	125	122.3	119.6 ± 3	

Table 3-5 Equilibrium bond distances (Å) and angles (°) calculated in this work and compared to earlier experimental and theoretical studies. Exp A. (Stevenson, *et al*., 1939) Exp B. (Gherman, *et al*., 2001) B3LYP (Rodriguez-Santiago, *et al*., 2001) Exp C. (Allen, *et al*., 1952), M06-2X (Boekfa, *et al*., 2010). [a]M06 – 2X = Minnesota 06 (Global hybrid functional with 54% HF exchange)

3.3.4 Interaction of acetaldehyde and acetone with acid sites in MOR and FER

The interaction of the basic molecules at the lowest energy proton location at each distinct T position in both zeolites involved a neutral acetaldehyde (acetone) stabilized on the surface by the formation of a H-bond between the carbonyl oxygen and the bridging hydroxyl of the Brønsted site (**Figure 3-12**). The molecules are not protonated and the proton remains bound to the framework O_A. This is in good agreement with previous experimental data using NMR and FTIR spectroscopy (Biaglow, *et al*., 1995, Florian and Kubelkova, 1994) in a variety of zeolites as well as earlier theoretical studies (Boekfa, *et al.*, 2010, Sepa, et al., 1996, Solans-Monfort, *et al*., 2002). Our results are in contrast to previous studies (Diaz, *et al*., 1992, Lee, *et al*., 2002) stating that the primary interaction is a proton-transferred structure, that is, forming an ion-pair between the adsorbed molecule and Brønsted site in various zeolites. All our attempts to optimize such a structure have spontaneously evolved back to a protonated framework. The equilibrium adsorption geometries are listed in **Table 3-6**. The H-bond between the carbonyl oxygen and proton (H_Z – O_C) presents a short distance of 1.281 – 1.545 Å, corresponding to a strong H-bond. Consequently, this localized H – bond causes the distance of the hydroxyl group (O_A – H_Z) at the BA site to be increased considerably from (0.972 – 1.020 Å) to (1.022 – 1.134 Å). The effect of adsorption on the carbonyl bond and carbon-carbon bond were not found to be site specific, lengthened by a maximum of 0.029 Å and weakened by ~ 0.05 Å compared to the isolated gas phase molecule.

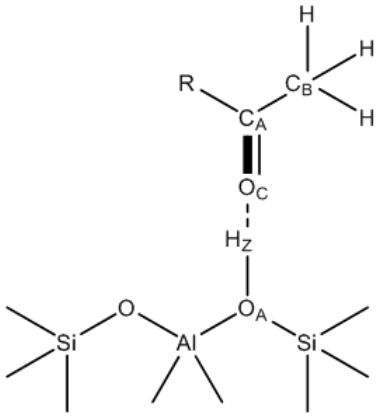

Figure 3-12 Adsorption of carbonyl compounds forming a localised H-bonded complex at the Brønsted site of zeolite. R = H or CH_3 representing acetaldehyde or acetone.

	FER							MOR				
	T1a	T1b	T1b	T2	T2	T3	T4	T1	T2	T3	T4	T4
Location	MC	MC	FER cavity	MC	FER cavity	MC	FER cavity	MC	MC	SC	MC	SP
Acetaldehyde												
$O_A - H_Z$	1.055	1.037	1.047	1.042	1.049	1.041	1.079	1.049	1.048	1.025	1.059	1.063
$H_Z - O_Z$	3.024	2.394	2.765	2.615	2.737	2.818	2.850	3.318	2.807	2.741	2.664	2.704
$H_Z - O_C$	1.429	1.505	1.476	1.489	1.478	1.487	1.395	1.470	1.466	1.541	1.435	1.428
$O_C - C_A$	1.232	1.229	1.233	1.230	1.232	1.229	1.236	1.234	1.231	1.230	1.234	1.234
$C_A - C_B$	1.498	1.495	1.495	1.497	1.496	1.496	1.490	1.491	1.492	1.476	1.492	1.487
$O_A - H_Z - O_C$	167.9	152.7	165.8	159.3	165.6	172.7	172.2	164.6	169.4	150.2	172.4	179.6
Acetone												
$O_A - H_Z$	1.068	1.043	1.039	1.095	1.053	1.089	1.022	1.098	1.124	1.066	1.077	1.108
$H_Z - O_Z$	3.483	2.360	3.168	2.732	3.232	2.794	2.963	3.294	2.766	2.773	2.837	2.720
$H_Z - O_C$	1.403	1.507	1.506	1.341	1.474	1.360	1.525	1.345	1.281	1.408	1.379	1.328
$O_C - C_A$	1.240	1.235	1.245	1.240	1.235	1.240	1.234	1.241	1.240	1.233	1.239	1.242
$C_A - C_B$	1.497	1.501	1.515	1.490	1.502	1.509	1.500	1.503	1.502	1.449	1.503	1.499
$C_A - C_C$	1.498	1.511	1.519	1.505	1.510	1.500	1.510	1.504	1.503	1.504	1.507	1.492
$O_A - H_Z - O_C$	173.5	151.1	165.0	170.1	165.6	174.5	152.1	176.5	169.3	172.2	177.3	170.1

Table 3-6 Main geometrical parameters of optimized structures of acetaldehyde and acetone forming localized H-bonded complex at lowest energy H positions of T sites (except T1a) in both zeolites FER and MOR. The atoms are labelled as shown in **Figure 3-12.** Bond distances (Å) and bond angles (°).

3.3.5 Adsorption energies of acetaldehyde and acetone in zeolites

The total adsorption energies, divided into the electronic and dispersion contributions, are summarized in **Table 3-7**. Our results indicate the dispersion contributions play a significant role in stabilizing the adsorption energies, reflecting the importance of capturing vdW interactions correctly. For both molecules in the zeolites we observe the order of stability altered when dispersive interactions are taken into consideration.

		Acetaldehyde			**Acetone**		
	Location	E_{Ads}	E_{elec}	E_{disp}	E_{Ads}	E_{elec}	E_{disp}
MOR							
T1	MC	-148.0	-69.7	-78.3	-167.2	-71.1	-96.1
T2	MC	-139.9	-62.3	-77.6	-151.7	-15.4	-136.3
T3	SC	-111.8	34.11	-145.9	-148.9	45.9	-194.7
T4	MC	-158.7	-67.3	-91.4	-168.4	-45.3	-123.1
T4	SP	-180.5	-40.1	-140.5	-192.1	12.5	-204.2
FER							
T1a	MC	-156.2	-48.4	-108.4	-179.9	-69.3	-110.6
T1b	MC	-125.3	-17.9	-107.4	-165.7	-23.2	-142.5
T1b	FER cavity	-138.0	-40.1	-97.9	-150.3	-17.2	-133.1
T2	MC	-135.5	-44.6	-90.9	-160.1	-57.1	-103.0
T2	FER cavity	-134.8	-37.6	-97.2	-165.1	-17.2	-147.9
T3	MC	-148.8	-31.6	-117.2	-195.0	-21.9	-173.1
T4	FER cavity	-161.0	-75.8	-85.3	-179.6	-56.4	-123.2

Table 3-7 Calculated total adsorption energy (E_{ads}) of the H-bonded complexes of acetaldehyde and acetone at the lowest energy H-position at each unique T position in MOR and FER zeolites. (kJ mol^{-1})

3.3.5.1 MOR

In MOR, we established a strong correlation between the adsorption energies of the basic molecules and the relative stability of the protonation site, displayed in **Figure 3-13.** The adsorption energy increases with decreasing stability of the isolated acid site. The optimized H-bonded complexes are shown in **Figure. 3-14**.

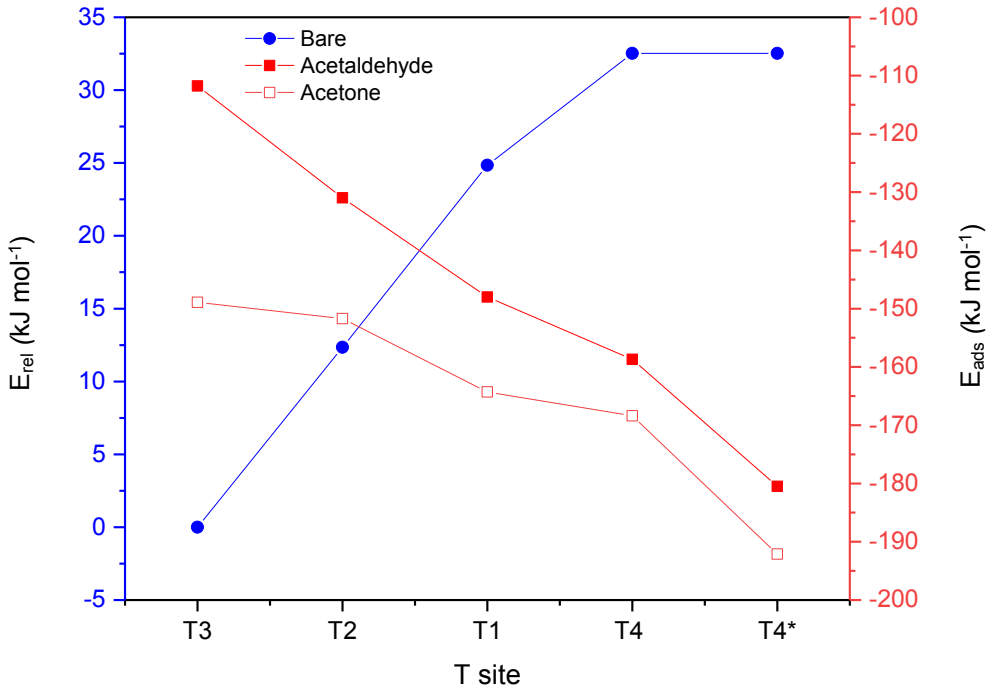

Figure 3-13 Comparison between the relative energy in MOR of isolated Brønsted site at lowest proton location (blue closed circles, left y-axis) and adsorption energies (right y-axis) of acetaldehyde (red closed squares) and acetone (red open squares) at these selected sites. (* the molecule is located in the SP)

Acetaldehyde. The adsorption energies decreases in the order T4 > T1 > T2 > T3. With Al atom located in T4 framework position, the proton is initially located at the intersection between the MC and SP (I_{MC-SP}); thus we calculated the stability of the adsorbate approaching the acid site from either the MC or SP (**Figure 3-14**). We found that acetaldehyde prefers to be located in the SP with an energy value of -180.5 kJ mol^{-1} compared to that with the adsorbate residing in the MC, -158.7 kJ mol^{-1}. The adsorption energies are similar with Al located at T1 and T2 position where the molecule is also orientated parallel to the MC, -148.0 and -139.9 kJ mol^{-1}. It has been previously established that adsorbates can be effectively stabilized if the size of the adsorbed species is comparable to the pore size of the zeolite (Chu, *et al*., 2013). The size of the acetaldehyde molecule is better suited in the SP (3.4 × 4.8 Å) than in the main

12-MR channel (6.5 × 7.0 Å). This explains why the confinement effect is stronger in the SP with E_{disp} value being nearly two times higher in the SP (-140.5 kJ mol^{-1}) than in the MC (-78.3 to -91.4 kJ mol^{-1}). Similarly, the confinement effect is also strong in the small 8-MR channel (2.6 × 5.7 Å) with Al located at T3 site with an E_{disp} value of -145.9 kJ mol^{-1}, however proves to stabilize acetaldehyde the least in comparison to the other T sites with an adsorption energy of -111.8 kJ mol^{-1}. Here, we find the largest contribution to acetaldehyde adsorption is not due to the empirical dispersion correction but to the electronic interaction that favours adsorption at the MC. Without dispersive interactions taken into account, we observe a positive binding energy in the SC, 34.1 kJ mol^{-1}, compared to the MC, -46.6 to -69.7 kJ mol^{-1}, and this is because of the smaller volume causes two – body repulsion to take place, other confinement also causes non-optimal adsorption geometries, as the possible orientations are limited by the size and shape of the void.

Acetone. The stability of the H-bonded complex on different BA sites decreases in the order T4 > T1 > T2 > T3, which is the same as for acetaldehyde. The energetically most favoured configuration of acetone is residing in the SP at T4 position with an adsorption energy of -192.1 kJ mol^{-1}. Here, we find the electronic interaction to be repulsive, 12.5 kJ mol^{-1}, in comparison to when acetaldehyde is adsorbed (E_{elec} = -40.1 kJ mol^{-1}), and so the contribution to such stabilization essentially comes from the dispersion contribution which is expected due to the shorter distances between the acetone molecule and the SP zeolite framework, with an E_{disp} value of -204.2 kJ mol^{-1}. This clearly shows how much

dispersion contributions affects the ranking order of the adsorption energies. In addition, the adsorption energies are higher for acetone compared to acetaldehyde at each T site by ~ 10 – 40 kJ mol^{-1}, as increasing the molecular size mm from acetaldehyde to acetone the confinement effect becomes more pronounced enhancing the stability in these channels with the E_{disp} values being increased at each T site by ~ 30 - 65 kJ mol^{-1}. From our results, it is clear that a higher electronic interaction results in a lower dispersion contribution and vice versa; this is apparent at the T sites located in the MC as a lack of dispersion favours adsorption at T1 with an electronic energy of -71.1 kJ mol^{-1} while being unfavourable at T2, -15.4 kJ mol^{-1}, and on the other hand, the larger dispersion stabilization is found at T2, -136.3 kJ mol^{-1}, compared to T1 (-96.1 kJ mol^{-1}). Thus it is the most favourable compromise between pore structure and local geometry of the acid site that determines the overall stability.

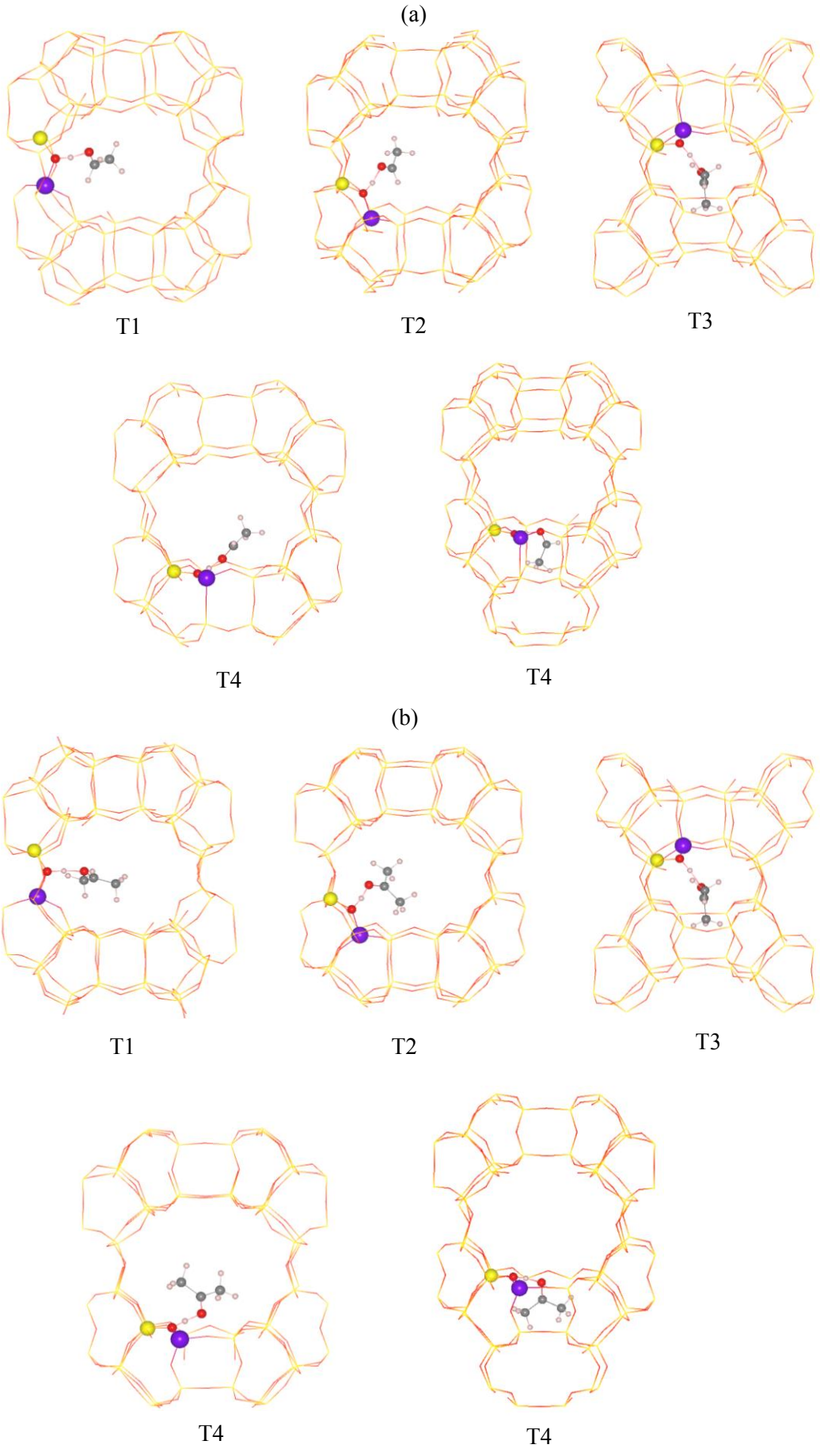

Figure 3-14 Optimized structures of single guest (a) acetaldehyde and (b) acetone molecule at T1, T2, T3, T4 positions in MOR zeolite. Colour legend of the balls: grey (C), white (H), red (O), yellow (Si), purple (Al).

3.3.5.2 FER

The study of acetaldehyde and acetone adsorption has been repeated for the FER framework. Compared to MOR zeolite, we observed a less clearant correlation between the adsorption energies of the carbonyl compounds and the relative energy of the proton locations at each distinct T position in FER zeolite, plotted in **Figure 3-15**. The optimized structures of the studied T sites interacting with a single guest acetaldehyde or acetone molecule are presented in **Figure 3-16**.

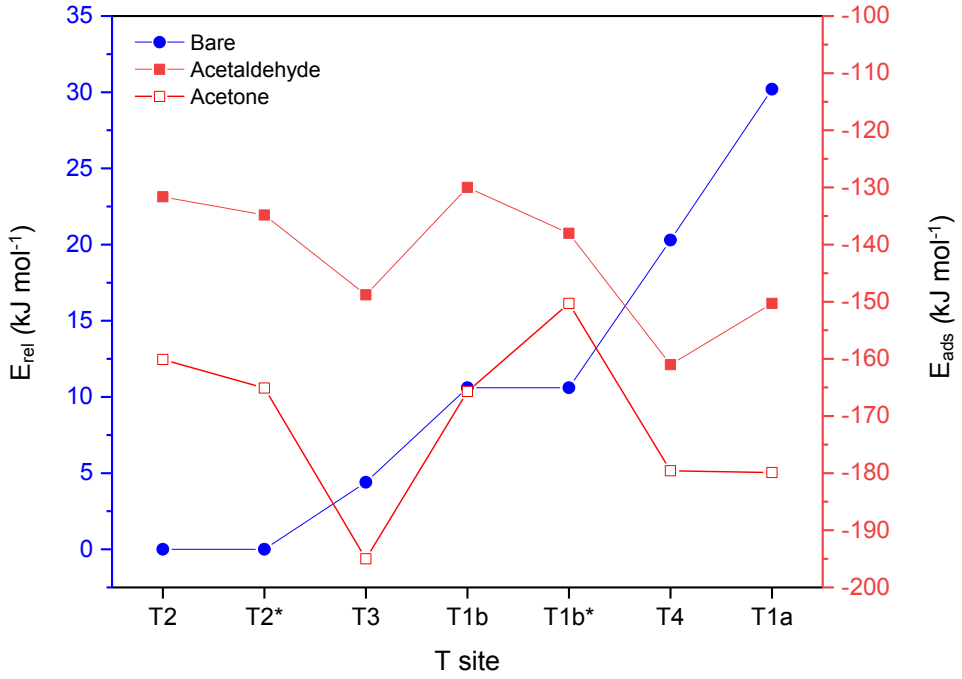

Figure 3-15. Comparison between the relative energy of isolated Brønsted site at lowest proton location (blue closed circles, left y-axis) and adsorption energies (right y-axis) of acetaldehyde (red closed squares) and acetone (red open squares) at these selected sites. (* the molecule is located in the FER cavity)

Acetaldehyde. A weaker correlation is established between the stability of the isolated acid sites and the adsorption energy, in particular with Al in T1b and T3 not following the pattern. The local geometry of the Brønsted site of T1b is equivalent to that of T2 (H_Z is located on the same oxygen site, O2). At these two sites proton is located at the 8-MR window intersection and thus can interact with

the guest molecules approaching from either the FER cavity or the MC **Figure 3-16**). We found the energies to be similar for these two sites in both locations, -125.3 to -138.0 kJ mol^{-1}; the adsorption is least favoured compared to the remaining T sites. From here, we can be more certain that the adsorption energies are dependent upon the local geometry of the acid site, more importantly the destabilization of H_Z of the BA site, as the environment of T1b and T2 are largely similar. This is also true for T3 and T1a where H_Z proton is located on O1 site, hence obtaining similar E_{ads} = (-148.8, -156.8) kJ mol^{-1}. Moreover, the dispersion contributions in the MC are slightly greater or similar to that in the FER cavity, which is not the case for MOR zeolite.

The adsorption of acetaldehyde is most favoured in the FER cavity when Al atom is located at T4 with an energy value of -161.0 kJ mol^{-1}, being higher than the adsorbate residing in the small 8-MR pore in MOR zeolite with Al atom located at T3 site, -111.8 kJ mol^{-1}. The acetaldehyde molecule is a better fit in the SC in MOR zeolite as dispersion forces are very strong (-145.9 kJ mol^{-1}) compared to the FER cavity (-85.3 kJ mol^{-1}). Although the electronic energy is repulsive at T3 site in MOR zeolite, 34.1 kJ mol^{-1}, the interaction is much greater in the FER cavity at T4 site, -75.8 kJ mol^{-1}, favouring the adsorption due to the amount of free volume available for optimal short-range interactions. Hence the electronic interaction favours the FER cavity while dispersion interaction favours the SC in the MOR zeolite.

For the T sites located in the MC in both zeolites, we found the total

adsorption energies to be similar (~120 to 160 kJ mol^{-1}). The electronic interaction is greater in the 12-MR pore (6.5 × 7.0 Å) of MOR zeolite allowing acetaldehyde to interact with the acid site more effectively without any steric effects, but at the same time the dispersion forces are stronger in the 10-MR pore (4.2 × 5.4 Å) of FER zeolite due to the shorter distances between the molecule and the zeolite framework.

Acetone. In general the adsorption energies are more exothermic with acetone adsorbed than acetaldehyde by ~ 10 – 50 kJ mol^{-1} as expected due to the increase in size leading to higher dispersion contributions, as already discussed for MOR. In terms of the isolated Brønsted sites, a weaker correlation is established between BA stability and adsorption energy with the T sites, T1b and T3 not following the pattern; similar to our findings with acetaldehyde. The acid group for Al in T1b has the same local geometry as T2 and so their adsorption energies are similar with acetone adsorbed in the FER cavity (-150.3 and -165.1 kJ mol^{-1}) and in the MC (-165.7 and -160.1 kJ mol^{-1}). Our results are in contrast to a previous study by Boekfa *et al*. (Boekfa, *et al*., 2010) establishing that at T2 site where the acid proton points towards to the small 8-MR window (which is the same in our study) is too small to accommodate the acetone molecule and so the adsorbed acetone must be located in the MC. The computed adsorption energy in their study was found to be -112.6 kJ mol^{-1} using ONIOM. The respective value in our study is -160.1 kJ mol^{-1} and the differences in values may be due

to the use of different computational methods.

At T3 position, the H-bonded complex is most stable with an adsorption energy of -195 kJ mol^{-1}, which is essentially due to the dispersion contribution being greatest at this site, -173 kJ mol^{-1}. The other T sites located in the MC have a lower dispersion stabilization as the orientation of the acetone molecule is different due to the local geometry of the acid site. While T1b and T2 have a similar local geometry in terms of isolated acid sites, their dispersion contributions differ with acetone residing in the MC. We found the electronic interaction being twice as high at T2 position (-57 kJ mol^{-1}) than at T1b (-23.2 kJ mol^{-1}), which would explain the larger dispersion stabilization obtained at T1b (-142.5 kJ mol^{-1}) than T2 (-103 kJ mol^{-1}); hence obtaining similar total adsorption energies. This occurrence is not apparent with acetone located in the FER cavity at these two sites as both electronic (-17.2 kJ mol^{-1}) and dispersion contributions (-133.1 and -147.9 kJ mol^{-1}) are similar. In addition, the dispersion contribution at T4 position is -123 kJ mol^{-1}, despite the electronic interaction being more than two times higher (-56.4 kJ mol^{-1}) than T1b and T2 position. From this we assume that in larger cavities the dispersion contributions are more likely to be affected not just by the destabilization of the H_Z but also the possible interaction and orientation of the adsorbate with respect to the acid site and in smaller cavities the dispersion contribution is more likely to be affected by the pore structure itself as the possible orientations of the adsorbate with respect to the acid site are limited. Dispersion effects are more obvious with acetone, it as being a larger base than acetaldehyde.

From our results, the adsorption energies are similar when dispersion is taken into account and so identifying an individual T position in stabilizing the basic molecules is difficult. Although Al located at T3 position is energetically stable as an isolated acid site and yet adsorption of both acetaldehyde and acetone is favoured at this particular site (**Figure 3-15**). In an earlier study by Solans-Monfort e*t al*. (Solans-Monfort, *et al*., 2002) the computed adsorption energies of acetaldehyde in H-ZSM-5 was found to be approximately -40 to -60 kJ mol^{-1}. The reason for these underestimated adsorption energies is due to the lack of dispersion interactions taken into account; in our study the electronic energies have similar values, roughly ~ 20 to 80 kJ mol^{-1}.

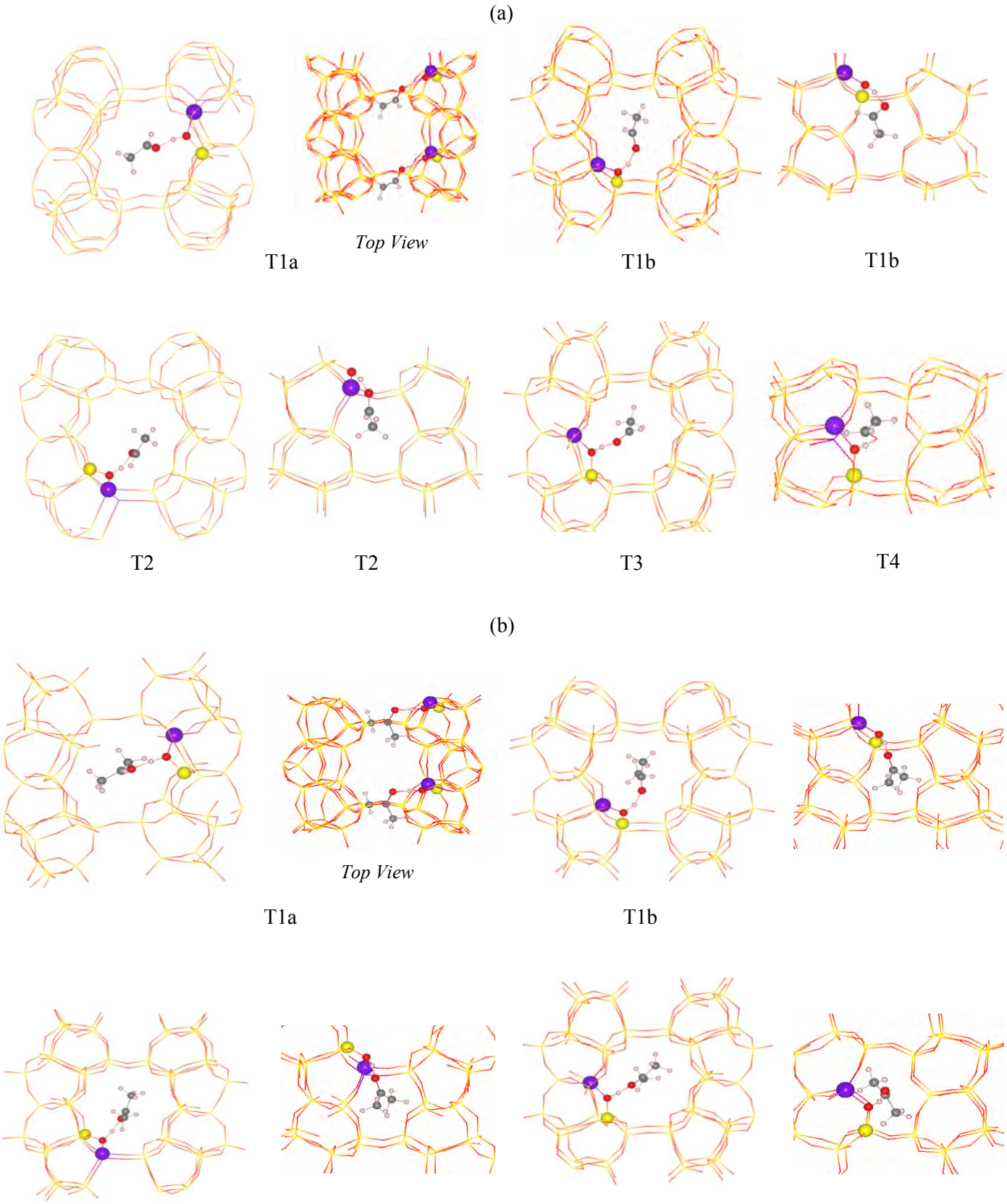

Figure 3-16 Optimized structures of single guest (a) acetaldehyde and (b) acetone molecule at T1a, T1b, T2, T3, T4 positions in FER zeolite. Colour legend of the balls: grey (C), white (H), red (O), yellow (Si), purple (Al).

3.3.6 Acid strength and structural parameters

Geometrical parameters affect acid strength, as shown by the sensitivity of the acid strength on geometrical parameters (Katada, *et al*., 2009, Simperler, *et al*., 2004). We studied the acid strength of the Brønsted site encountered by these sorbate molecules by plotting $r(O_A - H_Z)$ bond length against $r(H_Z - O_C)$ hydrogen bond distance (**Figure 3-17 (a and b)**) as interaction with the sorbate molecules is expected to induce the elongation of the hydroxyl bond and so a proton of strong acidity will be more easily donated into the H-bonding causing a stronger interaction.

Acetaldehyde. We found a perfect linear correlation in MOR zeolite, R^2 = 1. The ranking of the order of decreasing H-bond strength is T4 (SP) > T4 > T1 > T2 > T3. In FER zeolite, we found a good correlation, R^2 = 0.87. In general the T sites in the main 12-MR pore in MOR have a slightly higher acidity than the T sites in main 10-MR pore in FER in the presence of acetaldehyde. Overall as shown in **Figure 3-17 (a)**, T4 in FER cavity is the most acidic while T3 in smaller pores of MOR is the least acidic in the presence of acetaldehyde.

Acetone. Being a stronger base, the essential difference between acetaldehyde and acetone with the Brønsted site is the large elongation of the acidic hydroxyl bond by ~ 0.04 – 0.08 Å due to the shorter H-bond interaction of acetone by ~ 0.06 – 0.2 Å. The linear correlation in MOR zeolite is R^2 = 0.98 and the order of decreasing H-bond strength is T2 > T4 (SP) > T1 > T4 > T3. We also found a strong correlation in FER zeolite, R^2 = 0.96, where in general the T sites located in the MC have a higher acidity than the T sites located in FER cavity; especially with T4 being the least acidic opposed to when acetaldehyde is adsorbed. The larger pore of the MC in FER allows the acetone to access

the acid site without any major steric hindrance, whereas for the FER cavity the acidity experienced by the molecule is mediated by geometric constraints of the pore size. The T sites located in the MC for both zeolites have similar acid strengths, while T sites in the SC and SP in MOR zeolite have a stronger acidity than the T sites located in the FER cavity; highlighting the importance of shape selectivity with the more constrained space in the FER cavity restricting the acetone molecule access to the acid site. Overall as shown in **Figure 3-17 (b)**, the strongest acidity found in the presence of acetone molecule is at T2 site located in the MC in MOR zeolite while the weakest at T4 site located in FER cavity.

From this, we can conclude that both these distances characterise the H-bond strength, the longer the $r(O_A - H_Z)$ bond length, and the shorter the hydrogen bond length, $r(H_Z - O_C)$. Next we observed the relationship between the $r(H_Z - O_A)$ bond length versus the adsorption energies, shown in **Figure 3-17 (c and d)** as the $r(H_Z - O_A)$ bond length serves as a measure for the hydrogen bond interaction strength. The calculations of the adsorption energies clearly demonstrate the competing influences which govern the strength of adsorption: the hydrogen bond interaction and the more complex framework-admolecule interactions, which can either facilitate or hinder the access to the BA site. With regards to acetaldehyde, we found an excellent correlation between the $r(O_A - H_Z)$ and electronic energies ($R^2 = 0.90$) as well as adsorption energies ($R^2 = 0.98$) at the T sites in MOR, without taking T4 (SP) into account. This indicates that the dispersion-uncorrected adsorption energies still produce the same acidity trend as the total adsorption energies, because the influence of dispersion is minor. Hence, the adsorption of

acetaldehyde in MOR is dominated by the hydrogen-bond interactions. This becomes less obvious in FER, as the correlation between $r(O_A - H_Z)$ and E_{elec} is 0.89 although with dispersion taken into account changes the the acid trend slightly predicted by E_{ads} (0.71). This is due to the stronger confinement effect present in the smaller 10-MR channels in FER, especially at when Al is located at T3 where the dispersion interaction is even stronger (-117.2 kJ mol^{-1}). With regards to acetone adsorbed, we found no correlation between the $r(O_A - H_Z)$ and E_{ads} with and without dispersion contributions considered. In detail, adsorbed acetone is most activated at T2 position in MOR zeolite with the strongest H-bond interaction (1.281 Å) and an elongated hydroxyl bond of acid site (1.124 Å), yet has the lowest adsorption energy (-151.7 kJ mol^{-1}). On the other hand, adsorbed acetone is least activated at T4 position in FER cavity with the weakest H-bond interaction (1.525 Å) causing the hydroxyl bond only to increase slightly (1.022 Å) yet has the strong adsorption with an energy value of -179.6 kJ mol^{-1}. In comparison to acetaldehyde, the intrinsic acid strength is not a dominating factor when acetone is adsorbed, as it is more likely to experience short-range repulsive interactions and also stronger confinement effect enhancing the stability inside the pores.

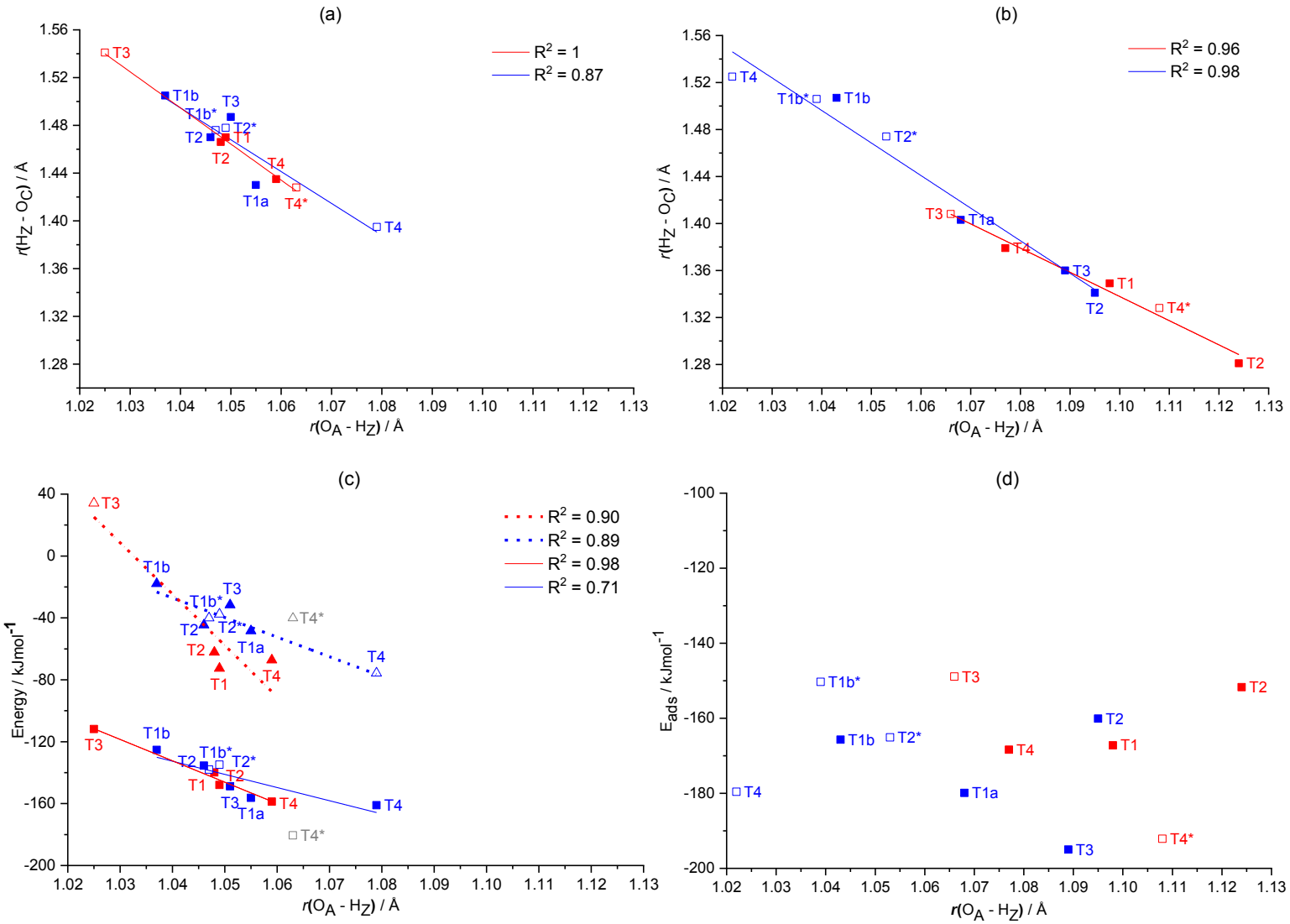

Figure 3-17 Plot of r(H$_Z$-O$_C$) distance against r(O$_A$ – H$_Z$) distance (a) acetaldehyde and (b) acetone, and against total E_{ads} energies of the molecules (c) acetaldehyde (Triangle squares correspond to E_{elec} energies) and (d) acetone. T sites in MOR (red squares, exception of T4* in grey square as considered an outlier data point for the linear correlation) and FER (blue squares) zeolites. Note: open squares correspond to molecule located in the smaller cavities (FER cavity, SC (T3) and SP (T4) in MOR zeolite).

3.4 Conclusion

We studied all the possible protonation sites for the non-equivalent T positions in MOR and FER zeolite using FF and periodic DFT methods. The FF method is less sophisticated although did provide a good starting geometry in terms of the proton location. We found the acid sites to be are evenly distributed between the different crystallographic positions in both zeolites. In FER zeolite, Al atom located at T1a and T1b position do differentiate in terms of their local geometry, proven by protonation on O2 site.

The adsorption of acetaldehyde and acetone were calculated at the lowest energy H location at each distinct T position for both zeolites. The adsorption energies are dependent upon the stability of the isolated acid sites in MOR. In FER, this correlation is less clearant: T1a and T3 as well as T1b and T2 have similar adsorption energies as their local geometry of the BA site are similar. The dispersion contributions play a significant role in stabilizing the adsorption energies. We found the electronic energies augmented with long-range dispersion effects lead to non-specific adsorption in the larger and small cavities for both zeolites. The electronic energies highlight the stability of the acid site while the dispersion energies highlight shape/size selectivity of the framework. The orientations of the molecules are mainly dependent on the diameters of the channels and on the curvature of the internal surface around the acid site. The molecule will orientate in such a way as to minimize the repulsive interaction with the framework. Although Al atom located at T3 position with proton located on O1 site proves to stabilize acetaldehyde and acetone effectively as it is energetically stable as an isolated acid site as well.

The H-bond geometry was used a predictor of the intrinsic acid strength: a proton of strong acidity will be more easily donated into the hydrogen bonding causing a very strong interaction. The intrinsic acid strength is determined by the adsorption energies of acetaldehyde in MOR, while in FER zeolite it is weakly correlated. The intrinsic acid strength is not a dominating factor in the zeolite-adsorbate interaction to when acetone is adsorbed as an increase in the size of the base leads to constraints of the particular pore topology and confinement effect which influence the geometry by which the molecule is able to interact with the acid site.

Chapter 4

H-transfer and enolisation mechanisms

4.1 Introduction

The reactivity of the stoichiometric, H-bonded complexes of acetaldehyde and acetone to nucleophillic attack is clearly demonstrated in the bimolecular, aldol condensation. In acid solution, the enol form of acetaldehyde and acetone provide the mechanism for the formation of condensation products and the loss of water. Despite the much higher stability of the keto form, it is the enol form which plays an essential role in many reactions as it leads to the formation of new C-C bonds. Hence the enolization mechanism of and the corresponding reaction barrier significantly affect the kinetics of these reactions.

Previous theoretical calculations reported that in the gas phase, acetaldehyde and acetone tautomerization required a high activation energy of ~ 268 to 292 kJ mol^{-1}. (Cucinotta, *et al*., 2006, Lee, *et al*., 1997, Solans-Monfort, *et al*., 2002, Wu and Lien, 1996, Zakharov, *et al*., 2008). The keto-enol tautomerization of acetaldehyde and acetone in zeolites has been studied previously with activation barriers drastically reducing to ~ 69 to 104 kJ mol^{-1}.

While the tautomeric process is simple in gas phase, several mechanisms have been proposed for tautomerism of acetone and acetaldehyde in water including two stepwise mechanisms, starting either from carbon deprotonation or from oxygen protonation, and a concerted mechanism involving two

simultaneous proton transfers. Cucinotta *et al*. (Cucinotta, *et al*., 2006) applied ab-intio metadynamics to understand the tautomerisation mechanism of acetone in the presence of water molecules and determined that C-β deprotonation is the kinetic bottleneck, being in good agreement with previous experimental observation.

In Chapter 3, with the adsorption of acetaldehyde and acetone we observed a physisorbed state involving the formation of a neutral H-bonded complex between the bridging hydroxyl of the Brønsted site and the carbonyl oxygen of the basic molecule at each of the T positions in MOR and FER zeolites; in good agreement with previous experimental studies, although the formation of the ion-pair structure cannot be entirely ruled out. The key step in the acid catalysis is then the activation of the complex by proton transfer. A notable point is that all the previous theoretical analyses of the enolisation mechanism have focused on determining the transition states for the alcohol and C-C double bond to be formed through the concerted mechanism, displayed in **Figure 4-1 (a)**. This approach neglects is the possibility of other intermediates. Kassab *et al*. (Kassab, *et al*., 1999) established that proton transfer from a zeolite may induce the formation of a silyl-ether addition compound, shown in **Figure 4-1 (b)**, using relatively small cluster models. This analogue of the enol form of the H-bonded adsorption complex, has not been experimentally identified and rarely explored theoretically (Sepa, *et al*., 1996); even though the enol form has been postulated as the reactive species in the aldol condensation reactions.

The fundamental question on how zeolite complexes promote nucelophillic attacks on the admolecule is therefore still unresolved. Here, we have revisited the initial proton transfer mechanism and formation of enol intermediates.

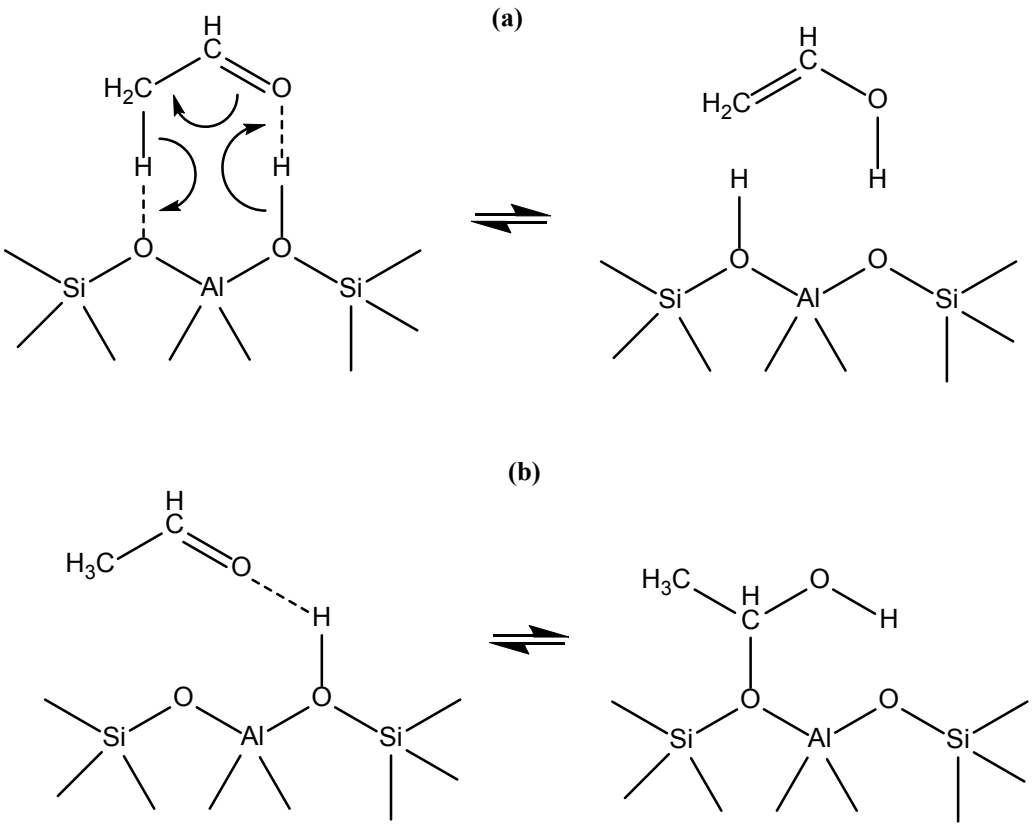

Figure 4-1 (a) Concerted Mechanism for keto-enol tautomerization (8-ring process) (b) Formation of a silyl-ether addition compound

We map the potential energy surfaces corresponding to proton transfer mechanisms and compare energetics obtained for Al dopants located in all symmetry distinct sites of both MOR and FER. We aim in this way to understand the effect of the framework topology on the mechanism pathway. Boekfa *et al.* and Solans-Monfort *et al.* used relatively large (34T and 63T) zeolite clusters yet only a few zeolite atoms were allowed to relax. We performed our calculations using periodic DFT. To our knowledge the keto-enol tautomerization of these guest molecules in zeolites has not yet been studied by periodic modelling. The substantial heterogeneity of acid sites additionally complicates establishing structure-performance relations solely from experimental data. In our computational study we aim to understand correlations between zeolite acidity and catalytic reactivity and the influence of confinement and steric effects generated by the framework structure on the intermediates and transition states.

4.2 Computational Details

We used the CRYSTAL code (Dovesi, *et al*., 2005) and the B3LYP hybrid-exchange functional (Becke, 1993, Lee, *et al*., 1988, Stephens, *et al*., 1994, Vosko, *et al*., 1980) was adopted for all calculations. The GTO basis set used for the geometry optimizations, consists equivalent split-valence triple-zeta basis sets plus polarization - 6-311G** [or 6-311G (d,p)] were applied to all atoms. These basis sets are provided from the online library of the CRYSTAL code. (Dovesi, *et al*., 2005) The long-range dispersion interactions were described by the semi-empirical method of Grimme. (Grimme, 2006)

For optimizations, a two-step procedure is adopted. Calculations are first initiated with a geometrical configuration corresponding to H-bonded complexes of acetaldehyde, where the unit cell parameters were left unconstrained. These structures were discussed in Chapter 3. In this chapter, the unit cell parameters were kept constant, and a series of constrained geometry optimizations were performed, in which a degree of freedom corresponding to the reaction coordinate is constrained at discrete steps between its value in reagents and products, allowing all other internal coordinates to relax. This procedure yields plots of calculating the internal energy of the system along the reaction coordinate of each elementary step. The reaction coordinate for the proton transfer reaction has been assumed to be one of the OH bond distances involved, either the one between the zeolitic O and the H (O_A - H_Z) i.e. the acid bond that is dissociating, or the carbonyl O and the proton (O_C - H_Z) i.e. the bond that forms in the reaction. The reaction coordinate was displaced in discrete steps of 0.1 Å to explore the section of the PES that connects the reactants to the products. At the various energy minima a full optimization was performed in order to

obtain more accurate values of the geometrical parameters. The activation energies and transition state geometries are identified as the local energy maximum along the reaction profile. TS's have been refined via second derivative methods and eigenvector-following modes.

4.3 Results and Discussion

4.3.1 Intramolecular Proton Transfer

Before examining the reaction mechanism inside the zeolite pores, we studied the intramolecular mechanism of keto-enol tautomerism of acetaldehyde in gas-phase. The uncatalyzed tautomerization of acetaldehyde has been studied previously and was found to occur via a concerted mechanism. The reaction profile is shown as in **Figure 4-2**, where the reaction coordinate is the bond length between one of the hydrogen atoms of the methyl group, H_A, and the oxygen of carbonyl group, O_C. The intrinsic activation barrier calculated for this endothermic process is 306.0 kJ mol^{-1}, slightly higher than previous theoretical studies, 284 – 295 kJ mol^{-1} (Rodriguez-Santiago, *et al*., 2001, Suenobu, *et al*., 1999). The keto-enol reaction energy computed is 47.5 kJ mol^{-1}, comparing well with previous experimental studies, 41.4 kJ mol^{-1} (Lammertsma and Prasad, 1994) as well as from previous B3LYP and MP2 calculations, 39 and 46 kJ mol^{-1} (Rodriguez-Santiago, *et al*., 2001).

The potential energy profile and the geometries of acetaldehyde, transition state and the enol product are shown in **Figure 4-2 and 4-3.** At the

four-coordinated transition state, we observed a simple proton transfer from the methyl to the keto group with a planar arrangement of the oxygen lone pair and the atoms involved in the reaction. The carboxyl group is $C_A - O_C$ is weakened from 1.21 to 1.25 Å, and at the same time the two new bonds, $H_A - O_C$ (2.58 to 1.20 Å) and $C_A - C_B$ (1.52 to 1.48 Å) double bond, were forming gradually. The high energy barrier is due to the orientation of the CH_2 group, which disfavours the formation of the $C_A - C_B$ π bond.

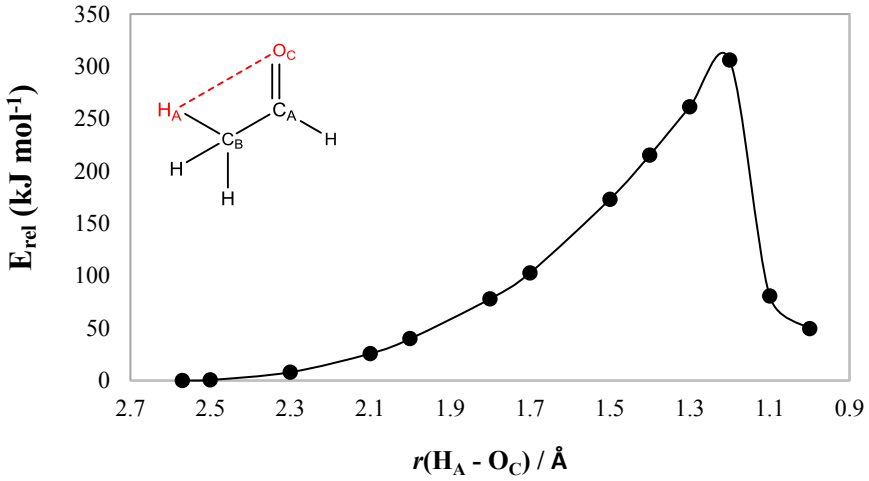

Figure 4-2 Energy variation profile of the tautomerization of acetaldehyde in an uncatalyzed gas phase environment as a function of the reaction coordinate, H_A - O_C.

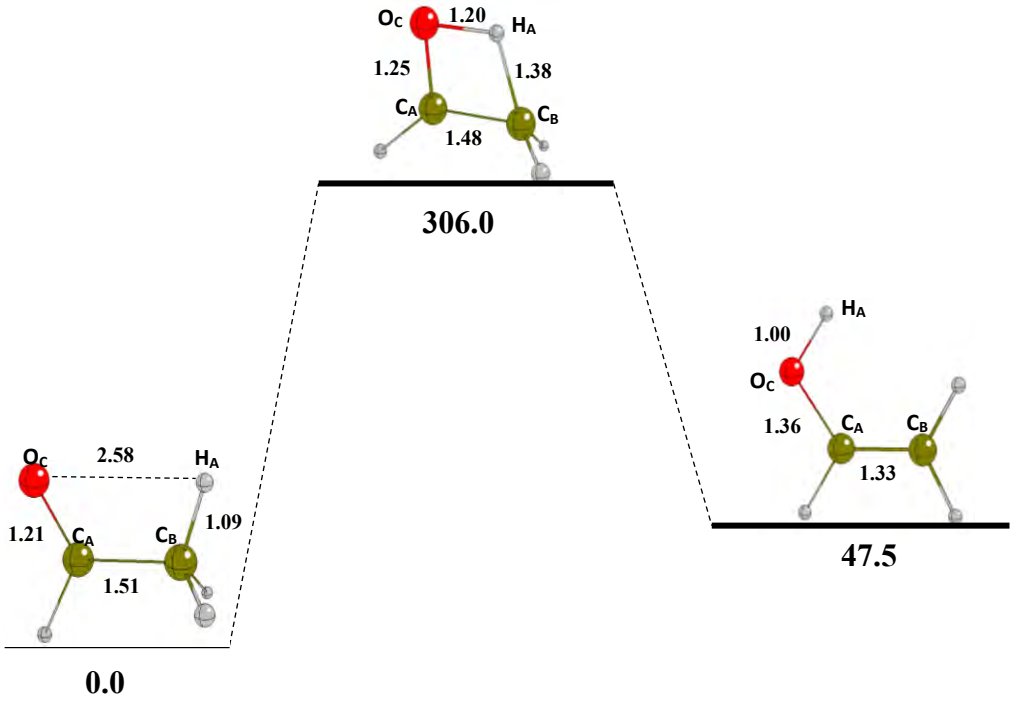

Figure 4-3 Potential energy diagram of the keto-enol tautomerization of acetaldehyde in gas phase. Relative energies are given in kJ mol^{-1}. Bond distances are given is Å.

4.3.2 Intermolecular Proton Transfers

Our study of the proton transfer mechanism starts from the geometry of the H – bonded complex formed between acetaldehyde and the BA site discussed in Chapter 3. Let us start with MOR. As already discussed in Chapter 3 by geometry optimizations alone we have been unable to identify the protonated admolecule as a stable species. All geometry optimizations converge back to the H-bonded complex with the proton on the framework O_A. We now aim to expand this study and characterize the energy profile of the H transfer through constrained optimization where the O_A – H_Z bond distances are displaced from equilibrium. The first acid site we studied is T3 – O9, in the small channels of MOR which is the situation discussed in Chapter 3, where the O_A – H_Z bond has the longest bond distance and the adsorption energy is highest (-161.2 kJ mol^{-1}). It is therefore expected to be the strongest acid site, for which the H-transfer is easiest to achieve. This was attributed to the instability of the bare T3 – O9 proton location. We contrast this site with the most stable location of the bare proton, T3 – O1, where the adsorption energy is of -111.8 kJ mol^{-1} only. The optimized structure of the acetaldehyde complex on T3 – O9 and T3 – O1 shown in **Figure 4-4** showing that a complete proton transfer does not occur between the bridging hydroxyl of the BA site and the carbonyl oxygen. At O9 site a stronger H-bond is formed with a H_Z – O_C bond length of 1.37 Å and the hydrogen bond angle (O_1 – H_Z – O_3) is close to a linear angle of 169.2 °; than at O1 site (1.54 Å and 150.2 °).

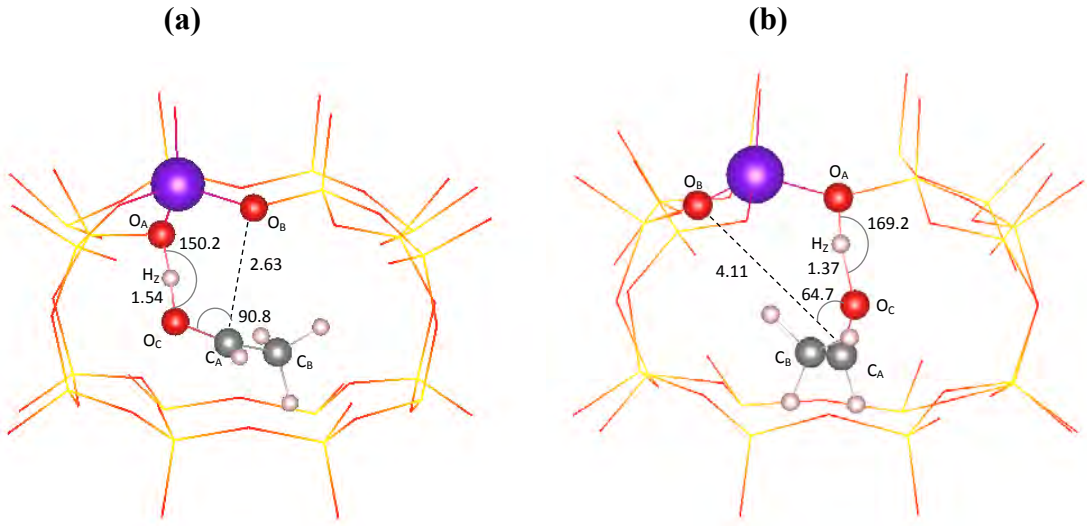

Figure 4-4 Optimized structures of H-bonded complex of acetaldehyde at (a) O1 and (b) O9 site with Al dopant located at T3 site in small channels of MOR zeolite. Bond distances (Å) and angles (°).

4.3.2.1 H-Transfer and formation of C-O bond

To study the activation of acetaldehyde through proton transfer, we explored the PES along the reaction coordinate, $r(H_Z - O_C)$, the distance between the carbonyl oxygen atom of acetaldehyde and hydrogen from the hydroxyl group of the BA site. Results are displayed in **Figure 4-5**. For both oxygen sites, O1 and O9, by elongating the $r(H_Z - O_C)$ intermolecular distance, the PES displayed only one minimum corresponding to the H-bonded complex of acetaldehyde. The ion-pair structure is not activated to form a second minimum, as it proved to be unstable with proton transfer energy increased to ~ 35 kJ mol^{-1} at O1 site and ~ 15 kJ mol^{-1} at O9 site, when the $r(H_Z - O_C)$ bond length constrained at 1.00 Å i.e the typical equilibrium OH bond distance in our calculations. An earlier study by Kubelkovà *et al.* (Kubelkova and Novakova, 1991) found stabilization of ion-pair structures of acetone and acetonitrile with proton transfer energies of 20 and 34 kJ mol^{-1}, by using computationally cheap HF/3-21G calculations and a zeolite fragment of 2 tetrahedral units. Clearly the 2T site isolated cluster model does not represent the behaviour of an extended zeolite.

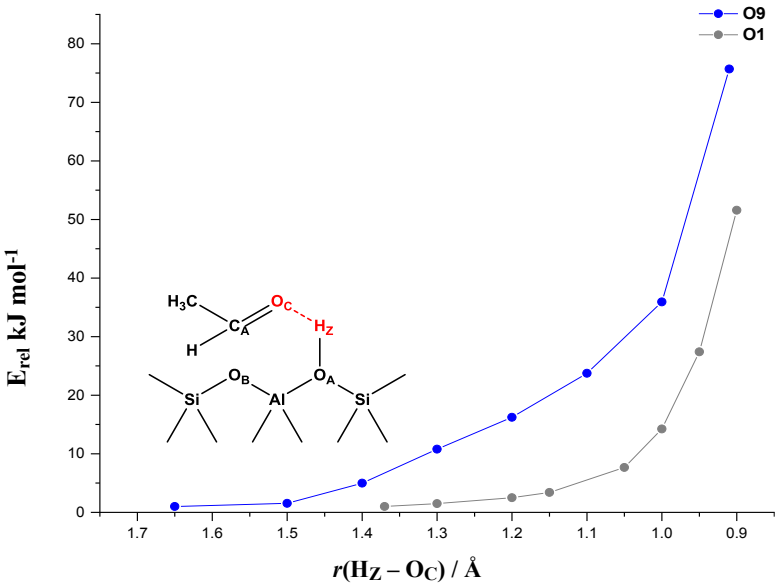

Figure 4-5 Internal energy profile for the proton transfer using the reaction coordinate, $H_Z - O_C$, the distance between the hydrogen from the Brønsted site and the oxygen atom of the carbonyl group of acetaldehyde at oxygen sites, O1 and O9, with Al dopant located at T3 site in MOR zeolite.

Next we explored the PES along by using $H_Z - O_A$ as reaction coordinate i.e the bond distance of the acid hydroxyl group. Results are displayed in **Figure 4-6.** The calculated PES of O1 and O9 are different. Starting with the H_Z on O9 site we observe a single minimum, while starting with H_Z on O1 site a double minimum is formed. At O1 site, the proton transfer does not activate the acetaldehyde, a similar situation to when reaction coordinate $r(H_Z - O_C)$ was constrained, with proton transfer energies rising to ~ 20 kJ mol^{-1} in the range of distances considered up to 1.8 Å in which the Brønsted acid site is dissociated. At O9 site, the minimum at short $r(H_Z - O_A)$ distances, ~ 1.00 Å, correspond to the H-bonded complex (intermediate I). The second minimum is formed at longer $r(H_Z - O_A)$ distances beyond ~ 2.00 Å. This geometry corresponds to a silyl ether addition compound (intermediate III) in which a C–O bond is formed

between the protonated admolecule and a framework O, nearest neighbour to Al as shown in **Figure 4-7**. The ion-pair proved to be unstable, although crucial as a transition state in order to form this stable additional compound. The proton transfer to the carbonyl group leaves a positive charge on the O_C atom forming the ox onium character of the conjugate acid. By considering the two resonance structures of the conjugate acid, the oxonium character is in equilibrium with the carbocation structure. Subsequently, the carbocation species binds to a framework oxygen atom (O_B) nearest neighbour to the Al dopant (which in this case is the least stable oxygen site – O9). Only upon the formation of this new C-O bond is the admolecule stable in its protonated form. The activation barrier obtained is 44.7 kJ mol^{-1} and the reaction energy is 11.0 kJ mol^{-1}. As a check of our methodology, we performed a similar run, but starting from intermediate III and shortening the $r(H_Z - O_A)$ distance (reverse reaction). The new reaction profile is shown in **Figure 4-6**. The reverse PES profile behaves in a similar manner to the forward reaction with the barrier obtained from this simulation, 40.6 kJ mol^{-1}, agreeing well with the above value of the forward barrier. The geometrical structures and parameters are shown in **Figure 4-8**, in which the reaction consists of a concerted mechanism via a six-coordinated transition state (TS $II^{\ddagger}$). TS $II^{\ddagger}$ and the intermediate III present similar geometries: at TS $II^{\ddagger}$ a complete proton transfer has occurred with the $H_Z - O_C$ distance of 1.07 Å causing the carbonyl group to lose its double bond character by lengthening to 1.31 Å. The C_A - O_B distance becomes shorter (1.80 Å) in order to stabilize the protonated structure. The reason as to why we did not form this additional stable intermediate III at the least stable O9 site is perhaps due to the $C_A - O_B$ bond distance being larger at the H-bonded complex (4.11 Å) compared to at O1 site (2.83 Å), as shown in **Figure 4-4**. Due to the enhanced steric hindrance, if the optimal orientation of

adsorbed H – bonded complex with regards to the Brønsted site was achieved then we could possibly form intermediate III.

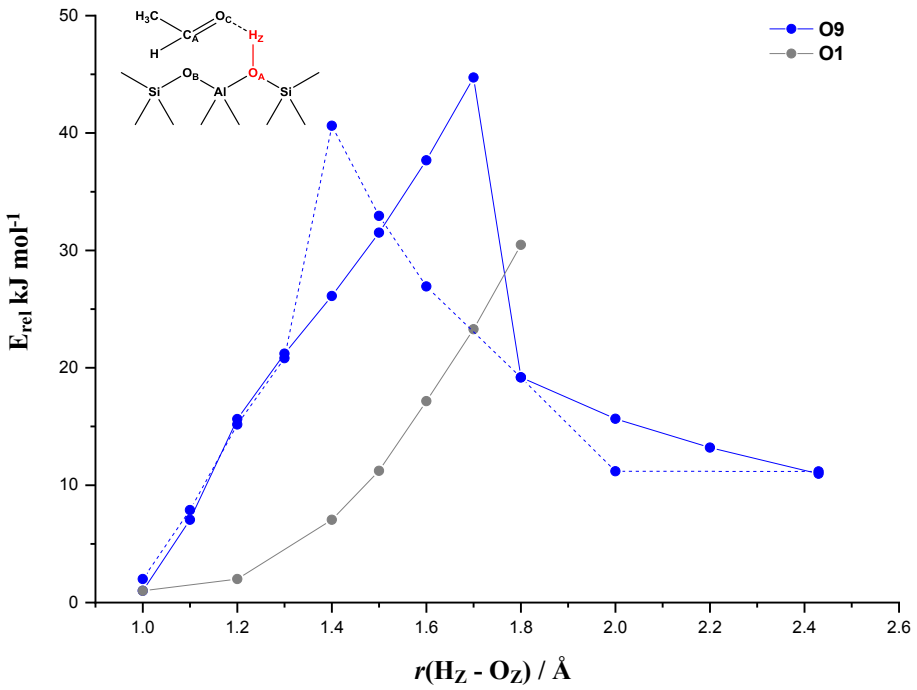

Figure 4-6 Internal energy profile for the proton transfer using the reaction coordinate, $H_Z - O_A$, the distance between the hydroxyl group of the Brønsted site, O1 and O9, with Al dopant located at T3 site in MOR zeolite. The solid line indicates the reaction starting with intermediate I and lengthening $r(H_Z - O_A)$ distance and the dashed line indicates the reaction starting with intermediate III and shortening $r(H_Z - O_A)$ distance.

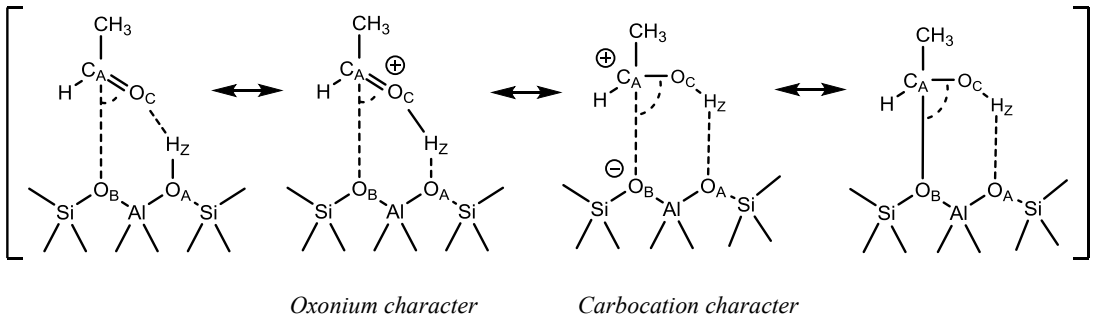

Figure 4-7 Electronic configuration of proton transfer reaction of the H-bonded complex in which the non-protonated oxygen (O_B) forms a C-O bond with the carbonyl carbon atom (C_A) atom of acetaldehyde.

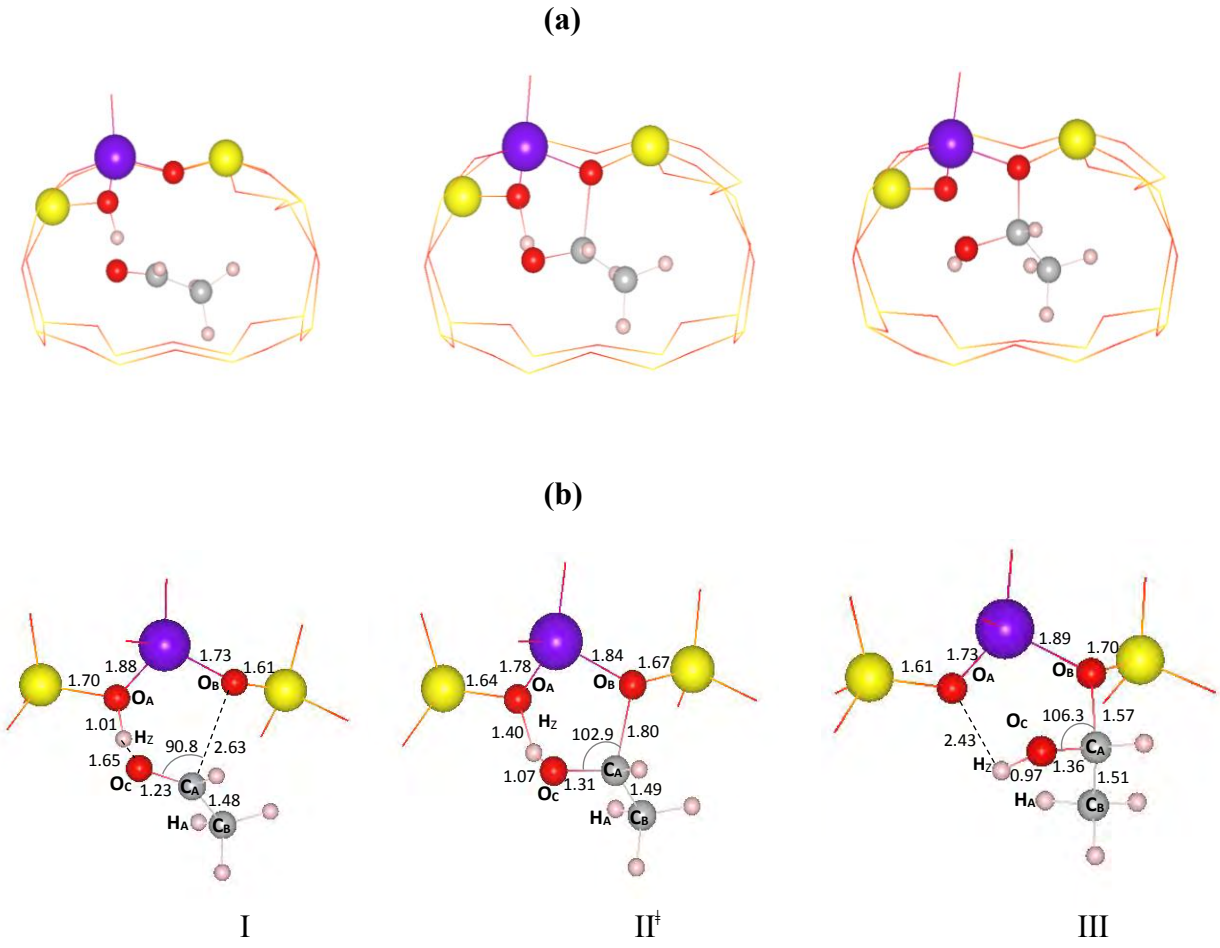

Figure 4-8 (a) Optimized structures and (b) geometrical parameters of the proton transfer reaction of H-bonded complex (intermediate I) forming stable addition compound (intermediate III) containing C_A - O_B via a concerted mechanism displayed as the transition state (TS II‡). Bond distances (Å) and bond angles (°).

The TS II‡ configuration and intermediate III has been confirmed by calculating the Γ- point phonon frequenices. One imaginary frequency, -212.6 cm^{-1}, is obtained for the TS, corresponding to the maximum associated to the reaction path forming intermediate III. We found that the approximate TS II‡ identified in the constrained search is very close to that obtained in the refinement, within the step size chosen to map the reaction coordinate and differing in energy with less than 0.1 kJ mol^{-1}. All positive eigenvalues were found for intermediate III, confirming it is a true minimum. The coordinates are listed shown in **Appendix: Figure 8-1**. In general, the reaction coordinate for a given reaction step cannot be known before the

reaction is investigated since, it traces a route on the multidimensional energy surface, and when chemical intuition is not strictly followed, defining the reaction pathways can be difficult. Intermediate III has been identified when constraining the O_A – H_Z bond distance, but not by constrained elongation of the O_C – H_Z bond. We have extended our study to understand why O_C protonation does not lead to the formation of intermediate III while O_A deprotonation does. Thus starting from intermediate III, we performed a backward reaction along the reaction coordinate, $r(H_Z – O_C)$ and the PES profile is shown in **Figure 4-9**. At 1.2 Å the C_A – O_B bond is broken although the H_A proton does not return back the O1 site to reform the Brønsted site and the H-bonded complex. Instead, the H_Z proton forms a bond with an oxygen atom located on the opposite side of the cavity (**Figure 4-9**) and not nearest neighbour to Al. Only by tuning the computational parameters (setting a tighter convergence criteria) did we reform intermediate I where at $r(H_Z – O_C)$ = 1.2 Å the energy drops and at 1.60 Å the original H-bonded complex is formed. The activation barrier, 38.6 kJ mol^{-1}, and reaction energy, 12.0 kJ mol^{-1}, correspond well with the values obtained earlier. The forward reaction using these tighter convergence criteria would produce a similar curvature although the PES failed yet again to yield a second minimum (protonated admolecule). This is essentially due to the fact that once a complete proton transfer is established with $r(H_Z – O_C)$ constrained at 1.00 Å, the ion-pair forms now a H-bond with the corresponding O_A site at ~ 1.47 Å (**Figure 4-9**) and so cannot form a second minimum. Thus we can confirm that the reaction coordinate $r(H_Z – O_C)$, is a poor coordinate by choice in forming a

second minimum and more importantly intermediate III.

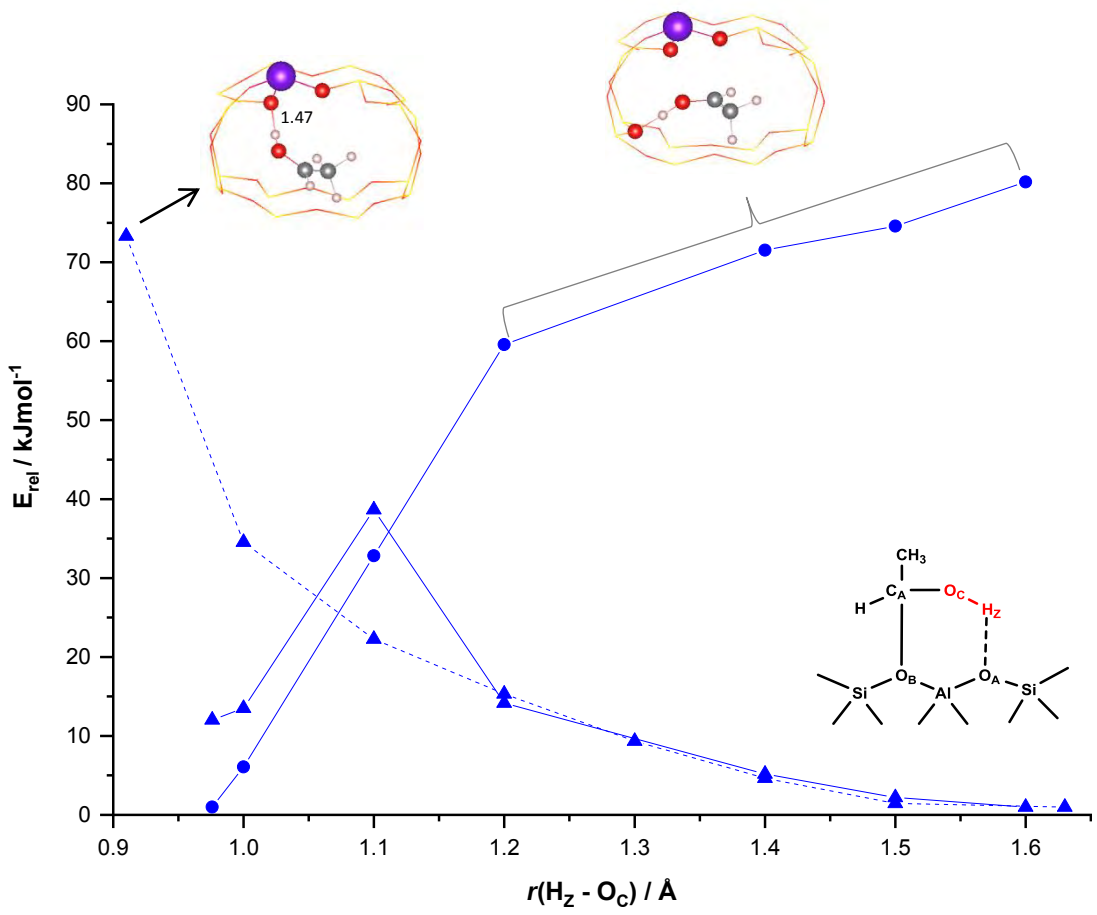

Figure 4-9 Internal energy profile for the proton transfer using reaction coordinate, $H_Z - O_Z$, with Al dopant located at T3 site in MOR zeolite. The solid line corresponds to the reaction starting from intermediate III and elongating $r(H_Z - O_C)$ distance. The triangle data plot points correspond to the tighter convergence criteria. The dashed-line corresponds to the forward reaction, starting from intermediate I, and shortening $r(H_Z - O_C)$ distance, forming the unstable ion-pair structure.

Lastly, we explored the reaction coordinate, $r(C_A - O_B)$, between the carbonyl carbon and the non-protonated oxygen atom nearest neighbour to the Al dopant **(Figure 4-10)** *i.e.* the bond between molecule and framework that stabilizes intermediate III. When the proton starts at the O1 site, intermediate III is successfully formed. When the proton starts at O9 site instead, formation of the $C_A - O_B$ bond proved unsuccessful and calculations yielded an

unstable ion-pair configuration. This is possibly due to the wrong initial orientation of the admolecule resulting in a longer initial $C_A - O_B$ distance when the proton is bonded to the O9 site.

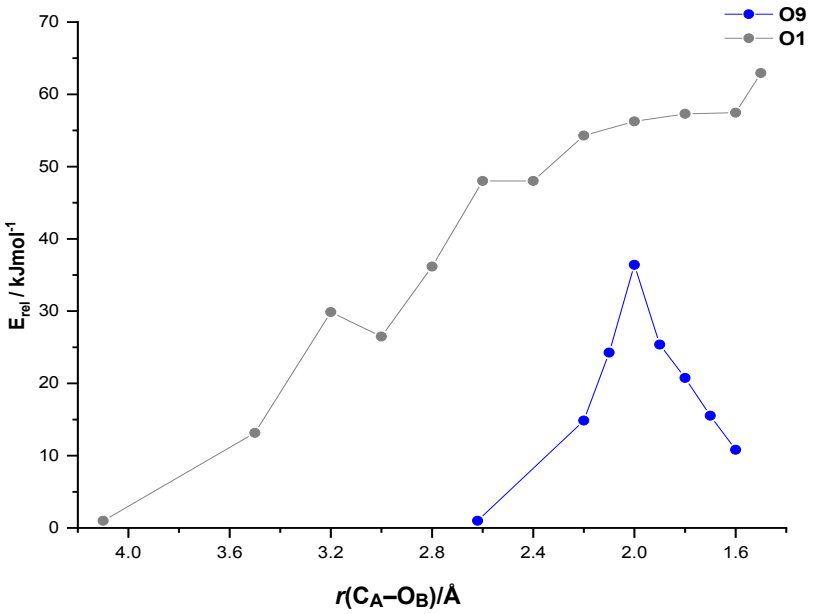

Figure 4-10 Internal energy profile for the proton transfer from intermediate I using the reaction coordinate $r(C_A - O_B)$, the distance between the carbonyl carbon of acetaldehyde and an oxygen site nearest neighbour to Al dopant in which a Brønsted site is not produced.

On the basis of our calculations, the formation of intermediate III from H-bonded complex is not described by a simple reaction coordinate. Its formation requires protonation of the admolecules, but simultaneously a cleavage of the H-bond to release the alcohol group, only then does the $C_A - O_B$ bond with a framework take place. The structure of intermediate III has not been yet been observed experimentally, but may exist under transient conditions. Kassab *et al.* (Kassab, *et al.*, 1999) performed ab initio calculations at HF and post-HF level with small cluster models ranging from 1 – 3 tetrahedral units to simulate intermediate III for weak bases including acetaldehyde. Their activation energy and reaction enery for intermediate III were ~ 75 kJ mol^{-1} and 30 kJ mol^{-1}. For qualitative purposes

this provides a good starting point as in our study the zeolite confinement and embedding effects have not been ignored as periodic DFT calculations have been used with the inclusion of larger sized basis sets and dispersion corrections. From all the reaction coordinates studied so far, we did not form the enol configuration via proton transfer.

4.3.2.2 Enol formation via C-O bond reaction mechanism

Kassab *et al*. (Kassab, *et al*., 1999) identified the presence of intermediate III in the reaction mechanism, but did not consider its further transformation into the enol configuration. Here we are interested in how the intermediate can sustain the aldol condensation, hence we consider its reaction. The first configuration we consider is that of intermediate III formed in the small channels of MOR zeolite with the Al dopant at the T3 position. The transfer of a hydrogen H_A from the methyl group to the framework oxygen atom (O_A) adjacent to Al dopant can yield the enol form of acetaldehyde. The mechanism we considered is displayed in **Figure 4-11**. The labelling of atoms and reaction mechanism are shown in **Figure 4-11**. The reaction coordinate we considered is the length of $H_A - O_A$ bond that dissociates to yield the enol molecule from intermediate III. The resulting energy profile is displayed in **Figure 4-12**. We find that the elongation of the $H_A - O_A$ bond is not an elementary reaction step, but a two-step reaction, with a stable intermediate corresponding to $H_A - O_A$ bond distance of ~ 1.5 Å. The schematic representation of the transition states and the intermediates is shown in **Figure 4-11**. The overall reaction is endothermic indicating the stability of intermediate III. Starting from intermediate III, by shortening the , $r(H_A - O_A)$ bond, the elongation of the $C_A - H_A$ bond of the methyl causes a small reorganization of the zeolite

framework and simultaneously the breakage of $C_A - O_B$ bond in a concerted manner through the six centered TS labeled as IV‡. In the intermediate labeled as V in **Figure 4-12** the bond distances involving the H_A are 1.19 Å with C_B of methyl group and 1.50 Å with a framework oxygen O_A. This indicates that with H_A is still bonded to the admolecule, but engaged in a strong H-bonding interaction with O_A. In the geometry the molecule has therefore abstracted the proton from the framework. In addition, the $C_A - O_C$ bond shortens to 1.28 Å. A further shortening of the $r(H_A - O_A)$ bond causes proton transfer to the O_A framework atom. The process shows an activation barrier, resulting in a 6-centered transition state VI‡. During this process, there is a reorientation of the alkyl fragment, such as to align both carbon atoms, the framework oxygen O_B and the H_A atom, almost in the same plane, with a dihedral angle near zero. At TS VI‡ , the $C_B - H_A$ bond distance is elongated to 1.49 Å, $H_A - O_A$ and $C_A - C_B$ bond lengths are shortened to 1.20 Å and 1.38 Å, implying the formation of the alcohol. The H_A atom is completely transferred to the framework O_A atom resulting in the regeneration of Brønsted acid, at the O1 site, and in the formation of the enol product.

From the energy profile shown in **Figure 4-12**, intermediate V is formed when the $r(H_A - O_A)$ bond distance is constrained at 1.50 Å. The stability of this intermediate is shown by the fact that there are small activation barriers for its conversion either towards the reactant, intermediate III, at longer $r(H_A - O_A)$ distances or towards the enol product at shorter $r(H_A - O_A)$. The reverse activation barrier towards intermediate III (15.9 kJ mol^{-1}) is slightly lower than the forward activation barrier towards the enol product (25.5 kJ mol^{-1}) meaning that equilibrium to reach the enol form is slow, shown in **Figure 4-11**.

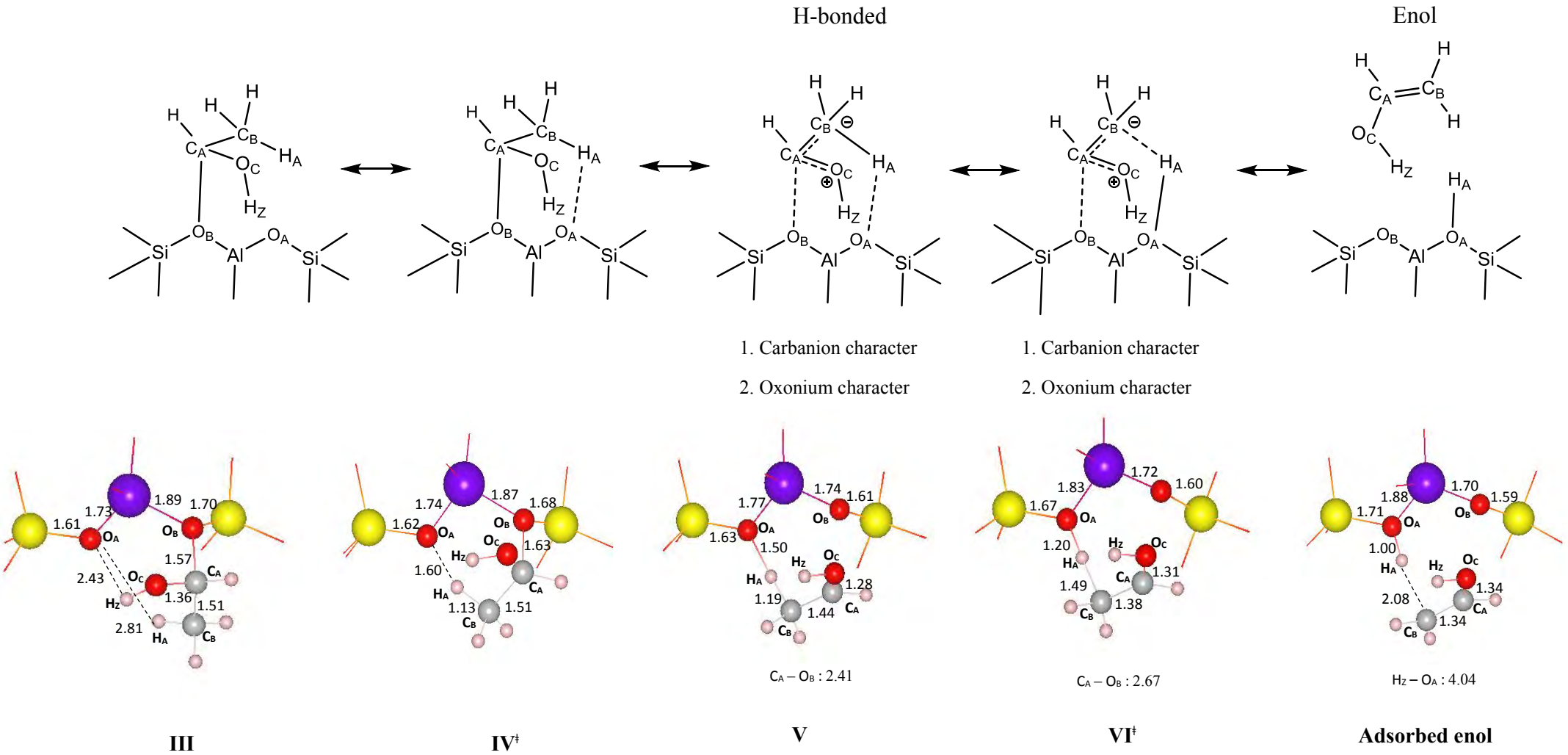

Figure 4-11 Intermolecular mechanism of for the formation of the enol structure from the stable addition intermediate III in MOR with the Al dopant located in the site T3. The bottom diagrams show selected geometrical parameters in the optimized structures. (O_A : O9 and O_B : O1).

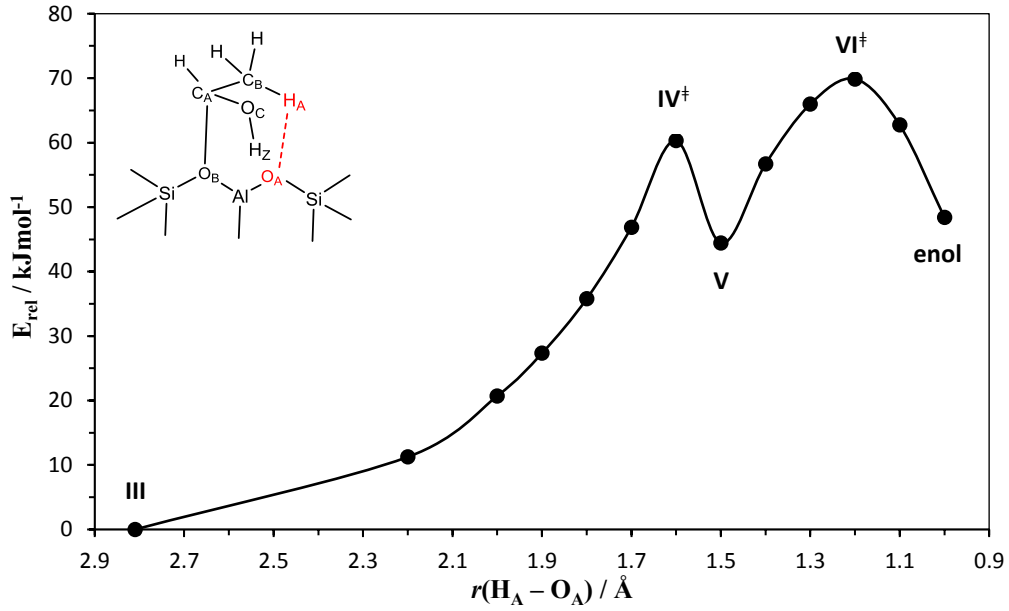

Figure 4-12 Energy diagram of the reaction intermediate III ↔ enol product with the fixation of reaction coordinate, $r(H_A - O_A)$, hydrogen of the methyl group and oxygen site nearest neighbour Al dopant at T3 position in the small channels of MOR zeolite.

Table 4-1 summarises the activation and reaction energies involved in the keto/enol transformation through intermediate III discussed here. The energy values are decomposed into their electronic and dispersion contributions **Table 4-1.** In general dispersion increases, as expected, for the adsorption energy of acetaldehyde at T3 site in MOR zeolite, although has a lesser effect on the activation and reaction energies. The formation of intermediate III and enol product require small atomic displacements due to the constrained geometry optimizations that cause minor changes in dispersion.

Reactions	**O_A / O_B sites**	***E_r***	***ΔE_{elec}***	***ΔE_{disp}***	***E_a* (forward)**	***ΔE_{elec}***	***ΔE_{disp}***	***E_a* (reverse)**
Z + Keto ↔ I*	O_1 / O_9	*-112.9*	*36.6*	*-149.5*				
I ↔ III		11.0	13.3	-2.4	40.6	35.9	4.7	29.7
III ↔ V		44.6	45.0	-0.4	60.50	56.34	4.16	15.3
V ↔ Enol		4.0	4.5	-0.5	25.5	23.8	1.7	21.5

Table 4-1 Summary of calculated reaction and activation energies for the forward and reverse reaction pathways considered of two-step procedure of enol configuration in 8-MR channels of MOR zeolite with Al atom located at T3 position, including both the change in electronic energy (E_{elec}) and dispersion energy (E_{disp}). (*) indicates the adsorption state (E_{ads}) of zeolite-adsorbate system calculated relative to them in the gas phase and the calculated E_{elec} and E_{disp} are the components of the respective (E_{ads}). Energy displayed in kJ mol^{-1}.

A complete PES profile for the two-step concerted mechanism of the enol form of acetaldehyde is shown in **Figure 4-13**. This reaction pathway provides an alternative route for the formation of the enol structure from the H-bonded acetaldehyde molecule via intermediate III. The TS IV‡ with an activation energy barrier of 60.5 kJ mol^{-1} is the rate-limiting step and controls the reaction kinetics.

To transform the adsorbed enol back to intermediate V is facile with a small activation barrier of 21.5 kJ mol^{-1}. Intermediate V can be further converted back to intermediate III, with a small activation barrier of 15.9 kJ mol^{-1}. The reason for these small activation energies is due to the relative instability of the enol product compared to intermediate III. The reaction energy for the transformation of intermediate III to the enol product is 48.4 kJ mol^{-1}. The higher endothermic E_r is due to the fact that intermediate III consists of a strong $C_A - O_B$ covalent bond as well as the stabilization of H-bonds between $O_A - H_Z$ (2.43 Å) and $O_A - H_A$ (2.81 Å) while the adsorbed enol is adsorbed on the acid site by a weak π interaction, $C_B - H_A$ (2.08 Å) **(Figure 4.11)**. This process becomes less thermodynamically favourable compared to the reaction energy for the formation of intermediate III from

intermediate I, 11.1 kJ mol^{-1}. This means that eeventhough the enol form has been proposed as the reactive species in the aldol condensation reactions, the presence of intermediate III can lead to alternative reaction pathways.

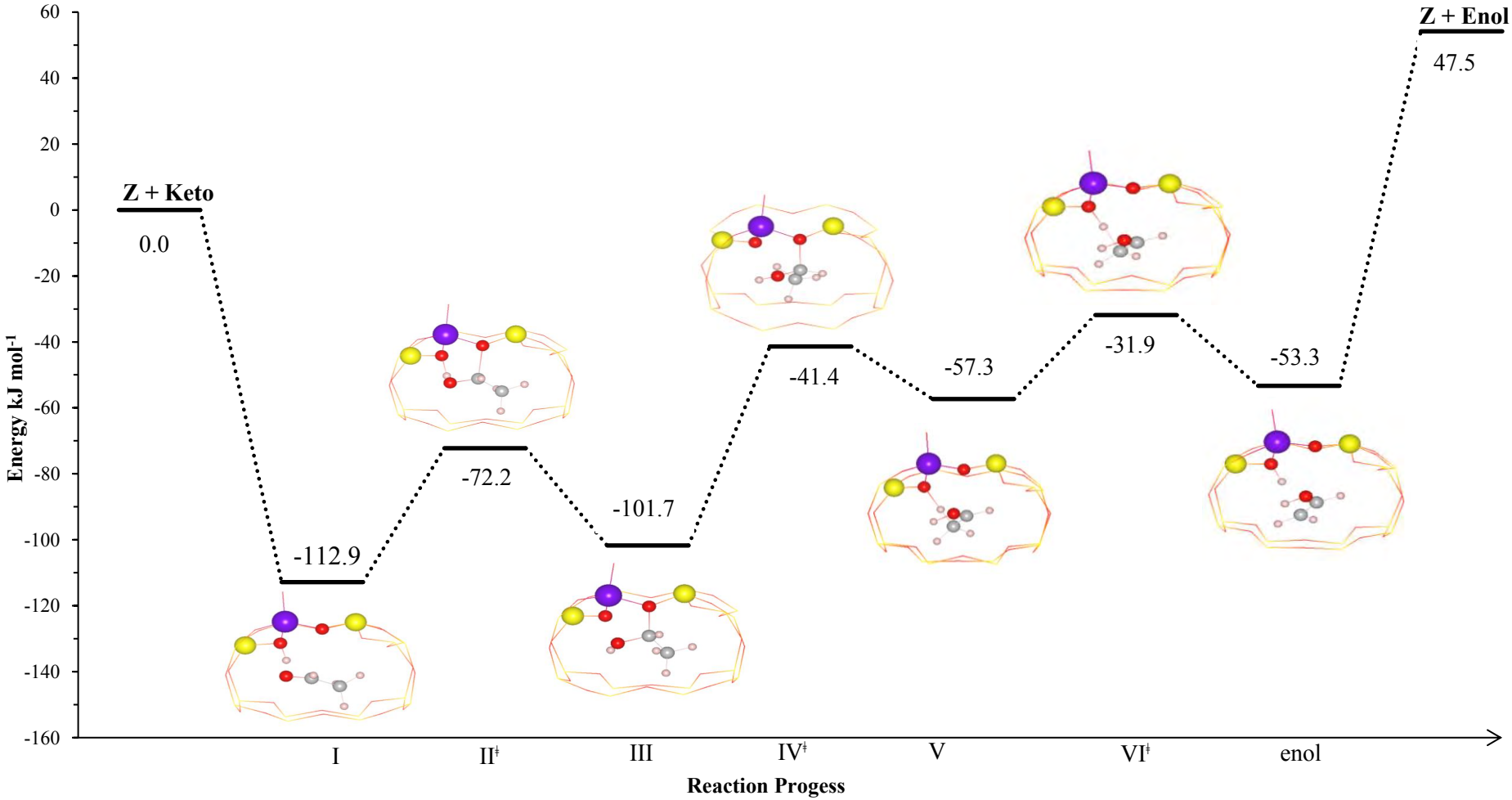

Figure 4-13 Complete energetic profile of the two-step mechanism for the enol structure of acetaldehyde at most stable oxygen (O1) site with Al dopant in T3 position in MOR zeolite.

4.3.3 Two-step concerted enolisation mechanism via C-O bond

4.3.3.1 MOR

In the previous section, we have discussed a two-step concerted enolisation mechanism for acetaldehyde occurring in the small pores of MOR with the Al dopant located at T3 site. We have replicated this mechanism in the larger pores and for Al located at each of the remaining T site positions to understand whether the constrained environment of T3 is necessary to enable this mechanism. Intermediate III, the stable additional compound with C_A bonded to framework oxygen O_B was generated in the input coordinates and optimized. Intermediate III proved stable for all the Al sites and acetaldehyde locations of the MOR structure. The constrained space of site T3 is therefore not necessary for this reaction pathway to occur. Intermediate III transforms into either species I, the H-bonded acetaldehyde complex on the BA site or species V, the H-bonded enol molecule by variation of two bond distances, taken as reaction coordinates. The energy profiles are shown in **Figure 4-14**. Constraining $r(O_A - H_Z)$ from its optimized value in intermediate III to shorter value yields intermediate I, the H-bonded complex. Instead by constraining $r(O_A - H_A)$ towards longer bond distances we formed the enol product (intermediate V). We observe in **Figure 4-14 (a)** that the shape of the PES for the reaction I $\leftrightarrow$ III is similar for all T sites. The PES leading away from intermediate III in **Figure 4-14** (b) with the reduction of the bond distance $r(O_A - H_A)$ shows a sharper drop in energy where where Al is located at site T4 and acetaldehyde in the larger pores, at 1.50 Å, due to the breakage of the $C_A - O_B$ bond and the formation of intermediate V. As the initial formation of intermediate V occurs the molecule reaches a flat shoulder at 1.40 Å in the PES (TS VI‡), before stabilizing the formation of adsorbed enol structure. The TS VI‡ proves to be barrierless and so the formation of enol is facile in

comparison to what we observed earlier for the reaction occurring at T3 position.

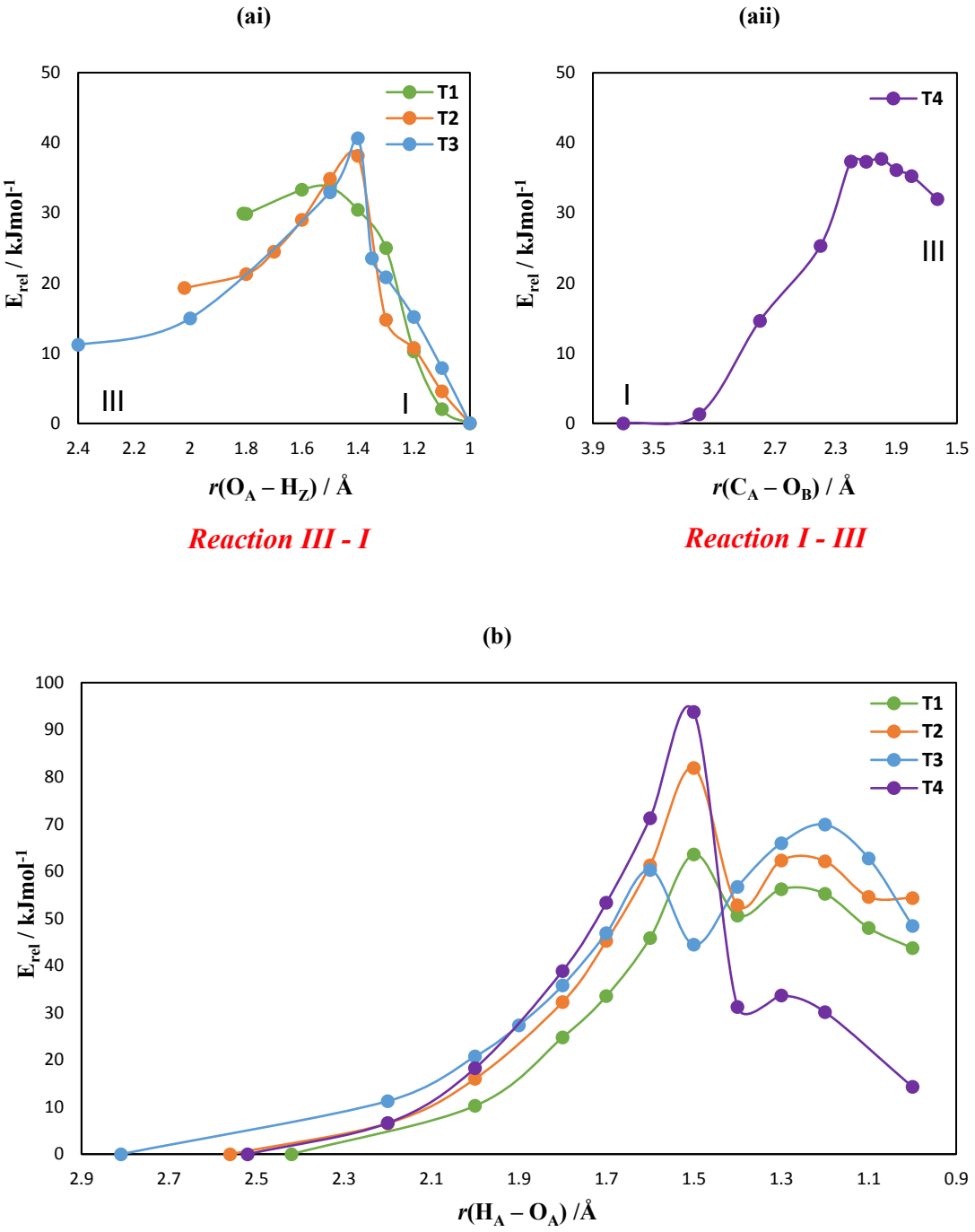

Figure 4-14 Reaction coordinate diagrams of the reactions consisting intermediates (a) I ↔ III wherein two different reaction coordinates are constrained for this process to occur (i) $r(O_A - H_Z)$ at T1, T2, T3 and (ii) $r(C_A - O_B)$ at T4 (Intermediate III was difficult to form initially as the reactant and so starting with intermediate I we constrained the bond length between carbonyl carbon, C_A, and O_B atom adjacent to Al atom and decreased the distance until intermediate III was formed), (b) III ↔ enol product whereby the presence of the temporary minima is shown representing intermediate V.

The activation and reaction energies are summarised in **Table 4-2** along with the dispersion corrections and a complete PES profile of this two-step mechanism in shown in **Figure 4-15**.

MOR	**Reactions**	O_A / O_B	E_r	ΔE_{elec}	ΔE_{disp}	E_a **(forward)**	ΔE_{elec}	ΔE_{disp}	E_a **(reverse)**
T1	*Z + Keto ↔ I**	O7 / O3	*-151.5*	*-69.1*	*-82.4*				
	I ↔ III		29.9	38.2	-8.3	33.7	36.1	-2.5	3.8
	III ↔ V		50.6	38.1	14.7	63.6	48.2	15.4	13.0
	V ↔ Enol		-6.9	-2.9	-4.0	5.6	12.2	-6.6	12.5
T2	*Z + Keto ↔ I**	O3 / O2	*-136.8*	*-49.2*	*-87.6*				
	I ↔ III		*17.1*	*25.5*	*-8.5*	35.9	34.0	1.9	18.8
	III ↔ V		*52.8*	*43.7*	*9.1*	*81.9*	*75.9*	*6.0*	29.1
	V ↔ Enol		*-6.5*	*-14.4*	*7.9*	9.5	7.5	1.9	8.0
T3	*Z + Keto ↔ I**	O1 / O9	*-112.9*	*36.6*	*-149.5*				
	I ↔ III		11.0	13.3	-2.4	40.6	35.9	4.7	29.7
	III ↔ V		44.6	45.0	-0.4	60.50	56.34	4.16	15.3
	V ↔ Enol		4.0	4.5	-0.5	25.5	23.8	1.7	21.5
T4	*Z + Keto ↔ I**	O2 / O10	-155.2	-65.2	-90.0				
	I ↔ III		32.0	32.1	-0.1	37.7	36.6	1.2	5.4
	III ↔ V		31.2	76.8	-45.5	93.8	97.7	-3.9	62.5
	V ↔ Enol		-16.2	-24.7	8.5	2.4	-6.4	8.8	19.4

Table 4-2 Calculated reaction (E_r) and activation (E_a) energies for the forward and reverse reaction pathways considered for the two-step mechanism of enol configuration of acetaldehyde at all T sites in MOR zeolite. ΔE_{elec} and ΔE_{disp} is the change in the electronic and dispersion energy. Note that (*) indicates the adsorption state (E_{ads}) of zeolite-adsorbate system calculated relative to them in the gas phase and the calculated E_{elec} and E_{disp} are the components of the respective (E_{ads}). Energy displayed in kJ mol^{-1}.

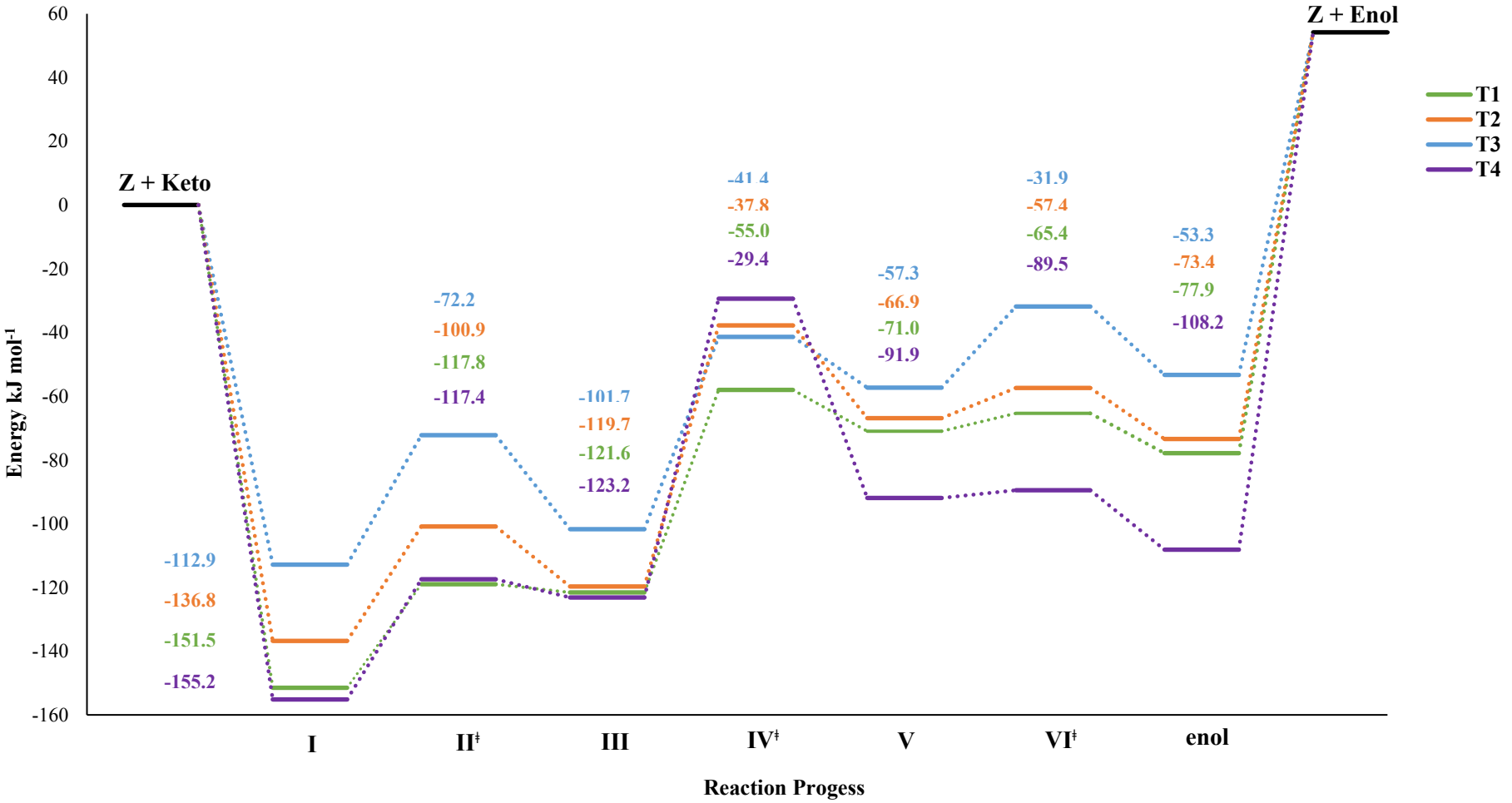

Figure 4-15. Complete energetic profile of the two-step reaction mechanism of enol configuration of acetaldehyde at each T position in MOR zeolite.

The location of Al does affect the reaction profile. The adsorption of acetaldehyde to form intermediate I varies as T4 (-155.2) > T1 (-151.5) > T2 (-136.8) > T3 (-112.9) kJ mol^{-1} as discussed in Chapter 3. The variation is associated with the strength of the H-bond formed. The activation barriers for transformation of the H-bonded complex into intermediate III are similar at all T sites (~ 35 to 41 kJ mol^{-1}). There is no appreciable correlation between activation barrier and absorption energy.

The reaction energy to form intermediate III is endothermic at all T sites and the process is most thermodynamically favourable in the following order: T3 (11.1) > T2 (17.1) > T1 (29.9) > T4 (32.0) kJ mol^{-1}. In addition, the reverse barrier energies to form intermediate I are very small at T1 (3.8) and T4 (5.7) kJ mol^{-1}, indicating that the newly formed C_A – O_B bond is easily broken. Barriers are higher instead at T2 (18.8) and T3 (29.7) kJ mol^{-1}. The reaction energies for the step I-III follow the reverse order as the adsorption energy of acetaldehyde on the acid site, indicating that formation of a very stable H-bonded complex on the acid site prevents reactivity through intermediate III.

The calculated activation energies for the transformation of intermediate III into V are lowest at T3 (60.3) and T1 (63.6) and increase at T2 (81.9) and T4 (93.8) kJ mol^{-1}. Intermediate V presents a local minimum, as shown in **Figure 4-14**, The enolisation step has lowest barrier in the larger pores, with activation energies of T4 (2.4), T1 (5.6) and T2 (9.5) kJ mol^{-1} and so the formation of the enol product is favoured over the reverse step to form intermediate III that has higher barriers when Al is in sites: T1 (13.0), T2

(29.1) and T4 (79.5) kJ mol^{-1}. This contrast with the situation discussed earlier of Al in the smaller pores at T3 position where starting from intermediate V the reverse reaction to intermediate III has a barrier (15.3 kJ mol^{-1}) is lower than for forward transformation to the enol (25.5 kJ mol^{-1}). The calculated reaction energies for the step III ↔ V vary in the following order: T4 (31.2) > T3 (44.4) > T1 (50.8) > T2 (52.8) kJ mol^{-1}. Neglecting the effect of dispersion leads to the reaction process being least favourable at T4 (76.8 kJ mol^{-1}). The confinement effect plays therefore a leading role for the stabilization of intermediate V in site T4 as the dispersion correction is large (-45.5 kJ mol^{-1}). This is due to the fact the admolecule orients itself away from the MC and into the SP, where also the adsorbed enol is formed. Hence, the position of the Al dopant does influence the formation of the adsorbed enol.

Figure 4-15 confirms that the adsorbed enol structure is most stabilized when Al is at T4 position. The rate determining step for the proposed mechanism is the transformation of intermediate III into V through transition state $IV^{‡}$, that involves the C_A - O_B bond breaking at all the T sites. TS $IV^{‡}$ requires deprotonation of the methyl group.

Vibrational frequency calculations were performed to ensure that geometries identified as barriers in the energy profiles, i.e those labeled as $II^{‡}$, $IV^{‡}$, and $VI^{‡}$, corresponded to real transition states. Imaginary frequencies characterising the selected transition states are given in **Table 4-3.** All cases yielded one imaginary mode corresponding to the reaction pathway discussed. Although in a small number of cases a second mode with smaller imaginary frequency was also found, the mode

was clearly of secondary importance as the frequency was an order of magnitude smaller than the other.

MOR	Transition State	Imaginary Frequency (cm^{-1})	
T1	$II^{\ddagger}$	-107.7	
	$IV^{\ddagger}$	-136.6	
	$VI^{\ddagger}$	-816.3	
T2	$II^{\ddagger}$	-153.4	-14.1
	$IV^{\ddagger}$	-123.3	-12
	$VI^{\ddagger}$	-804.4	-83.6
T3	$II^{\ddagger}$	-212.6	
	$IV^{\ddagger}$	-101.5	
	$VI^{\ddagger}$	-1033.8	
T4	$II^{\ddagger}$	-121.1	
	$IV^{\ddagger}$	-99.6	
	$VI^{\ddagger}$	-924.5	-93.4

Table 4-3 Vibrational frequencies obtained at the selected transition states for two-step enolisation mechanism at the T sites in MOR zeolite.

The frequency for TS $II^{\ddagger}$ and $IV^{\ddagger}$ for the T sites has a value of ~ 100 cm^{-1}, while for TS VI the value is of ~ 1000 cm^{-1}. This is consistent with TS $II^{\ddagger}$ and $IV^{\ddagger}$ requiring bond formation between heavy atoms (C_A - O_B) while TS VI consisting in cleavage of a C_B - H_A bond. At T2 position, we found an additional second mode of ~ 14 cm^{-1} at TS $II^{\ddagger}$ and ~ 12 cm^{-1} at TS $VI^{\ddagger}$. These correspond to the translation and rotation modes and thus can be considered negligible. For the TS $VI^{\ddagger}$ at T2 and T4 sites, we have obtained two negative frequencies, (-804.4 and -83.6 cm^{-1}) and (-924.5 and -93.4 cm^{-1}).The lower frequency modes are low energy torsional vibrations that do not alter the overall mechanism.

Table 4-4 summarizes the main geometrical parameters of the two-step concerted mechanism of enolisation at the different T sites in MOR zeolite. Since the mechanism is similar at all T sites, the geometrical parameters are comparable within each intermediate and transition state. The geometries of the TS $II^{\ddagger}$ and

intermediate III are more similar at T1 and T4 than at T2 and T3, correlating well with the reaction energies. The variation of bond distances and angles along the reaction profile is smaller for Al in site T3, since the reaction takes place in the smaller space of the SP and site/shape selectivity constraint imposed by the framework are pronounced in this case. Intermediate I for instance the $C_A - O_B$ distance is 2.63 Å and the $O_C - C_A - O_B$ angle is 90.8 ° and undergoes minimal changes to form intermediate III because of the smaller pore volume limiting the possible orientations of the admolecule. The remaining T sites in the larger pores have longer $C_A - O_B$ distances (~ 3.7 to 4.2 Å) and more acute $O_C - C_A - O_B$ angles (~ 70 °). The $C_A - O_B$ distance is decreased to ~ 1.57 to 1.63 Å and $O_C - C_A - O_B$ angle is increased to ~ 107° at intermediate III. This comparison explains the stability of intermediate III in the smaller pores.

The zeolite framework in the vicinity of the active site also undergoes several rearrangements with the bond lengths $Al - O_A$ and $Si - O_A$ increasing and $Al - O_B$ and $Si - O_B$ decreasing when O_A site is deprotonated to form the $C_A - O_B$ bond, and vice versa when O_B site is protonated again to form the enol product.

MOR	Si-O_A	Si-O_B	Al-O_A	Al-O_B	O_A-H_Z	H_Z-O_C	O_C-C_A	C_A-C_B	C_B-H_A	H_A-O_B	C_A-O_B	O_A-H_Z-O_C	O_C-C_A-O_B
T1													
I	1.68	1.60	1.85	1.72	1.04	1.46	1.23	1.49			4.02	169.5	69.7
II‡	1.64	1.62	1.79	1.77	1.50	1.05	1.27	1.49			2.27	153.7	94.4
III	1.62	1.68	1.74	1.86	1.82	0.99	1.34	1.52	1.09	2.42	1.63	143.3	107.4
IV‡	1.62	1.68	1.75	1.86	2.99	0.98	1.34	1.50	1.13	1.50	1.68		
V	1.64	1.60	1.79	1.74	3.64	1.00	1.28	1.42	1.24	1.40	2.69		
VI‡	1.65	1.60	1.81	1.73	3.27	1.00	1.30	1.40	1.33	1.30	2.74		
enol	1.69	1.60	1.87	1.71	3.70	0.98	1.33	1.35	1.83	1.02	2.90		
T2													
I	1.68	1.60	1.86	1.72	1.06	1.43	1.23	1.50			4.21	172.5	71.1
II‡	1.63	1.61	1.81	1.76	1.40	1.08	1.26	1.49			2.33	151.7	95.3
III	1.61	1.69	1.73	1.87	2.02	0.98	1.36	1.52	1.10	2.56	1.59	127.6	107.5
IV‡	1.62	1.68	1.76	1.85	2.53	0.98	1.35	1.50	1.15	1.50	1.69		
V	1.63	1.60	1.79	1.73	4.10	1.00	1.28	1.43	1.23	1.41	2.75		
VI‡	1.64	1.60	1.81	1.72	4.05	0.99	1.29	1.41	1.32	1.30	2.89		
enol	1.68	1.60	1.88	1.70	4.00	0.98	1.33	1.35	1.81	1.01	3.26		
T3													
I	1.70	1.61	1.88	1.73	1.01	1.65	1.23	1.48			2.63	150.2	90.8
II‡	1.64	1.67	1.78	1.84	1.40	1.07	1.31	1.49			1.80	150.5	102.9
III	1.61	1.70	1.73	1.89	2.43	0.98	1.36	1.51	1.10	2.81	1.57	112.7	106.3
IV‡	1.62	1.68	1.74	1.87	3.11?	0.97	1.35	1.51	1.13	1.60	1.63		
V	1.63	1.61	1.77	1.74	3.95	0.99	1.28	1.44	1.19	1.50	2.41		
VI‡	1.67	1.60	1.83	1.72	3.09	0.98	1.31	1.38	1.49	1.20	2.67		
enol	1.71	1.59	1.88	1.70	4.04	0.97	1.34	1.34	2.08	1.00	2.79		
T4													
I	1.68	1.60	1.86	1.71	1.05	1.45	1.23	1.50			3.70	171.0	70.3
II‡	1.63	1.64	1.77	1.79	1.63	1.02	1.29	1.50			2.00	151.1	100.0
III	1.62	1.70	1.74	1.86	1.88	0.98	1.35	1.52	1.10	2.53	1.63	144.3	106.8
IV‡	1.62	1.68	1.76	1.84	2.74	0.98	1.34	1.50	1.14	1.50	1.75		
V	1.63	1.59	1.79	1.72	4.06	1.00	1.29	1.41	1.25	1.43	3.90		
VI‡	1.64	1.59	1.81	1.71	3.99	0.99	1.30	1.39	1.36	1.30	3.86		
enol	1.68	1.59	1.87	1.70	3.85	0.98	1.34	1.35	1.84	1.02	3.85		

Table 4-4 Geometrical parameters of the two-step enolisation mechanism of acetaldehyde at T sites in MOR zeolite.

4.3.3.2. FER

The two-step enolisation mechanism of acetaldehyde discussed in the previous section for MOR was replicated in FER zeolite, in order to discriminate the importance of the zeolite environment. The study was performed for Al located in each of the symmetry unique T sites. The mechanism proved to be feasible only at the T sites located in the larger pores. Despite our efforts, we were unable to optimize the structure of intermediate III in the FER cavity corresponding to Al in site T4. The formation of the $C_A - O_B$ bond is in this case highly unstable due to the high steric repulsion between the admolecule and the cavity walls. The reaction coordinate diagrams is shown in **Appendix: Figure 8-2 and 8-3.**

In the larger pores, the reaction coordinate diagrams leading to formation of intermediate III and of the enol product are shown in **Figure 4-16**. From **Figure 4-16 (a)**, the energy profile for the reaction I ↔ III is substantially different, at the T sites in the larger pores of FER, with different activation barriers ranging between 30 and 60 kJ mol^{-1}. This contrasts with MOR, where all T sites had similar energy profile. In **Figure 4-16 (b)**, only one clear transition state can be observed. The local minimum corresponding to intermediate V discussed for MOR is not present in FER. Due to the smaller pore size in FER, intermediate III can be directly converted to adsorbed enol. The calculated activation and reaction energies, along with the dispersion energies at the intermediates and TS's are listed in **Table 4-5.** Geometrical parameters are shown in **Table 4-6.**

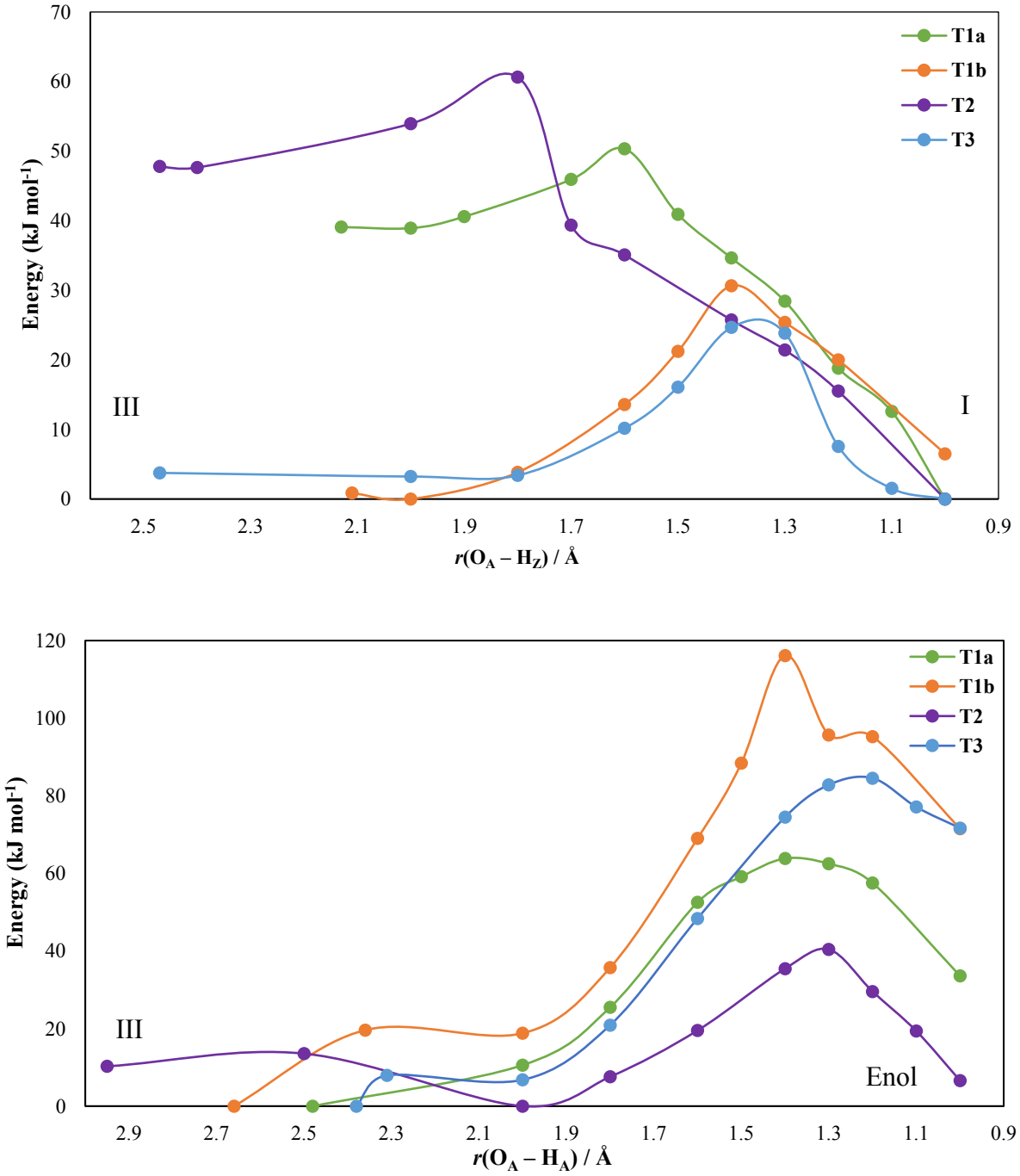

Figure 4-16 Reaction coordinate diagrams of the reactions consisting intermediates (a) I ↔ III where the reaction coordinate constrained is the Brønsted group, $r(O_A - H_Z)$ at T1, T2, T3 and (b) III ↔ enol product whereby the presence of the temporary minima is shown representing intermediate.

As we observed in Chapter 3, the T sites in the larger pores of FER and MOR zeolites have similar acid strengths, yet the activation barriers for the formation of intermediate III differ in the 2 zeolites. This may be originated from the stronger steric repulsion between acetaldehyde and the zeolite walls in the smaller pore size (4.2 × 5.4 Å) of FER than in the larger pore size (6.5 × 7.0 Å) of MOR. In the TS II ‡, for Al located at sites T1a and T2 the distance between the $C_A - O_B$ bond is much shorter in FER (1.69 – 1.87 Å) than in MOR (~ 2.00 – 2.33 Å). Although this provides stronger dispersion stabilization of TS II ‡ in FER, the steric effect also becomes significant, which destabilizes the TS II‡ and increases the activation barrier. When Al is in sites T1b and T3, the energy barriers to form intermediate III are reduced greatly (24.2 and 24.7 kJ mol^{-1}) and are lower than in MOR.

FER	Reactions	*O_A / O_B*	*E_r*	*ΔE_{elec}*	*ΔE_{disp}*	*E_a (forward)*	*ΔE_{elec}*	*ΔE_{disp}*	*E_a (reverse)*
T1a	*Z + Keto ↔ I**	*O1 / O4*	*-156.8*	*-48.4*	*-108.4*				
	I ↔ III		*39.1*	*95.3*	*-56.3*	50.3	51.3	-0.9	11.3
	III ↔ Enol		*33.6*	*-18.5*	*52.1*	63.8	18.8	45.0	30.2
T1b	*Z + Keto ↔ I**	*O2/ O1*	*-125.3*	*-17.9*	*-110.8*				
	I ↔ III		-5.7	22.8	-28.4	24.2	36.5	-12.3	29.8
	III ↔ Enol		71.5	59.1	12.4	116.1	104.9	11.3	44.6
T2	*Z + Keto ↔ I**	*O2 / O5*	*-129.3*	*-42.3*	*-87.0*				
	I ↔ III		59.6	51.7	8.0	72.4	64.4	8.0	12.8
	III ↔ Enol		-3.7	-18.8	15.2	40.4	43.3	-2.9	33.8
T3	*Z + Keto ↔ I**	*O1 / O1*	-148.8	-31.6	-117.2				
	I ↔ III		3.8	14.7	-11.0	24.7	32.2	-7.6	20.9
	III ↔ Enol		71.7	65.1	6.6	84.6	81.4	3.1	12.9

Table 4-5 Calculated reaction (E_r) and activation (E_a) energies for the forward and reverse reaction pathways considered for the two-step mechanism of enol configuration of acetaldehyde at all T sites in FER zeolite. ΔE_{elec} and ΔE_{disp} is the change in the electronic and dispersion energy. Note that (*) indicates the adsorption state (E_{ads}) of zeolite-adsorbate system calculated relative to them in the gas phase and the calculated E_{elec} and E_{disp} are the components of the respective (E_{ads}). Energy displayed in kJ mol^{-1}.

As we determined in Chapter 3, the adsorption energies of the H-bonded complexes of acetaldehyde do not follow the order of stability of the isolated acid sites ; at T1b and T2 as well as T1a and T3 the acid proton is located at the same oxygen site (O2) and (O1) and yields similar absorption energies (-125.3, -129.3) and (-148.8, -156.8) kJ mol^{-1}. Thus we expected similar activation energies for the same pairs of the T sites. No correlation was found instead. We believe this may be due to the position and the intrinsic basicity of the O_B site, dependent upon the Al location that strongly influences the stability of intermediate III. In other words, while the H-bonded complex involves only one framework O, the one with the proton, intermediates III and V have the admolecule interacting with two zeolite framework oxygens (labelled O_A and O_B in our reaction schemes), hence reactivity does not depend only on the feature of the acid site oxygen. T1a and T2 sites form $C_A - O_B$ bond at oxygen sites located at the 8-MR (O_4 and O_5) and hence induce larger steric repulsion, as noted by the shorter intermolecular C – O distance at TS $II^{\ddagger}$ (1.69 and 1.72 Å) increasing the activation barrier (50.3 and 72.4 kJ mol^{-1}) along with a higher endothermic reaction (39.1 and 59.6 kJ mol^{-1}). On the other hand, T1b and T3 sites with E_{act} values of ~ 24 kJ mol^{-1}, form the $C_A - O_B$ bond on the same oxygen site (O1), located at the 10-MR, which also exhibits a high basicity, facilitating the transformation to the point where the stability of intermediate I and III are comparable as the calculated reaction energy at T3 is 3.8 kJ mol^{-1} and becomes even more favourable at T1b (-5.7 kJ mol^{-1}). More importantly, the activation energies for forming intermediate III are directly related to the initial $C_A - O_B$ bond distance when acetaldehyde is adsorbed (**Figure 4-17**).The formation of intermediate III is easier at T1b, reflected by a closer intermolecular distance of the C – O bond distance (3.49 Å) than at T2 (4.14 Å).

FER	Si-O_A	Si-O_B	Al-O_A	Al-O_B	O_A-H_Z	H_Z-O_C	O_C-C_A	C_A-C_B	C_B-H_A	H_A-O_B	C_A-O_B	O_A-H_Z-O_C	O_C-C_A-O_B
T1a													
I	1.69	1.60	1.87	1.72	1.05	1.46	1.23	1.50			3.91	177.3	68.6
II‡	1.61	1.69	1.75	1.84	1.60	1.01	1.34	1.52			1.69	143.9	104.8
III	1.60	1.71	1.72	1.86	2.13	0.98	1.36	1.52	1.09	2.48	1.60	122.1	106.2
IV‡	1.62	1.61	1.80	1.74	2.79	1.00	1.29	1.41	1.25	1.40	3.21		
enol	1.69	1.62	1.87	1.72	4.31	0.97	1.34	1.35	1.88	1.02	3.29		
T1b													
I	1.69	1.60	1.85	1.71	1.03	1.50	1.23	1.49			3.49	168.1	73.4
II‡	1.64	1.66	1.77	1.82	1.40	1.06	1.31	1.51			1.79	150.2	103.4
III	1.61	1.69	1.72	1.87	2.11	0.98	1.36	1.51	1.09	2.67	1.58	124.8	106.9
IV‡	1.63	1.67	1.76	1.84	2.71	0.98	1.35	1.50	1.18	1.40	1.70		
enol	1.71	1.60	1.87	1.71	4.13	0.98	1.34	1.35	1.98	1.01	3.09		
T2													
I	1.69	1.59	1.87	1.70	1.03	1.55	1.23	1.49			4.14	163.5	70.8
II‡	1.62	1.67	1.75	1.87	1.80	0.99	1.33	1.51			1.72	136.6	113.1
III	1.60	1.68	1.72	1.89	2.47	0.98	1.34	1.51	1.09	2.95	1.64	105.4	107.1
IV‡	1.65	1.59	1.82	1.72	2.70	0.99	1.30	1.39	1.37	1.30	3.24		
enol	1.69	1.59	1.87	1.70	3.09	0.98	1.35	1.35	1.98	1.01	3.20		
T3													
I	1.68	1.61	1.84	1.73	1.05	1.45	1.23	1.49			3.61	172.6	68.3
II‡	1.63	1.65	1.77	1.81	1.40	1.06	1.30	1.51			1.87	157.4	69.3
III	1.60	1.69	1.71	1.88	2.47	0.98	1.36	1.52	1.09	2.38	1.56	119.6	101.7
IV‡	1.61	1.66	1.72	1.83	4.01	0.99	1.31	1.38	1.47	1.20	2.85		
enol	1.60	1.69	1.71	1.87	3.99	0.98	1.34	1.35	1.89	1.02	2.95		

Table 4-6 Geometrical parameters of the two-step enolisation mechanism of acetaldehyde at T sites in FER zeolite.

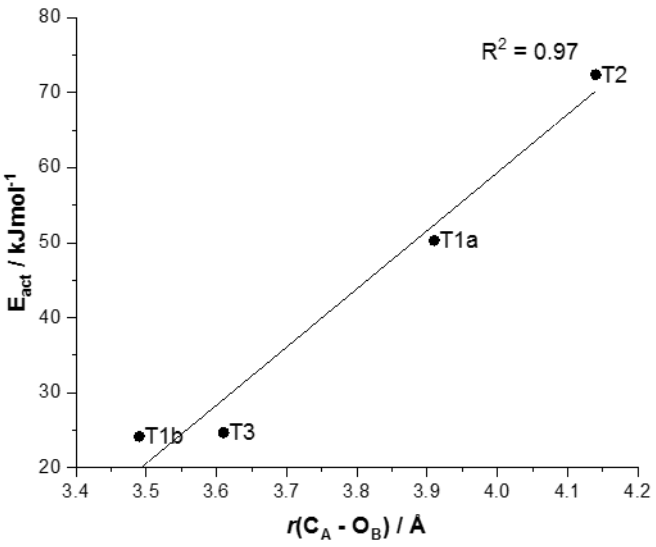

Figure 4-17 Activation energies directly related to $C_A - O_B$ bond lengths obtained intermediate I at T positions in FER zeolite.

At T1b, the reaction is exothermic due to an increase of ΔE_{disp} (-22.8 kJ mol^{-1}). In MOR, the formation of intermediate III is endothermic at all T sites even with the inclusion of dispersion correction (which is negligible).

The activation energies for the formation of adsorbed enol is dependent upon the stability of intermediate III with energy barriers being higher at T1b and T3 (111.6 and 84.6 kJ mol^{-1}), and significantly lower at T1a and T3 (63.8 and 40.4 kJ mol^{-1}). Here dispersion interactions affect the activation energies insignificantly at all T sites except at T1a, increasing the barrier energy considerably (ΔE_{disp} = 45.0 kJ mol). The enol formation is exothermic at T2 with an E_r value of -3.7 kJ mol^{-1} and becomes thermodynamically less favourable in the following order, T1a (33.6) > T1b (71.5) > T3 (71.7) kJ mol^{-1}.

Looking at the complete PES profile in **Figure 4-18**, the rate-determining step is TS IV‡ involving the proton transfer from the methyl group to form the adsorbed enol,

which is equivalent to this mechanism occurring in MOR. The only exception is at T2 where TS $II^{\ddagger}$ for formation of the $C_A - O_B$ bond is rate-limiting with an activation barrier of 72.4 kJ mol^{-1}.

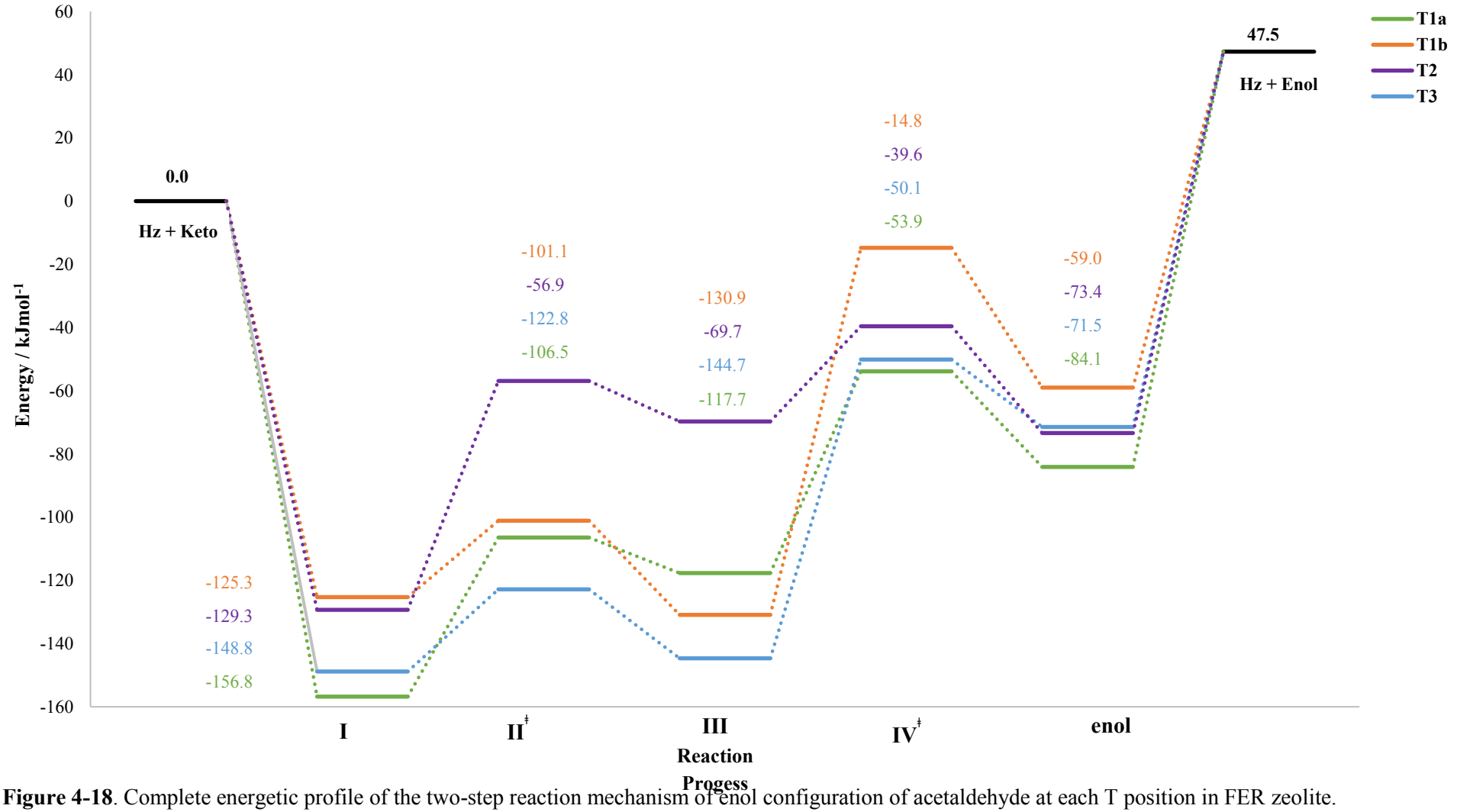

Figure 4-18. Complete energetic profile of the two-step reaction mechanism of enol configuration of acetaldehyde at each T position in FER zeolite.

4.3.4 One-step enolisation mechanism

Our intention at the start of the study was to characterise the enolisation mechanism of acetaldehyde involving the protonation of the carbonyl oxygen (O_C); instead of the intended product, the protonated form of acetaldehyde, we obtained intermediate III. Our attempt to form the enol structure was only possible when the C_B atom was deprotonated, with proton transfer from the methyl group being the rate-limiting step. As alternative mechanism, we now consider the keto-enol transformation of acetaldehyde at all T position in MOR and FER zeolites, starting from the H-bonded complex, intermediate I, and constraining the distance, $H_A - O_B$, between one of the hydrogen atoms of the methyl group and an oxygen site nearest neighbour to the Al dopant, as shown in **Figure 4-19**. This corresponds to direct (one-step) enolisation through cyclic 8-membered transition state that does not require complete proton transfer from the framework to the admolecule (which as we have seen in Chapter 3 does not yield a stable intermediate). This mechanism also avoids intramolecular H transfer within the admolecule, and takes place by protonation of a second framework O next to the Al site, O_B. This is the same oxygen that formed the $C_A - O_B$ bond in intermediate III of the two-step mechanism. Upon shortening the distance, $H_A - O_B$, C_B deprotonation occurs, and eventually we formed the enol product. The reaction process is endothermic at all T positions in both zeolites and consists concerted of a mechanism as shown in **Figure 4-20**. As the acetaldehyde molecule contains only one hydrogen bond acceptor, the transfer of H_A from the methyl group to the O_B site is partly compensated by a shift in the position of the H_Z proton towards the carbonyl oxygen. The movement of the two

protons (H_A and H_Z) is strongly coupled. A cyclic tautomerisation occurs with the formation of enol product and regeneration of the Brønsted site on a different oxygen site adjacent to Al dopant. This mechanism has been studied by Boefka *et al*. (Boekfa, *et al*., 2010) and Solans-Monfort *et al*. (Solans-Monfort, *et al.*, 2002), although they did not demonstrate that this coupling can only occur due to deprotonation of C_B atom.

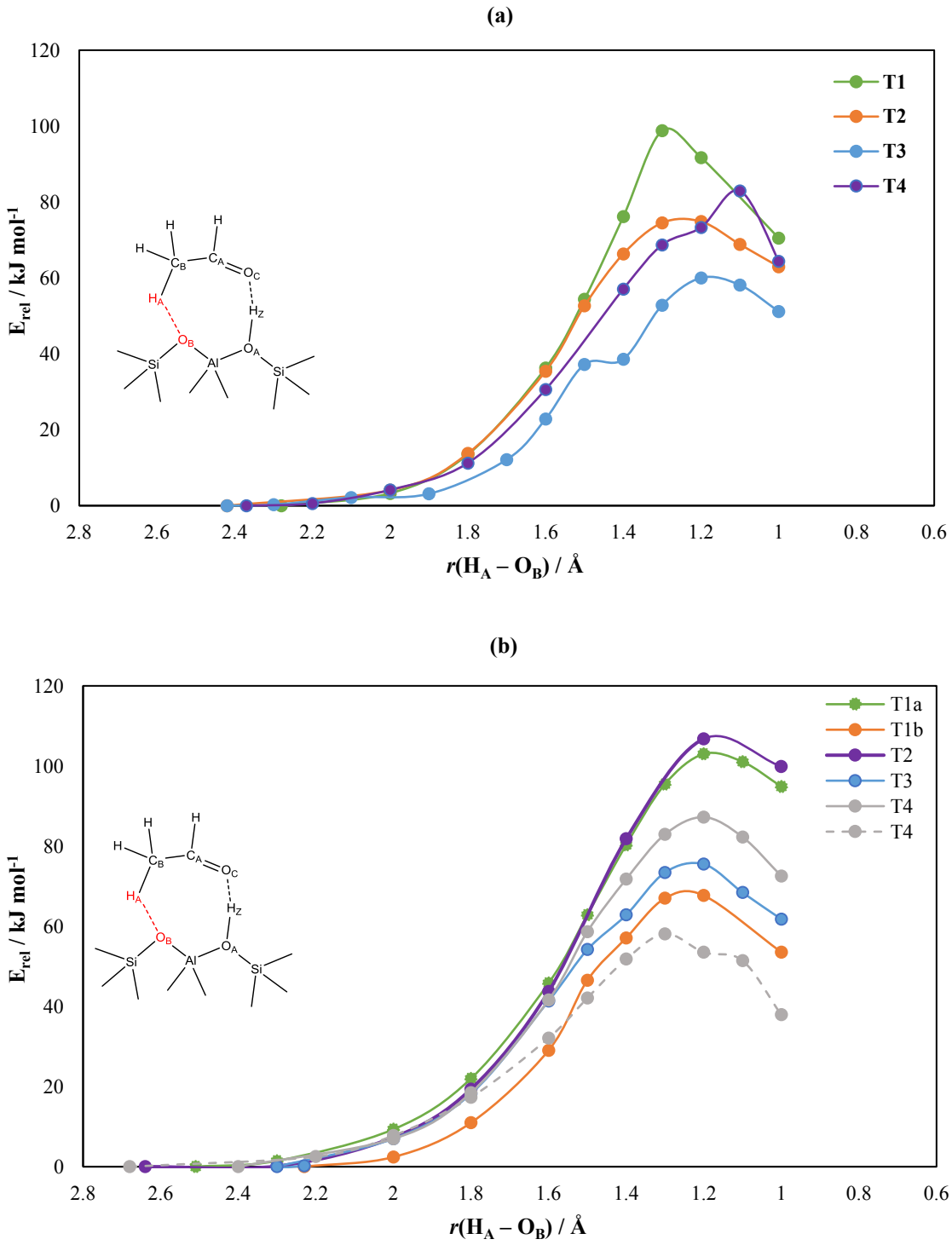

Figure 4-19 Internal energy profile of the reaction I ↔ enol by constraining the reaction coordinate, H_A – O_B, hydrogen atom of the methyl group of acetaldehyde and an oxygen site adjacent to Al dopant in which the proton is not bound in (a) MOR and (b) FER. The dashed line is the same reaction taking place where the formation of enol product is more favourable .

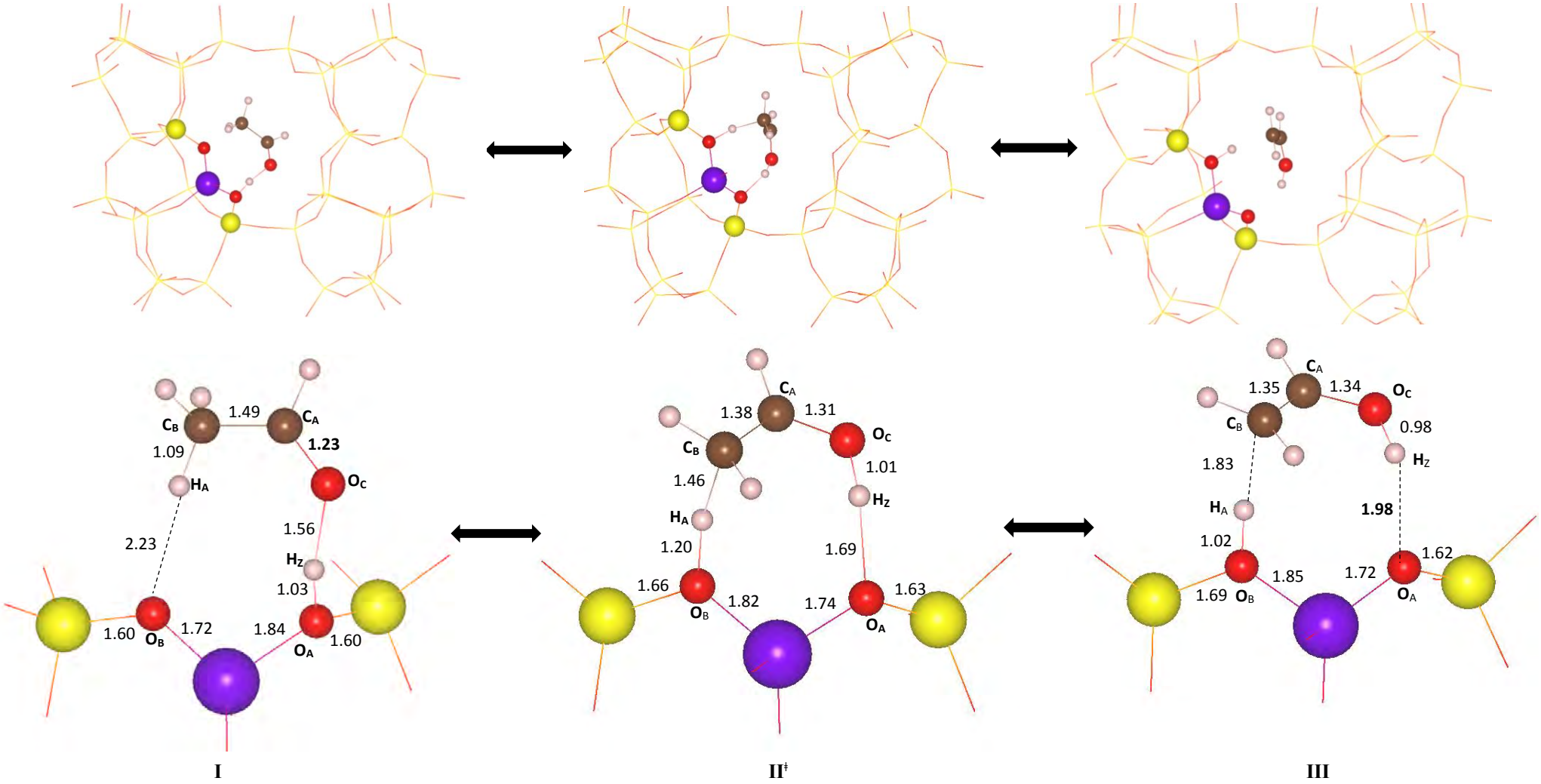

Figure 4-20 Optimized structures with geometrical parameters involving the concerted mechanism forming enol structure at T1b site in FER zeolite.

As shown in **Figure 4-20**, the geometrical structure of TS $II^{\ddagger}$ is similar to that of the adsorbed enol product, as expected for this endothermic reaction. At the transition state, the alcohol is nearly formed with the $H_Z - O_C$ bond distance of 1.03 Å while H_A lies somewhat midway between the C_B atom and the O_B site ($H_A - C_B$: 1.46 and $H_A - O_B$:1.20 Å). The carbonyl bond distance increases from 1.23 to 1.31 Å, shifting its double bond character to $C_A - C_B$, with the intermolecular C-C distance reducing from 1.49 to 1.38 Å. The zeolite presents a small reorganisation as well. The main changes correspond to $Al - O_A$ and $Al - O_B$, those related to the catalytic process. In FER at T1b site, $Al - O_A$ distance decreases 1.85 to 1.74 Å while the $Al - O_B$ distance increases from 1.72 to 1.82 Å at the transition state. Consequently, in the enol configuration the two distances are similar. The same process occurs at all T sites in both zeolites and the geometrical parameters are illustrated in **Table 4-7** and **4-8.**

MOR		Si – O_A	Si – O_B	Al – O_A	Al – O_B	O_A – H_Z	H_Z – O_C	O_C – C_A	C_A – C_B	C_B – H_A	H_A – O_B	O_A – H_Z – O_C	Al – O_A – Si	Al – O_B – Si
T1	I	1.69	1.60	1.86	1.72	1.05	1.47	1.23	1.49	1.09	2.28	158.1	125.5	132.2
	VII‡	1.69	1.64	1.83	1.77	1.11	1.34	1.25	1.44	1.25	1.30	158.0	124.0	129.3
	III	1.62	1.69	1.73	1.86	2.44	0.97	1.34	1.35	1.89	1.00	108.1	125.0	131.9
T2	I	1.68	1.60	1.86	1.71	1.05	1.46	1.23	1.50	1.09	2.42	174.5	134.3	141.2
	VII‡	1.62	1.67	1.75	1.82	1.74	1.00	1.31	1.38	1.49	1.19	159.3	135.5	132.4
	III	1.62?	1.70	1.73	1.87	1.89	0.98	1.34	1.35	1.94	0.99	155.9	137.0	131.6
T3	I	1.69	1.60	1.87	1.72	1.02	1.54	1.23	1.48	1.09	2.97	121.8	132.3	150.2
	VII‡	1.63	1.65	1.77	1.81	1.52	1.03	1.29	1.38	1.35	1.30	124.9	128.9	164.4
	III	1.61	1.69	1.72	1.87	2.47	0.98	1.38	1.33	3.86	1.03	123.0	125.6	164.5
T3	I	1.71	1.59	1.88	1.71	1.02	1.68	1.22	1.50	1.09	2.42	125.0	120.2	139.8
	VII‡	1.63	1.66	1.76	1.82	1.56	1.02	1.30	1.38	1.44	1.20	172.0	121.2	128.1
	III	1.63	1.69	1.74	1.86	1.67	0.99	1.33	1.35	1.78	1.03	170.3	122.1	129.3
T4	I	1.68	1.60	1.86	1.71	1.06	1.44	1.23	1.50	1.10	2.37	131.1	138.7	171.0
	VII‡	1.62	1.60	1.75	1.82	1.64	1.01	1.31	1.38	1.47	1.19	134.6	131.6	165.8
	III	1.62	1.69	1.73	1.86	1.77	0.99	1.34	1.36	1.86	1.03	135.2	131.2	162.2

Table 4-7 Geometrical parameters of the intermediates and transition states at all T positions in MOR zeolite involved in the one-step enolisation mechanism.

FER		Si – O_A	Si – O_B	Al – O_A	Al – O_B	O_A – H_Z	H_Z – O_C	O_C – C_A	C_A – C_B	C_B – H_A	H_A – O_B	O_A – H_Z – O_C	Al – O_A – Si	Al – O_B – Si
T1a	I	1.68	1.60	1.84	1.71	1.05	1.43	1.23	1.50	1.10	2.51	175.3	122.7	150.0
	VII‡	1.63	1.67	1.76	1.82	1.51	1.02	1.30	1.39	1.47	1.20	168.4	122.9	139.2
	III	1.62	1.71	1.73	1.87	1.64	0.99	1.33	1.35	2.00	1.00	165.7	121.8	137.5
T1b	I	1.70	1.60	1.84	1.72	1.03	1.56	1.23	1.49	1.09	2.23	163.8	124.1	124.2
	VII‡	1.63	1.66	1.74	1.82	1.69	1.01	1.31	1.38	1.46	1.20	155.8	124.8	124.5
	III	1.62	1.69	1.72	1.86	1.95	0.98	1.34	1.35	1.86	1.00	143.0	125.6	124.9
		1.62	1.69	1.72	1.85	1.98	0.98	1.34	1.35	1.83	1.02	141.2	125.8	126.1
T2	I	1.68	1.58	1.85	1.70	1.05	1.47	1.23	1.50	1.09	2.64	171.4	124.8	162.9
	VII#	1.63	1.66	1.76	1.83	1.55	1.02	1.30	1.39	1.44	1.20	172.1	122.3	130.1
	III	1.62	1.69	1.74	1.88	1.71	0.99	1.33	1.36	1.86	1.03	168.3	122.3	131.5
T3	I	1.69	1.61	1.85	1.73	1.04	1.49	1.23	1.50	1.09	2.43	172.7	130.5	140.0
	VII‡	1.63	1.67	1.76	1.84	1.63	1.01	1.31	1.38	1.47	1.20	170.0	130.7	131.5
	III	1.62	1.70	1.73	1.89	1.76	0.99	1.34	1.35	1.93	1.00	166.5	131.0	131.5
T4	I	1.68	1.60	1.85	1.71	1.04	1.48	1.23	1.49	1.09	2.41	166.3	133.6	148.0
	VII‡	1.63	1.66	1.76	1.82	1.77	1.00	1.31	1.38	1.47	1.20	167.5	129.5	145.4
	III	1.59	1.69	1.71	1.86	3.88	0.98	1.35	1.35	1.88	1.01	120.8	141.6	135.2
T4	I	1.71	1.62	1.85	1.70	1.08	1.39	1.24	1.49	1.10	2.68	172.2	168.7	173.5
	VII‡	1.63	1.67	1.75	1.80	1.64	1.01	1.30	1.38	1.46	1.20	132.2	134.4	137.9
	III	1.62	1.70	1.73	1.84	1.74	0.99	1.33	1.35	1.79	1.03	126.4	127.5	126.9

Table 4-8 Geometrical parameters of the intermediates and transition states at all T positions in FER zeolite involved in the one-step enolisation mechanism.

The activation and reaction energies are listed in **Table 4-9**, along with the dispersion and electronic contributions.

	Reactions	O_A / O_B	E_r	ΔE_{elec}	ΔE_{disp}	E_{act} *(forward)*	ΔE_{elec}	ΔE_{disp}	E_a *(reverse)*
MOR									
T1	*Z + Keto ↔ I**	*O7 / O3*	*-145.9*	*-68.3*	*-77.6*				
	I ↔ III		70.5	71.0	-0.5	88.1	102.5	-14.4	17.7
T2	*Z + Keto ↔ I**	*O3 / O2*	*-139.9*	*-57.6*	*-82.3*				
	I ↔ III		63.0	74.31	-11.4	76.2	85.3	-9.1	13.2
T3	*Z + Keto ↔ I**	*O1 / O9*	*-114.7*	*48.5*	*-163.2*				
	I ↔ III		51.2	33.90	17.3	60.0	41.6	18.4	8.9
T4	*Z + Keto ↔ I**	*O2 / O10*	*-155.2*	*-65.2*	*-90.0*				
	I ↔ III		67.0	66.8	-2.5	82.6	89.3	-6.7	15.6
FER									
T1a	*Z + Keto ↔ I**	*O1 / O4*	*-156.8*	*-59.1*	*-97.2*				
	I ↔ III		*94.9*	*99.3*	*-4.4*	103.0	108.4	-5.4	8.1
T1b	*Z + Keto ↔ I**	*O2 / O1*	*-128.6*	*-17.9*	*-110.8*				
	I ↔ III		53.5	46.9	6.7	67.7	61.6	6.1	14.2
T2	*Z + Keto ↔ I**	*O2 / O5*	-135.5	-44.6	-90.9				
	I ↔ III		99.9	97.3	2.6	106.8	104.3	2.5	6.9
T3	*Z + Keto ↔ I**	*O1 / O1*	*-148.8*	*-31.6*	*-117.2*				
	I ↔ III		61.5	57.9	3.6	75.3	71.5	3.7	13.7
T4	*Z + Keto ↔ I**	*O6 / O6*	*-153.4*	*-57.6*	*-95.8*				
	I ↔ III		72.5	68.2	4.4	87.2	89.1	-1.9	14.7
T4	*Z + Keto ↔ I**	*O6 / O7*	*-161.0*	*-75.8*	*-85.3*				
	I ↔ III		37.9	94.2	-56.3	58.1	67.4	-9.3	20.2

Table 4-9 Calculated reaction (E_r) and activation (E_{act}) energies for the forward and reverse reaction pathways considered for the one-step enolisation mechanism of acetaldehyde at all T sites in MOR and FER. Note that (*) indicates the adsorption state (Eads) of zeolite-adsorbate system calculated relative to them in the gas phase and the calculated E_{elec} and E_{disp} are the components of the respective (E_{ads}). Energy displayed in kJ mol^{-1}.

We found an excellent correlation between E_{ads} and E_{act} (**Figure 4-21**) for both total and electronic – only (without dispersion) energies. The dispersion interaction decreases the reaction barriers by ~ 10 – 20 kJ mol^{-1} for the T sites located in the larger pores. However, at T3 the inclusion of dispersion effects raises the barrier by ~ 20 kJ mol^{-1}. The E_{act} are similar in the larger pores (~ 76 to 88 kJ mol^{-1}) as the steric effect are similar, and reduced at T3 with an energy barrier of 60.0 kJ mol^{-1}, due to intermediate I being least stabilised in the smaller pores, with an adsorption energy value of -114.8 kJ mol^{-1}.

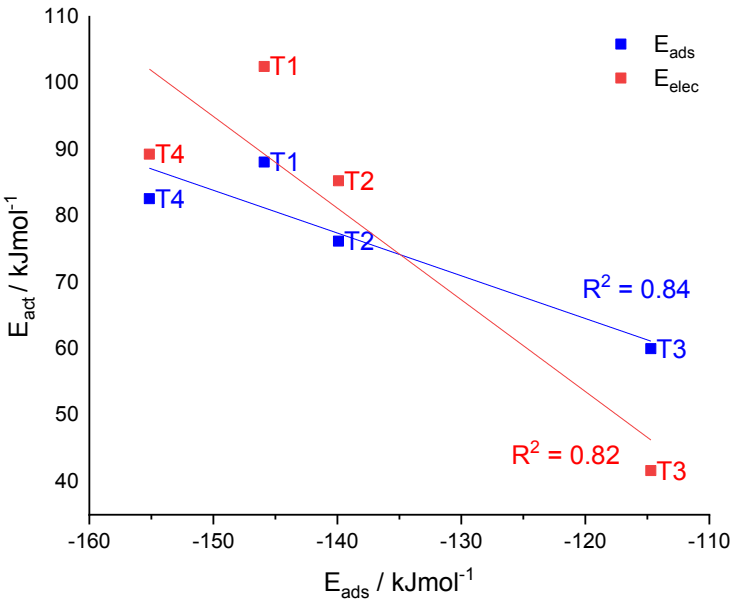

Figure 4-21 Scaling relations between adsorption energies and activation barriers of enol transformation. The activation barriers with (E_{act}) and without (ΔE_{elec}) dispersion corrections are indicated in blue and red.

Imaginary frequencies corresponding to the transition states are shown in **Table 4-10.** At $TS^{‡}$ the $C_B - H_A$ bond breaking occurs which explains the higher frequency of the imaginary modes obtained ~ (-840 to -980.9 cm^{-1}).

MOR	Imaginary Frequency (cm^{-1})	
T1	-841.6	-87.5
T2	-821.0	
T3	-980.9	-207.4
T4	-879.6	-73.9

Table 4-10 Vibrational frequencies obtained at the $TS^{‡}$ for the one-step concerted enolisation mechanism at the T sites in the MOR zeolite.

We found no correlation between E_{ads} and E_{act} in FER amongst the T sites, either or and without dispersion correction, similar to what we observed in the two-step enolisation mechanism in the formation of intermediate III. This feature highlights the specificity of shape selectivity imposed by the framework. T1a and T2 have similar activation barriers (103.0 and 106.8 kJ mol^{-1}); despite the higher stability of intermediate I at T1a (-156.8 kJ mol^{-1}) compared to T2 (-128.6 kJ mol^{-1}), the H_A atom of the methyl group is transferred to the same oxygen site, O2, located at the 8-MR window, hindering the transformation process. At T1b and T3, we obtained lower activation energies (67.7 kJ mol^{-1}) and (75.3 kJ mol^{-1}) even though intermediate I is more stabilised at T3 (-148.8 kJ mol^{-1}) than T1b (-128.6 kJ mol^{-1}). As already discussed for the two–step mechanism, the involvement of 2 framework oxygen in the one–step reaction path does not allow similar correlations to be observed with the properties of a single O site. The $H_A - O_B$ bond is formed at O1 site, located at the 10-MR, facilitating the enolisation step and acquires a stronger basicity compared to the other oxygen sites. More importantly, the activation energies are related to the initial $H_A - O_B$ bond distance when acetaldehyde is

adsorbed (**Figure 4-21**). The formation of the enol form is easier at T1b, reflected by a closer intermolecular distance of the H_A – O_B bond distance (2.23 Å) than at T2 (2.64 Å) when acetaldehyde is adsorbed.

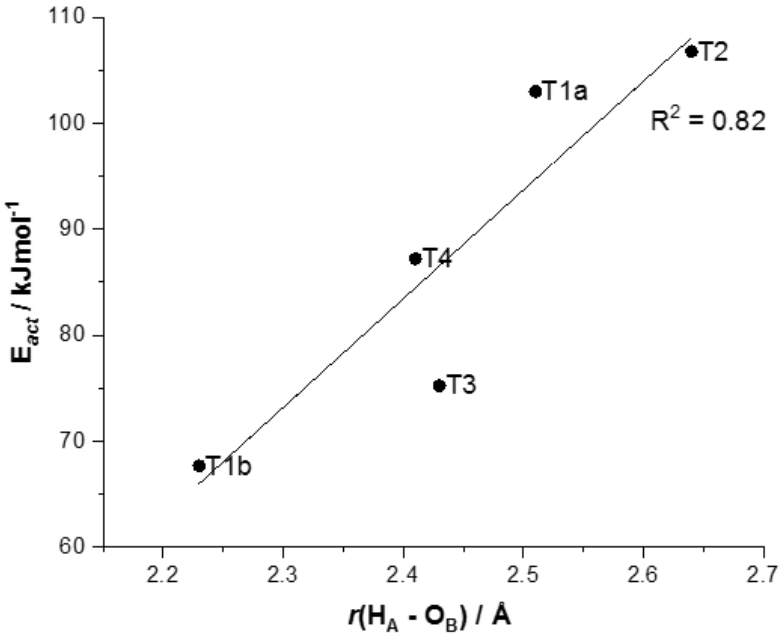

Figure 4-22 Activation energies directly related to C_A – O_B bond lengths obtained intermediate I at T positions in FER.

We were able to form the adsorbed enol at T4 position in FER using this concerted mechanism with an activation barrier of 87.2 kJ mol^{-1} and a higher endothermic reaction energy of 72.5 kJ mol^{-1}. The adsorbed enol could also be formed by intermolecular H transfer involving 2 admolecules that can interact with each other along the FER cavity because of our PBC modelling approach (**Figure 4-23**). The H_A atom from the methyl group of adsorbed keto form is able to interact with an oxygen atom nearest neighbour to Al dopant in the next unit cell with an initial bond distance of 2.68 Å. This reduces the activation barrier to 58.1 kJ mol^{-1} with a higher stability of adsorbed enol (E_r = 37.9 kJ mol^{-1}). Here the dispersion stabilization is very strong; it decreases the reaction energy by 56.3 kJ mol^{-1}. In **Figure 4-23,** the adsorbed enol is forming a H-bond (1.74 Å) with the oxygen site in the next repeating unit cell.

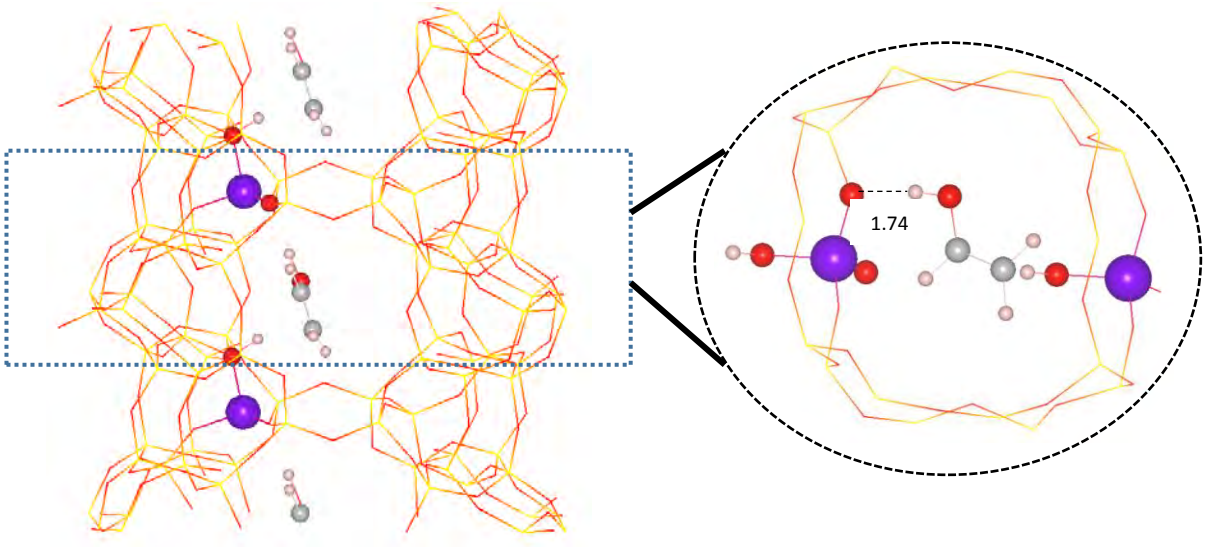

Figure 4-23 Optimized structure of adsorbed enol at T4 in FER cavity in top view with unit cell dotted line) illustrated. The adsorbed enol is formed with the H_A transferred to an oxygen atom nearest neighbour to Al dopant in next unit cell.

A complete PES profile of this concerted mechanism shown in **Figure 4-24**. Similar to the two-step mechanism, the adsorbed enol is unstable as the reverse energy barrier to transform adsorbed enol to adsorbed keto is facile (7 – 20 kJ mol^{-1}).

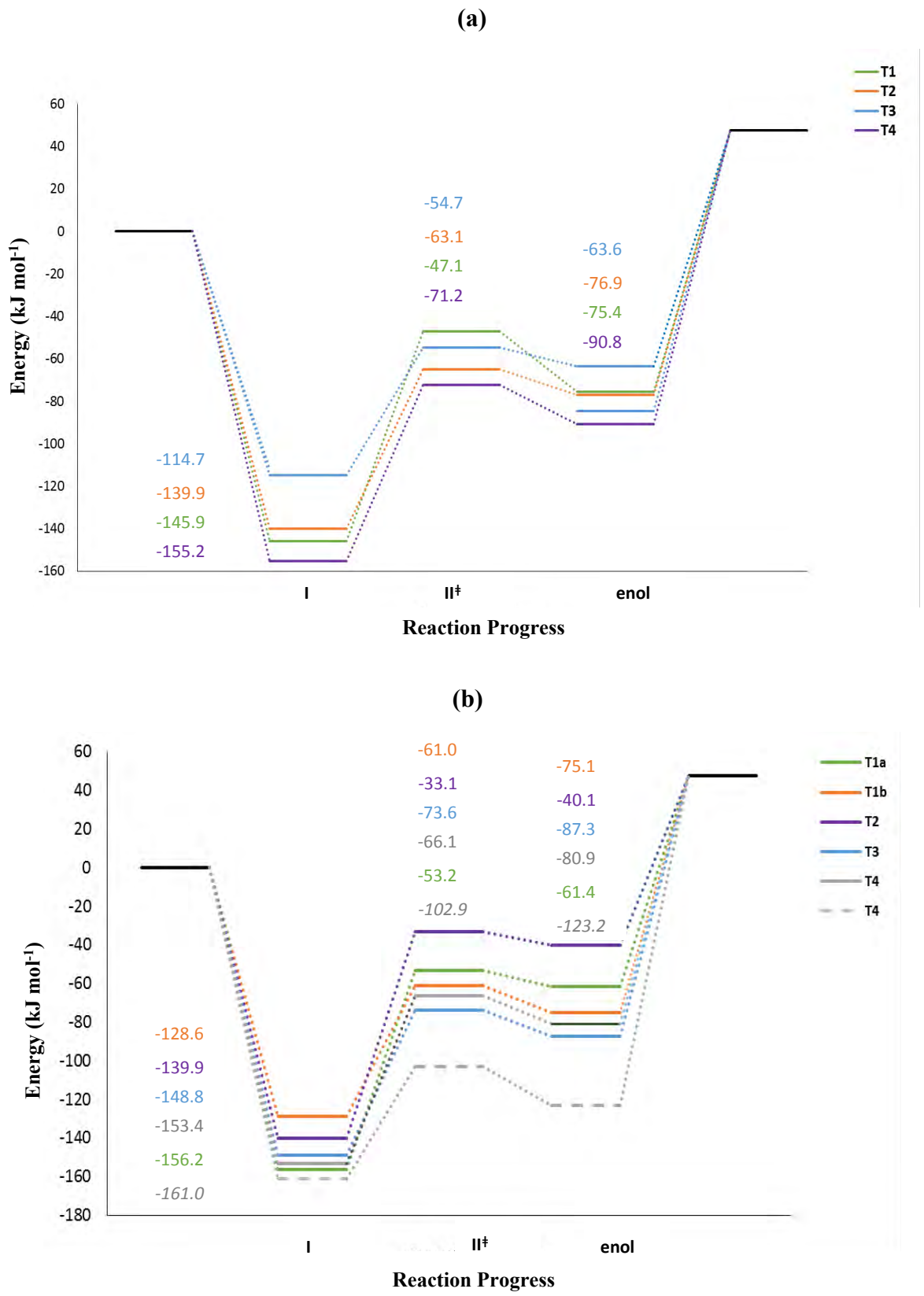

Figure 4-24 Complete PES profile of the one-step concerted mechanism of enolisation in (a) MOR and (b) FER. The dashed line at T4 position in FER is the reaction occurring in the next repeating unit cell.

From our results, the essential difference between the two mechanisms is that formation of intermediate III containing the C-O bond is in general energetically favourable compared to the formation of adsorbed enol. The activation energies to form the enol product are similar in MOR using both mechanisms (6 – 94 kJ mol^{-1}). In FER the formation of intermediate III reduces the energy barrier in order to form the enol product at the T sites, T1a (63.8 kJ mol^{-1}) and T2 (4.3 kJ mol^{-1}). Hence, the formation of adsorbed enol at T1a and T2 is more favourable using the two-step concerted mechanism. The stability of intermediate I and III is similar at T1b and T3, hence the formation of adsorbed enol becomes less favourable here, E_{act} = 116.1 and 84.6 kJ mol^{-1}. Thus, the formation of enol at T1b and T3 is more favourable using the one-step mechanism, without the need of intermediate III to be formed. Although the stability of adsorbed enol is higher when formed via intermediate III as the reaction energies are similar or lower at each T site in both zeolites compared to when using the one-step mechanism.

4.4 Conclusion

In summary, we have carried out a series of constrained optimizations using periodic DFT in order to understand the keto-enol tautomeric mechanism in both gas phase and zeolites. For the gas-phase intramolecular mechanism we show that no other H-transfer reactions can compete with the simple keto–enol tautomerism. In MOR and FER, proton transfer from the BA site does not form the intended product, adsorbed enol; it rather induces the formation of intermediate III containing C-O bond with a framework oxygen (O_B) that stabilizes the protonated form of

acetaldehyde. This intermediate was observed at all T positions in both zeolites, expect at the T4 position located in the FER cavity due to steric repulsion. We obtained similar activation barriers to form intermediate III at all the T sites in MOR. In FER, formation of intermediate III is dependent upon the local geometry of the BA site: it is favourable at T1b and T3 and unfavourable at T1a and T2. This is mainly due to the position and basicity of the O_B site influencing the energetics. From these results, the proton transfer is a consequence of a cooperation between the acid site and its total environment acting on the molecular adsorbate. It is the complex interplay of the adsorbate and the zeolite environment that tunes the acidity of the system, rather than simply the intrinsic property related to the composition and structure of the molecular sieve.

The formation of intermediate III provided an alternate route to form the adsorbed enol form in a two-step concerted mechanism. The calculations reveal that C-β deprotonation is the kinetic bottleneck for enol formation. At T4 in MOR, the adsorbed enol is most stabilized by dispersion effects as the enol product is formed in the SP. For the remaining T sites in both zeolites, the stability of adsorbed enol is dependent upon the stability of intermediate III.

The keto-enol tautomerisation was then investigated through a one-step concerted mechanism again requiring via C-β deprotonation. Using this one-step concerted mechanism, we were able to form adsorbed enol in the FER cavity at T4. The correlation between zeolite acidity and catalytic activity was explored. In MOR, we found adsorption and activation energies to correlate well. This correlation was not found in FER, due to the presence of stronger steric repulsion and shape selectivity imposed by the framework.

Chapter 5

Keto-enol tautomerism of acetaldehyde in the presence of solvent molecules

5.1 Introduction

During a catalytic transformation, the substrate molecule is often accompanied by the presence of other chemical species. One example is water, which is a by-product of the aldol condensation, but other oxygenated organic compounds such as methanol are often present in the reaction environment. They have similar acid/base behaviour to acetaldehyde and acetone; understanding their effect on reaction energetics is therefore very important.

The keto-enol tautomerization of acetaldehyde and acetone as molecules studied in isolated gas phase is endothermic and has a very high activation barrier of 284 – 295 kJ mol^{-1} (Rodriguez-Santiago, *et al*., 2001, Suenobu, *et al*., 1999). In solvent-assisted systems, the presence of water molecules can reduce the energy barrier to 140 – 170 kJ mol^{-1}. The catalytic effect of the solvent molecules is due to the formation of H-bonds that contribute to stabilize the transition state and to a smaller geometry distortion of acetaldehyde along the process.

The effect of water loading on the acidity of BA sites in zeolites is well known (Sauer *et al*., 1994). To our knowledge, no previous computational studies have investigated the role of the solvent molecules on the keto-enol

tautomerization of aldehydes or ketones. In this chapter, we present an in-depth mechanism of keto-enol interconversion of acetaldehyde in FER zeolite in the presence of a water or methanol molecule. Due to the participation of these additional molecules, we studied the possible alternative pathways to establish whether these solvent molecules enhance or suppress the catalytic reaction. Since water and methanol can act as both proton donors and acceptors, our results highlight the crucial role of the H-bonded network and demonstrate that the C-β deprotonation remains the kinetic bottleneck. The computational details are noted in Chapter 4.

5.2 Results and Discussion

5.2.1 Keto-enol tautomerization of acetaldehyde assisted by a solvent molecule in gas phase

5.3.1.1 Water

We start by considering the keto-enol equilibrium in the gas phase. The reaction considered is displayed in **Figure 5-1**, when the water molecule acts a proton shuttle between methyl and carboxyl group of acetaldehyde, by accepting the methyl proton H_A and donating proton H_S to the CO group. This reaction profile has been studied by constraining the r(H_A –O_S), bond distance between a hydrogen atom from the methyl group and the oxygen atom of water molecule. The internal energy profile and the optimized structures and transition states are shown in **Figure 5-1**. The presence of a water molecule leads to two stable adducts: the

the hydrated keto and the hydrated enol form. For the keto form, the water molecule interacts with the hydrogen atom of the methyl group as a proton acceptor ($H_A - O_S$), and with the carbonylic oxygen as proton donor ($H_S - O_C$). For the enol isomer, the water molecule interacts mainly with the OH group of the vinyl alcohol ($H_S - O_S$: 1.80 Å), as a proton acceptor. There is also an additional weaker H-bond interaction between the water molecule and a H atom from the CH_2 group (2.58 Å). Both intermediates show a similar interaction energy with water (keto – H_2O : 43.1 kJ mol^{-1} and enol – H_2O: 43.7 kJ mol^{-1}) and so the reaction energy for the transformation is similar (43.1 kJ mol^{-1}), as the one obtained for the isolatedacetaldehyde (47.5 kJ mol^{-1}). However, the calculated energy barrier of, 149.6 kJ mol^{-1}, is significantly smaller than that of the uncatalyzed process (305.6 kJ mol^{-1}). The catalysis of such tautomeric processes by solvent molecules has been previously studied (Chiang, *et al*., 1989, Kaweetirawatt, *et al*., 2012, Rodriguez-Santiago, *et al*., 2001, Tapuhi and Jencks, 1982), and is attributed to smaller distortion of CH_3 – COH in the transition state. In the uncatalyzed process, the CCO angle of acetaldehyde suffers a larger distortion in the four-centered transition state than in the presence of a water molecule via a six-centered transition state, making the process less strained. The transition state in the presence of a water molecule presents two short H-bonds that contribute to stabilize the transition state, which essentially means that two protons are transferred simultaneously creating a concerted mechanism.

(a)

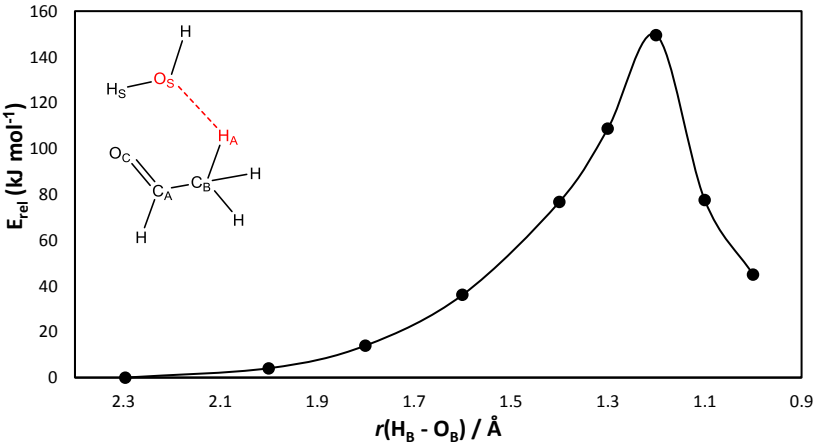

(b)

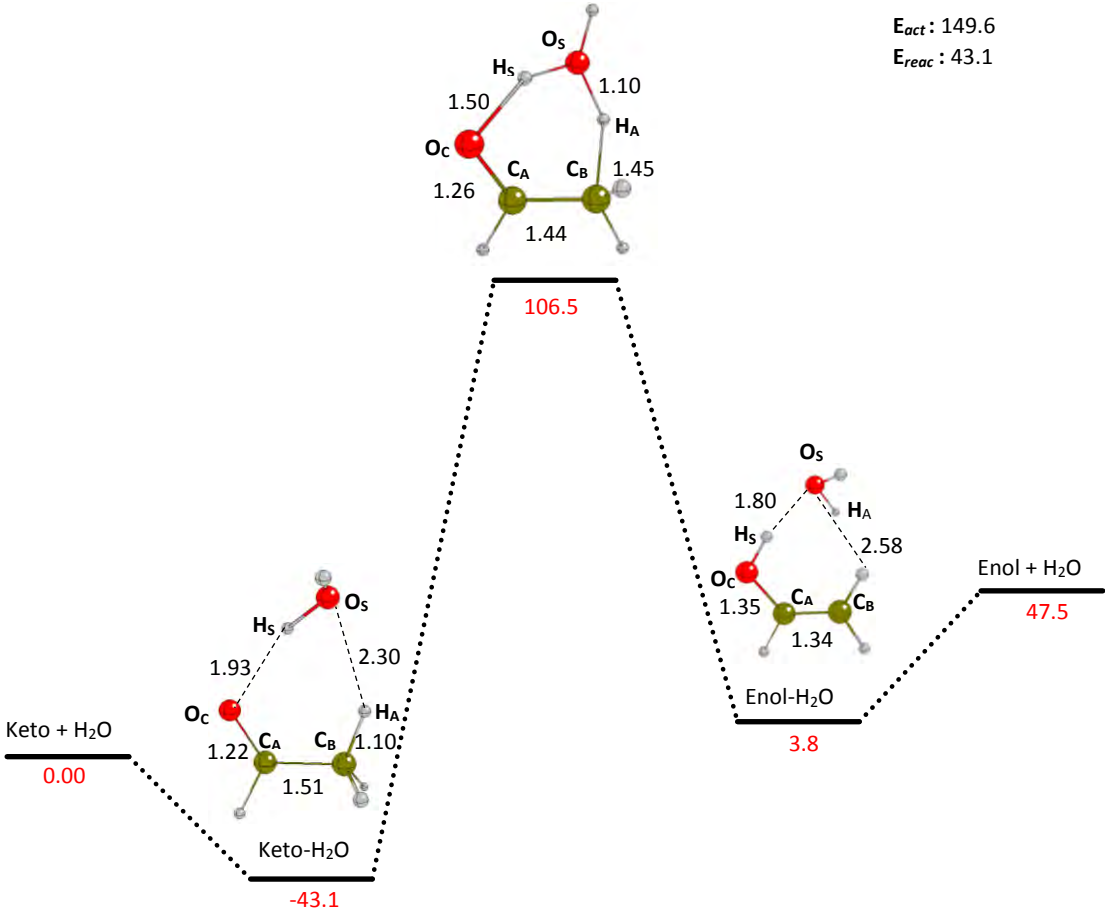

Figure 5-1 **(a)** Internal energy profile of keto-enol tautomerism in the presence of a single water molecule in gas phase by constraining the reaction coordinate, H_A – O_S, hydrogen atom of the methyl group of acetaldehyde and an oxygen atom of water. **(b)** PES profile and geometrical parameters. Bond distances are given is Å.

Starting from the keto form, we also constrained the bond, $r(H_s - O_C)$, between the hydrogen from the water molecule and carbonyl oxygen of acetaldehyde and obtained the same profile as **Figure 5-1**.

5.2.1.2 Methanol

In the presence of a methanol molecule, we constrained the reaction coordinate, $r(H_A - O_S)$, i.e. the distance between the hydrogen atom of the methyl group of acetaldehyde and the oxygen atom of methanol. The energy profile and geometrical structures are shown in **Figure 5-2**. The reaction takes place through a concerted mechanism comparable to that described in the presence of a water molecule. The keto and enol adducts with CH_3OH have similar energy (keto – CH_3OH : -40.9 kJ mol^{-1} and enol – CH_3OH : -45.2 kJ mol^{-1}); the reaction energy for the process does not change in presence of a methanol molecule (45.2 kJ mol^{-1}), but the activation barrier is lower (136.0 kJ mol^{-1}) in methanol than in the water (149.6 kJ mol^{-1}).

(a)

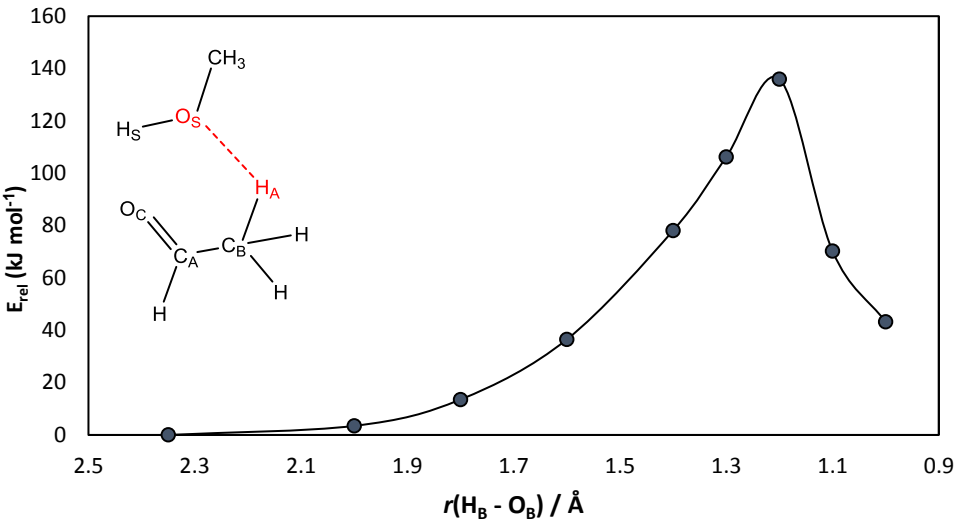

(b)

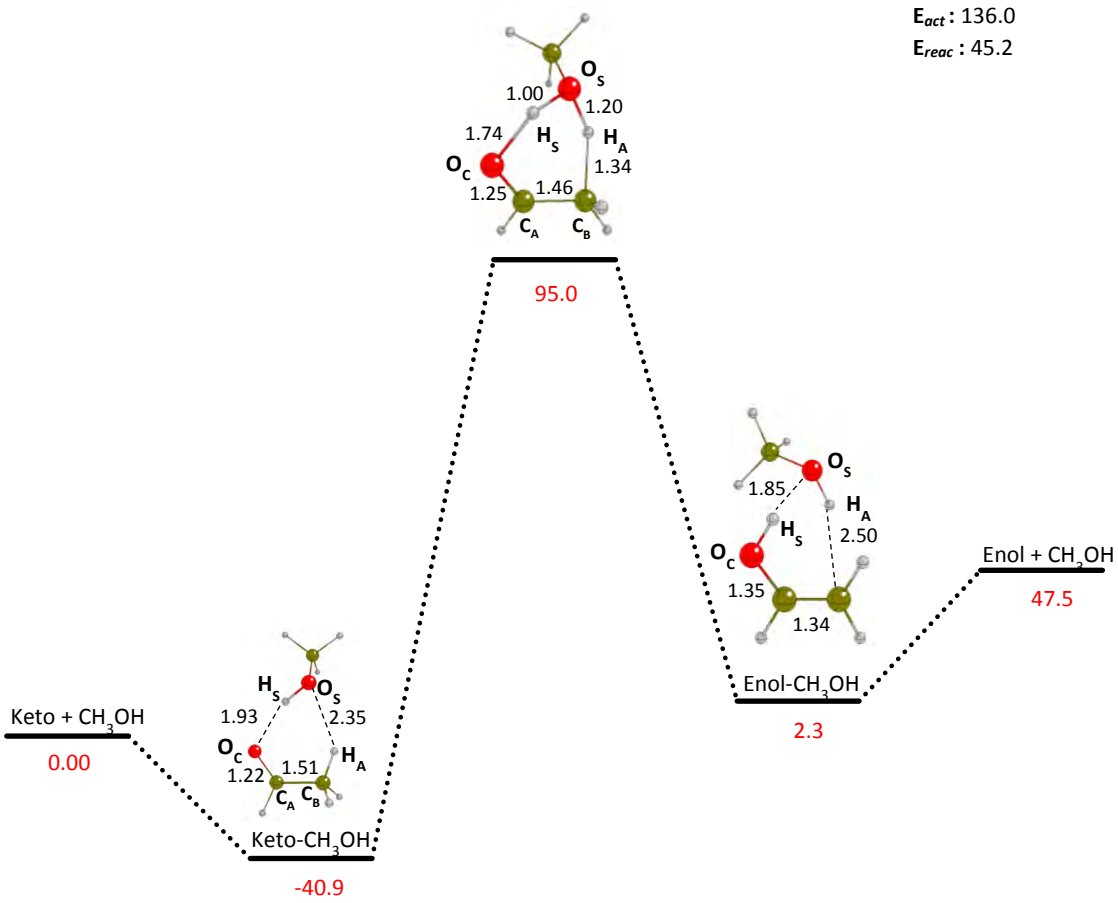

Figure 5-2 (a) Internal energy profile of keto-enol tautomerism in the presence of a single methanol molecule in gas phase by constraining the reaction coordinate, H_A – O_S, hydrogen atom of the methyl group of acetaldehyde and an oxygen atom of water. **(b)** PES profile and geometrical parameters. Bond distances are given is Á.

From the keto form, we also constrained the reaction coordinate, $r(H_S - O_C)$, the distance between the hydrogen from the water molecule and carbonyl oxygen of acetaldehyde, and the energy profile and geometrical structures are shown in **Appendix: Figure 8-4**. Instead of forming enol – CH_3OH, we formed formaldehyde and ethanol. Although the computed activation barrier is higher (171.0 kJ mol^{-1}). Hence for the keto-enol tautomerisation of acetaldehyde to occur in the presence of a methanol molecule, C-β deprotonation proves tobe the kinetic bottleneck.

5.2.2 Keto-enol tautomerization of acetaldehyde assisted by a solvent molecule in zeolites

We studied the presence of a single solvent molecule, water or methanol. In the initial configuration, we generated the solvent admolecule interacting with a previously adsorbed H-bonded acetaldehyde molecule at the Brønsted site. We chose to study this with Al dopant at T3 position in the larger pores of FER due to its high stability as an isolated acid site as well as the higher stability of the adsorbed enol form compared to the remaining T sites. The stable configuration is shown in **Figure 5-3**. The water or methanol molecule locates between the methyl group of acetaldehyde and the O_B framework oxygen with which it forms an H-bond. Acetaldehyde is not displaced by water or methanol and stays H-bonded to the BA site. In addition, the solvent molecule does not enhance the basicity of the proton acceptor acetaldehyde molecule as the hydroxyl group remains bound to the BA site. More importantly, the length of the H-bond with and without a solvent molecule present is identical (1.45 Å).

The keto-enol tautomerization of acetaldehyde in the presence of a single water or

methanol molecule was studied, and the reaction mechanism is shown in **Figure 5-3**. In Chapter 4, we concluded that the C-β deprotonation is the rate – limiting step for enolisation to occur, and hence we investigated in detail this step of the overall mechanism. To this goal, we constrained the distance, $r(H_A - O_S)$ between the hydrogen atom from the methyl group and the oxygen atom of the solvent molecule. The energy profiles are shown in **Figure 5-4**. Enolisation follows a stepwise mechanism illustrated in **Figure 5-3**. The leaving proton (H_A) from the methyl group leads to the formation of CH_2COH^- with the negative charge residing on the keto group by shifting the double bond to the carbanion side, forming an enolate anion. The negative charge localised around the enolate group facilitates the proton transfer (H_Z) from the BA site, and tautomeric transformation is completed. This also induces a zeolite rearrangement and the oxygen atom nearest neighbour to the Al dopant (O_B) accepts a proton (H_S) from the protonated water/methanol, recreating the solvent molecule and BA site on a different oxygen site. The water/methanol molecule demonstrates its catalytic function in the interconversion and emphasizes the specific role of hydrogen bonding.

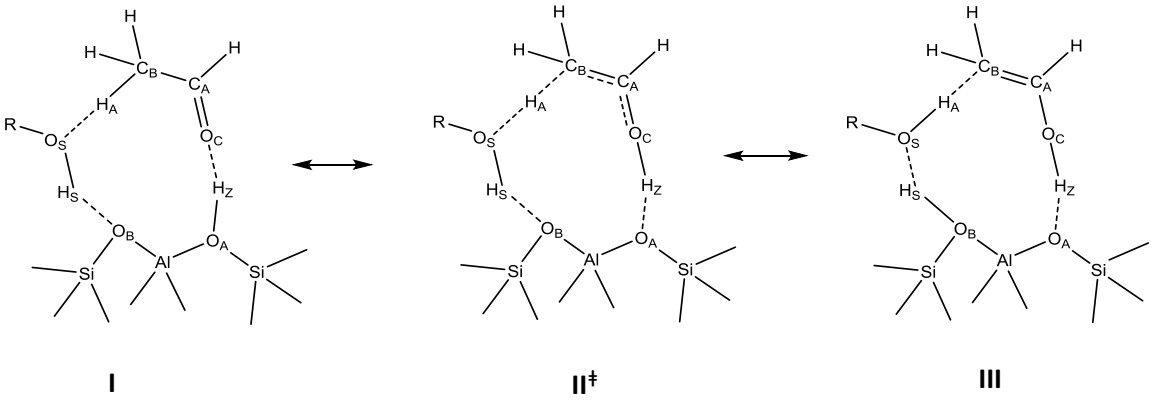

Figure 5-3 Reaction mechanism of keto-enol tautomerization of acetaldehyde adsorbed in zeolites in the presence of a single solvent molecule (water or methanol). R = H, CH_3.

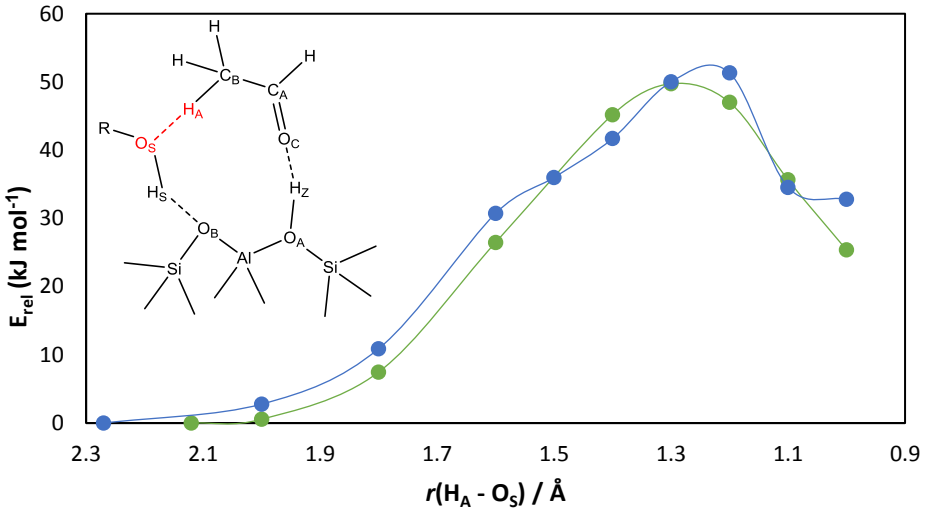

Figure 5-4 Internal energy profile of the keto-enol tautomerism at T3 position in FER zeolite. Data points in blue: water and in green: methanol.

The geometrical structures are shown in **Figure 5-5.**

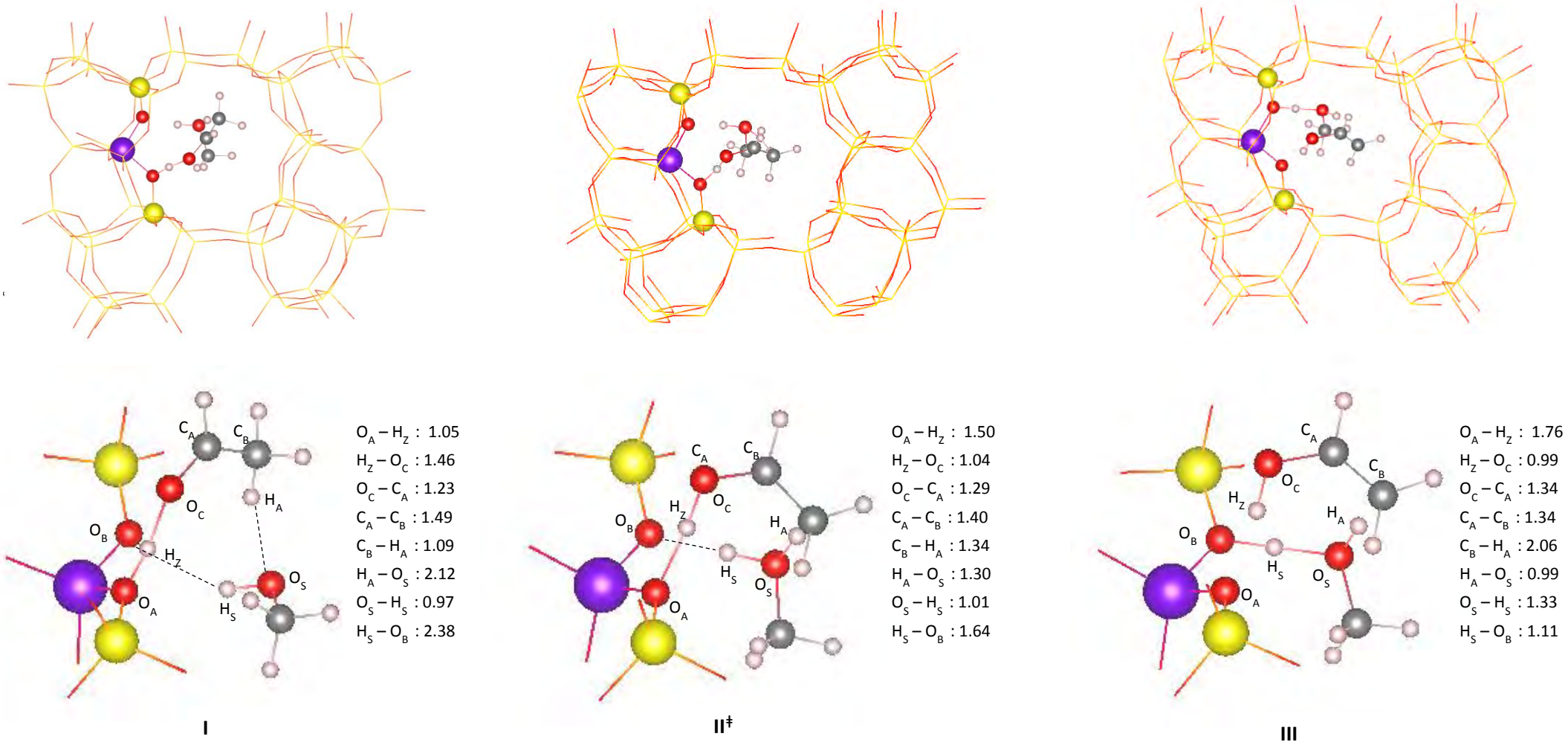

Figure 5-5 Geometrical structures of the keto-enol tautomerization of acetaldehyde in the presence of a single methanol molecule at T3 in FER zeolite. Bond lengths in Å.

The complete PES profile of this concerted mechanism is shown in **Figure 5-6**, the activation and reaction energies, along with the dispersion contributions are listed in **Table 5-1**.

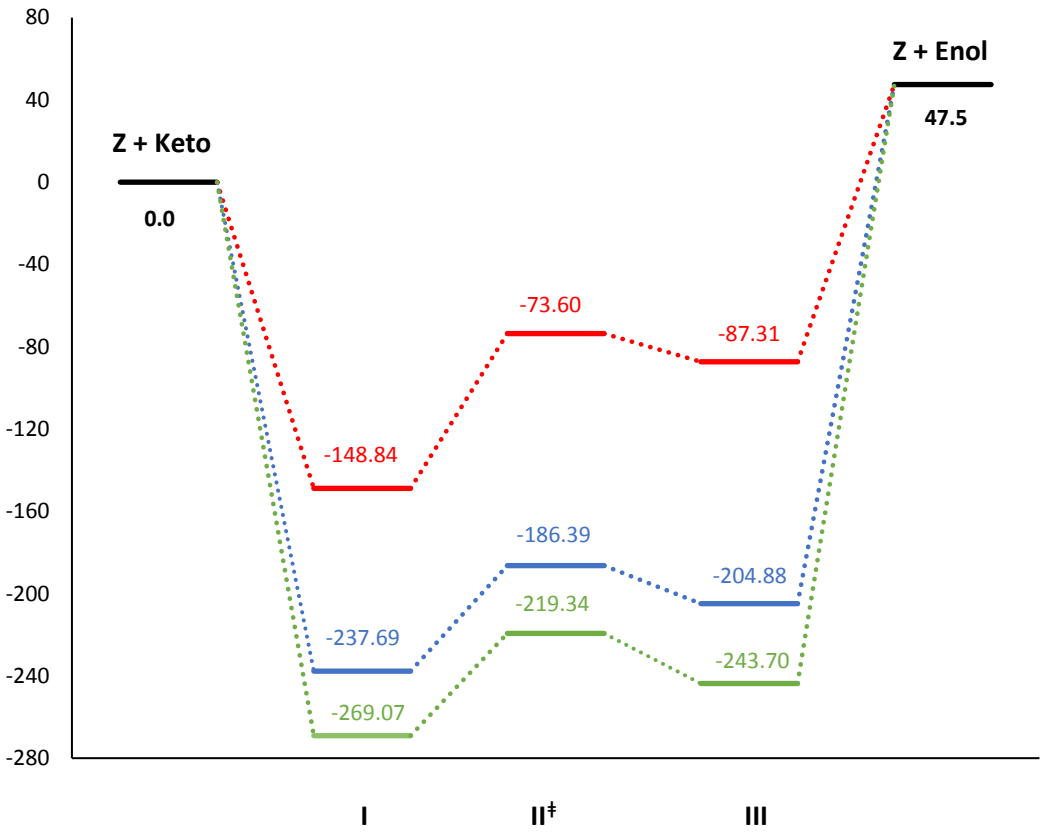

Figure 5-6 Complete PES profile of the keto-enol tautomerism of acetaldehyde at T3 in FER zeolite. Red = no solvent, blue = water, green = methanol.

	Reactions	E_r	ΔE_{elec}	ΔE_{disp}	E_a (forward)	ΔE_{elec}	ΔE_{disp}	E_a (reverse)	Imaginary Frequency (cm^{-1})
No solvent	*Z + Keto ↔ I**	*-148.8*	*-31.6*	*-117.2*					
	I ↔ III	61.5	57.9	3.6	75.3	71.5	3.7	13.7	
Water	*Z + Keto ↔ I**	-237.7	-66.6	-171.1					
	I ↔ III	32.8	27.2	5.6	51.1	45.2	6.1	14.0	-855.1
Methanol	*Z + Keto ↔ I**	*-269.1*	*-60.6*	*-208.4*					
	I ↔ III	25.4	26.7	-1.4	49.7	50.5	-0.7	26.7	-872.3

Table 5-1 Calculated reaction (E_r) and activation (E_{act}) energies for the forward and reverse reaction pathways for the keto-enol tautomerism of acetaldehyde at T3 in FER zeolite. Note that (*) indicates the adsorption state (E_{ads}) of zeolite-adsorbate system calculated relative to them in the gas phase and the calculated E_{elec} and E_{disp} are the components of the respective (E_{ads}). Energy displayed in kJ mol^{-1}.

The co-adsorption of water or methanol has little effect on the strength of the H-bonded complex of acetaldehyde on the BA site, it results in an increased adsorption energy but this is due to the H_2O/ CH_3OH direct interaction with the framework. This is demonstrated by the fact that with CH_3OH and H_2O adsorbed, the electronic interaction is similar ~ (-60 to -65 kJ mol^{-1}). The change is due to dispersion only and is stronger with CH_3OH due to the larger size of the molecule, hence higher stability is achieved with methanol is co-adsorbed (-269.1 kJ mol^{-1}) than with water (-237.7 kJ mol^{-1}). The activation and reaction energies for the keto-enol tautomerization in the presence of the water or methanol molecule is similar, E_{act} : 49.7 and 51.1 kJ mol^{-1} and E_r : 32.8 and 25.4 kJ mol^{-1}, but much smaller than the value of $E_{a=}$ 75.3 kJ mol^{-1} inabsence of the solvent. Hence water and methanol facilitate the enolisation step. By calculating phonons at the TS geometries, we obtained one imaginary frequency when the solvent is co-adsorbed; confirming the transition state obtained. We can conclude that the presence of these solvent molecules enhances the catalytic reactivity as it reduces the activation barrier by ~ 20 kJ mol^{-1} and increases the stability of adsorbed enol in comparison to when no solvent molecule is present.

We further investigated whether constraining other reaction coordinates would lead to adsorbed enol structure, as the solvent molecules are both proton donors and acceptors. We constrained the reaction coordinate, $r(H_S - O_B)$, the bond distance of the hydrogen from the hydroxyl group of the solvent and oxygen site nearest neighbour to Al dopant and additionally the reaction coordinate $r(O_A - H_Z)$, the bond distance of the hydroxyl group of the Brønsted site. No minima was observed, as acetaldehyde can only act as a proton acceptor and hence shortening the reaction coordinate, $r(H_S - O_B)$, leads to the formation of methoxide ion or

hydroxide in which the methyl group of acetaldehyde cannot act as a proton donor to complete the tautomerism. In the second case, elongating the reaction coordinate $r(O_A - H_Z)$, leads to protonated acetaldehyde although the positive charge is not located on the C_B atom and so the solvent molecule does not act as a proton acceptor for the hydrogen of the methyl group to complete the process. Thus we conclude that keto-enol tautomerization process of acetaldehyde in water or methanol is driven by C_B deprotonation.

We repeated this mechanism at the T3 position in the small pores of MOR. A complete PES profile is shown in **Figure 5-7. Table 5-2** lists the activation and reaction energies along with the dispersion contributions. Here, we find the presence of a water molecule substantially increases the adsorption energy of intermediate I, -177.2 kJ mol^{-1}, compared to when no solvent is present, -114.7 kJ mol^{-1}. Water in this case does not enhance the keto-enol tautomerization of acetaldehyde, as the activation barrier is very high (+118.6 kJ mol^{-1}) compared to what we observed at the larger pores in FER zeolite. In this case the catalytic reactivity is determined by the pore structure, as in the smaller pores of MOR the coadsorption of water or methanol is prevented by steric repulsion. The electronic contribution, ΔE_{elec} = 123.8 kJ mol^{-1}, which explains the higher energy barrier obtained. Hence, water suppresses the tautomeric process although increases the stability of adsorbed enol, much to the point where its stability if comparable to that of adsorbed keto, with a reaction energy of 6.3 kJ mol^{-1}. With regards to methanol co-adsorbed, the adsorption of acetaldehyde is much weaker at the BA site and in our optimization run we observed acetaldehyde is quickly displaced by methanol and bounded to the BA site.

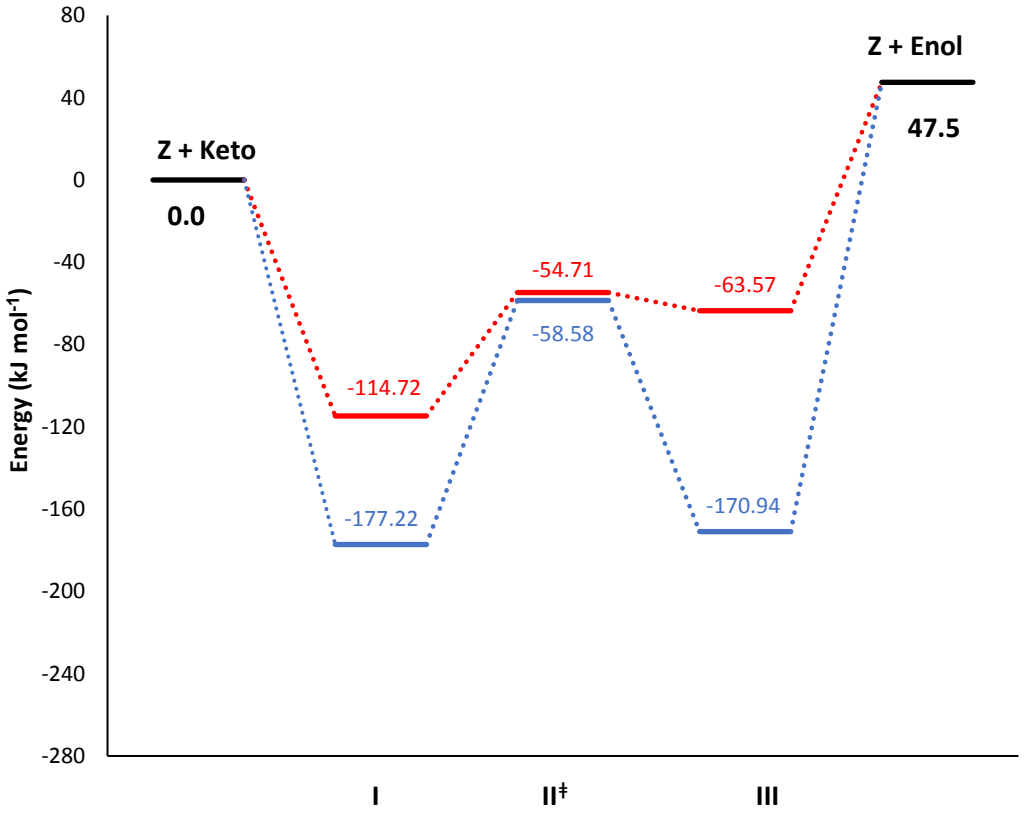

Figure 5-7 Complete PES profile of the keto-enol tautomerism of acetaldehyde at T3 in MOR zeolite. Red = no solvent, blue = water.

	Reactions	E_r	ΔE_{elec}	ΔE_{disp}	E_a (forward)	ΔE_{elec}	ΔE_{disp}	E_a (reverse)	Imaginary Frequency (cm^{-1})
No solvent	*Z + Keto ↔ I**	*-114.7*	*48.5*	*-163.2*					
	I ↔ III	51.2	33.9	17.3	60.0	41.6	18.4	8.9	-980.9
Water	*Z + Keto ↔ I**	-177.2	9.3	-186.5					
	I ↔ III	6.3	4.3	2.0	118.6	123.8	-5.1	112.4	-960.5

Table 5-2 Calculated reaction (E_r) and activation (E_{act}) energies for the forward and reverse reaction pathways for the keto-enol tautomerism of acetaldehyde at T3 in MOR zeolite. Note that (*) indicates the adsorption state (Eads) of zeolite-adsorbate system calculated relative to them in the gas phase and the calculated E_{elec} and E_{disp} are the components of the respective (E_{ads}). Energy displayed in kJ mol^{-1}.

5.3 Conclusion

In summary, we have carried out a series of constrained geometry optimizations to describe the keto-enol tautomeric interconversion of acetaldehyde in the presence of a single water or methanol molecule. We found that the presence of a water molecule reduces the activation barrier by about 150 kJ mol^{-1} in gas phase. Using methanol, the activation barrier reduces by a further ~ 15 kJ mol^{-1}. The important outcome of our study is the detailed picture of the intermolecular mechanism of the tautomeric process in the zeolite pores in the presence of these solvent molecules. We considered water or methanol co-adsorbed onto a previously adsorbed acetaldehyde H-bonded at T3 position in the larger pores in FER and T3 position in the smaller pores of MOR zeolite. The co-adsorption of a second molecules results in increased adsorption energy. We found that in FER, the solvent molecules enhance the keto-enol tautomerism with activation energies reducing, and also increase the stability of the adsorbed enol form with larger reverse energy barriers. We establish the importance of the specific role of the H-bonding using these solvent molecules. In the smaller pores of MOR, the presence of a water molecule suppresses the catalytic interconversion due to steric repulsion. When methanol is co-adsorbed, acetaldehyde bounded to the BA site and is displaced by methanol at T3 position in MOR zeolite.

Chapter 6

Location of alkali ions and mobility of cesium ion in FER zeolite

6.1 Introduction

As stated in the introduction of this thesis, the anionic character of the zeolite structure due to the substitution of Si by Al can be neutralized by exchangeable cations located in well-defined surface sites surrounded by oxygen atoms of the framework. This is essential as the extra-framework cations can influence the distribution of the electron density in the framework and hence the interactions with the adsorbed species, leading to changes in the adsorption and catalytic properties. (Maurin, *et al*., 2004, Van Reenen, *et al*., 2004)

In this chapter, we focus on the location of alkali metal cations (Na^+, K^+, Rb^+ and Cs^+) in FER at each T position where the Al dopant resides. Ion-exchange FER with alkali cations, Na^+ and K^+, (Arean, *et al*., 2006, Garrone, *et al*., 2006) have been previously studied both experimentally and theoretically in processes such as CO and H_2 adsorption. While very few experimental studies exist for the ion-exchanged selectivity in this zeolite for the larger cations, Rb^+ and Cs^+, In addition, no previous theoretical study presents a detailed analysis of accurately locating the alkali ions in FER. We carried these calculations using force fields in GULP and further optimized to more accurate structures with B3LYP functional via CRYSTAL code. From our analysis, we determined that the preferential location

of alkali ions in the FER cavity. In the next section this chapter, we explore the effect of hydration on the mobility of the Cs^+ ion in cavities of FER using static DFT calculations supplemented with *ab initio* molecular dyanmics (AIMD) to gain understanding from a dynamical viewpoint; via CP2K code utilizing PBE functional. This study was performed because water plays a crucial role in many applications involving adsorption and more importantly, in ion exchange carried out in aqueous solution. The high-silica FER consisting of the narrow channel with small pore size allows strong ion-sieving ability to large hydrated cation (Mimura, *et al*., 1994, Van Reenen, *et al*., 2004) which explains why we chose to study Cs^+ ion. We aim to understand the balance of coordination of Cs^+ to framework oxygens and water molecules as well as the influence of the Al dopant on the position of these species.

6.2 Computational Details

6.2.1 Location of alkali ions

In the first part of our study we simulate the equilibrium location of the extra-framework cations in FER. The calculation was performed using PBC and the unit cell is represented in Chapter 3. In the zeolite framework, the Al^{3+} has been charged balanced by incorporating one Na^+, K^+, Rb^+ or Cs^+ ion. Taking into account that the extra-framework cations are often closely related to the distribution of Al over the T sites, we introduced these cations in such a way that they were in the same channels as the Al atoms. The minimisations were carried out without symmetry constraints using constant pressure optimization algorithm in the program GULP (i.e. both atomic positions and cell parameters are optimized) (Gale and Rohl, 2003). The potential energy surface of the system was evaluated by appropriate pair potential

models. We used the potentials reported by Catlow *et al*. (Gale and Henson, 1994, Jackson and Catlow, 1988, Sanders, *et al*., 1984, Schroder, *et al*., 1992) to describe the interactions within the zeolite framework, and between the framework and cations by means of the Buckingham potential. The zeolite framework is considered to be fully flexible by introducing three body terms for O – Al – O and O – Si – O and polarisable via a shell model for the oxygen atoms. The parameters for each of these potentials are fully detailed in **Appendix: Table 8-3 to 8-6**. For each of these minimisation procedures, the Ewald summation was used to calculate the coulombic interactions and the cut-off was set to at 12 Å for the short-range contributions. (Maurin, *et al*., 2004, Olson, *et al*., 1981)

The GULP minimized structures were then further optimized to more accurate structures using periodic DFT in the CRYSTAL code (Dovesi, *et al*., 2005) The B3LYP hybrid exchange-correlation functional (Becke, 1993, Lee, *et al*., 1988, Stephens, *et al*., 1994, Vosko, *et al*., 1980) was adopted for all the calculations. The FER and MOR framework was calculated using PBC in P1 space group to allow full optimization without symmetry constraints. The electronic distribution was described as a linear combination of atomic orbitals and the basis functions are expressed analytically as a contraction of Gaussian-type orbitals (GTO). The GTO basis sets were used for the geometry optimization of all the structures, consists of split-valence triple-zeta basis sets including a set of polarization functions on all atoms, 6-311G **. All basis sets were provided from the online library of the CRSYTAL code (Dovesi, *et al*., 2005). The empirical dispersion correction was proposed by Grimme (Grimme, 2006).

6.2.2 Dehydrated and Hydrated System of Cs^+

All calculations were carried out with the "Quickstep" part of the CP2K program, a DFT code that uses a mixed Gaussian and plane-wave approach. (VandeVondele, *et al*., 2005) Static geometry optimizations were performed with Cs^+ ion located in the FER cavity with the Al dopant at the T4 position in both a dehydrated and hydrated system. The actual cell used was doubled in the c direction, giving a repeat distance in that direction of 15.0 Å, so as to minimize the error due to spurious interactions between a defect and its periodically repeated image. The set up consists of $1 \times 1 \times 2$ supercell of FER consisting of ~ 230 atoms with the inclusion of Cs^+ ion and depending on the number of water molecules included. The exchange-correlation energy has been calculated using the PBE functional as implemented in the CP2K code. (Perdew, *et al*., 1996) For the core electrons, the relativistic Goedecker-Teter-Hutter pseudopotentials optimized for the PBE function were employed (Krack, 2005). The calculations used the DVZP double-zeta plus polarisation basis from the series of highly contracted MOLOPT basis sets developed by VandeVondele and Hutter (VandeVondele and Hutter, 2007). The short range version of the basis set was chosen, which is optimised for calculations in the solid state due to its less diffuse nature. A plane-wave cut off of 400 Ry was used for the auxiliary grid. To account for the dispersion interactions the DFT-D3 method implemented in the CP2K package was used.

Static calculations were supplemented by ab initio molecular dynamics (AIMD) simulations performed in NVT ensemble with canonical sampling with velocity rescaling (CSVR) thermostat, with a time constant of 50 fs. All simulations correspond to a temperature of 300 K and the time step was set to 0.5 fs for the integration of the equations of motion. The length of trajectories was 10 ps whereby

whereby the initial period of 1 ps is considered as equilibration.

6.3 Results and Discussion

6.3.1 Location of alkali ions at each T position

The location of alkali-metal cations (M^+) in FER was investigated systematically, considering the framework Al at all the distinguishable positions and all possible coordinations of metal cations in the vicinity of the framework Al atom. The different starting positions of the cations were performed at force field level and selected configurations were further optimized at periodic DFT level. The coordination numbers (CN), $r(M^+ - O)$ bond distances, and relative energies are summarized in **Table 6-1**. The overall number of framework oxygen atoms in coordination with each cation, *CN (O)*, and the number of oxygen atoms of the AlO_4 tetrahedron in coordination with the cation, $CN\ (O_{Al})$, are reported. We found the relative stabilities of the individual M^+ binding sites depend on the position of the Al atom.

	Force Field					Periodic DFT				
Al Position	*Site Type*	*CN (O)*	*CN (O_{Al})*	*r(M^+- O)*	*E_{rel}*	*Site Type*	*CN (O)*	*CN (O_{Al})*	*r(M^+- O)*	*E_{rel}*
Na^+										
T1a	I		2	*2.502 , 2.627*	19.12	I	2	2	*2.241, 2.449,* 2.541, 2.659	31.49
	M7	1	2	*2.672, 2.700,* 2.743	40.96	M7	3	2	*2.353,* 2.419, *2.453,* 2.547, 2.598	37.42
T1b	I		2	*2.455, 2.603*	22.90	I	2	2	*2.316, 2.367,* 2.523, 2.699	25.43
	M7		2	*2.584, 2.680*	41.44	M7	4	2	*2.370,* 2.460, *2.480,* 2.526, 2.651, 2.734	29.43
T2	I	1	1	2.651 *2.799*	0.00	I	2	2	*2.489 2.501* 2.528 2.640	23.67
	P6	2	1	*2.543,* 2.705, 2.772	52.84	P6	3	2	*2.308, 2.314,* 2.377, 2.466, 2.468	37.04
T3	M7	2	2	*2.489, 2.597* 2.672 2.787	26.43	M7	3	2	*2.294,* 2.368, *2.479,* 2.531, 2.611	11.42
	P8		2	*2.511, 2.691*	34.13	P8	3	2	*2.352.* 2.463, *2.485*, 2.750	0.00
T4	P6		2	*2.476 2.551*	55.46	P6	2	2	*2.255 2.273* 2.3762.431	35.71
K^+										
T1a	M7		1	*3.219*	25.73	I	4	2	2.684, *2.715, 2.732,* 2.982, 3.070, 3.108	18.09
	P8		2	*3.094, 3.108*	25.09	P8	3	2	*2.623, 2.831,*	41.88
T1b	M7		2	*3.156, 3.165*	29.24	M7	3	2	*2.623, 2.831,* 2.855, 2.989, 3.121	39.96
	P8	1	2	*3.078, 3.090,* 3.397	30.84	I	4	2	*2.609, 2.786,* 2.887, 2.933, 2.957, 3.279	13.13
T2	P8	2	2 / 1	*3.175,* 3.242, *3.289*, 3.293*	0.00	I	3	2 / 1*	*2.848,* 2.767, 2.859, *2.895, 2.991*,* 3.140	4.15
	M7		1/ 1*	*3.021, 3.345**	12.26	I	2	2 / 1*	*2.302, 2.675,* 2.766, 2.955, *3.367**	1.59
T3	M7		2	*3.053, 3.111*	27.29	M7	4	2	*2.677, 2.684,* 2.814, 3.076, 3.194, 3.259	39.33
	P8	1	2	*3.173, 3.216,* 3.233	30.43		4	2	2.418 ,*2.738, 2.951,* 2.991, 3.002, 3.167	12.83
T4	P8	1	2 / 2*	*3.196,* 3.356, *3.379*, 3.429**	12.31	P8	3	1 / 2*	*2.783, 2.770*,* 2.824, 2.908, *2.950*,* 3.330	0.00

	Force Field					Periodic DFT				
Al Position	*Site type*	*CN (O)*	*CN (O_{Al})*	*r(M^+- O)*	*E_{rel}*	*Site Type*	*CN (O)*	*CN (O_{Al})*	*r(M^+-O)*	*E_{rel}*
Rb^+										
T1a	M7	1	1	*3.474,* 3.634	20.30	I /M7	4	3	*3.010,* 3.060, *3.111, 3.120,* 3.203, 3.295, 3.456	23.41
	P8		2	*3.378, 3.525*	25.88	P8	4	2	*2.883, 2.888,* 3.023, 3.088, 3.232, 3.368	16.25
T1b	M7		2	*3.406, 3.408*	24.67	M7	3	2	3.013, *3.041, 3.045,* 3.237, 3.248	33.26
	P8		2	*3.409, 3.539*	31.76	P8	4	2	*2.949,* 3.138, 3.145, 3.182, *3.217,* 3.727	
T2	P8		1	*3.563*	0.00	I	4	2 / 1*	3.018, *3.042*, 3.073,* 3.127, *3.195,* 3.288, 3.421	1.78
	M7			*3.406, 3.408*	12.26	I	3	2 / 2*	3.030, *3.077*, 3.122,* 3.131, *3.188*, 3.294,* 3.399	2.03
T3	M7	2	2	*3.109, 3.264,* 3.373, 3.533	23.43	M7	4	2	*2.842,* 3.039, *3.115,* 3.224, 3.364	34.54
	P8	1	2	3.499, *3.536, 3.580*	30.02	P8	4	2	2.967, *3.046, 3.050,* 3.052, 3.100, 3.202	12.85
T4	P8		1	*3.475*	8.84	P8	5	1 / 2*	*2.912, 2.931*,* 3.075, 3.180, *3.188*,* 3.350	0.00
Cs^+										
T1a	MC	1	2	*3.615,* 3.692, *3.783*	19.63	M7	4	3	*3.166,* 3.351, *3.358,* 3.428, *3.449,* 3.498, 3.565	25.88
	P8	1		3.687	26.84	P8	5	2	*3.133,* 3.268, *3.273,* 3.293, 3.400, 3.435, 3.652	38.54
T1b	MC		2	*3.529, 3.541*	24.66	M7	6	2	*3.254,* 3.283, *3.284,* 3.356, 3.403, 3.504, 3.610, 3.634	33.22
	P8		2	*3.409, 3.539*	32.84	P8	4	2	*2.949,* 3.138, 3.145, 3.182, *3.217,* 3.272	
T2	P8		2 / 1*	*3.677, 3.750*, 3.799*	0.00	P8	3	2 / 2*	*3.180, 3.249*, 3.281*,* 3.308, *3.387,* 3.388, 3.427	2.61
	M7	1		3.573	9.84	M5	6	2	*3.240, 3.285,* 3.392, 3.431, 3.511, 3.534, 3.642, 3.688	34.06
T3	M7	1	2	*3.455, 3.615,* 3.718	23.71	M7	7	2	*3.190, 3.256,* 3.416, 3.418, 3.423, 3.612, 3.619, 3.769, 3.777	12.53
T4	P8	1		3.680	30.24		6	2	*2.864, 3.065,* 3.267, 3.365, 3.392, 3.426, 3.456, 3.789	17.50

Table 6-1 Site types, coordination numbers, M^+ - O distances (in Å) and binding energies of M^+ with FER at each T position (in kJ mol^{-1}) obtained at FF and periodic DFT level. Number of oxygen atoms in coordination with M^+ (atoms closer than 2.8 Å for Na^+ 3.2 Å, for K^+ 3.4 Å, for Rb^+ 3.6 Å and for Cs^+ 3.8 Å are considered). The number in italics correspond to the M^+ - O bond distances between M^+ and oxygen atoms adjacent to Al. The * denotes the number of oxygen atoms in the next repeating unit cell of AlO_4 tetrahedron in coordination with M^+. The relative binding energies with respect to the energy of lowest structure for each particular cation. Highlighted in blue and red is the lowest energy obtained at FF and periodic DFT level.

6.3.1.1 Na^+

The relative energies obtained using FF do not correspond well with the ones obtained at periodic DFT level with regards to the most stable structures of Na^+. The Na^+ is most stable at the channel intersection with the Al located at the T2 position at FF level and at P8 site in FER cavity with the Al located at the T3 position at periodic DFT level. In the cavity, the Na^+ ion is coordinated to five oxygen atoms of the 8-MR of the perpendicular channel with Na – O bond distances of 2.352, 2.483, 2.485, 2.750 and 2.827 Å (**Figure 6-1**). The second most stable location of the cation is at M7 site with the Al located at T3 position consisting of a relative energy of 11.42 kJ mol^{-1}. Thus, we can confirm that Na^+ is most stable when the Al atom is located at T3 position in FER which is also in good agreement with previous theoretical studies by Arean *et al*. (Arean, et al., 2006) using PBE functional at MP2 level. The P6 site proves to be unfavourable for the location of Na^+ at both levels whether the Al is located at the T2 or T4 position, ~ 37 kJ mol^{-1} using periodic DFT. In addition, we found no differentiation in terms of both energy and Na^+ position when Al is located at the T1a or T1b. At these two T1 positions, we cannot distinguish where Na^+ prefers to be located at the channel intersection or at the M7 site as the energy difference between the two sites is less than ~ 6 kJ mol^{-1}. This is in good agreement with a previous theoretical study by Klein *et al.* (Klein *et al.,* 2015) which showed no difference between T1a and T1b positions when Li was incorporated.

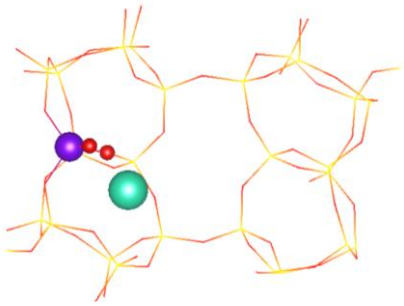

Figure 6-1 Most stable location of Na^+ at P8 site located in FER cavity with the Al dopant at T3 position.

6.3.1.2 K^+ Rb^+ and Cs^+

With an increase in the ionic radii, the most stable position of these cations is at the P8 site in FER cavity with the Al at the T4 position, obtained at periodic DFT level (**Figure 6-2**). At force field level, the most stable location is again at P8 site in the FER cavity although with the Al dopant at the T2 position, which is also favourable when reoptimized at periodic DFT level, making it the second most stable position with an increase in energy of less than 5 kJ mol^{-1}. As shown in **Figure 6-2,** at these two T positions, the cation is able to interact not only with the framework oxygens in the vicinity of the Al dopant at T2 or T4 position, but is also able to interact with the same Al dopant present in the next unit cell *via* PBC, which could possibly explain the increased stability. At periodic DFT level, the K^+ and Rb^+ ions migrate from P8 site to the channel intersection due to position of Al at T2 is located at the intersection. The larger Cs^+ ion does not migrate to the channel intersection and remains at P8 site; hence establishing that the intersection between both channels accommodate the Cs^+ ion. We also observed this occurrence yet again at T2 position where the K^+ and Rb^+ ions migrate from the M7 site (at force field level) to the channel intersection (at periodic DFT level), while the Cs^+ ion does not migrate to the channel intersection and instead relocates from the symmetrical position in the

centre (close to M7 at force field level) to the side (close to M5 at periodic DFT level) of the MC; resulting in a higher energy (34.06 kJ mol^{-1}) – **Figure 6-3.**

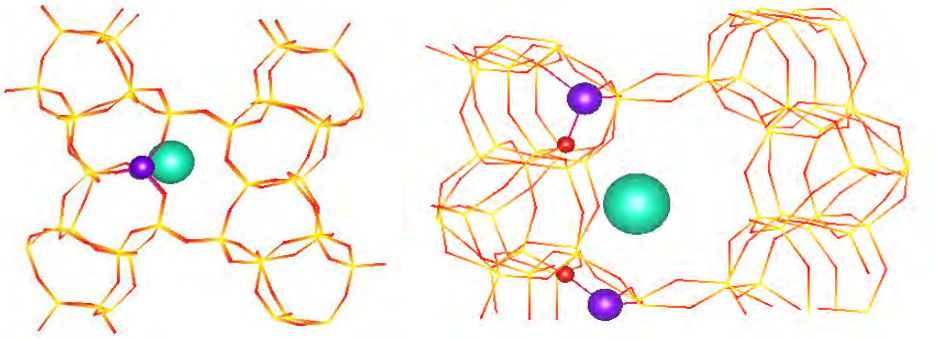

Figure 6-2 Most stable location of Cs^+ located at P8 site in the FER cavity with the Al dopant located T4 position. (Right side – Cs^+ is able to interact with oxygen frameworks nearest neighbour to Al dopant in the next repeating unit cell *via* PBC approach. (K^+ and Rb^+ have similar positions to Cs^+).

(a)

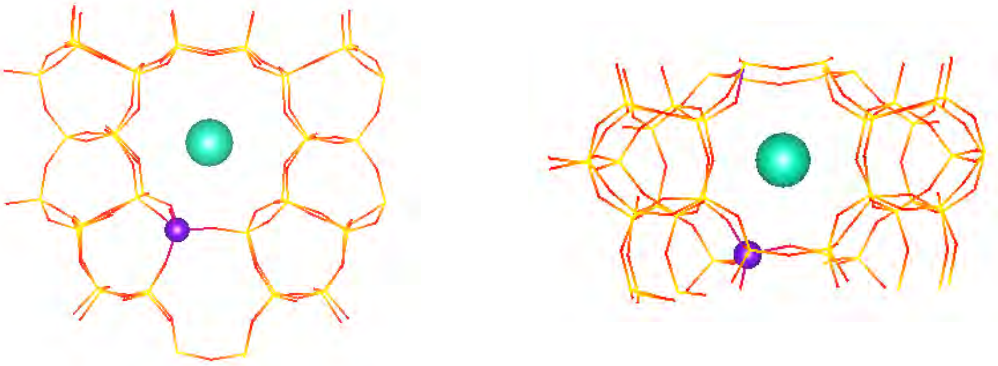

(b)

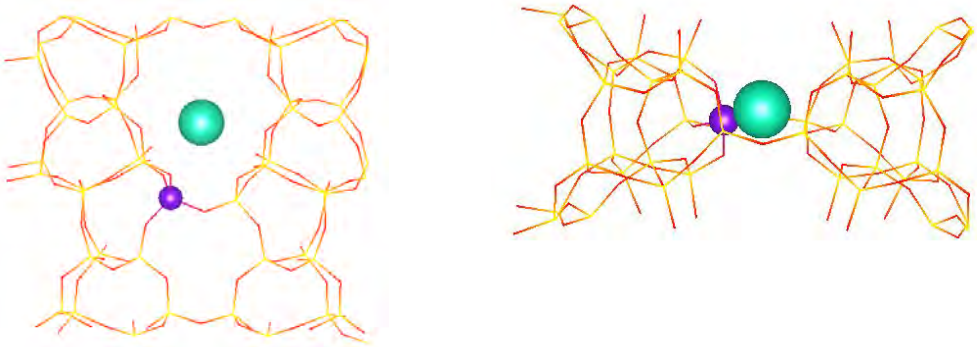

Figure 6-3 Cs^+ in FER with Al dopant at T2 position (a) at force field level where the cation is located in the centre of the channel close to M7 site (b) at periodic DFT level where the cation migrates to the side of the MC close to M5 site.

We obtained similar energies at FF level when these cations are located at M7 or P8 site with the Al positioned at the T1a or T1b. Although, the reoptimization of these structures at periodic DFT level establish a difference between the T1a and T1b, mainly noticeable with K^+ ion (**Figure 6-4**). With the Al at T1a, the K^+ ion migrates from the M7 site to the channel intersection; preferentially located here with an energy of 18.09 kJ mol^{-1}. With Al at T1b, the K^+ ion remains positioned in the less favoured M7 site, with an energy of 39.96 kJ mol^{-1}. With regards to the K^+ ion located at the P8 site at FF level with the Al at both T1 positions, at periodic DFT level - K^+ ion does not relocate when the Al is positioned at the T1a acquiring an unfavourable energy of 41.88 kJ mol^{-1}, while the cation does migrate to the channel intersection when the Al is positioned at the T1b, stabilising K^+ ion with an energy value of 13.13 kJ mol^{-1} (see **Figure 6-4**).

With the larger cations, the difference between T1a and T1b becomes less obvious, as an increase in the ionic radii is less likely to migrate towards the 8-MR window. Thus for Rb^+ ion, with Al at T1a and T1b, the difference in energies is reduced at M7 site (T1a : 24.41 and T1b : 33.26 kJ mol^{-1}) and P8 site (T1a : 22.25 and T1b : 16.89 kJ mol^{-1}) ; and even more so with the larger Cs^+ ion at M7 site (T1a : 25.88 and T1b : 33.22 kJ mol^{-1}) and at P8 site (21.54 and 18.61 kJ mol^{-1}).

(T1a)

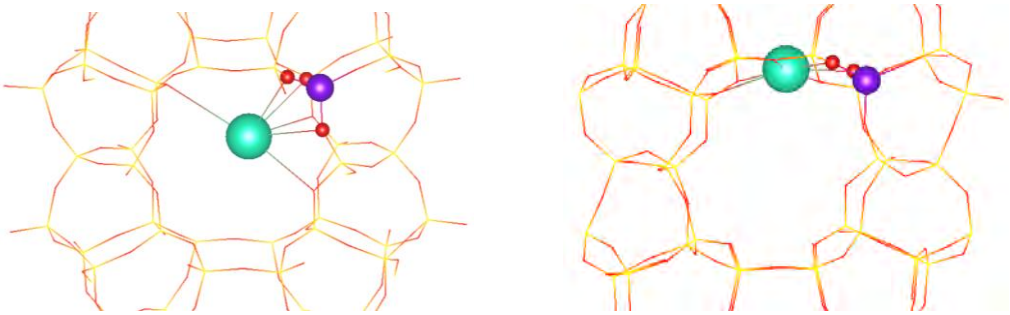

FF : M7 periodic DFT : I

(T1b)

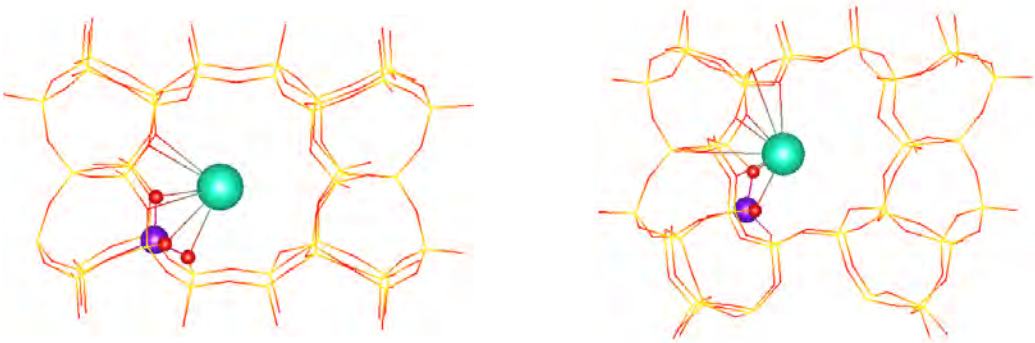

FF : M7 periodic DFT : M7

(T1a)

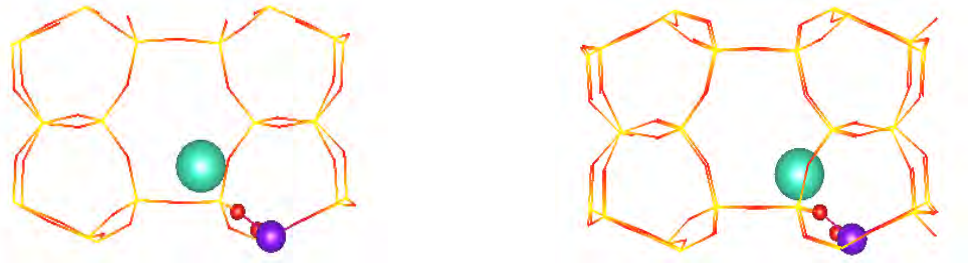

FF : P8 periodic DFT : P8

(T1b)

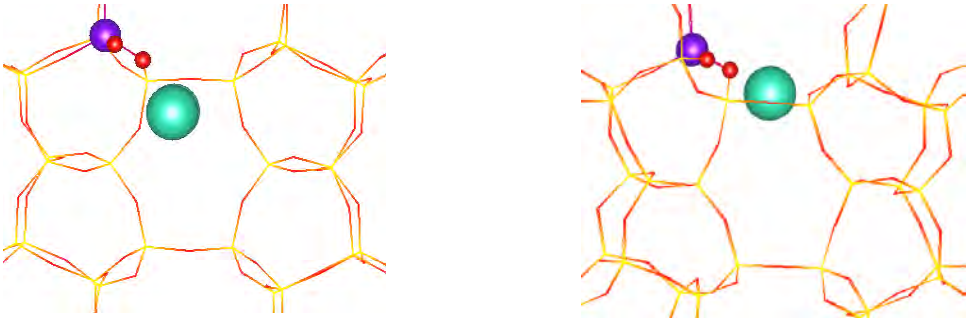

FF : P8 periodic DFT : I

Figure 6-4 K^+ in FER with Al at T1a and T1b position.

In **Table 6-1** – while the relative energies for framework sites at each T position for the alkali ions are in reasonable agreement at the force field and periodic DFT levels, the coordination number obtained at these two levels do not agree in most cases. While the *CN* (O_{Al}) is good agreement using both levels for each cation, the *CN (O)* obtained at FF level is lower than those obtained at periodic DFT level. The $r(M^+ - O)$ of the oxygens adjacent to Al dopant is shorter at periodic DFT level. The average coordination number obtained at force field and periodic DFT level for each cation is Na^+ (2.4, 4.4), K^+ (2.7, 5.5), Rb^+ (1.9, 6.4) and Cs^+ (1.8, 6.8). From this we can establish that the differences between the two methods is more apparent with the larger cations.

6.3.2 Static Simulations

6.3.2.1 Migration of Cs^+ ion in dehydrated FER

We established that Cs^+ ion is the most stable at P8 in FER cavity with Al dopant located at T4 position. The next step involves exploring the pathway for Cs^+ migration in the FER framework. Energy minimizations were performed in which the *y* coordinate of Cs^+ ion was moved into increments of 2 along the *y* direction (see **Figure 6-5 (a). Figure 6-5 (b)** shows the energetic migration profile of Cs^+ ion from P8 → I → MC → I→ P8. The migration profile confirms that Cs^+ ion located at P8 site in FER cavity is the energy minima. P8 site has the lowest energy minima on our surface, whilst Cs^+ ion located in the MC is a local minimum. In our previous analysis we established that even with Al dopant located at the channel intersection, T2 position, the Cs^+ ion remains located in the MC (M7), and never relocates away to the channel intersection unlike the other smaller cations.

This can be further explained from our surface that Cs^+ ion is sitting between two energy barriers both in the region of ~ 35 kJ mol^{-1} in order to migrate the cation from the MC to the FER cavity. Although the barrier is not as significantly higher than when migrating the cation from FER cavity to the MC, ~ 65 kJ mol^{-1}, and thus the cation would rather avoid migrating to the MC in the first place, making P8 site both the kinetic and thermodynamic configuration (trapped in a deep minimum). The channel intersection, I site, can be considered to the maximum from our energy surface validating our previous analysis that the channel intersection is not a favourable site for the Cs^+ ion. We can also confirm that the static calculations using PBE functional are in good agreement with our previous analysis on the location of Cs^+ in FER using B3LYP functional.

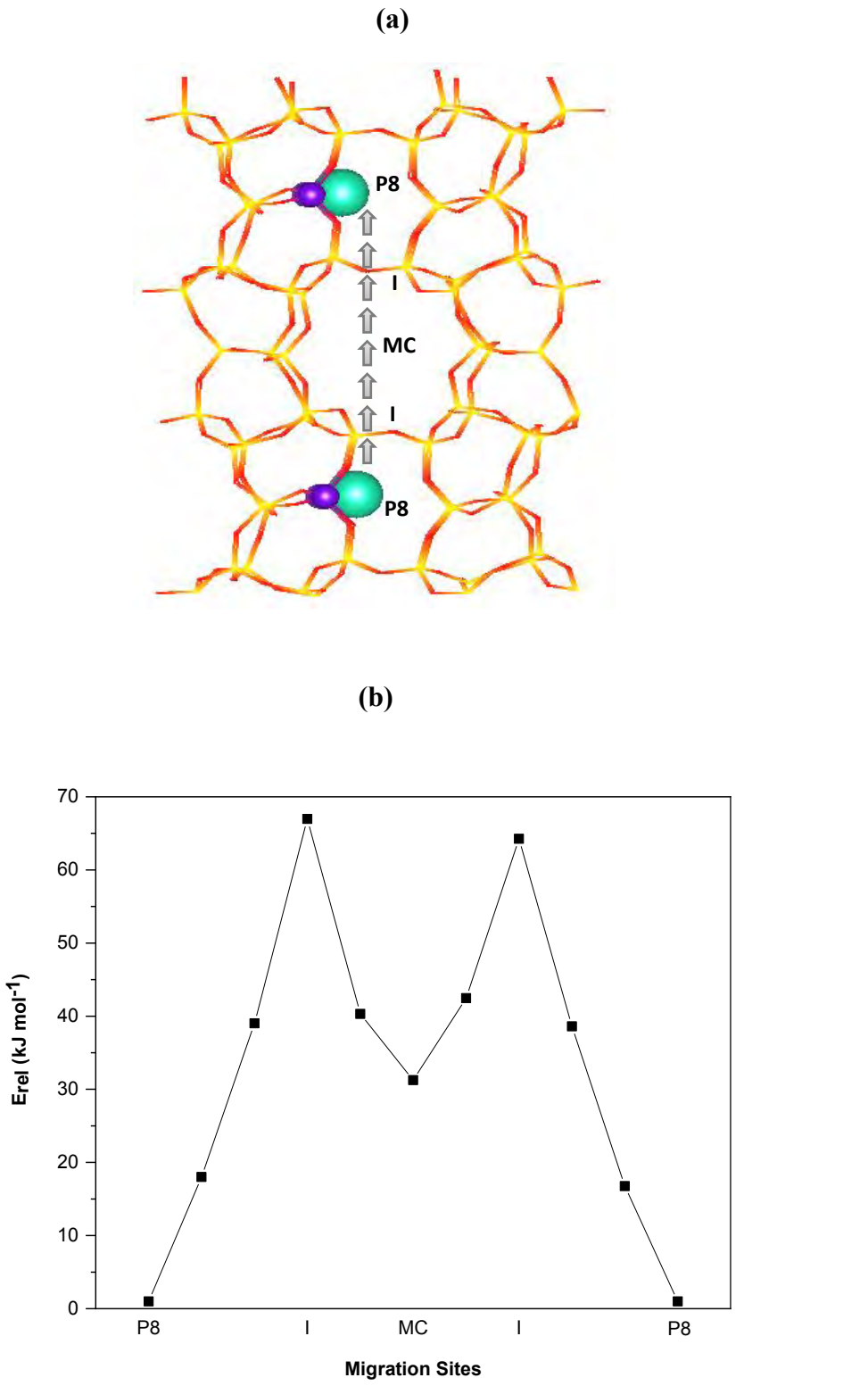

Figure 6-5 (a) Migration pathway of Cs^+ along the *y* direction and (b) Energetic migration profile of Cs^+ from P8 → I → MC → I→ P8.

6.3.2.2 Migration of Cs^+ in hydrated FER

The next step of this work was to explore the effect of water on the migration of the Cs^+ ion. From a theoretical perspective, the study of hydrated cluster of Cs^+ ion, $Cs^+ - (H_2O)_n$, have been studied by Kaupp and Schleyer (Kaupp and Schleyer, 1992) for n = 3 and by Glendening and Feller (Glendening and Feller, 1995) for n = 4 at the HF and MP2 levels of theory. Ali *et al*. (Ali, *et al*., 2007) further studied $Cs^+ - (H_2O)_n$ (n = 1 – 10) using B3LYP functional and found that Cs^+ ion has six water molecules in the first hydration shell. In our study, we introduced H_2O (n = 1 - 6) in FER zeolite where Cs^+ ion is located at P8 site in the cavity with Al dopant at T4 position, $Z - Cs^+ - (H_2O)_n$.

With $Z - Cs^+ - (H_2O)_n$ where n = 1 – 3, the water molecules are directly linked to the Cs^+ ion (**Figure 6-6**). We also tried the initial configuration where one or two water molecules is directly linked to the Cs^+ ion and the other is linked to the first or second water molecule through H-bond. These configurations proved to be less stable establishing that the water molecules prefer to be directly linked to the cation.

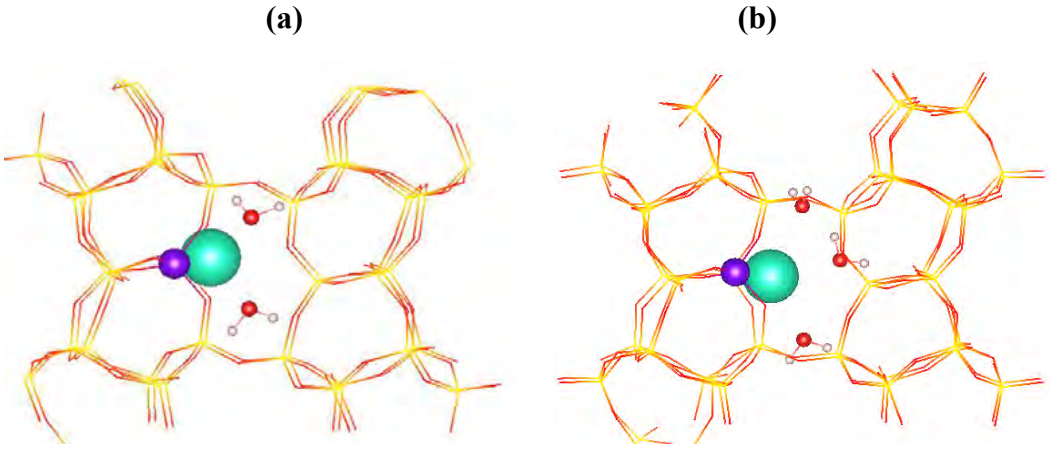

Figure 6-6 Hydrated Cs^+ at P8 site in FER cavity with the Al dopant at the T4 position. (a) 2 and (b) 3 H_2O molecules.

With $Z - Cs^+ - (H_2O)_n$ where $n = 4$, the structures in which all four water molecules are directly attached to the Cs^+ ion is the least stable one. With 4 water molecules, the most stable configuration is when 3 water molecules in the FER cavity are directly linked to the Cs^+ ion and the remaining one is connected through H-bonding. This clearly demonstrates that for hydrated Cs^+ $n \leq 3$ water molecules can only be present in the FER cavity and an additional water molecule is likely to form H-bonding. (**Figure 6-7**)

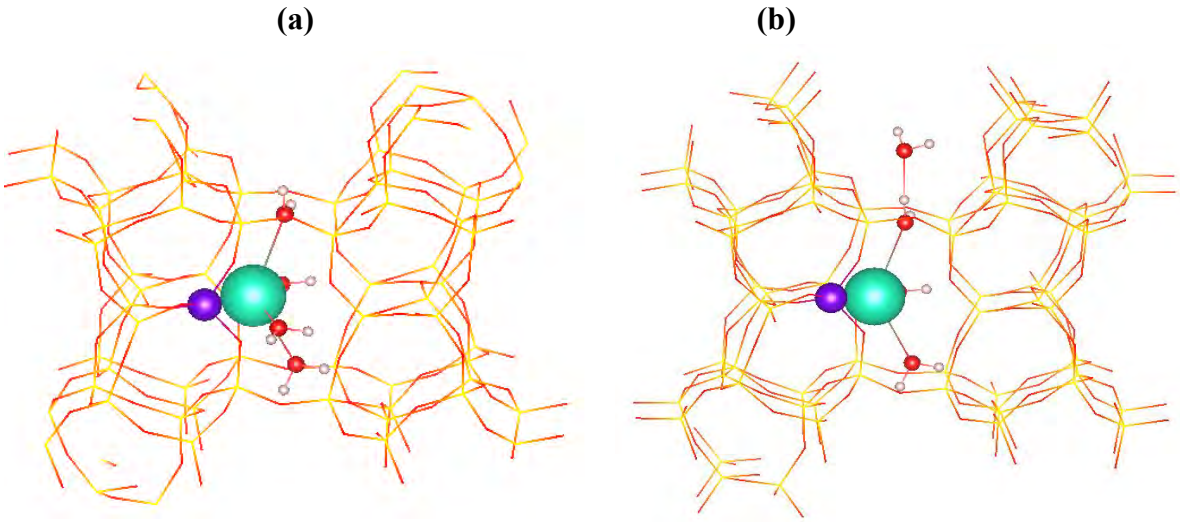

Figure 6-7 Hydrated Cs^+ at P8 site in FER cavity with the Al dopant at the T4 position with 4 H_2O molecules. (a) all 4 water molecules are coordinated to the Cs^+ ion. (b) 3 water molecules are coordinated to Cs^+ and the remaining is involved in H-bonding.

With $Z - Cs^+ - (H_2O)_n$ where $n = 5 - 8$, we found 2 - 3 water molecules are directly linked to the Cs^+ ion and the remaining forming an inter-water H-bonding. In addition, it is clear that there is self-assembly of the water molecules across the perpendicular channel connecting the Cs^+ ion. (**Figure 6-8**).

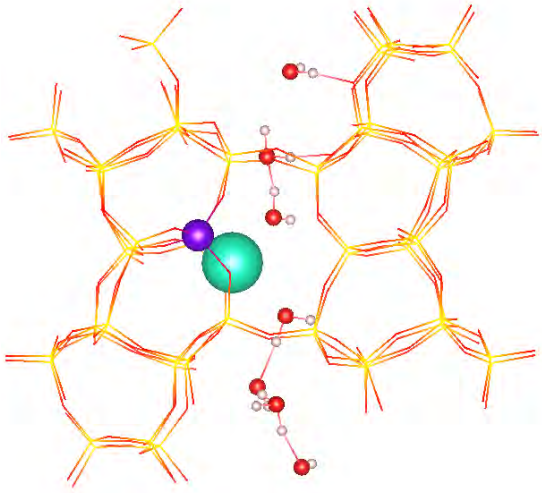

Figure 6-8 Hydrated Cs^+ at P8 site in FER cavity with the Al dopant at the T4 position with 5 H_2O molecules with 2 water molecules coordinated to Cs^+ and the remaining self-assembly across the channel through H-bonding.

We deal with the two most important energy parameters that are frequently encountered in hydration of ions, interaction energy (E^{int}) and hydration energy (E^{hyd}). **Table 6-2** displays the calculated values of these two energies.

Z – Cs^+ - $(H_2O)_n$	**E^{int} (kJ mol^{-1})**	**E^{hyd} (kJ mol^{-1})**
1	-56.58	-56.58
2	-90.18	-98.60
3	-102.88	-129.65
4	-77.64	-179.63
5	-79.02	-188.89
6	-70.05	-208.11
7	-77.38	-246.46
8	-84.70	-274.58

Table 6-2 Calculated values of interaction and hydration energies of *n* H_2O with Cs^+ located at P8 site in FER cavity with Al dopant at T4 position.

The E^{int} is calculated by the following relation:

$$E^{int} = E_{[Z-Cs^+-(H_2O)_{n+1}]} - E_{[Z-Cs^+-(H_2O)_n]} - E_{(H_2O)}$$

where $E_{[Z-Cs^+-(H_2O)_{n+1}]}$ and $E_{[Z-Cs^+-(H_2O)_n]}$ refers to the total energy of the FER zeolite consisting of the Cs^+ ion and n H_2O molecules inside. $E_{(H_2O)}$ refers to the energy of a single water molecule. The plot of the interaction energies against the number of water molecules inserted in zeolite system is shown in **Figure 6-9.** We can observe that the calculated largest interaction energy is found with 3 H_2O molecules, all are directly linked to the Cs^+ ion. The curvature shows after 3 H_2O molecules saying that the Cs^+ does not interact with water molecules: those are being added after 3 water molecules. The increase in energy $n \geq 3$ water molecules is probably due to the constrained space available in the FER cavity for the water molecules to interact effectively with the Cs^+ ion. This is further supported in the case of inserting an additional water molecule to a system consisting of with 3 H_2O where either all 4 H_2O are directly linked to the Cs^+ ion with a drastic increase in energy of + 3.6 kJ mol^{-1} or where the additional water molecule is connected through H-bonding with an energy of -77.64 kJ mol^{-1}; proving to be the more stable structure.

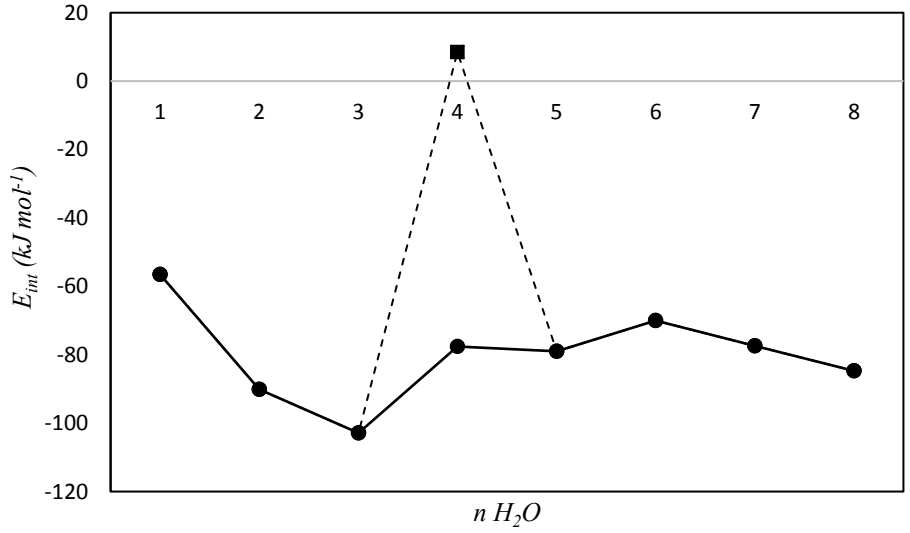

Figure 6-9 Interaction energy vs number of water molecules in hydrated system of Cs^+ located at P8 site in the FER cavity with the Al dopant at the T4 position. (Dotted line – the point where all 4 water molecules are interacting with the Cs^+ directly.)

The hydration energy E^{hyd} is defined by the following reaction:

$$E^{hyd} = E_{[Z-Cs^{+}-(H_2O)_n]} - E_{(Z-Cs)} - nE_{(H_2O)}$$

where $E_{(Z-Cs)}$ refers to the zeolite system containing the Cs^+ ion. The calculated values on the hydration energies for all the conformers are provided in **Table 6-2**. The calculated values on the hydration energy of the system increase with the increase in the number of solvent water molecules accounting ion-solvent interaction as well as intersolvent H-bonding interaction (**Figure 6-10**). From **Table 6-2**, there is a large difference between the E^{int} and E^{hyd} for $n = 4$, i.e., after the first hydration shell of $n = 3$. This is due to the fact that the interaction energy mainly accounts of the interaction of the Cs^+ ion with the water molecules. Thus the value of E^{int} for the hydrated systems increases as long as the individual solvent molecule binds to the cation directly and rather independently. However, the E^{hyd} for the hydrated systems increases continuously with the increase in the number of solvent molecules. It is also clear that the E^{int} saturates after 3 water molecules whereas the E^{hyd} increases continuously with the addition of water molecules and the increase in hydration energy is due to the increases number of H-bonding.

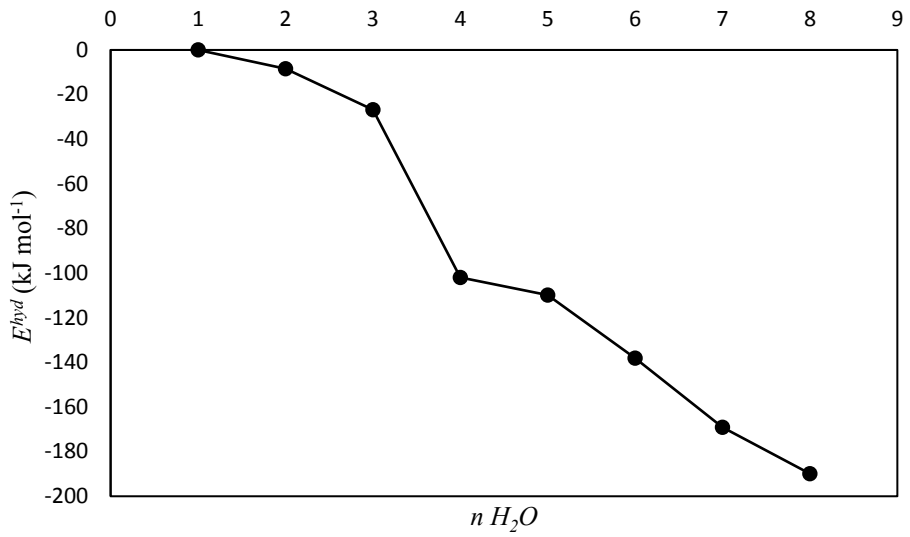

Figure 6-10 Hydration energy vs the number of water molecules with Cs^+ located in FER cavity with Al dopant located at the T4 position.

6.3.3 AIMD Simulations

From the inexpensive static calculations, we show that water molecules are the migrating species and the Cs^+ ion is rather immobile and trapped in the FER cavity whatever the hydration level. The static calculations are supplemented by AIMD simulations to attain a better description of the various configurations of the guest molecules and the flexibility of the zeolite framework.

6.3.3.1 Cs^+ in FER cavity

6.3.3.1.1 Dehydrated

Initially we observed the mobility of the Cs^+ ion located in FER cavity with Al at T4 position, as this was the most stable configuration found using the B3LYP functional via CRYSTAL code. The AIMD simulations support the previous findings that the Cs^+ ion proves to be immobile and trapped in the FER cavity (**Figure 6-11**).

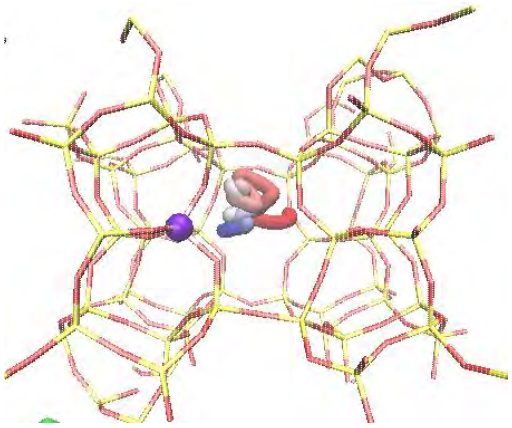

Figure 6-11 Trajectory (beginning in red, middle in white and the end in blue) of Cs^+ in FER cavity with Al dopant at T4 position.

6.3.3.1.2 Hydrated

Al at T4 position

We further explored the first hydration shell of Cs^+ in FER cavity consisting of 3 water molecules with Al at T4 position obtained from static calculations. **Figure 6-12** shows the initial and final geometries as well as the trajectories of Cs^+ and the water molecules obtained from the simulation run.

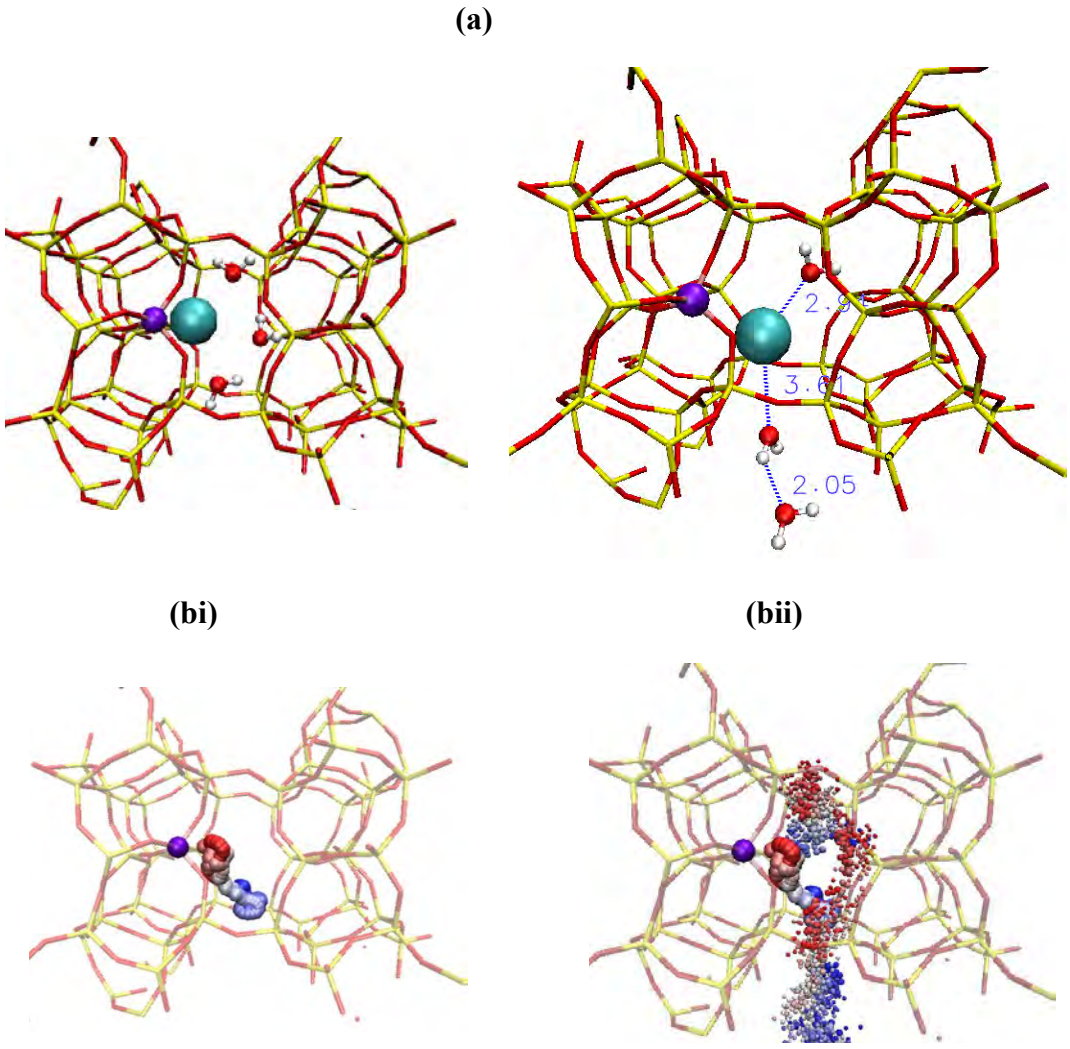

Figure 6-12 Al dopant at T4 position with Cs^+ initially located in the FER cavity in the presence of 3 H_2O molecules. Initial (left-side) and Final (right side) of a) geometry and b) trajectory of i) Cs^+ and ii) Cs^+ and 3 H_2O molecules during the simulation run.

In the final geometry obtained from the simulation run, Cs^+ ion is directly coordinated to 2 H_2O molecules, 2.91 and 3.61 Å, with the remaining H_2O is connected through H-bonding, 2.05 Å. Additionally, during the simulation two of the water molecules are pushed out of the cavity and into the MC, proving that the Cs^+ ion prefers to be coordinated to the framework zeolite oxygens than the water molecules. The Cs^+ migrates slightly towards the 8-MR window although remains trapped in the FER cavity during the simulation run, agreeing well with our previous findings obtained from static calculations. We plotted the coordination

number of Cs^+ as a function of simulation time, and each frame represents 5 fs (**Figure 6-13)** From this we were able to calculate the average (μ) number of framework oxygens (Cs^+ - O_Z) and water oxygens (Cs^+ - O_W) coordinated to Cs^+. The average values obtained are Cs^+ - O_Z : 7.46 and Cs^+ - O_W : 2.24. During the simulation run, the number of water oxygens coordinated to Cs^+ remains unaltered with a standard deviation (σ) of 0.49 while the number of framework oxygens coordinated to Cs^+ is rather labile, σ = 1.11.

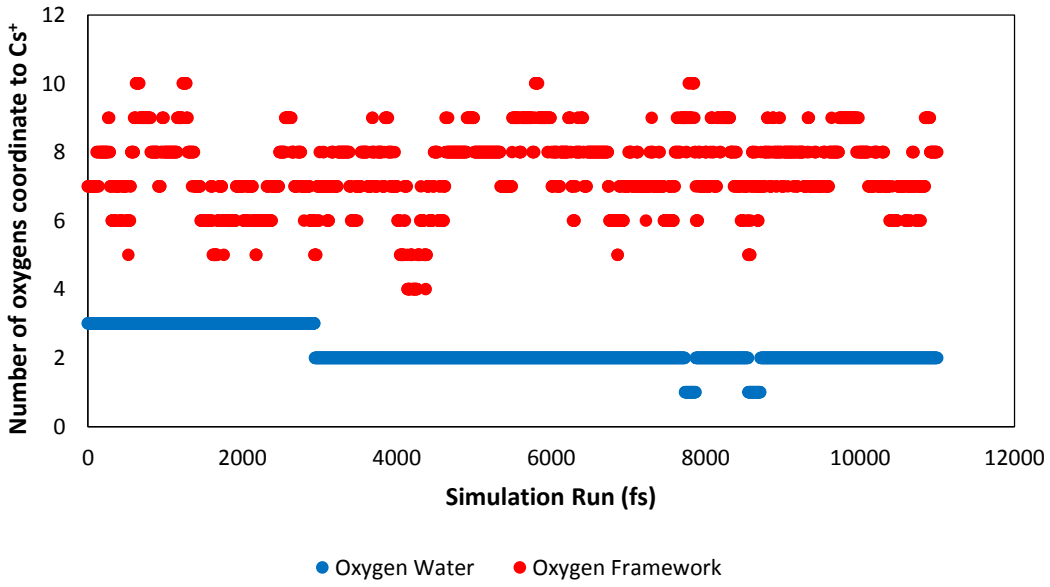

	Cs^+ - O_W	Cs^+ - O_Z
μ	2.24	7.46
σ	0.49	1.11

Figure 6-13 Al dopant at T4 with 3 H_2O molecules and Cs^+ initially located in FER cavity. Plot of the coordination number of Cs^+ as a function of simulation time, and each frame represents 5 fs. The average number and standard deviation of the number of framework oxygen (Cs^+ - O_Z) and water oxygens (Cs^+ - O_W) coordinated to the Cs^+ are presented.

Al at T2 position

Next we looked the same system although with Al dopant located at T2 position in order to determine whether the location of Al influences the coordination of Cs^+ with the water molecules, shown in **Figure 6-14**.

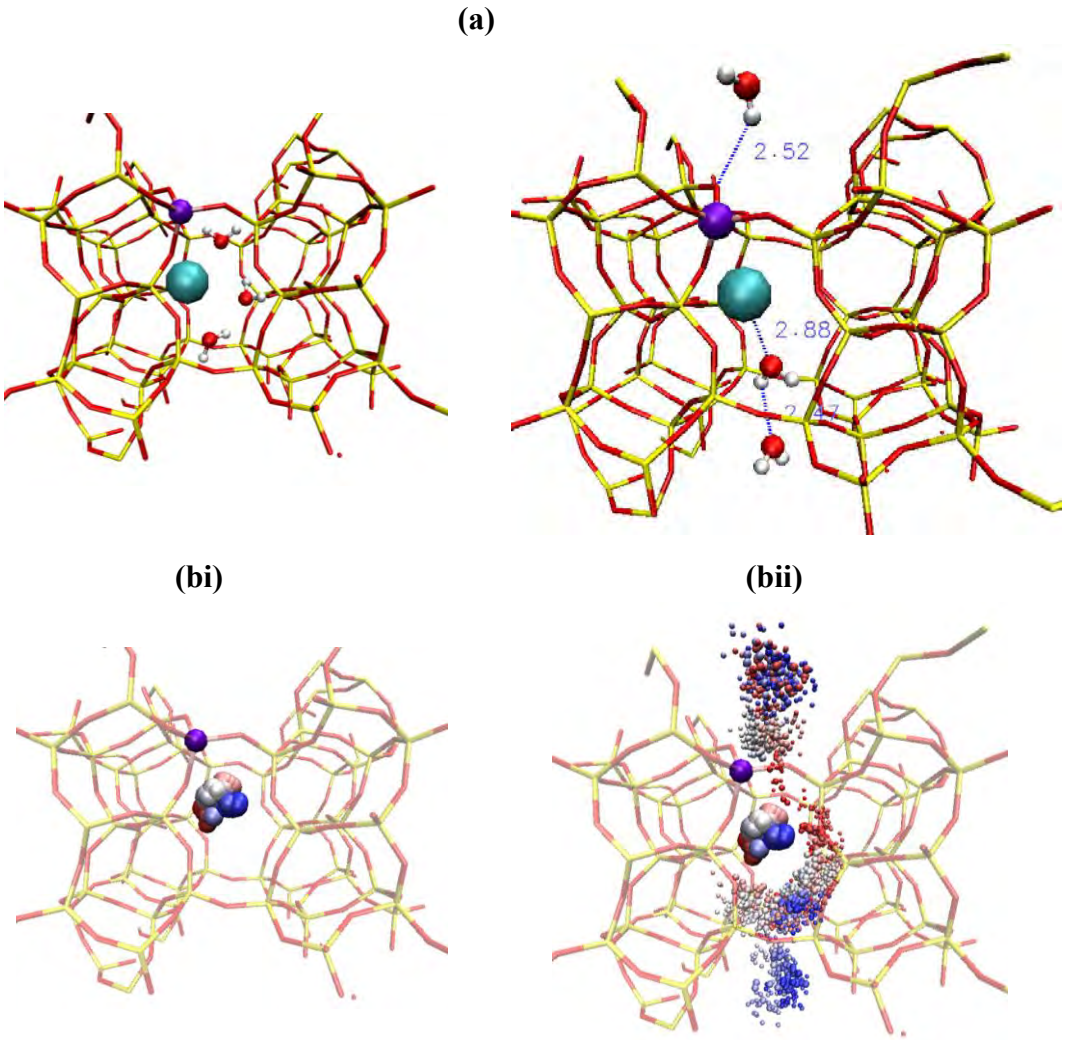

Figure 6-14 Al dopant at T2 position with Cs^+ initially located in the FER cavity in the presence of 3 H_2O molecules. Initial (left-side) and Final (right side) of a) geometry and b) trajectory of i) Cs^+ and ii) Cs^+ and 3 H_2O molecules during the simulation run.

In the final geometry, only one water molecule remains in the FER cavity, while the other two are pushed away into the MC, similar to what we observed with Al at T4. The Cs^+ is directly coordinated to one H_2O which is involved in H-bonding with the second water molecule. Due to the position of Al at T2 position located at the channel intersection, the remaining H_2O forms a H-bond (2.52 Å) with an oxygen atom nearest neighbour to Al instead of directly interacting with the Cs^+ which is what we observed with Al at T4 position. Hence, with Al located in the 8-MR window prevents Cs^+ - O_W interaction. The plot of the simulation run

against the number of oxygens coordinated to Cs^+ is shown in **Appendix: Figure 8-5 and 8-6**. **Table 6-3** shows the average and standard deviation of the Cs^+ - O_Z and Cs^+ - O_W during the simulation run. These values are similar to the ones we obtained with the simulation is performed with Al at T4 position.

	Cs^+ - O_W	**Cs^+ - O_Z**
μ	1.99	7.43
σ	0.83	1.22

Table 6-3 Al dopant at T2 with 3 H_2O molecules and Cs^+ initially located in FER cavity. The average number and standard deviation of the number Cs^+ - O_Z and Cs^+ - O_W coordinated to the Cs^+.

6.3.3.2 Cs^+ in channel intersection

All results obtained here are shown in **Appendix: Figure 8-7 to 8-10**. Initially we placed the Cs^+ at the intersection between the two channels with Al at T4 position. During the simulation run we found the cation migrates into the FER cavity due to the influence of the Al position located in the perpendicular channel. Next we introduced 4 H_2O into the system with Al located at T4 and T2 position. At both Al positions we found the Cs^+ coordinated to framework oxygens is labile compared to when coordinated with the water molecules. **Table 6-4** shows the average and standard deviation of the Cs^+ - O_Z and Cs^+ - O_W during the simulation run. With Al located at T4 the average Cs^+ - O_W coordination is 2.37 while at T2 it is 1.97. This is again due to the position of Al at T2 located at the channel intersection preventing Cs^+ – O_W interaction. We can therefore confirm that Cs^+ can coordinate with a water molecule across the 8-MR window if there is no Al dopant located in the 8-MR window.

	T4		**T2**	
	Cs^+ - O_W	Cs^+ - O_Z	Cs^+ - O_W	Cs^+ - O_Z
μ	2.37	7.55	1.97	8.30
σ	0.85	1.09	0.72	1.00

Table 6-4 Al dopant at T4 or T2 position with 4 H_2O molecules and Cs+ initially located in channel intersection of FER. The average number and standard deviation of the number Cs^+ - O_Z and Cs^+ - O_W coordinated to the Cs^+ are presented.

6.3.3.3 Cs^+ in MC

6.3.3.3.1 Dehydrated

With Cs^+ located in the MC with Al at T4 position, the trajectory of the simulation run establishes that the location of the cation remains unchanged, probably due to no Al present in the MC (**Figure 6-15**)

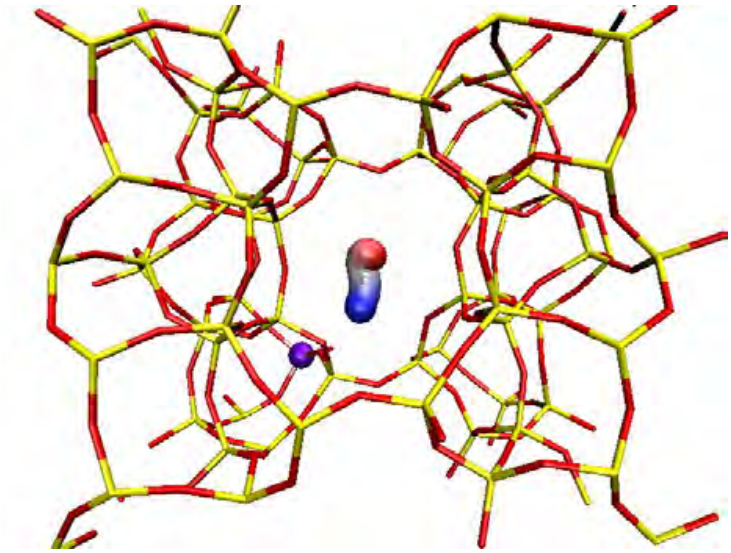

Figure 6-15 Trajectory of Cs^+ located in MC with Al dopant at T4 position in top view.

6.3.3.3.2 Hydrated

Al at T4 position

From our previous results, the total coordination number of Cs^+ is ~ 8 - 11 and thus we initially incorporated 8 H_2O molecules directly interacting with the Cs^+ ion. The initial and final geometries as well as the trajectory of Cs^+ during the simulation is shown in **Figure 6-16.** Plot of the coordination number of Cs^+ as a function of the simulation time is presented in **Figure 6-17.** In the initial stages of the simulation run we observe that the Cs^+ instantaneously loses the water molecules from 8 to 3 H_2O

molecules ending up directly coordinated to the cation. This further confirms that the cation prefers to be coordinated to the framework oxygens than the water molecules. The remaining water molecules instead prefer to migrate and self-assemble across the main channel through H-bonding. Additionally, the Cs^+ migrates from the centre to the side of the MC, in good agreement with our findings using the B3LYP functional via CRYSTAL code. With Cs^+ located in the MC, the Cs^+ - O_Z reduces to 6.87 compared to when Cs^+ is hydrated in FER cavity , ~ 7.4, due to the available space in the MC allowing 3 water molecules to interact effectively.

(a)

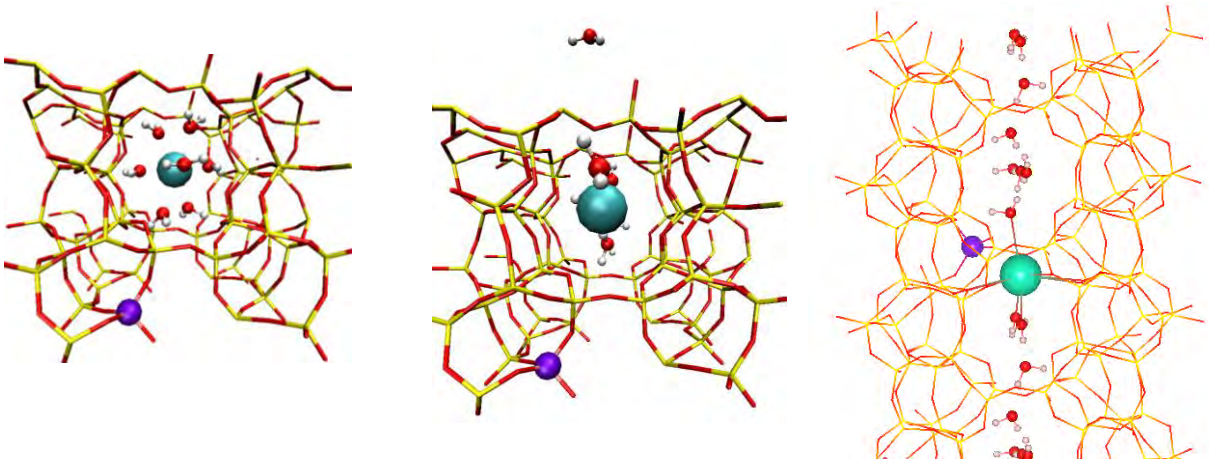

Initial *Final (Front View)* *Final (Top View)*

(b)

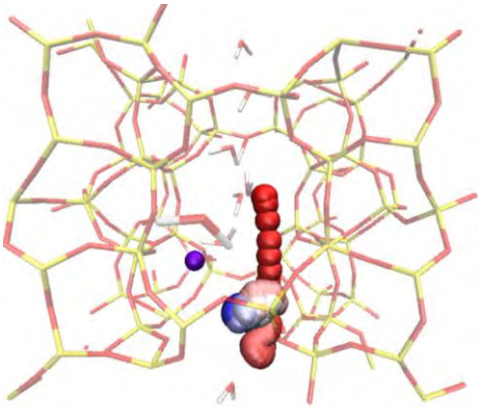

Figure 6-16 Al dopant at T4 position and Cs^+ is initially located at the centre of the MC in the presence of 8 H_2O molecules in FER. (a) geometries and (b) trajectory of Cs^+ during the simulation run.

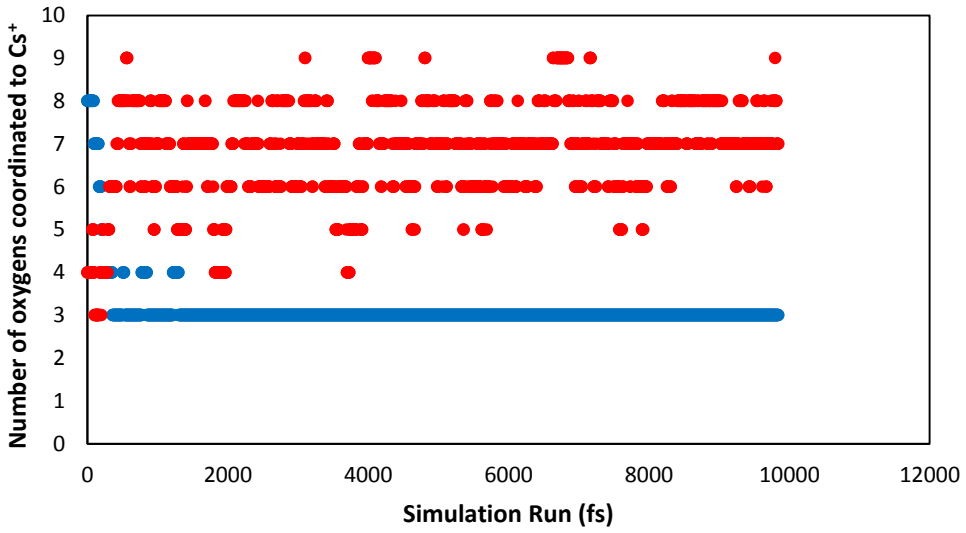

	Cs^+ - O_W	Cs^+ - O_Z
μ	3.12	6.87
σ	0.64	1.12

Figure 6-17 Al dopant at T4 and Cs^+ initially located in MC of FER in the presence of 8 H_2O molecules. Plot of the coordination number of Cs^+ as a function of simulation time, and each frame represents 5 fs. The average number and standard deviation of the number Cs^+ - O_Z and Cs^+ - O_W coordinated to the Cs^+ are presented.

Al at T2 position

Next we looked at the same system although with Al dopant located at T2 position and the geometries and the trajectory of Cs^+ during the simulation run is shown in **Figure 6-18.** Plot of the coordination number of Cs^+ as a function of the simulation time is presented in **Appendix: Figure 8-11. Table 6-5** shows the average and standard deviation of the Cs^+ - O_Z and Cs^+ - O_W during the simulation run.

	Cs^+ - O_W	Cs^+ - O_Z
μ	2.37	7.55
σ	0.85	1.09

Table 6-5 Al dopant at T4 and Cs^+ initially located in MC of FER in the presence of 8 H_2O molecules. The average number and standard deviation of the number Cs^+ - O_Z and Cs^+ - O_W coordinated to the Cs^+ are presented.

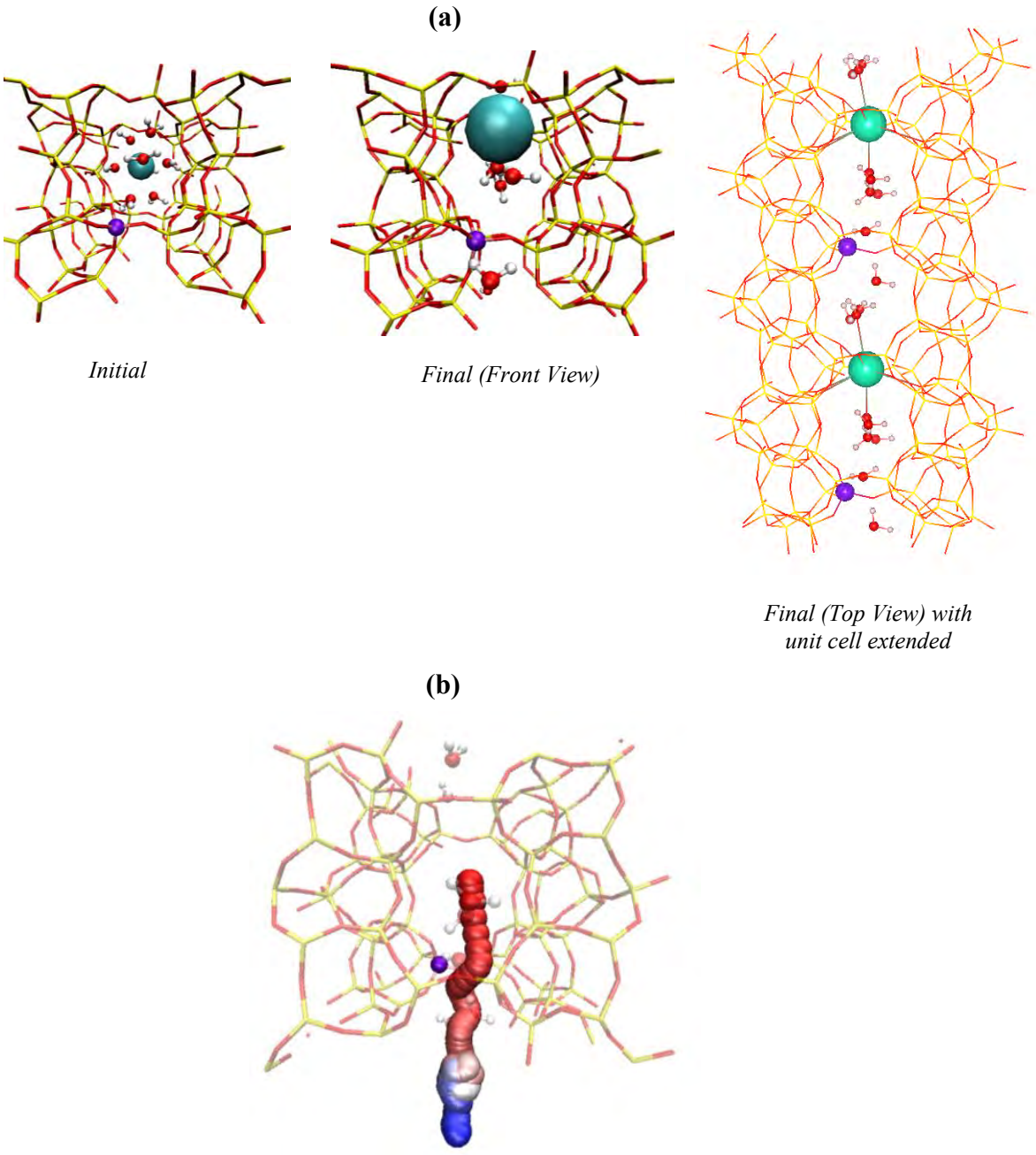

Figure 6-18 Al dopant at T2 position Cs^+ is initially located at the centre of the MC in FER in the presence of 8 H_2O molecules. (a) geometries and (b) trajectory of Cs^+ during the simulation run.

The Cs^+ ion is mobile in the presence of the water molecules much to the point where it migrates to the side of the MC in the next unit cell. The observations are similar to when Al dopant is located at T4 position in which there is a reorganization of the water molecules across the MC. The average coordination number of Cs^+ to the framework oxygens is higher, 7.55 (than with Al at T4: 6.87) again due to Al at

T2 position allowing H-bonding interaction between the hydrogen atom of the water molecule and oxygen atom nearest neighbour to Al dopant.

6.4 Conclusion

In this chapter, the location of monovalent cations in FER zeolite was studied at each of the inequivalent T positions of Al. We found the most stable location of the cations to be located at P8 site in the FER cavity and dependent on the Al position. The force field calculations underestimate the coordination number of the cation with the framework oxygens, especially with larger Rb^+ and Cs^+. We found a difference in the position of K^+ located when located at T1a and T1b position. In addition, the channel intersection cannot accommodate the larger Cs^+ ion. We focused on the hydration system of Cs^+ using static and AIMD calculations and established that the position of Cs^+ ion is affected by the Al distribution: Cs^+ can coordinate with H_2O across the 8MR window if there is no Al in the 8MR window between the channels. Al at T2 site in the 8MR, however, prevents Cs^+ - H_2O interaction as the framework oxygens rather form an H – bond with the water molecules. Moreover, Cs^+ is most stable in the small channel (SC) when Al is located at T4 position and can only interact with up to two water molecules in SC. From all our calculations, the coordination number of Cs^+ is ~ 10: Cs – H_2O is 1-3 and Cs^+ to framework O interaction is 7 – 9 and rather labile during the simulation, proving that Cs^+ rather interacts with the framework oxygens than oxygen atoms of water molecules. In addition, we identified a self-organization of water molecules across the channels next to Cs^+ and observed that migration of Cs^+ across the main channel is facile, however migration of Cs^+ across the SC is rather challenging.

Chapter 7

Conclusions and Future Work

7.1 Summary and conclusions

In this thesis, the main objective was to understand, at an atomistic scale, the interaction of aldehydes and ketones in acidic zeolites and the reaction mechanism for the formation of the enol structure required for the condensation products in the aldol reaction.

To provide insight into those two aspects, we have used first principal methods based on the density functional theory to understand the geometric and electronic structures of acetaldehyde and acetone and their interactions with the acid sites in FER an MOR zeolites. Acid catalysed reactions involving zeolites requires transfer of a proton from the Brønsted site to the adsorbed molecule. We first, in Chapter 3, built a unit cell of FER and MOR zeolite in its acidic form. Starting from a pure silica form, each of the symmetrically distinct T atoms was substituted with an Al atom and to compensate the charge difference, a proton (H^+) was placed on each of the four adjacent bridging oxygen atoms. Minimizations were carried out to locate all the possible locations of the BA sites in both zeolites using both force field and periodic DFT methods. The force field method was used to provide a good starting geometry, which an be further optimized using periodic DFT. We found that the acid sites were evenly distributed between the crystallographic positions as energy differences were not substantial, suggesting a variety of distinct BA sites. In FER, we found that T1 site is indeed split into T1a and T1b, as they differ in their local geometry. We then, in Chapter 3, studied the adsorption and interaction of acetaldehyde and acetone at the lowest energy proton location at each inequivalent

T position in both zeolites. In MOR, the adsorption energies were clearly dependent upon the stability of the isolated acid sites. In FER, this observation did not exist. In terms of the energy components, the electronic energies describe the H-bonding interaction between the adsorbate and acid site, while the dispersion energies describe the shape selectivity of the zeolite framework. The H-bond geometry was used a predictor of the intrinsic acid strength: a proton of strong acidity will be more easily donated into the hydrogen bonding causing a very strong interaction. We found that the adsorption of acetaldehyde in MOR is dependent upon the H-bond interaction and more importantly the intrinsic acid strength as the the influence of dispersion is minor due to MOR being a larger-pored zeolite. In terms of FER, the trend for acetaldehyde is weakly correlated. This is due FER being a smaller-pored zeolite and hence shape selectivity effects becomes more pronounced. When acetone is adsorbed in both zeolites, the intrinsic acid strength does not dominate the zeolite-acetone interaction. Acetone, being a larger molecule, means that the orientation of the molecule is mainly dependent on the diameters of the channels and on the curvature of the internal surface around the acid site. Here, the short-range repulsive and long-range attractive interactions become more important. Thus, the pore topology, local geometry as well as the confinement effect all influence the acetone molecule to be able to interact with the acid site. The conclusions also demonstrated that from all the possibilities of the acid sites in both zeolites, Al atom located at T3 position and the proton at O1 site in FER, proves to stabilize acetaldehyde and acetone effectively as it is also energetically stable as an isolated acid site.

In Chapter 4, we wanted to understand the mechanism of keto-enol tautomerization of acetaldehyde in gas phase and zeolites at an atomistic scale. To do this, we used

the distinguished reaction coordinate (DRC) method adopted by the CRYSTAL code. This involves a scan calculation along the internal coordinate that governs the reaction. This scan calculation consists in evolving, step by step and in a controlled way, the selected internal coordinate so to move from reactants to products by crossing a point of maximum energy. At each step, constrained geometry optimizations are performed and a complete reaction profile can be obtained for each elementary step along the chosen reaction coordinate. In gas phase, proton transfer simply occurs via an intramolecular mechanism from the methyl group to the keto group of acetaldehyde to form adsorbed enol. Previous studies suggested that for the enol form to occur in zeolites, proton transfer must take place between the acid site and acetaldehyde. Hence, we assumed that the internal coordinate that would govern the keto-enol tautomerization reaction would be the bond length between the proton of the acid site and the carbonyl oxygen of acetaldehyde. The results showed that ion-pair was not stabilized and indeed does not form a second minima, the enol product.

From our understanding, proton transfer from the acid site to acetaldehyde does not drive the formation of the enol structure. Our aim was to understand what is the kinetic bottleneck for the keto-enol tautomerization process and since the mechanism is still unknown we tried constraining several different reaction coordinates to see which one governs the reaction. The conclusions provided us an insight to the formation of a silyl ether complex, instead of the intended product, adsorbed enol. The silyl ether complex, known as intermediate III in Chapter 3, consists of the protonated acetaldehyde stabilized by a C-O bond, carbonyl carbon of acetaldehyde and a framework oxygen nearest neighbour to Al dopant. By analysing the geometries, energies and vibrational modes of a true transition state

and second minima, we can confirm the existence of this complex. This intermediate was observed at all distinct T positions in the larger and smaller channels of MOR, and only in the larger channels of FER, by the DRC method. Intermediate III could not be formed through constrained geometry optimizations at T4 position in the FER cavity due to steric repulsion. We obtained similar activation barriers forming intermediate III at the BA sites in both large and small channels of MOR. In FER, the formation of intermediate III was dependent upon the local geometry of th BA site, favourable at T1b and T3 and unfavourable at T1b and T2. This is mainly due to the position and basicity of O_B site influencing the energetics. The conclusions suggest that proton transfer is a consequence of a cooperation between the acid site and its total environment acting on the molecular adsorbate. It is the complex interplay of the adsorbate and the zeolite environment that tunes the acidity of the system, rather than simply an intrinsic property related to the composition and structure of a molecular sieve.

The formation of the silyl ether complex provided an alternate route to form the adsorbed enol product via a two-step concerted mechanism. To form the adsorbed enol from the silyl ether complex the internal coordinate constrained was the bond between a H atom from the methyl group of protonated acetaldehyde and an oxygen framework nearest neighbour to Al dopant. The overall reaction pathway reveals the second transition state, the formation of adsorbed enol from intermediate III, is the rate limiting step. This essentially means that the C-β deprotonation is the kinetic bottleneck. The stability of the adsorbed enol was dependent upon the stability of intermediate III at all T positions in both zeolites, except for T4 position in MOR, here the adsorbed enol was stabilized due to the substantial increase in dispersion

effects as the enol is formed in the side pockets.

In the remaining of Chapter 3, we then studied the keto-enol tautomerization through a one-step concerted mechanism via C-β deprotonation. Using this one-step concerted mechanism, we were able to form adsorbed enol at all T positions in both zeolites, including T4 in the FER cavity. We explored any relations between the zeolite acidity and the catalytic activity and found that in MOR the adsorption and activation energies do indeed correlate, indicating the independency of the dispersion contribution on the acid strength. In FER, this correlation was not found, due to the presence of stronger steric repulsion and confinement effect as well as the local geometry of the BA site, more importantly the position of the O_B site.

The main conclusions from Chapter 3 is that the essential difference between the two mechanisms is that formation of intermediate III containing the C-O bond is in general energetically favourable compared to the formation of adsorbed enol. The activation energies to form the enol product are similar in MOR using both mechanisms. The formation of adsorbed enol in FER at acid sites, T1a and T2, is more favourable using the two-step concerted mechanism. The stability of intermediate I and III is similar at acid sites, T1b and T3, hence the formation of adsorbed enol becomes less favourable here. This means that the formation of the enol product at T1b and T3 is more favourable using the one-step mechanism, without the need of intermediate III to be formed.

In chapter 3, we determined that the activation energy for the keto-enol tautomierzation of acetaldehyde in gas phase is very high as this mechanism occurs via an intramolecular route. We then, in Chapter 5, carried out a series of

constrained geometry optimizations to describe the keto-enol tautomeric interconversion of acetaldehyde in the presence of a single water or methanol molecule. We found that the presence of a solvent molecule reduces the activation barrier compared to in gas phase due to the presence of H-bonded interactions. The important outcome of our study is the detailed picture of the intermolecular mechanism of the tautomeric process in the presence of these solvent molecules. We have shown that with water for enolization to occur the kinetic bottleneck is not necessarily the C-β deprotonation, although with methanol it is. Constraining other reaction coordinates leads to to the formation of other unintended products - formaldehyde and ethanol.

After determining the reaction mechanism of the keto-enol tautomerization of acetaldehyde in MOR and FER zeolites, we decided in Chapter 5 to add a single water or methanol molecule to the existing system (previously adsorbed H-bonded acetaldehyde at the acid sites in zeolites) and observe whether these co-adsorbates facilitate or suppress the formation of adsorbed enol. We chose to study this with Al located at the T3 position in the larger pores of FER zeolite. This particular site has previously proved to be the most effective in stabilizing acetaldehyde as well as being energetically stable in its isolated form. We found that the presence of these solvent molecules facilitate the keto-enol tautomerism in the larger pores of FER reducing the activation barriers and stabilizing the adsorbed enol form with larger reverse barriers. The C-β deprotonation still proves to be the rate-limiting step as constraining other reaction coordinates did not result in the formation of adsorbed enol. We then wanted to replicated this system in the smaller pores of MOR zeolite and found that the presence of a water molecule suppresses the catalytic keto-enol interconversion due to the pore dimensions inviting steric repulsions. With regards to a methanol

molecule, in our optimizations we observe that this molecule prefers to be bounded to the acid site and quickly displaces the H-bonded acetaldehyde.

Up until now, the anion character of the zeolite structure due to the substitution of Si by Al has been compensated by a proton, creating Brønsted acid. The negative charged structure can also be compensated by alkali ions, which can also influence the distribution of the electron density in the framework and hence the interactions with the adsorbed species, leading to changes in the adsorption and catalytic properties. In Chapter 6, we studied the location of monovalent alkali ions - Na^+, K^+, Rb^+ and Cs^+, in FER zeolite at each distinct T positions of Al. We used force field methods to provide an initial geometry for further optimizations using periodic DFT. The force field calculations underestimate the coordination number of the cation with the framework oxygens, especially with larger ions, Rb^+ and Cs^+. We established a difference in the position of K^+ when located at T1a and T1b position, confirming the difference in there local geometry of AlO_4^-. In addition, the channel intersection between the larger pores and FER cavity cannot accommodate the larger Cs^+.

In the second part of Chapter 6, we then focused on the effect of hydration on the cesium ion using static and ab initio molecular dynamics (AIMD). The static calculations provide a faster and computationally inexpensive approach in guessing the starting geometry. We introduced 1-6 H_2O water molecules and the interaction and hydration energies demonstrated that for hydrated Cs^+ between 1-3 water molecules can only be present in the FER cavity due to shape selectivity effects and an additional H_2O molecule is likely to form H-bonding. The AIMD simulations provided us an insight in terms of a dynamical point of view on the various configurations of the guest molecules and the flexibility of the zeolite framework.

The simulations established that a maximum of 2 water molecules can be present in the FER cavity and directly linked to the Cs^+ and the remaining form a H-bond network across the channels. From the simulations, we observed that the water molecules are the migrating species and cesium ion is rather immobile and trapped in the FER cavity regardless of the hydration level. We found that Cs^+ is most stable in the FER cavity when the Al is located at T4 position. In the main channels, the Cs^+ interacts with a maximum of 3 H_2O molecules and the remaining water molecules instead migrate and self-assemble across the main channel through H-bonding. Here, the presence of water molecules facilitate the migration of Cs^+ compared to a dehydrated system. From these analyses, the location of Al affects the coordination of cesium ion with the water molecules. Cs^+ can coordinate with a H_2O across the 8MR window if there is no Al in the 8MR window. Al located at T2 position in the 8MR window, however, prevents $Cs^+ - H_2O$ interaction as the framework oxygens rather form an H – bond with the water molecule. We found that Cs^+ is most stable in the FER cavity when the Al is located at T4 position. From our calculations, the coordination number of $Cs^+ \sim 10$ whereby $Cs^+ - H_2O$ is 1-3 and Cs^+ to framework O (Cs^+ - O_Z) interaction is 7 – 9. $Cs^+ - O_Z$ proves to be rather labile during the simulations and in addition cesium ion prefers to interact with the framework oxygens than oxygen atoms of water molecules.

7.2 Future Work

Concerning the main objective of this thesis, i.e. understanding the keto-enol tautomerization mechanism in zeolites, we have identified a one and two step concerted reaction mechanism for acetaldehyde. We would like to extend the investigation by replicating these mechanisms for acetone in both MOR and FER,

and compare the geometry, activation barriers and the potential energy surface with acetaldehyde. In this way, we can identify the role of acidity, confinement effect and shape/size selectivity since acetone is a larger base molecule. We would also consider the presence of a solvent molecule i.e. water and methanol, on the enolization mechanism in the larger pores of MOR and compare the findings with the larger pores of FER in order to discriminate the zeolite environment. We would also reconstruct the self and cross condensation reaction of these base molecules, acetaldehyde and acetone, to produce the aldol product in both zeolites. By doing this, we can understand the reaction mechanism at an atomistic scale whether it is similar to what have been observed previously in gas phase and solution or it is completely different in zeolites and ultimately determine the rate-limiting step by performing several constrained geometry optimizations.

Regarding the final part of the thesis *i.e.* the migration of cesium ion in FER, we could consider performing metadynamics simulations which is specifically designed to sample rare events, taking into account the hydration effects by sampling free energy surfaces. This would allow us to explore the reaction pathway of hydrated cesium from the FER cavity and across the 8-MR window, which proves to be challenging. We would consider exploring the migration of sodium ion in FER in a dehydrated/ hydrated system and compare the findings with cesium ion. In addition, we could also extend the investigation by determining the stability of monovalent alkali ions in MOR at the inequivalent T positions in both dehydrated and hydrated system and identify the role of pore topology influencing the migration process and coordination number; and compare these findings with FER.

Chapter 8

Appendix

8.1 Tables related to Chapter 3

Pair potential parameters and charges carried by the atoms in force field reported by Catlow *et al.*

Species	Charge/ *e*	Core-shell interactions/ eV Å $^{-2}$
Al	3.000000	
Si	4.000000	
O1 (core)	0.869020	
O1 (shell)	-2.869020	74.920000
O2 (core)	-1.426000	
H	0.426000	

Table 8-1 Buckingham potential (short range cut off: 12 Å): $V(r) = A \exp(-\rho r) + C/r^6$

Ion pair	*A* / eV	*P* / Å	*C* / eV Å^6
Si – O1	1283.9070	0.320520	10.66158
Al – O1	1460.3000	0.299120	0.00000
Si – O2	983.55660	0.320520	10.66158
Al – O2	1142.6775	0.299120	0.00000
O1 – O1	22764.000	0.149000	27.88000
O1 – O2	22764.000	0.149000	27.88000
O2 – O2	22764.000	0.149000	27.88000
H – O1	311.97000	0.250000	0.00000
H – O2	311.97000	0.250000	0.00000

Table 8-2 Hamonic three-body potential: $V(\theta_{ijk}) = k(\theta_{ijk} - \theta_0)^2$

8.2 Figures related to Chapter 4

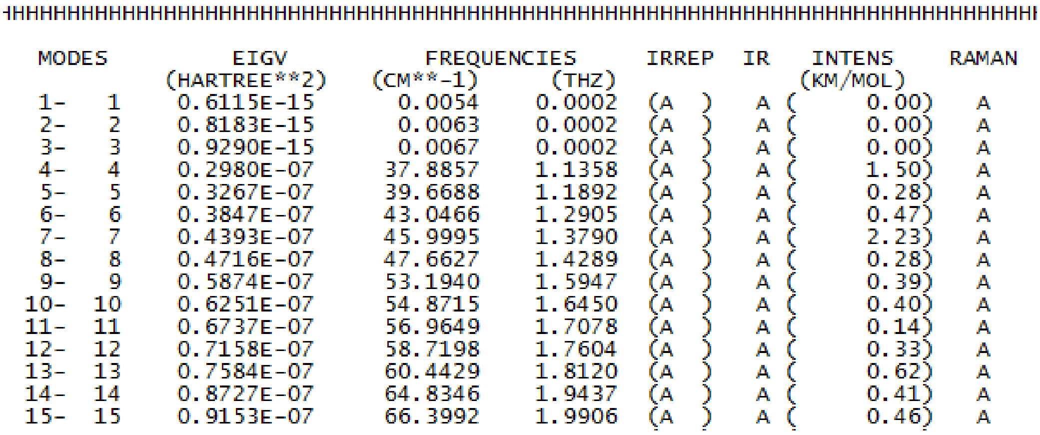

```
HHHHHHHHHHHHHHHHHHHHHHHHHHHHHHHHHHHHHHHHHHHHHHHHHHHHHHHHHHHHHHHHHHHHHHHHHHHHH

 MODES         EIGV          FREQUENCIES     IRREP  IR   INTENS    RAMAN
           (HARTREE**2)   (CM**-1)     (THZ)             (KM/MOL)
  1-   1    0.6115E-15      0.0054    0.0002  (A  )   A (     0.00)   A
  2-   2    0.8183E-15      0.0063    0.0002  (A  )   A (     0.00)   A
  3-   3    0.9290E-15      0.0067    0.0002  (A  )   A (     0.00)   A
  4-   4    0.2980E-07     37.8857    1.1358  (A  )   A (     1.50)   A
  5-   5    0.3267E-07     39.6688    1.1892  (A  )   A (     0.28)   A
  6-   6    0.3847E-07     43.0466    1.2905  (A  )   A (     0.47)   A
  7-   7    0.4393E-07     45.9995    1.3790  (A  )   A (     2.23)   A
  8-   8    0.4716E-07     47.6627    1.4289  (A  )   A (     0.28)   A
  9-   9    0.5874E-07     53.1940    1.5947  (A  )   A (     0.39)   A
 10-  10    0.6251E-07     54.8715    1.6450  (A  )   A (     0.40)   A
 11-  11    0.6737E-07     56.9649    1.7078  (A  )   A (     0.14)   A
 12-  12    0.7158E-07     58.7198    1.7604  (A  )   A (     0.33)   A
 13-  13    0.7584E-07     60.4429    1.8120  (A  )   A (     0.62)   A
 14-  14    0.8727E-07     64.8346    1.9437  (A  )   A (     0.41)   A
 15-  15    0.9153E-07     66.3992    1.9906  (A  )   A (     0.46)   A
```

Figure 8-1 The output file from using CRYSTAL code illustrating the calculation of the vibrational frequency. No negative eigenvalues found confirming the presence of a local minima corresponding to intermediate III obtained at T3 position in small channels of MOR zeolite.

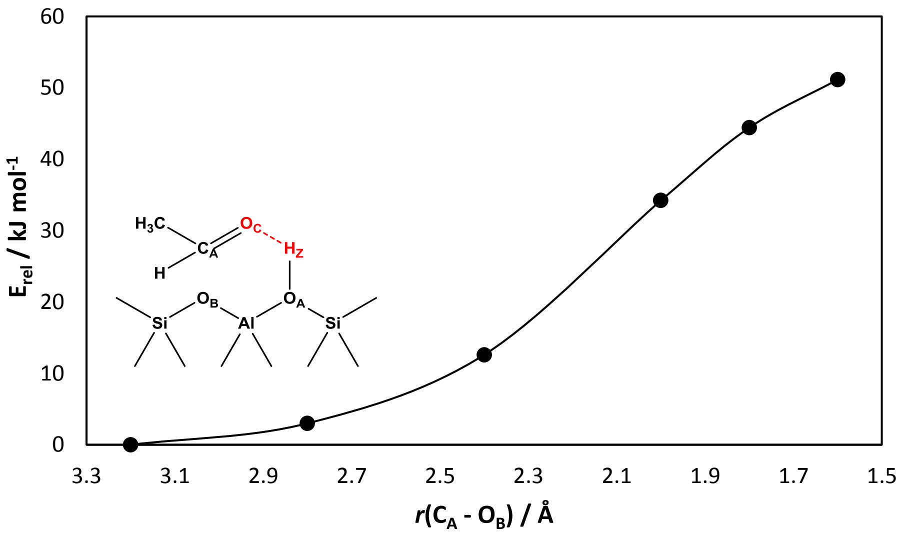

Figure 8-2 Internal energy profile for the proton transfer using reaction coordinate, r**(**C_A **–** O_B**)**, the distance between the carbon atom of the keto group and a neighbouring oxygen atom nearest neighbour to Al dopant, at T4 position located in the FER cavity. (a) O_A and O_B site: O6.

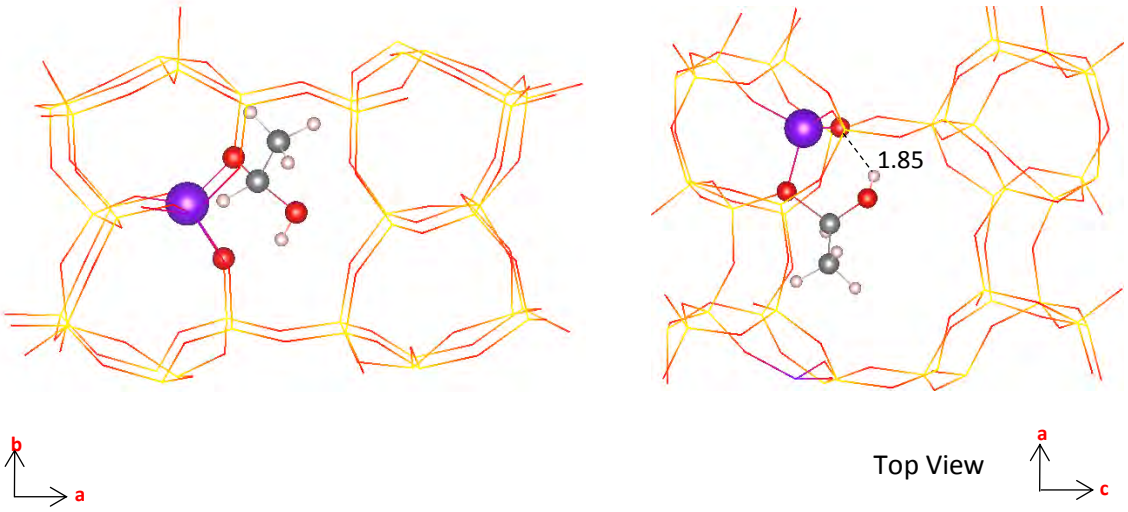

Figure 8-3 Geometrical structure corresponding to the internal reaction coordinate, ***r*(C$_A$ – O$_B$)**, shown in Figure 8-2, constrained at 1.60 Å. The formation of C_A – O_B stabilizing the protonated acetaldehyde is unstable and hence intermediate III cannot be accomplished. The O_A – H_Z bond distance is 1.85 and due to the pore size of FER cavity, a full optimization would lead the H_Z proton returning back to O_A site recreating the BA site and H-bonded complex of acetaldehyde.

8.3 Figures related to Chapter 5

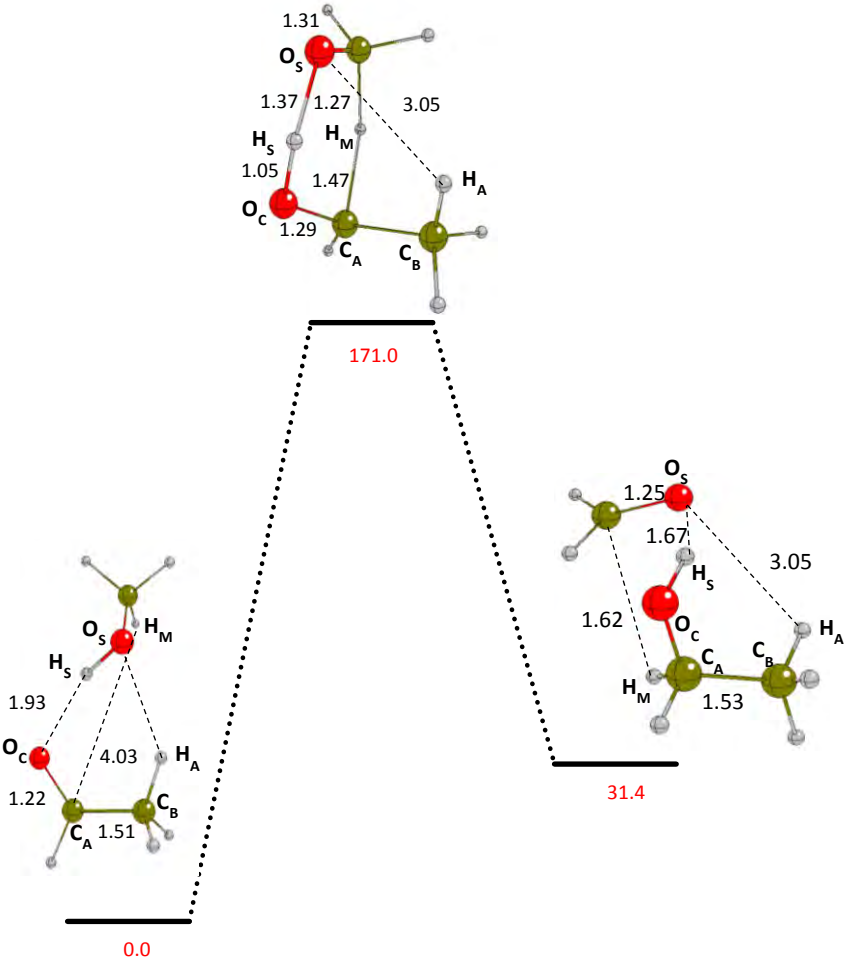

Figure 8-4 PES profile of acetaldehyde interacting with a methanol molecule by constraining the reaction coordinate, $r(H_S - O_C)$, the distance between the hydrogen from the water molecule and carbonyl oxygen of acetaldehyde. Instead of forming enol – CH_3OH, we formed formaldehyde and ethanol Energy in kJ mol^{-1}.

8.4 Figures related to Chapter 6

Pair potential parameters and charges carried by the atoms in force field reported by Catlow *et* al.

Species	Charge/ *e*	Core-shell interactions/ eV Å $^{-2}$
Al	3.000000	
Si	4.000000	
O (core)	0.869020	
O (shell)	-2.869020	74.920000
Na	1.00000	

Table 8-3 Buckingham potential (short range cut off: 12 Å): $V(r) = A \exp(-\rho r) + C/r^6$

Ion pair	*A* / eV	*P* / Å	*C* / eV Å^6
Si – O	1283.9070	0.320520	10.66158
Al – O1	1460.3000	0.299120	0.00000
O – O	22764.000	0.149000	27.88000
Na – O	1226.840	0.30650	0.00000
Na – Na	7895.400	0.17090	0.00000

Table 8-4 Hamonic three-body potential: $V(\theta ijk) = k(\theta ijk - \theta 0)^2$

Ion pair	*k* / eV rad^{-2}	Θ_0 / °
O – Si – O	2.09724	109.47
O – Al – O	2.09724	109.47

Table 8-5 Buckingham potential (short range cut off: 12 Å): $V(r) = A \exp(-\rho r) + C/r^6$

Ion pair	*A* / eV	*P* / Å	*C* / eV Å^6
K – O	1000.3000	0.361980	10.56900
Rb – O	1030.8000	0.379300	0.00000
Cs – O	1065.3000	0.391100	0.00000

Table 8-6 Pair potential parameters model the interactions between cations and the zeolite framework.

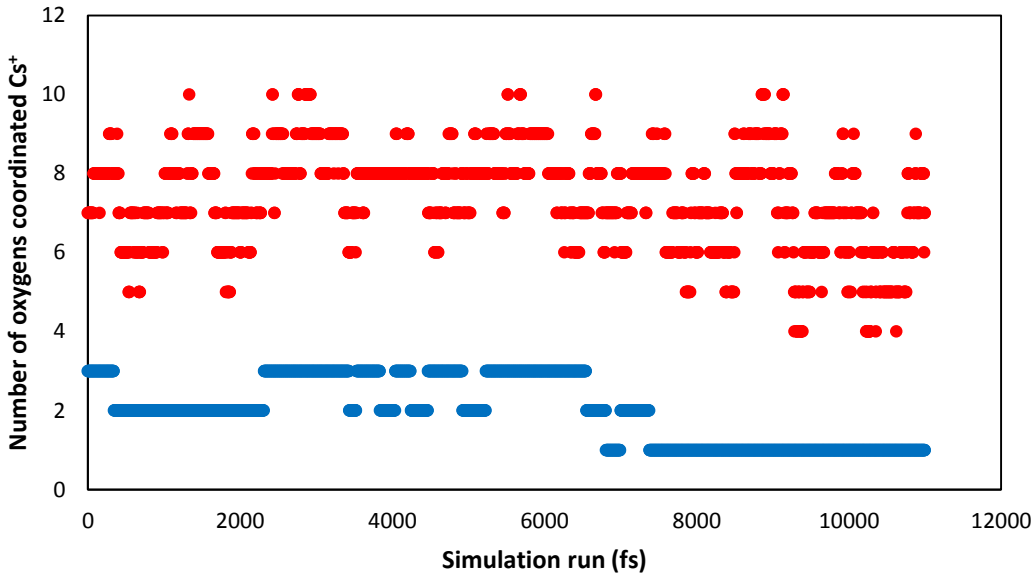

Figure 8-5 Al dopant at T2 with 3 H_2O molecules and Cs^+ initially located in FER cavity. Plot of the coordination number of Cs^+ as a function of simulation time, and each frame represents 5 fs.

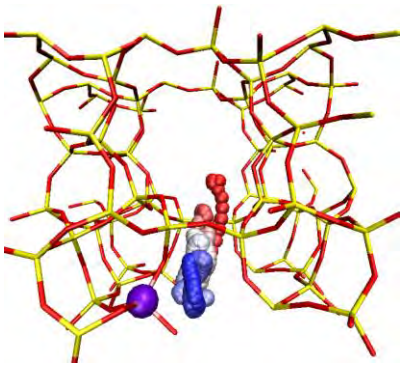

Figure 8-6 Trajectory of Cs^+ initially located in channel intersection of FER with Al dopant at T4 position.

(a)

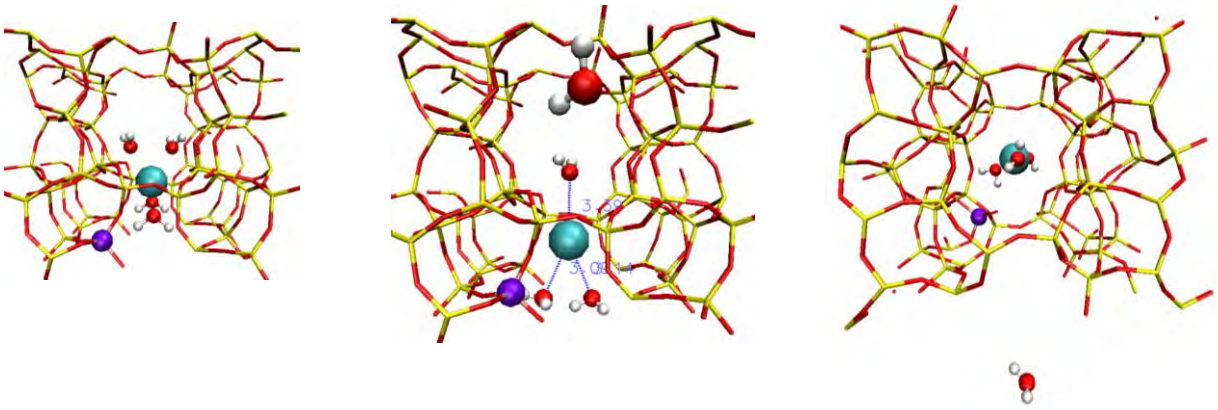

Initial *Final (Front View)* *Final (Top View)*

(b)

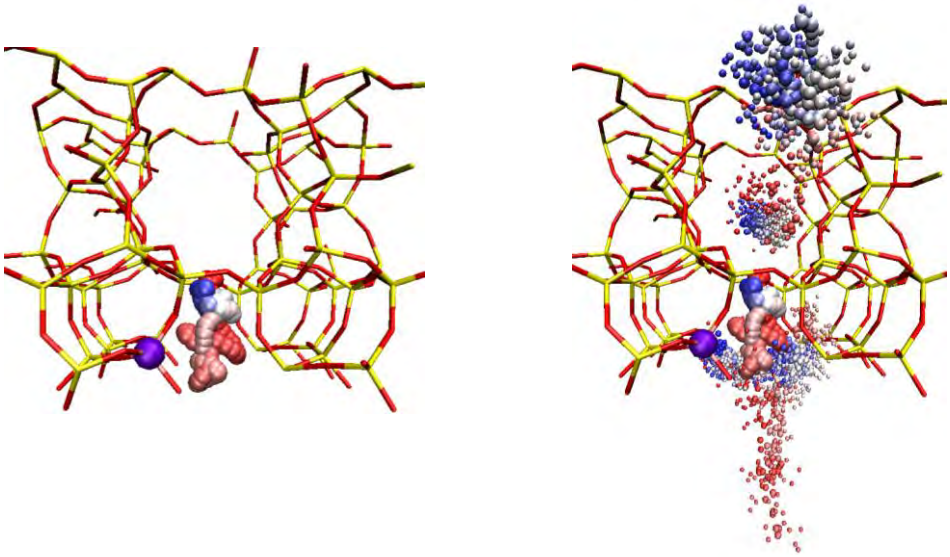

Initial *Final*

Figure 8-7 Al dopant at T4 position with Cs^+ initially located in the channel intersection in the presence of 4 H_2O molecules in FER. (a) Geometries and (b) Trajectories of (i) Cs^+ and (ii) Cs^+ and 4 H_2O during the simulation run.

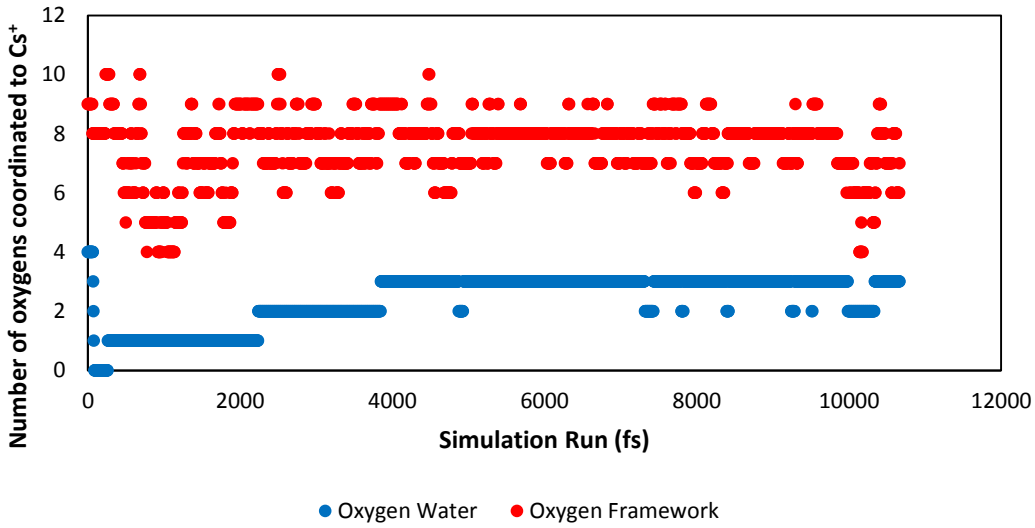

Figure 8-8 Al dopant at T4 position with Cs^+ initially located in the channel intersection in the presence of 4 H_2O molecules in FER. Plot of the coordination number of Cs^+ as a function of simulation time, and each frame represents 5 fs.

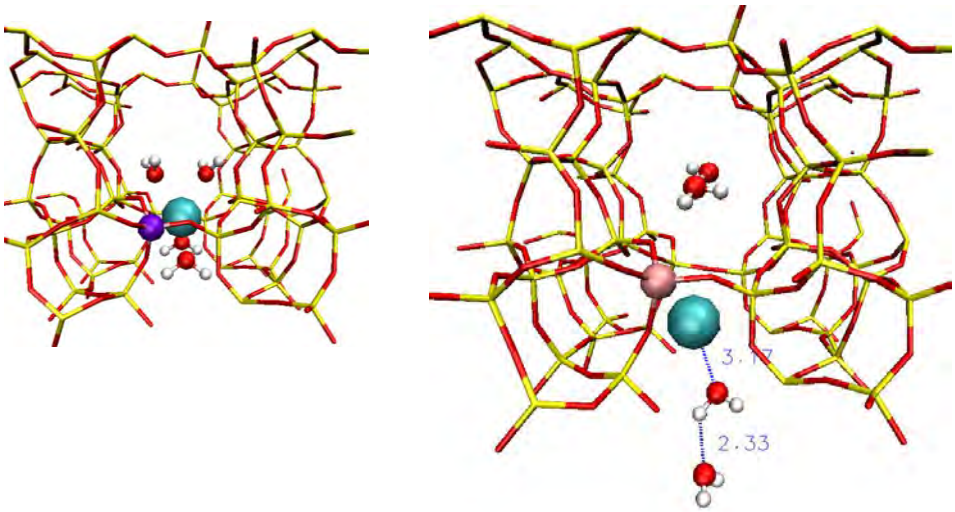

Initial *Final*

Figure 8-9 Al dopant at T2 position with Cs^+ initially located in the channel intersection in the presence of 4 H_2O molecules in FER. (a) Geometries and (b) Trajectories of (i) Cs^+ and (ii) Cs^+ and 4 H_2O during the simulation run.

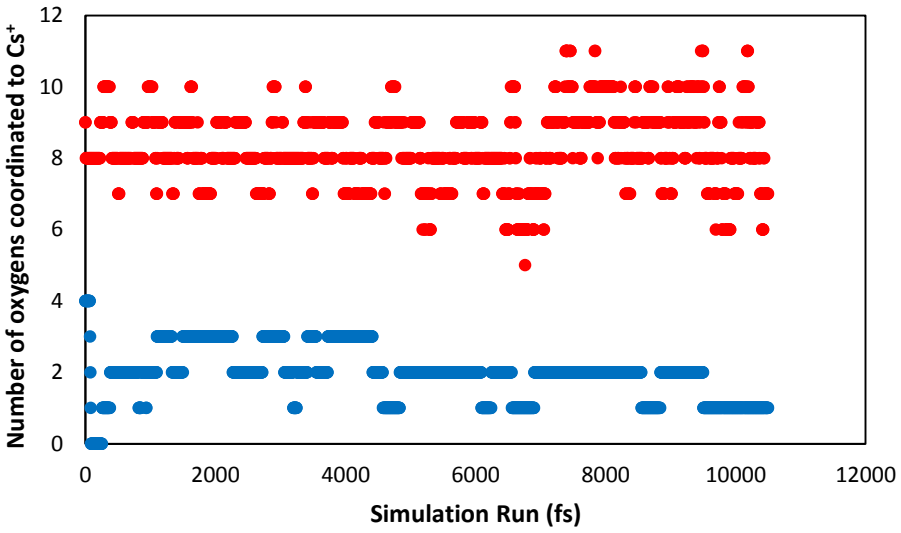

Figure 8-10 Al dopant at T2 position with Cs^+ initially located in the channel intersection in the presence of 4 H_2O molecules in FER. Plot of the coordination number of Cs^+ as a function of simulation time, and each frame represents 5 fs.

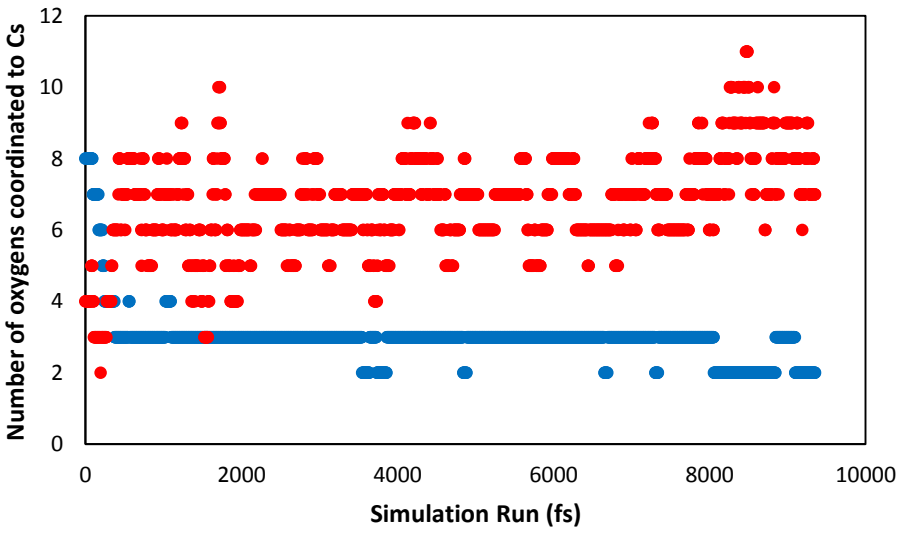

Figure 8-11 Al dopant at T2 position with Cs^+ initially located in the MC of FER in the presence of 8 H_2O molecules. Plot of the coordination number of Cs^+ as a function of simulation time, and each frame represents 5 fs.

References

Agullo, J., N. Kumar, D. Berenguer, D. Kubicka, A. Marcilla, A. Gomez, T. Salmi and D. Y. Murzin. (2007), 'Catalytic Pyrolysis of Low Density Polyethylene over H-Beta, H-Y, H-Mordenite, and H-Ferrierite Zeolite Catalysts: Influence of Acidity and Structures', *Kinetics and Catalysis* Vol. 48, No. 4, pp. 535-540.

Alberti, A. (1997), 'Location of Bronsted Sites in Mordenite', *Zeolites* Vol. 19, No. 5-6, pp. 411-415.

Alberti, A., P. Davoli and G. Vezzalini. (1986), 'The Crystal-Structure Refinement of a Natural Mordenite', *Zeitschrift Fur Kristallographie* Vol. 175, No. 3-4, pp. 249-256.

Ali, S. M., S. De and D. K. Maity. (2007), 'Microhydration of Cs+ Ion: A Density Functional Theory Study on Cs+-(H2o)(N) Clusters (N=1-10)', *Journal of Chemical Physics* Vol. 127, No. 4, pp. 11.

Allen, P. W., H. J. M. Bowen, L. E. Sutton and O. Bastiansen. (1952), 'The Molecular Structure of Acetone', *Transactions of the Faraday Society* Vol. 48, No. 11, pp. 991-995.

Anbarasan, P., Z. C. Baer, S. Sreekumar, E. Gross, J. B. Binder, H. W. Blanch, D. S. Clark and F. D. Toste. (2012), 'Integration of Chemical Catalysis with Extractive Fermentation to Produce Fuels', *Nature* Vol. 491, No. 7423, pp. 235-239.

Arean, C. O., G. T. Palomino, E. Garrone, D. Nachtigallova and P. Nachtigall. (2006), 'Combined Theoretical and Ftir Spectroscopic Studies on Hydrogen Adsorption on the Zeolites Na-Fer and K-Fer', *Journal of Physical Chemistry B* Vol. 110, No. 1, pp. 395-402.

Auroux, A. and J. Datka. (1997), 'Microcalorimetric and Ir Spectroscopic Studies of Pyridine Sorption in Nah-Mordenites', *Applied Catalysis a-General* Vol. 165, No. 1-2, pp. 473-479.

Baerlocher, C., L. B. McCusker and D. H. Olson. (2007), *Atlas of Zeolite Framework Types*, Elsevier Science.

Bankos, I., J. Valyon, G. I. Kapustin, D. Kallo, A. L. Klyachko and T. R. Brueva. (1988), 'Acidic and Catalytic Properties of Hydrogen Sodium Mordenite', *Zeolites* Vol. 8, No. 3, pp. 189-195.

Barthomeuf, D. (1987), 'Zeolite Acidity Dependence on Structure and Chemical Environment - Correlations with Catalysis', *Materials Chemistry and Physics* Vol. 17, No. 1-2, pp. 49-71.

Barthomeuf, D. (1991), 'Acidity and Basicity in Zeolites', *Catalysis and Adsorption by Zeolites* Vol. 65, pp. 157-169.

Becke, A. D. (1993), 'Density-Functional Thermochemistry .3. The Role of Exact Exchange', *Journal of Chemical Physics* Vol. 98, No. 7, pp. 5648-5652.

Bell, V. A. and H. S. Gold. (1983), 'C-13 Nuclear Magnetic-Resonance Studies of the Aldol Condensation Products of Acetone on an Activated Alumina Catalyst', *Journal of Catalysis* Vol. 79, No. 2, pp. 286-290.

Benco, L., T. Bucko, R. Grybos, J. Hafner, Z. Sobalik, J. Dedecek and J. Hrusak. (2007), 'Adsorption of No in Fe2+-Exchanged Ferrierite. A Density Functional Theory Study', *Journal of Physical Chemistry C* Vol. 111, No. 2, pp. 586-595.

Berendsen, H. J. C., J. P. M. Postma, W. F. Vangunsteren, A. Dinola and J. R. Haak. (1984), 'Molecular-Dynamics with Coupling to an External Bath', *Journal of Chemical Physics* Vol. 81, No. 8, pp. 3684-3690.

Bevilacqua, M. and G. Busca. (2002), 'A Study of the Localization and Accessibility of Bronsted and Lewis Acid Sites of H-Mordenite through the Ft-Ir Spectroscopy of Adsorbed Branched Nitriles', *Catalysis Communications* Vol. 3, No. 11, pp. 497-502.

Bhan, A., A. D. Allian, G. J. Sunley, D. J. Law and E. Iglesia. (2007), 'Specificity of Sites within Eight-Membered Ring Zeolite Channels for Carbonylation of Methyls to Acetyls', *Journal of the American Chemical Society* Vol. 129, No. 16, pp. 4919-4924.

Bhan, A. and E. Iglesia. (2008), 'A Link between Reactivity and Local Structure in Acid Catalysis on Zeolites', *Accounts of Chemical Research* Vol. 41, No. 4, pp. 559-567.

Biaglow, A. I., J. Sepa, R. J. Gorte and D. White. (1995), 'A C-13 Nmr-Study of the Condensation Chemistry of Acetone and Acetaldehyde Adsorbed at the Bronsted Acid Sites in H-Zsm-5', *Journal of Catalysis* Vol. 151, No. 2, pp. 373-384.

Bludsky, O., M. Silhan, P. Nachtigall, T. Bucko, L. Benco and J. Hafner. (2005), 'Theoretical Investigation of Co Interaction with Copper Sites in Zeolites:

Periodic Dft and Hybrid Quantum Mechanical/Interatomic Potential Function Study', *Journal of Physical Chemistry B* Vol. 109, No. 19, pp. 9631-9638.

Bodart, P., J. B. Nagy, G. Debras, Z. Gabelica and P. A. Jacobs. (1986), 'Aluminum Siting in Mordenite and Dealumination Mechanism', *Journal of Physical Chemistry* Vol. 90, No. 21, pp. 5183-5190.

Boekfa, B., P. Pantu, M. Probst and J. Limtrakul. (2010), 'Adsorption and Tautomerization Reaction of Acetone on Acidic Zeolites: The Confinement Effect in Different Types of Zeolites', *Journal of Physical Chemistry C* Vol. 114, No. 35, pp. 15061-15067.

Bordiga, S., C. Lamberti, F. Bonino, A. Travert and F. Thibault-Starzyk. (2015), 'Probing Zeolites by Vibrational Spectroscopies', *Chemical Society Reviews* Vol. 44, No. 20, pp. 7262-7341.

Bordiga, S., G. T. Palomino, C. Paze and A. Zecchina. (2000), 'Vibrational Spectroscopy of H-2, N-2, Co and No Adsorbed on H, Li, Na, K-Exchanged Ferrierite', *Microporous and Mesoporous Materials* Vol. 34, No. 1, pp. 67-80.

Borges, P., R. R. Pinto, M. Lemos, F. Lemos, J. C. Vedrine, E. G. Derouane and F. R. Ribeiro. (2005), 'Activity-Acidity Relationship for Alkane Cracking over Zeolites: N-Hexane Cracking over Hzsm-5', *Journal of Molecular Catalysis a-Chemical* Vol. 229, No. 1-2, pp. 127-135.

Boronat, M. and A. Corma. (2015), 'Factors Controlling the Acidity of Zeolites', *Catalysis Letters* Vol. 145, No. 1, pp. 162-172.

Boronat, M. and A. Corma. (2019), 'What Is Measured When Measuring Acidity in Zeolites with Probe Molecules?', *Acs Catalysis* Vol. 9, No. 2, pp. 1539-1548.

Boronat, M., P. M. Viruela and A. Corma. (2004), 'Reaction Intermediates in Acid Catalysis by Zeolites: Prediction of the Relative Tendency to Form Alkoxides or Carbocations as a Function of Hydrocarbon Nature and Active Site Structure', *Journal of the American Chemical Society* Vol. 126, No. 10, pp. 3300-3309.

Brand, H. V., L. A. Curtiss and L. E. Iton. (1992), 'Computational Studies of Acid Sites in Zsm-5 - Dependence on Cluster Size', *Journal of Physical Chemistry* Vol. 96, No. 19, pp. 7725-7732.

Brand, H. V., L. A. Curtiss and L. E. Iton. (1993), 'Ab-Initio Molecular-Orbital Cluster Studies of the Zeolite Zsm-5 .1. Proton Affinities', *Journal of Physical Chemistry* Vol. 97, No. 49, pp. 12773-12782.

Brandle, M. and J. Sauer. (1998), 'Acidity Differences between Inorganic Solids Induced by Their Framework Structure. A Combined Quantum Mechanics Molecular Mechanics Ab Initio Study on Zeolites', *Journal of the American Chemical Society* Vol. 120, No. 7, pp. 1556-1570.

Breck, D. W. (1974), *Zeolite Molecular Sieves: Structure, Chemistry and Use*, John Wiley & Sons.

Brogaard, R. Y., C. M. Wang and F. Studt. (2014), 'Methanol-Alkene Reactions in Zeotype Acid Catalysts: Insights from a Descriptor-Based Approach and Microkinetic Modeling', *Acs Catalysis* Vol. 4, No. 12, pp. 4504-4509.

Bucko, T., L. Benco, T. Demuth and J. Hafner. (2002), 'Ab Initio Density Functional Investigation of the (001) Surface of Mordenite', *Journal of Chemical Physics* Vol. 117, No. 15, pp. 7295-7305.

Bucko, T. and J. Hafner. (2015), 'The Role of Spatial Constraints and Entropy in the Adsorption and Transformation of Hydrocarbons Catalyzed by Zeolites', *Journal of Catalysis* Vol. 329, pp. 32-48.

Catlow, C. R. A., R. G. Bell, J. D. Gale and D. W. Lewis. (1995), 'Modelling of Structure and Reactivity in Zeolites', *Zeolites: a Refined Tool for Designing Catalytic Sites* Vol. 97, pp. 87-100.

Chen, D. T., S. B. Sharma, I. Filimonov and J. A. Dumesic. (1992), 'Microcalorimetric Studies of Zeolite Acidity', *Catalysis Letters* Vol. 12, No. 1-3, pp. 201-212.

Chen, D. T., L. Zhang, C. Yi and J. A. Dumesic. (1994), 'Methylamine Synthesis over Solid Acid Catalysts - Microcalorimetric and Infrared Spectroscopic Studies of Adsorbed Species', *Journal of Catalysis* Vol. 146, No. 1, pp. 257-267.

Cherkasov, N., T. Vazhnova and D. B. Lukyanov. (2016), 'Quantitative Infra-Red Studies of Bronsted Acid Sites in Zeolites: Case Study of the Zeolite Mordenite', *Vibrational Spectroscopy* Vol. 83, pp. 170-179.

Chiang, Y., A. J. Kresge and N. P. Schepp. (1989), 'Temperature Coefficients of the Rates of Acid-Catalyzed Enolization of Acetone and Ketonization of Its Enol in Aqueous and Acetonitrile Solutions - Comparison of Thermodynamic Parameters for the Keto-Enol Equilibrium in Solution with Those in the Gas-Phase', *Journal of the American Chemical Society* Vol. 111, No. 11, pp. 3977-3980.

Chibani, S., M. Chebbi, S. Lebegue, T. Bucko and M. Badawi. (2016), 'A Dft Investigation of the Adsorption of Iodine Compounds and Water in H-, Na-, Ag-, and Cu- Mordenite', *Journal of Chemical Physics* Vol. 144, No. 24, pp. 10.

Chu, Y. Y., B. Han, A. M. Zheng, X. F. Yi and F. Deng. (2013), 'Pore Selectivity for Olefin Protonation Reactions Confined inside Mordenite Zeolite: A Theoretical Calculation Study', *Journal of Physical Chemistry C* Vol. 117, No. 5, pp. 2194-2202.

Civalleri, B., P. D'Arco, R. Orlando, V. R. Saunders and R. Dovesi. (2001), 'Hartree-Fock Geometry Optimisation of Periodic Systems with the Crystal Code', *Chemical Physics Letters* Vol. 348, No. 1-2, pp. 131-138.

Corma, A. (1995), 'Inorganic Solid Acids and Their Use in Acid-Catalyzed Hydrocarbon Reactions', *Chemical Reviews* Vol. 95, No. 3, pp. 559-614.

Cucinotta, C. S., A. Ruini, A. Catellani and A. Stirling. (2006), 'Ab Initio Molecular Dynamics Study of the Keto-Enol Tautomerism of Acetone in Solution', *Chemphyschem* Vol. 7, No. 6, pp. 1229-1234.

Datka, J., B. Gil and A. Kubacka. (1996), 'Heterogeneity of Oh Groups in H-Mordenites: Effect of Dehydroxylation', *Zeolites* Vol. 17, No. 5-6, pp. 428-433.

Debras, G., J. B. Nagy, Z. Gabelica, P. Bodart and P. A. Jacobs. (1983), 'Determination of Silicon-Aluminium Orderings in Mordenite and Its Aluminum Deficient Forms Using High-Resolution Magic-Angle-Spinning Si-29-Nmr', *Chemistry Letters*, No. 2, pp. 199-202.

Dedecek, J., M. J. Lucero, C. B. Li, F. Gao, P. Klein, M. Urbanova, Z. Tvaruzkova, P. Sazama and S. Sklenak. (2011), 'Complex Analysis of the Aluminum Siting in the Framework of Silicon-Rich Zeolites. A Case Study on Ferrierites', *Journal of Physical Chemistry C* Vol. 115, No. 22, pp. 11056-11064.

Demuth, T., J. Hafner, L. Benco and H. Toulhoat. (2000), 'Structural and Acidic Properties of Mordenite. An Ab Initio Density-Functional Study', *Journal of Physical Chemistry B* Vol. 104, No. 19, pp. 4593-4607.

Derouane, E. G., J. M. Andre and A. A. Lucas. (1988), 'Surface Curvature Effects in Physisorption and Catalysis by Microporous Solids and Molecular-Sieves', *Journal of Catalysis* Vol. 110, No. 1, pp. 58-73.

Derouane, E. G., J. C. Vedrine, R. R. Pinto, P. M. Borges, L. Costa, M. Lemos, F. Lemos and F. R. Ribeiro. (2013), 'The Acidity of Zeolites: Concepts, Measurements and Relation to Catalysis: A Review on Experimental and Theoretical Methods for the Study of Zeolite Acidity', *Catalysis Reviews-Science and Engineering* Vol. 55, No. 4, pp. 454-515.

Diaz, C. D. C., S. Locatelli and E. E. Gonzo. (1992), 'Acetaldehyde Adsorption on Hzsm-5 Studies by Infrared-Spectroscopy', *Zeolites* Vol. 12, No. 7, pp. 851-857.

Diaz, L., A. Sierraalta, M. A. C. Nascimento and R. Anez. (2013), 'Evaluation of Bronsted Sites inside the H-Mor Employing Nh3: A Theoretical Study', *Journal of Physical Chemistry C* Vol. 117, No. 10, pp. 5112-5117.

Dick, B. G. and A. W. Overhauser. (1958), 'Theory of the Dielectric Constants of Alkali Halide Crystals', *Physical Review* Vol. 112, No. 1, pp. 90-103.

DiCosimo, J. I., V. K. Diez and C. R. Apesteguia. (1996), 'Base Catalysis for the Synthesis of Alpha,Beta-Unsaturated Ketones from the Vapor-Phase Aldol Condensation of Acetone', *Applied Catalysis a-General* Vol. 137, No. 1, pp. 149-166.

Dominguez-Soria, V. D., P. Calaminici and A. Goursot. (2007), 'Theoretical Study of the Structure and Properties of Na-Mor and H-Mor Zeolite Models', *Journal of Chemical Physics* Vol. 127, No. 15, pp. 8.

Domokos, L., L. Lefferts, K. Seshan and J. A. Lercher. (2000), 'The Importance of Acid Site Locations for N-Butene Skeletal Isomerization on Ferrierite', *Journal of Molecular Catalysis a-Chemical* Vol. 162, No. 1-2, pp. 147-157.

Dovesi, R., R. Orlando, B. Civalleri, C. Roetti, V. R. Saunders and C. M. Zicovich-Wilson. (2005), 'Crystal: A Computational Tool for the Ab Initio Study of the Electronic Properties of Crystals', *Zeitschrift Fur Kristallographie* Vol. 220, No. 5-6, pp. 571-573.

Dumitriu, E., V. Hulea, I. Fechete, A. Auroux, J. F. Lacaze and C. Guimon. (2001), 'The Aldol Condensation of Lower Aldehydes over Mfi Zeolites with Different Acidic Properties', *Microporous and Mesoporous Materials* Vol. 43, No. 3, pp. 341-359.

Dwyer, J. and P. J. OMalley. (1988), 'Keynotes in Energy-Related Catalysis', *Studies in Surface Sciences and Catalysis*, Kaliaguine, S.

Ehresmann, J. O., W. Wang, B. Herreros, D. P. Luigi, T. N. Venkatraman, W. G. Song, J. B. Nicholas and J. F. Haw. (2002), 'Theoretical and Experimental Investigation of the Effect of Proton Transfer on the Al-27 Mas Nmr Line Shapes of Zeolite-Adsorbate Complexes: An Independent Measure of Solid Acid Strength', *Journal of the American Chemical Society* Vol. 124, No. 36, pp. 10868-10874.

Faba, L., E. Diaz and S. Ordonez. (2013), 'Gas Phase Acetone Self-Condensation over Unsupported and Supported Mg-Zr Mixed-Oxides Catalysts', *Applied Catalysis B-Environmental* Vol. 142, pp. 387-395.

Farneth, W. E. and R. J. Gorte. (1995), 'Methods for Characterizing Zeolite Acidity', *Chemical Reviews* Vol. 95, No. 3, pp. 615-635.

Feng, P., X. F. Chen, X. J. Li, D. Zhao, S. J. Xie, L. Y. Xu and G. Z. He. (2017), 'The Distribution Analysis on the Proton Siting and the Acid Strength of the Zeolite Ferrierite: A Computational Study', *Microporous and Mesoporous Materials* Vol. 239, pp. 354-362.

Filippi, C., C. J. Umrigar and M. Taut. (1994), 'Comparison of Exact and Approximate Density Functionals for an Exactly Soluble Model', *Journal of Chemical Physics* Vol. 100, No. 2, pp. 1290-1296.

Flanigen, E. M. (2001), 'Zeolites and Molecular Sieves: An Historical Perspective', *Introduction to Zeolite Science and Practice*.

Florian, J. and L. Kubelkova. (1994), 'Proton-Transfer between H-Zeolite and Adsorbed Acetone or Acetonitrile - Quantum-Chemical and Ftir Study', *Journal of Physical Chemistry* Vol. 98, No. 35, pp. 8734-8741.

Gabriels, D., W. Y. Hernandez, B. Sels, P. Van Der Voort and A. Verberckmoes. (2015), 'Review of Catalytic Systems and Thermodynamics for the Guerbet Condensation Reaction and Challenges for Biomass Valorization', *Catalysis Science & Technology* Vol. 5, No. 8, pp. 3876-3902.

Gale, J. D. and N. J. Henson. (1994), 'Derivation of Interatomic Potentials for Microporous Aluminophosphates from the Structure and Properties of Berlinite', *Journal of the Chemical Society-Faraday Transactions* Vol. 90, No. 20, pp. 3175-3179.

Gale, J. D. and A. L. Rohl. (2003), 'The General Utility Lattice Program (Gulp)', *Molecular Simulation* Vol. 29, No. 5, pp. 291-341.

Garrone, E., R. Bulanek, K. Frolich, C. O. Arean, M. R. Delgado, G. T. Palomino, D. Nachtigallova and P. Nachtigall. (2006), 'Single and Dual Cation Sites in Zeolites: Theoretical Calculations and Ftir Spectroscopic Studies on Co Adsorption on K-Fer', *Journal of Physical Chemistry B* Vol. 110, No. 45, pp. 22542-22550.

Gherman, B. F., R. A. Friesner, T. H. Wong, Z. Y. Min and R. Bersohn. (2001), 'Photodissociation of Acetaldehyde: The Ch4+Co Channel', *Journal of Chemical Physics* Vol. 114, No. 14, pp. 6128-6133.

Glendening, E. D. and D. Feller. (1995), 'Cation Water Interactions - the M(+)(H2o)(N) Clusters for Alkali-Metals, M=Li, Na, K, Rb, and Cs', *Journal of Physical Chemistry* Vol. 99, No. 10, pp. 3060-3067.

Goltl, F., A. Gruneis, T. Bucko and J. Hafner. (2012), 'Van Der Waals Interactions between Hydrocarbon Molecules and Zeolites: Periodic Calculations at Different Levels of Theory, from Density Functional Theory to the Random Phase Approximation and Moller-Plesset Perturbation Theory', *Journal of Chemical Physics* Vol. 137, No. 11, pp. 17.

Gomes, J., P. M. Zimmerman, M. Head-Gordon and A. T. Bell. (2012), 'Accurate Prediction of Hydrocarbon Interactions with Zeolites Utilizing Improved Exchange-Correlation Functionals and Qm/Mm Methods: Benchmark Calculations of Adsorption Enthalpies and Application to Ethene Methylation by Methanol', *Journal of Physical Chemistry C* Vol. 116, No. 29, pp. 15406-15414.

Gorte, R. J. and D. White. (1997), 'Interactions of Chemical Species with Acid Sites in Zeolites', *Topics in Catalysis* Vol. 4, No. 1-2, pp. 57-69.

Gounder, R. and E. Iglesia. (2012), 'The Roles of Entropy and Enthalpy in Stabilizing Ion-Pairs at Transition States in Zeolite Acid Catalysis', *Accounts of Chemical Research* Vol. 45, No. 2, pp. 229-238.

Grajciar, L., C. O. Arean, A. Pulido and P. Nachtigall. (2010), 'Periodic Dft Investigation of the Effect of Aluminium Content on the Properties of the Acid Zeolite H-Fer', *Physical Chemistry Chemical Physics* Vol. 12, No. 7, pp. 1497-1506.

Grimme, S. (2004), 'Accurate Description of Van Der Waals Complexes by Density Functional Theory Including Empirical Corrections', *Journal of Computational Chemistry* Vol. 25, No. 12, pp. 1463-1473.

Grimme. S. (2006), 'Semiempirical Gga-Type Density Functional Constructed with a Long-Range Dispersion Correction', *Journal of Computational Chemistry* Vol. 27, No. 15, pp. 1787-1799.

Guisnet, M., P. Ayrault and J. Datka. (1997), 'Acid Properties of Dealuminated Mordenites Studied by Ir Spectroscopy .1. Accessibility of Acid Sites and Their Interaction with Adsorbed Molecules', *Polish Journal of Chemistry* Vol. 71, No. 10, pp. 1445-1454.

Haw, J. F., W. G. Song, D. M. Marcus and J. B. Nicholas. (2003), 'The Mechanism of Methanol to Hydrocarbon Catalysis', *Accounts of Chemical Research* Vol. 36, No. 5, pp. 317-326.

Hohenberg, P. and W. Kohn. (1964), 'Inhomogeneous Electron Gas', *Physical Review B* Vol. 136, No. 3B, pp. B864-+.

Holmes, J. L. and F. P. Lossing. (1982), 'Heats of Formation of the Ionic and Neutral Enols of Acetaldehyde and Acetone', *Journal of the American Chemical Society* Vol. 104, No. 9, pp. 2648-2649.

Houzvicka, J. and V. Ponec. (1997), 'Skeletal Isomerization of N-Butene', *Catalysis Reviews-Science and Engineering* Vol. 39, No. 4, pp. 319-344.

Huo, H., L. M. Peng, Z. H. Gan and C. P. Grey. (2012), 'Solid-State Mas Nmr Studies of Bronsted Acid Sites in Zeolite H-Mordenite', *Journal of the American Chemical Society* Vol. 134, No. 23, pp. 9708-9720.

Jackson, R. A. and C. R. A. Catlow. (1988), 'Computer Simulation Studies of Zeolite Structure', *Molecular Simulation* Vol. 1, No. 4, pp. 207-U27.

Ji, W. J., Y. Chen and H. H. Kung. (1997), 'Vapor Phase Aldol Condensation of Acetaldehyde on Metal Oxide Catalysts', *Applied Catalysis a-General* Vol. 161, No. 1-2, pp. 93-104.

Jones, A. J. and E. Iglesia. (2015), 'The Strength of Bronsted Acid Sites in Microporous Aluminosilicates', *Acs Catalysis* Vol. 5, No. 10, pp. 5741-5755.

Jones, J. E. (1924), 'On the Determinations of Molecular Fields - 1 from the Variation of the Viscosity of a Gas with Temperature', *Proceedings of the Royal Society of London Series a-Containing Papers of a Mathematical and Physical Character* Vol. 106, No. 738, pp. 441-462.

Kassab, E., H. Jessri, M. Allavena and D. White. (1999), 'Ab Initio Calculations of Carbonyl Adsorption Complexes at Zeolitic Bronsted Sites Simulated by

Model Clusters: Role of Modeling', *Journal of Physical Chemistry A* Vol. 103, No. 15, pp. 2766-2774.

Katada, N., K. Suzuki, T. Noda, G. Sastre and M. Niwa. (2009), 'Correlation between Bronsted Acid Strength and Local Structure in Zeolites', *Journal of Physical Chemistry C* Vol. 113, No. 44, pp. 19208-19217.

Kaupp, M. and P. V. Schleyer. (1992), 'Do Low-Coordinated Group-1-3 Cations M(N+)L(M) (M(N+) = K+, Rb+, Cs+, Ca2+, Sr2+, Ba2+, Sc3+, Y3+, La3+, L = Nh3, H2o, Hf, M = 1-3) with a Formal Noble-Gas Electron Configuration Favor Regular or Abnormal Shapes', *Journal of Physical Chemistry* Vol. 96, No. 18, pp. 7316-7323.

Kaweetirawatt, T., T. Yamaguchi, T. Higashiyama, M. Sumimoto and K. Hori. (2012), 'Theoretical Study of Keto-Enol Tautomerism by Quantum Mechanical Calculations (the Qm/Mc/Fep Method)', *Journal of Physical Organic Chemistry* Vol. 25, No. 12, pp. 1097-1104.

Klein, P., J. Dedecek, H. M. Thomas, S. R. Whittleton, V. Pashkova, J. Brus, L. Kobera and S. Sklenak. (2015), 'Nmr Crystallography of Monovalent Cations in Inorganic Matrixes: Li+ Siting and the Local Structure of Li+ Sites in Ferrierites', *Chemical Communications* Vol. 51, No. 43, pp. 8962-8965.

Klimes, J. and A. Michaelides. (2012), 'Perspective: Advances and Challenges in Treating Van Der Waals Dispersion Forces in Density Functional Theory', *Journal of Chemical Physics* Vol. 137, No. 12, pp. 12.

Kohn, W. and L. J. Sham. (1965), 'Self-Consistent Equations Including Exchange and Correlation Effects', *Physical Review* Vol. 140, No. 4A, pp. 1133-&.

Kozlowski, J. T. and R. J. Davis. (2013), 'Heterogeneous Catalysts for the Guerbet Coupling of Alcohols', *Acs Catalysis* Vol. 3, No. 7, pp. 1588-1600.

Krack, M. (2005), 'Pseudopotentials for H to Kr Optimized for Gradient-Corrected Exchange-Correlation Functionals', *Theoretical Chemistry Accounts* Vol. 114, No. 1-3, pp. 145-152.

Kubelkova, L., J. Cejka and J. Novakoya. (1991), 'Surface Reactivity of Zsm-5 Zeolites in Interaction with Ketones at Ambient-Temperature (a Ft-Ir Study)', *Zeolites* Vol. 11, No. 1, pp. 48-53.

Kubelkova, L. and J. Novakova. (1991), 'Temperature-Programmed Desorption and Conversion of Acetone and Diethyl Ketone Preadsorbed on Hzsm-5', *Zeolites* Vol. 11, No. 8, pp. 822-826.

Kunkes, E. L., E. I. Gurbuz and J. A. Dumesic. (2009), 'Vapour-Phase C-C Coupling Reactions of Biomass-Derived Oxygenates over Pd/Cezrox Catalysts', *Journal of Catalysis* Vol. 266, No. 2, pp. 236-249.

Lammertsma, K. and B. V. Prasad. (1994), 'Imine-Reversible-Arrow-Enamine Tautomerism', *Journal of the American Chemical Society* Vol. 116, No. 2, pp. 642-650.

Lazo, N. D., B. R. Richardson, P. D. Schettler, J. L. White, E. J. Munson and J. F. Haw. (1991), 'Insitu Variable-Temperature Mas C-13 Nmr-Study of the Reactions of Isobutylene in Zeolites Hy and Hzsm-5', *Journal of Physical Chemistry* Vol. 95, No. 23, pp. 9420-9425.

Lee, C. T., W. T. Yang and R. G. Parr. (1988), 'Development of the Colle-Salvetti Correlation-Energy Formula into a Functional of the Electron-Density', *Physical Review B* Vol. 37, No. 2, pp. 785-789.

Lee, D., C. K. Kim, B. S. Lee, I. Lee and B. C. Lee. (1997), 'A Theoretical Study on Keto-Enol Tautomerization Involving Simple Carbonyl Derivatives', *Journal of Computational Chemistry* Vol. 18, No. 1, pp. 56-69.

Lee, S. O., S. J. Kitchin, K. D. M. Harris, G. Sankar, M. Dugal and J. M. Thomas. (2002), 'Acid-Catalyzed Trimerization of Acetaldehyde: A Highly Selective and Reversible Transformation at Ambient Temperature in a Zeolitic Solid', *Journal of Physical Chemistry B* Vol. 106, No. 6, pp. 1322-1326.

Lercher, J. A., C. Grundling and G. EderMirth. (1996), 'Infrared Studies of the Surface Acidity of Oxides and Zeolites Using Adsorbed Probe Molecules', *Catalysis Today* Vol. 27, No. 3-4, pp. 353-376.

Liu, C., I. Tranca, R. A. van Santen, E. J. M. Hensen and E. A. Pidko. (2017), 'Scaling Relations for Acidity and Reactivity of Zeolites', *Journal of Physical Chemistry C* Vol. 121, No. 42, pp. 23520-23530.

Liu, R., J. Zhang, X. L. Sun, C. P. Huang and B. H. Chen. (2014), 'An Oniom Study on the Distribution, Local Structure and Strength of Bronsted Acid Sites in Fer Zeolite', *Computational and Theoretical Chemistry* Vol. 1027, pp. 5-10.

Loewenstein, W. (1954), 'The Distribution of Aluminum in the Tetrahedra of Silicates and Aluminates', *American Mineralogist* Vol. 39, No. 1-2, pp. 92-96.

Lukyanov, D. B., T. Vazhnova, J. L. Casci and J. J. Birtill. (2004), 'On the Catalytic Properties of Bronsted Acid Sites Located in the Small and Large Channels in

Zeolite Mordenite', *Book of Abstracts 1:13th International Congress on Catalysis*.

Lukyanov, D. B., T. Vazhnova, N. Cherkasov, J. L. Casci and J. J. Birtill. (2014), 'Insights into Bronsted Acid Sites in the Zeolite Mordenite', *Journal of Physical Chemistry C* Vol. 118, No. 41, pp. 23918-23929.

Makarova, M. A., A. E. Wilson, B. J. vanLiemt, C. Mesters, A. W. deWinter and C. Williams. (1997), 'Quantification of Bronsted Acidity in Mordenites', *Journal of Catalysis* Vol. 172, No. 1, pp. 170-177.

Marcus, R. A. (1966), 'On Analytical Mechanics of Chemical Reactions . Quantum Mechanics of Linear Collisions', *Journal of Chemical Physics* Vol. 45, No. 12, pp. 4493-+.

Marie, O., P. Massiani and F. Thibault-Starzyk. (2004), 'Infrared Evidence of a Third Bronsted Site in Mordenites', *Journal of Physical Chemistry B* Vol. 108, No. 16, pp. 5073-5081.

Martucci, A., G. Cruciani, A. Alberti, C. Ritter, P. Ciambelli and M. Rapacciuolo. (2000), 'Location of Bronsted Sites in D-Mordenites by Neutron Powder Diffraction', *Microporous and Mesoporous Materials* Vol. 35-6, pp. 405-412.

Maslov, S. A. and E. A. Blyumberg. (1976), 'Liquid-Phase Oxidation of Aldehydes', *Uspekhi Khimii* Vol. 45, No. 2, pp. 303-328.

Maurin, G., R. G. Bell, S. Devautour, F. Henn and J. C. Giuntini. (2004), 'Modeling the Effect of Hydration in Zeolite Na+-Mordenite', *Journal of Physical Chemistry B* Vol. 108, No. 12, pp. 3739-3745.

McCusker, L. B. (2007), 'Zeolites Structure', *Introduction to Zeolite Molecular Sieves*, ELSEVIER SCIENCE & TECHNOLOGY.

Meier. (1968), 'Zeolite Structures', *Molecular Sieves*, Journal of Society of Chemical Industry.

Meier, W. M. (1986), 'Zeolites and Zeolite-Like Materials', *Pure and Applied Chemistry* Vol. 58, No. 10, pp. 1323-1328.

Migues, A. N., S. Vaitheeswaran and S. M. Auerbach. (2014), 'Dft Study of the Mixed Aldol Condensation Reaction Catalyzed by Acidic Zeolites Hzsm-5 and Hy', *Abstracts of Papers of the American Chemical Society* Vol. 248.

Mills, G. and H. Jonsson. (1994), 'Quantum and Thermal Effects in H-2 Dissociative Adsorption - Evaluation of Free-Energy Barriers in Multidimensional Quantum-Systems', *Physical Review Letters* Vol. 72, No. 7, pp. 1124-1127.

Mimura, H., K. Akiba and H. Igarashi. (1994), 'Elution Behavior of Cesium from Ferrierite Column by Using Inorganic Salt and Acid-Solutions', *Journal of Nuclear Science and Technology* Vol. 31, No. 7, pp. 711-715.

Mishin, I. V., A. L. Klyachko, G. I. Kapustin and H. G. Karge. (1993), 'The Effect of Exchange Degree on the Heterogeneity of Acid Sites in Decationated Mordenites', *Kinetics and Catalysis* Vol. 34, No. 5, pp. 828-834.

Monkhorst, H. J. and J. D. Pack. (1976), 'Special Points for Brillouin-Zone Integrations', *Physical Review B* Vol. 13, No. 12, pp. 5188-5192.

Mooiweer, H. H., K. P. Dejong, B. Kraushaarczarnetzki, W. H. J. Stork and B. C. H. Krutzen. (1994), 'Skeletal Isomerization of Olefins with the Zeolite Ferrierite as Catalyst', *Zeolites and Related Microporous Materials: State of the Art 1994* Vol. 84, pp. 2327-2334.

Morris, R. E., S. J. Weigel, N. J. Henson, L. M. Bull, M. T. Janicke, B. F. Chmelka and A. K. Cheetham. (1994), 'A Synchrotron X-Ray-Diffraction, Neutron-Diffraction, Si-29 Mas-Nmr, and Computational Study of the Siliceous Form of Zeolite Ferrierite', *Journal of the American Chemical Society* Vol. 116, No. 26, pp. 11849-11855.

Morse, P. M. (1929), 'Diatomic Molecules According to the Wave Mechanics. Ii. Vibrational Levels', *Physical Review* Vol. 34, No. 1, pp. 57-64.

Mortier, W. J., J. J. Pluth and J. V. Smith. (1975), 'Positions of Cations and Molecules in Zeolites with Mordenite-Type Framework .2. Dehydrated Hydrogen-Ptilolite', *Materials Research Bulletin* Vol. 10, No. 12, pp. 1319-1325.

Munson, E. J. and J. F. Haw. (1993), 'Reaction Tuning in Zeolites - an Insitu Mas Nmr-Study of Acetaldehyde on Hzsm-5', *Angewandte Chemie-International Edition in English* Vol. 32, No. 4, pp. 615-617.

Nachtigall, P., O. Bludsky, L. Grajciar, D. Nachtigallova, M. R. Delgado and C. O. Arean. (2009), 'Computational and Ftir Spectroscopic Studies on Carbon Monoxide and Dinitrogen Adsorption on a High-Silica H-Fer Zeolite', *Physical Chemistry Chemical Physics* Vol. 11, No. 5, pp. 791-802.

Nachtigallova, D., P. Nachtigall, M. Sierka and J. Sauer. (1999), 'Coordination and Siting of Cu+ Ions in Zsm-5: A Combined Quantum Mechanics Interatomic

Potential Function Study', *Physical Chemistry Chemical Physics* Vol. 1, No. 8, pp. 2019-2026.

Namuangruk, S., P. Khongpracha, P. Pantu and J. Limtrakul. (2006), 'Structures and Reaction Mechanisms of Propene Oxide Isomerization on H-Zsm-5: An Oniom Study', *Journal of Physical Chemistry B* Vol. 110, No. 51, pp. 25950-25957.

Niwa, M., K. Suzuki, N. Katada, T. Kanougi and T. Atoguchi. (2005), 'Ammonia Irms-Tpd Study on the Distribution of Acid Sites in Mordenite', *Journal of Physical Chemistry B* Vol. 109, No. 40, pp. 18749-18757.

Olson, D. H., G. T. Kokotailo, S. L. Lawton and W. M. Meier. (1981), 'Crystal-Structure and Structure-Related Properties of Zsm-5', *Journal of Physical Chemistry* Vol. 85, No. 15, pp. 2238-2243.

Oumi, Y., T. Kanai, B. W. Lu and T. Sano. (2007), 'Structural and Physico-Chemical Properties of High-Silica Mordenite', *Microporous and Mesoporous Materials* Vol. 101, No. 1-2, pp. 127-133.

Panov, A. G. and J. J. Fripiat. (1998), 'Acetone Condensation Reaction on Acid Catalysts', *Journal of Catalysis* Vol. 178, No. 1, pp. 188-197.

Parrillo, D. J. and R. J. Gorte. (1993), 'Characterization of Acidity in H-Zsm-5, H-Zsm-12, H-Mordenite, and H-Y Using Microcalorimetry', *Journal of Physical Chemistry* Vol. 97, No. 34, pp. 8786-8792.

Pellet, R. J., C. S. Blackwell and J. A. Rabo. (1988), 'Catalytic Cracking Studies and Characterization of Steamed Y-Zeolites and Lz-210-Zeolites', *Journal of Catalysis* Vol. 114, No. 1, pp. 71-89.

Perdew, J. P., K. Burke and M. Ernzerhof. (1996), 'Generalized Gradient Approximation Made Simple', *Physical Review Letters* Vol. 77, No. 18, pp. 3865-3868.

Perdew, J. P. and Y. Wang. (1992), 'Accurate and Simple Analytic Representation of the Electron-Gas Correlation-Energy', *Physical Review B* Vol. 45, No. 23, pp. 13244-13249.

Pickering, I. J., P. J. Maddox, J. M. Thomas and A. K. Cheetham. (1989), 'A Neutron Powder Diffraction Analysis of Potassium-Exchanged Ferrierite', *Journal of Catalysis* Vol. 119, No. 1, pp. 261-265.

Pieterse, J. A. Z., S. Veefkind-Reyes, K. Seshan, L. Domokos and J. A. Lercher. (1999), 'On the Accessibility of Acid Sites in Ferrierite for Pyridine', *Journal of Catalysis* Vol. 187, No. 2, pp. 518-520.

Pinar, A. B., L. Gomez-Hortiguela, L. B. McCusker and J. Perez-Pariente. (2013), 'Controlling the Aluminum Distribution in the Zeolite Ferrierite Via the Organic Structure Directing Agent', *Chemistry of Materials* Vol. 25, No. 18, pp. 3654-3661.

Pinar, A. B., C. Marquez-Alvarez, M. Grande-Casas and J. Perez-Pariente. (2009), 'Template-Controlled Acidity and Catalytic Activity of Ferrierite Crystals', *Journal of Catalysis* Vol. 263, No. 2, pp. 258-265.

Rekoske, J. E. and M. A. Barteau. (2011), 'Kinetics, Selectivity, and Deactivation in the Aldol Condensation of Acetaldehyde on Anatase Titanium Dioxide', *Industrial & Engineering Chemistry Research* Vol. 50, No. 1, pp. 41-51.

Resasco, D. E., B. Wang and S. Crossley. (2016), 'Zeolite-Catalysed C-C Bond Forming Reactions for Biomass Conversion to Fuels and Chemicals', *Catalysis Science & Technology* Vol. 6, No. 8, pp. 2543-2559.

Rodriguez-Santiago, L., O. Vendrell, I. Tejero, M. Sodupe and J. Bertran. (2001), 'Solvent-Assisted Catalysis in the Enolization of Acetaldehyde Radical Cation', *Chemical Physics Letters* Vol. 334, No. 1-3, pp. 112-118.

Roman-Leshkov, Y., M. Moliner and M. E. Davis. (2011), 'Impact of Controlling the Site Distribution of Al Atoms on Catalytic Properties in Ferrierite-Type Zeolites', *Journal of Physical Chemistry C* Vol. 115, No. 4, pp. 1096-1102.

Rowlinson, J. S. (1986), 'The Lennard-Jones Lecture - the Statistical-Mechanics of Small Systems', *Journal of the Chemical Society-Faraday Transactions Ii* Vol. 82, pp. 1801-1815.

Salvapati, G. S., K. V. Ramanamurty and M. Janardanarao. (1989), 'Selective Catalytic Self-Condensation of Acetone', *Journal of Molecular Catalysis* Vol. 54, No. 1, pp. 9-30.

Sanders, M. J., M. Leslie and C. R. A. Catlow. (1984), 'Interatomic Potentials for Sio2', *Journal of the Chemical Society-Chemical Communications*, No. 19, pp. 1271-1273.

Sandoval-Diaz, L. E., J. A. Gonzalez-Amaya and C. A. Trujillo. (2015), 'General Aspects of Zeolite Acidity Characterization', *Microporous and Mesoporous Materials* Vol. 215, pp. 229-243.

Sankaranarayanapillai, S., S. Sreekumar, J. Gomes, A. Grippo, G. E. Arab, M. Head-Gordon, F. D. Toste and A. T. Bell. (2015), 'Catalytic Upgrading of Biomass-Derived Methyl Ketones to Liquid Transportation Fuel Precursors by an Organocatalytic Approach', *Angewandte Chemie-International Edition* Vol. 54, No. 15, pp. 4673-4677.

Sarv, P., B. Wichterlova and J. Cejka. (1998), 'Multinuclear Mqmas Nmr Study of Nh4/Na-Ferrierites', *Journal of Physical Chemistry B* Vol. 102, No. 8, pp. 1372-1378.

Sato, H. (1997), 'Acidity Control and Catalysis of Pentasil Zeolites', *Catalysis Reviews-Science and Engineering* Vol. 39, No. 4, pp. 395-424.

Sauer, J. (1989), 'Molecular Models in Ab Initio Studies of Solids and Surfaces: From Ionic Crystals and Semiconductors to Catalysts', *Chemical Reviews* Vol. 89, No. 1, pp. 199-255.

Sauer, J. and M. Sierka. (2000), 'Combining Quantum Mechanics and Interatomic Potential Functions in Ab Initio Studies of Extended Systems', *Journal of Computational Chemistry* Vol. 21, No. 16, pp. 1470-1493.

Sauer, J., P. Ugliengo, E. Garrone and V. R. Saunders. (1994), 'Theoretical-Study of Van-Der-Waals Complexes at Surface Sites in Comparison with the Experiment', *Chemical Reviews* Vol. 94, No. 7, pp. 2095-2160.

Saul, P., C. R. A. Catlow and J. Kendrick. (1985), 'Theoretical-Studies of Protons in Sodium-Hydroxide', *Philosophical Magazine B-Physics of Condensed Matter Statistical Mechanics Electronic Optical and Magnetic Properties* Vol. 51, No. 2, pp. 107-117.

Schroder, K. P., J. Sauer, M. Leslie and C. R. A. Catlow. (1992), 'Siting of Al and Bridging Hydroxyl-Groups in Zsm-5 - a Computer-Simulation Study', *Zeolites* Vol. 12, No. 1, pp. 20-23.

Schrodinger, E. (1926), 'An Undulatory Theory of the Mechanics of Atoms and Molecules', *Physical Review* Vol. 28, No. 6, pp. 1049-1070.

Sepa, J., C. Lee, R. J. Gorte, D. White, E. Kassab, E. M. Evleth, H. Jessri and M. Allavena. (1996), 'Carbonyl C-13 Shielding Tensors and Heats of Adsorption of Acetone Adsorbed in Silicalite and the 1:1 Stoichiometric Complex in H-Zsm-5', *Journal of Physical Chemistry* Vol. 100, No. 47, pp. 18515-18523.

Simperler, A., R. G. Bell, M. D. Foster, A. E. Gray, D. W. Lewis and M. W. Anderson. (2004), 'Probing the Acid Strength of Bronsted Acidic Zeolites with

Acetonitrile: An Atomistic and Quantum Chemical Study', *Journal of Physical Chemistry B* Vol. 108, No. 22, pp. 7152-7161.

Smit, B. and T. L. M. Maesen. (2008), 'Molecular Simulations of Zeolites: Adsorption, Diffusion, and Shape Selectivity', *Chemical Reviews* Vol. 108, No. 10, pp. 4125-4184.

Smit, B. and T. L. M. Maesen. (2008), 'Towards a Molecular Understanding of Shape Selectivity', *Nature* Vol. 451, No. 7179, pp. 671-678.

Smith, J. V. (1988), 'Topochemistry of Zeolites and Related Materials .1. Topology and Geometry', *Chemical Reviews* Vol. 88, No. 1, pp. 149-182.

Solans-Monfort, X., J. Bertran, V. Branchadell and M. Sodupe. (2002), 'Keto-Enol Isomerization of Acetaldehyde in Hzsm5. A Theoretical Study Using the Oniom2 Method', *Journal of Physical Chemistry B* Vol. 106, No. 39, pp. 10220-10226.

Spiewak, B. E., B. E. Handy, S. B. Sharma and J. A. Dumesic. (1994), 'Microcalorimetric Studies of Ammonia Adsorption on Gamma-Al2o3, Hna-Y Zeolite, and H-Mordenite', *Catalysis Letters* Vol. 23, No. 3-4, pp. 207-213.

Stephens, P. J., F. J. Devlin, C. F. Chabalowski and M. J. Frisch. (1994), 'Ab-Initio Calculation of Vibrational Absorption and Circular-Dichroism Spectra Using Density-Functional Force-Fields', *Journal of Physical Chemistry* Vol. 98, No. 45, pp. 11623-11627.

Stevenson, D. P., H. D. Burnham and V. Schomaker. (1939), 'The Molecular Structure of Acetaldehyde', *Journal of the American Chemical Society* Vol. 61, No. 10, pp. 2922-2925.

Subrahmanyam, A. V., S. Thayumanavan and G. W. Huber. (2010), 'C-C Bond Formation Reactions for Biomass-Derived Molecules', *Chemsuschem* Vol. 3, No. 10, pp. 1158-1161.

Suenobu, K., M. Nagaoka and T. Yamabe. (1999), 'The Faster Conversion of Ethene Thiol Than Vinyl Alcohol in Tautomerization Reactions in Aqueous Solution - Theoretical Prediction', *Journal of Molecular Structure-Theochem* Vol. 461, pp. 581-588.

Svensson, M., S. Humbel, R. D. J. Froese, T. Matsubara, S. Sieber and K. Morokuma. (1996), 'Oniom: A Multilayered Integrated Mo+Mm Method for Geometry Optimizations and Single Point Energy Predictions. A Test for Diels-Alder Reactions and Pt(P(T-Bu)(3))(2)+H-2 Oxidative Addition', *Journal of Physical Chemistry* Vol. 100, No. 50, pp. 19357-19363.

Taarning, E., C. M. Osmundsen, X. B. Yang, B. Voss, S. I. Andersen and C. H. Christensen. (2011), 'Zeolite-Catalyzed Biomass Conversion to Fuels and Chemicals', *Energy & Environmental Science* Vol. 4, No. 3, pp. 793-804.

Tapuhi, E. and W. P. Jencks. (1982), 'Base-Catalyzed Halogenation of Acetone', *Journal of the American Chemical Society* Vol. 104, No. 21, pp. 5758-5765.

Trombetta, M., G. Busca, S. Rossini, V. Piccoli, U. Cornaro, A. Guercio, R. Catani and R. J. Willey. (1998), 'Ft-Ir Studies on Light Olefin Skeletal Isomerization Catalysis Iii. Surface Acidity and Activity of Amorphous and Crystalline Catalysts Belonging to the Sio(2)-Al(2)O(3) System', *Journal of Catalysis* Vol. 179, No. 2, pp. 581-596.

Tsuchida, T., J. Kubo, T. Yoshioka, S. Sakuma, T. Takeguchi and W. Ueda. (2008), 'Reaction of Ethanol over Hydroxyapatite Affected by Ca/P Ratio of Catalyst', *Journal of Catalysis* Vol. 259, No. 2, pp. 183-189.

Tsutsumi, K. and K. Nishimiya. (1989), 'Differential Molar Heats of Adsorption of Ammonia on Silicious Mordenites at High-Temperature', *Thermochimica Acta* Vol. 143, pp. 299-309.

Ugliengo, P., D. Viterbo and G. Chiari. (1993), 'Moldraw - Molecular Graphics on a Personal-Computer', *Zeitschrift Fur Kristallographie* Vol. 207, pp. 9-23.

Van Reenen, C. G., B. Engel, L. F. M. Ruis-Heutinck, J. T. N. Van der Werf, W. G. Buist, R. B. Jones and H. J. Blokhuis. (2004), 'Behavioural Reactivity of Heifer Calves in Potentially Alarming Test Situations: A Multivariate and Correlational Analysis', *Applied Animal Behaviour Science* Vol. 85, No. 1-2, pp. 11-30.

Van Santen, R. A. and G. J. Kramer. (1995), 'Reactivity Theory of Zeolitic Broensted Acidic Sites', *Chemical Reviews* Vol. 95, No. 3, pp. 637-660.

Van Speybroeck, V., K. Hemelsoet, L. Joos, M. Waroquier, R. G. Bell and C. R. A. Catlow. (2015), 'Advances in Theory and Their Application within the Field of Zeolite Chemistry', *Chemical Society Reviews* Vol. 44, No. 20, pp. 7044-7111.

VandeVondele, J. and J. Hutter. (2007), 'Gaussian Basis Sets for Accurate Calculations on Molecular Systems in Gas and Condensed Phases', *Journal of Chemical Physics* Vol. 127, No. 11, pp. 9.

VandeVondele, J., M. Krack, F. Mohamed, M. Parrinello, T. Chassaing and J. Hutter. (2005), 'Quickstep: Fast and Accurate Density Functional Calculations Using a Mixed Gaussian and Plane Waves Approach', *Computer Physics Communications* Vol. 167, No. 2, pp. 103-128.

Vansanten, R. A. and G. J. Kramer. (1995), 'Reactivity Theory of Zeolitic Bronsted Acidic Sites', *Chemical Reviews* Vol. 95, No. 3, pp. 637-660.

Vaughan, P. A. (1966), 'Crystal Structure of Zeolite Ferrierite', *Acta Crystallographica* Vol. 21, pp. 983-&.

Verlet, L. (1967), 'Computer Experiments on Classical Fluids .I. Thermodynamical Properties of Lennard-Jones Molecules', *Physical Review* Vol. 159, No. 1, pp. 98-+.

Vosko, S. H., L. Wilk and M. Nusair. (1980), 'Accurate Spin-Dependent Electron Liquid Correlation Energies for Local Spin-Density Calculations - a Critical Analysis', *Canadian Journal of Physics* Vol. 58, No. 8, pp. 1200-1211.

Wang, C. M., R. Y. Brogaard, B. M. Weckhuysen, J. K. Norskov and F. Studt. (2014), 'Reactivity Descriptor in Solid Acid Catalysis: Predicting Turnover Frequencies for Propene Methylation in Zeotypes', *Journal of Physical Chemistry Letters* Vol. 5, No. 9, pp. 1516-1521.

Wichterlova, B., N. Zilkova, E. Uvarova, J. Cejka, P. Sarv, C. Paganini and J. A. Lercher. (1999), 'Effect of Broensted and Lewis Sites in Ferrierites on Skeletal Isomerization of N-Butenes', *Applied Catalysis a-General* Vol. 182, No. 2, pp. 297-308.

Wu, C. C. and M. H. Lien. (1996), 'Ab Initio Study on the Substituent Effect in the Transition State of Keto-Enol Tautomerism of Acetyl Derivatives', *Journal of Physical Chemistry* Vol. 100, No. 2, pp. 594-600.

Xu, M. C., W. Wang and M. Hunger. (2003), 'Formation of Acetone Enol on Acidic Zeolite Zsm-5 Evidenced by H/D Exchange', *Chemical Communications*, No. 6, pp. 722-723.

Xu, T., E. J. Munson and J. F. Haw. (1994), 'Toward a Systematic Chemistry of Organic-Reactions in Zeolites - in-Situ Nmr-Studies of Ketones', *Journal of the American Chemical Society* Vol. 116, No. 5, pp. 1962-1972.

Yilmaz, B. and U. Muller. (2009), 'Catalytic Applications of Zeolites in Chemical Industry', *Topics in Catalysis* Vol. 52, No. 6-7, pp. 888-895.

Zakharov, A., A. E. Masunov and A. Dreuw. (2008), 'Catalytic Role of Calix 4 Hydroquinone in Acetone-Water Proton Exchange: A Quantum Chemical

Study of Proton Transfer Via Keto-Enol Tautomerism', *Journal of Physical Chemistry A* Vol. 112, No. 41, pp. 10405-10412.

Zheng, A. M., S. H. Li, S. B. Liu and F. Deng. (2016), 'Acidic Properties and Structure-Activity Correlations of Solid Acid Catalysts Revealed by Solid-State Nmr Spectroscopy', *Accounts of Chemical Research* Vol. 49, No. 4, pp. 655-663.

Zholobenko, V. L., D. B. Lukyanov, J. Dwyer and W. J. Smith. (1998), 'Ferrierite and Suz-4 Zeolite: Characterization of Acid Sites', *Journal of Physical Chemistry B* Vol. 102, No. 15, pp. 2715-2721.

Zholobenko, V. L., M. A. Makarova and J. Dwyer. (1993), 'Inhomogeneity of Bronsted Acid Sites in H-Mordenite', *Journal of Physical Chemistry* Vol. 97, No. 22, pp. 5962-5964.